

VOLUME 31

MAY 1953

NUMBER 4

Canadian Journal of Physics

Editor: G. M. VOLKOFF

Published by THE NATIONAL RESEARCH COUNCIL
OTTAWA CANADA

CANADIAN JOURNAL OF PHYSICS

(Formerly Section A, Canadian Journal of Research)

The CANADIAN JOURNAL OF PHYSICS is published bimonthly by the National Research Council of Canada under the authority of the Chairman of the Committee of the Privy Council on Scientific and Industrial Research. Matters of general policy are the responsibility of a joint Editorial Board consisting of members of the National Research Council of Canada and the Royal Society of Canada.

The National Research Council of Canada publishes also: *Canadian Journal of Botany*, *Canadian Journal of Chemistry*, *Canadian Journal of Medical Sciences*, *Canadian Journal of Technology*, *Canadian Journal of Zoology*.

EDITORIAL BOARD

Representing

NATIONAL RESEARCH COUNCIL	ROYAL SOCIETY OF CANADA	
DR. J. H. L. JOHNSTONE (<i>Chairman</i>), Professor of Physics, Dalhousie University, Halifax, N.S.	DR. G. M. VOLKOFF, Professor of Physics, University of British Columbia, Vancouver, B.C.	} Section III
DR. OTTO MAASS, Macdonald Professor of Physical Chemistry, McGill University, Montreal, P.Q.	DR. T. THORVALDSON, Dean Emeritus of Graduate Studies, University of Saskatchewan, Saskatoon, Sask.	
DR. CHARLES W. ARGUE, Dean of Science, University of New Brunswick, Fredericton, N.B.	DR. D. L. BAILEY, Department of Botany, University of Toronto, Toronto, Ont.	} Section V
DR. A. G. MCCALLA, Dean, Faculty of Agriculture, University of Alberta, Edmonton, Alta.	DR. E. HORNE CRAIGIE, Department of Zoology, University of Toronto, Toronto, Ont.	
THE CANADIAN ASSOCIATION OF PHYSICISTS	THE CHEMICAL INSTITUTE OF CANADA	
DR. G. M. VOLKOFF, Professor of Physics, University of British Columbia, Vancouver, B.C.	DR. H. G. THODE, Department of Chemistry, McMaster University, Hamilton, Ont.	

Ex officio

DR. LÉO MARION (<i>Editor-in-Chief</i>), Director, Division of Pure Chemistry, National Research Laboratories, Ottawa.	DR. H. H. SAUNDERSON, Director, Division of Information Services, National Research Council, Ottawa.
-----------------------------------------------------------------------------------------------------------------------------------	---------------------------------------------------------------------------------------------------------------

Manuscripts should be addressed to:

DR. LÉO MARION,
Editor-in-Chief,
Canadian Journal of Physics,
National Research Council,
Ottawa, Canada.

Each manuscript should be typewritten, double-spaced, and the original and one extra copy submitted (see **Notice to Contributors** inside of back cover).

Subscriptions, renewals, and orders for back numbers should be addressed to:

Administrative Services,
National Research Council,
Ottawa, Canada.

Subscription rate: \$3.00 a year; single numbers: 50 cents. Special rates can be obtained for subscriptions to more than one of the Journals published by the National Research Council.

Canadian Journal of Physics

Issued by THE NATIONAL RESEARCH COUNCIL OF CANADA

VOLUME 31

MAY, 1953

NUMBER 4

ENERGY SELECTION OF CHARGED PARTICLES BY A MAGNETIC FIELD¹

By J. W. GARDNER²

ABSTRACT

We examine the problem of obtaining a sharply defined mono-energetic beam of particles from an omnidirectional, poly-energetic source without the use of slits. A magnetic field is suggested which will achieve this in the idealized case when the source and counter are of vanishingly small dimensions and the particles are confined to the median plane. We then investigate the proportional spread in energy ($\Delta E/E$) of particles arriving at the counter due to the finite dimensions of the source and counter and a small component of particle velocity out of the median plane. Finally some numerical estimates are made of $\Delta E/E$ and of the magnetic fields required in particular cases.

1. INTRODUCTION

A problem which arises in experimental atomic and nuclear physics is that of obtaining a sharply defined mono-energetic beam of particles without recourse to slits or other devices liable to give confusing secondary radiations. The problem may be idealized as follows: O in Fig. 1 is a point source emitting charged particles of many energies in all directions and B is a counter whose dimensions are negligible compared with its distance, a , from O . We wish to arrange that all particles emitted with some particular kinetic energy E are collected by B , and all other particles miss it. This selection is to be done without slits and therefore presumably only by using a suitable magnetic or electric field or combination of such fields; if it can be achieved with only one type of field (say magnetic) so much the simpler.

In the present paper we do not attempt to solve the problem in its most general form; we first of all consider the two-dimensional problem of designing a magnetic field which will direct into the counter only those particles of energy E whose velocities lie in a particular plane (the "median" plane, designated hereinafter as the $r-\theta$ plane). Subsequently, in considering the energy spread ΔE in E due to the finite dimensions of the source and counter, we do allow for small components of particle velocities in a direction perpendicular to the median plane (the z -direction); but no solution for the general three-dimensional problem is offered at present.

The present treatment is completely relativistic if the ' m ' in the equations of motion be taken as the relativistic mass, related to the rest mass m_0 by a Lorentz

¹ Manuscript received October 7, 1952.

Contribution from the Atomic Energy of Canada Limited, Chalk River Laboratory, Chalk River, Ont. Issued as A.E.C.L. No. 32.

² National Research Council Postdoctoral Fellow.

transformation; for the motion of a relativistic charged particle in a time-independent, purely magnetic field is that of a classical particle with the rest mass replaced by the relativistic mass (see, for example, McCrea (3)). A practical upper limit to the energies which can be handled is set by considerations of magnetic field strength and physical size of the apparatus and for this reason it was unnecessary to extend Table II of Section 6 to relativistic heavy particle energies. A lower energy limit is set (for all particles) by our neglect of such disturbing effects as stray fields and collisions, the actual value of this lower limit being determined by the conditions of any particular experiment.

2. CONDITIONS FOR ASYMPTOTIC ORBIT

The problem is clearly one of cylindrical symmetry about a z -axis through O , and the magnetic field must be everywhere parallel to Oz if the particles are to be confined to the r - θ plane. We note at once that a uniform field parallel to Oz is useless for our purpose, for in such a field a particle of charge e (e.s.u.) and (relativistic) mass m moves in a circle whose radius is fixed by the energy according to a well known relation, and it is clear from Fig. 1 that particles of any energy greater than a certain critical energy ($\sqrt{m_0^2 c^4 + (Hae)^2} - m_0 c^2$) moving in this way can reach B if emitted in the appropriate direction from O , while particles of the required energy E will miss B unless emitted in the direction OO' . After consideration one sees that what is required is a field which will cause

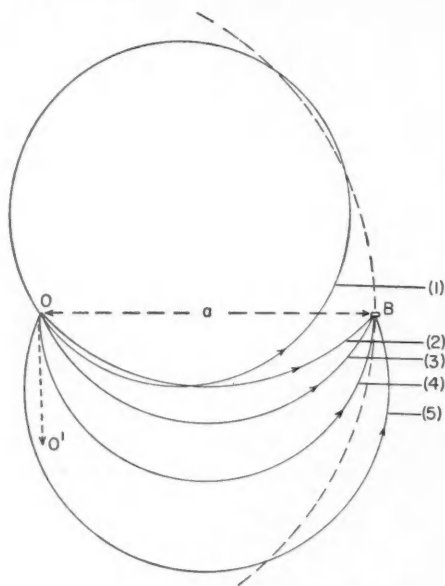


FIG. 1. Orbits for particles of the same mass and charge and various energies in a uniform magnetic field. (1) and (4) are for particles of energy E , (2) and (3) for particles of energy $> E$, (5) for particle of energy $< E$.

particles of energy E to spiral asymptotically towards the circle $r = a$. Then all particles of this energy eventually reach the counter at B ;^{*} on the other hand particles of energy $< E$ will never travel out as far as B — either they will return to O or they will move in some smaller asymptotic orbit; whilst particles of energy $> E$ will travel beyond B . (It is of course conceivable for a particle of energy $< E$ to have an orbit which is tangential to the circle $r = a$ exactly at the counter, and for a particle of energy $> E$ to have an orbit crossing this circle exactly at the counter. However, the mere fact that we are, for the moment, idealizing the counter as the geometrical "point B " means that we cannot assign any finite probability to such orbits.)

To investigate the conditions for this asymptotic orbit it will be convenient to work in terms of the magnetic vector potential \mathbf{A} , related to the field \mathbf{H} (e.m.u.) by $\mathbf{H} = \text{curl } \mathbf{A}$. By writing out the particle Lagrangian in cylindrical coordinates and using symmetry, together with two obvious restrictions on \mathbf{H} ($\text{curl } \mathbf{H} = 0$, and $H_r = H_\theta = 0$ in the median plane), we find, as has been shown elsewhere by the present author (2),

$$[1] \quad mr^2\dot{\theta} + \frac{erA}{c} = P.$$

Here the dot signifies differentiation with respect to time; P is a constant of the motion, to wit the angular momentum about Oz , which is zero in the present case since the particles start from O ; A is a function of r only, and is in fact just A_θ , the only nonvanishing component of \mathbf{A} . Equation [1] can therefore be rewritten:

$$[2] \quad r\dot{\theta} = -\frac{e}{mc} \cdot A(r).$$

Also, from energy conservation,

$$[3] \quad (2m_0c^2 + E) \frac{E}{m^2c^2} = \frac{p^2}{m^2} = \dot{r}^2 + (r\dot{\theta})^2$$

where p is the magnitude of the linear momentum associated with kinetic energy E .

The geometry of the orbit is examined by eliminating the time variable between [2] and [3] to obtain a differential equation between r and θ :

$$[4] \quad \left(\frac{\dot{r}}{\dot{\theta}}\right)^2 = \left(\frac{dr}{d\theta}\right)^2 = \frac{p^2 - \left(\frac{eA(r)}{c}\right)^2}{\left(\frac{eA(r)}{c} \cdot \frac{1}{r}\right)^2}.$$

Now a necessary condition for the orbit to have the asymptote $r = a$ is that $dr/d\theta$ vanish at this radius, and from [4] this requires

$$[5] \quad A(a) = \pm \frac{pc}{e}.$$

^{*}In order that the particles shall not take an infinite time to reach the counter we may suppose it to be located an infinitesimal distance in from $r = a$.

For the sake of definiteness we shall suppose $A(a)$ and e both to be positive so that the $+$ sign is the one required in [5]. (A of course can always be made positive since its definition includes an arbitrary additive constant.) Although necessary, condition [5] is not sufficient to ensure that the orbit is asymptotic to the circle $r = a$; for example it also applies to an orbit which returns to O after touching this circle. We must therefore invoke the further condition that θ increase indefinitely as r approaches a :

$$[6] \quad \int_b^a \left(\frac{d\theta}{dr} \right) dr = \infty$$

where $0 < b < a$. Let us write [4] as

$$[7] \quad \frac{dr}{d\theta} = \pm r \left\{ \left(\frac{p}{y} \right)^2 - 1 \right\}^{\frac{1}{2}}$$

where $y = eA(r)/c$, and where the $+$ sign must again be taken on the right side since r increases continually with θ , albeit at an infinitesimal rate near a . Since condition [6] must apply however near b is to a , provided only that it is less than a , we shall suppose b to be so close to a that y is adequately represented over the region of integration by the first few terms of a Taylor expansion in powers of $(r - a)$. Using such an expansion, together with condition [5] (which, incidentally, gives $y(a) = p$), [6] and [7] yield:

$$[8] \quad \frac{1}{a} \int_b^a \frac{dr}{\{k_1(r-a) + k_2(r-a)^2 + \dots\}^{\frac{1}{2}}} = \infty$$

$$[9] \quad \text{with} \quad k_1 = -\frac{2}{p} \left(\frac{dy}{dr} \right)_{r=a}$$

$$[10] \quad \text{and} \quad k_2 = \left\{ \frac{3}{p^2} \left(\frac{dy}{dr} \right)^2 - \frac{1}{p} \cdot \frac{d^2y}{dr^2} \right\}_{r=a}.$$

Terminating the expansion in the denominator at the first term, and integrating, makes it immediately apparent that k_1 must vanish for the integral to diverge to first order. That is to say, $dy/dr = dA/dr = 0$ at $r = a$. Condition [8] has therefore now become:

$$[11] \quad \frac{1}{a} \int_b^a \frac{dr}{\{k_2(r-a)^2 + \dots\}^{\frac{1}{2}}} = \infty$$

$$[12] \quad \text{with} \quad k_2 = -\frac{1}{p} \left(\frac{d^2y}{dr^2} \right)_{r=a} = -\frac{e}{pc} \left(\frac{d^2A}{dr^2} \right)_{r=a}.$$

The integral on the left side of [11] diverges to second and higher orders for finite k 's. To avoid an imaginary second order integrand k_2 must be positive, i.e. d^2y/dr^2 , and hence d^2A/dr^2 , must be negative at $r = a$.

Recapitulating then, the necessary and sufficient conditions for particles of energy E to spiral asymptotically towards the circle $r = a$ are:

$$\begin{aligned}
 [13] \quad & A = \frac{pc}{e} \\
 [14] \quad & \text{at } r = a \quad \left\{ \begin{aligned} \frac{dA}{dr} &= 0 \\ \frac{d^2A}{dr^2} &< 0 \end{aligned} \right\} \quad \text{i.e. } A(r) \text{ has a maximum at } r = a. \\
 [15] \quad &
 \end{aligned}$$

The condition that $A(r)$ have a maximum at $r = a$ is of course consistent with the physical consideration that the orbit be stable against small oscillations about this radius.

3. EFFECT OF FINITE COUNTER WIDTH

On account of its finite radial extent the counter will admit not only particles of exactly that energy E corresponding to the asymptote $r = a$, but also particles whose energies lie in a small range about E , and it is this energy spread which is investigated in the present section. First we note that if a finite counter extends right up to the asymptote a certain part of it will be inaccessible to particles of energy E . For suppose it extends from $r = b$ out to $r = a$, then the greatest radius that a particle of energy E can attain before entering the counter is attained by that particle which just misses it at $r = b$ and so makes one more revolution before entering it at $r = b'$, say, where in view of [7] and [11] b' is determined by

$$[16] \quad 2\pi = \frac{1}{a} \int_b^{b'} \frac{1}{\sqrt{k_2}} \frac{dr}{a-r}.$$

Thus for maximum efficiency a counter of finite radial width $b' - b = w$, say, should be placed not exactly at $r = a$, but some distance $a - b' = u$, say, in from the asymptote, where from [16],

$$[17] \quad u = \frac{w}{\exp(2\pi a \sqrt{k_2}) - 1}.$$

Equation [16] may be taken to define the response of the counter to particles of energy E ; we wish to know how much the response drops from its maximum value of 2π when E changes by $\pm \Delta E$. Let us therefore replace p in [7] by $p + \Delta p$, with

$$[18] \quad \frac{\Delta p}{p} = \left(\frac{E + m_0 c^2}{E + 2m_0 c^2} \right) \frac{\Delta E}{E} = \lambda \frac{\Delta E}{E}, \text{ say.}$$

Then expanding y as before near $r = a$, and using the results of Section 2, we have:

$$[19] \quad \frac{d\theta}{dr} = \frac{1}{r \left\{ 2\lambda \frac{\Delta E}{E} + \lambda^2 \left(\frac{\Delta E}{E} \right)^2 + k_2(r-a)^2 + \dots \right\}^{1/2}}.$$

Integrating over the counter to obtain the new response, Θ , say, gives to first order:*

*We are assuming here that particles of all energies are equally abundant; if the abundance were a function $n(E)$ of E the left sides of [20] and [21] should be multiplied by $n(E + \Delta E)/n(E)$, resulting in obvious corrections to [23] and [24].

$$[20] \quad \Theta = \frac{w}{a} \left(\frac{E}{2\lambda \Delta E} \right)^{\frac{1}{2}}$$

and to second order:

$$[21] \quad \Theta = \frac{1}{a \sqrt{k_2}} \ln \left[\frac{\{(u+w)^2 + \alpha^2\}^{\frac{1}{2}} - (u+w)}{\{u^2 + \alpha^2\}^{\frac{1}{2}} - u} \right]$$

where u and w are related as in [17], and where

$$[22] \quad \alpha^2 = \frac{1}{k_2} \left\{ 2\lambda \frac{\Delta E}{E} + \lambda^2 \left(\frac{\Delta E}{E} \right)^2 \right\}.$$

The proportional change in energy at which the response has dropped to half maximum ($\Theta = \pi$) is, according to [20],

$$[23] \quad \frac{\Delta E}{E} = \frac{w^2}{2\lambda \pi^2 a^2}$$

or according to [21]

$$[24] \quad \frac{\Delta E}{E} = \frac{1}{2\lambda} \left\{ \gamma - \frac{1}{4} \gamma^2 \right\}$$

$$[25] \quad \text{with} \quad \gamma = \frac{1}{2} k_2 w^2 (\operatorname{cosech}^4 \beta) (\cosh \beta + \cosh 2\beta)$$

$$[26] \quad \text{and where } \beta^2 = k_2 (\pi a)^2 = - \frac{e(\pi a)^2}{pc} \left(\frac{d^2 A}{dr^2} \right)_{r=a}.$$

Equation [23] shows that to first order the "energy width" ΔE varies as the square of the counter width and is independent of the detailed behavior of the vector potential (and hence the field) at $r = a$, provided [13]–[15] are satisfied.

4. EFFECT OF FINITE SOURCE WIDTH

The calculations so far have been based on the assumption of a point source but in practice of course this too will have finite dimensions so let us suppose that it extends out to radius $r = t$, with $t/a \ll 1$. Then it is no longer true that the (constant) angular momentum about Oz of every particle is zero: it can be anything between $\pm pt$, depending on how the particle is emitted initially. If we arrange matters so that all particles of the particular energy E (momentum p) are counted, whatever their angular momentum, then some particles of different energy will also be counted if they happen to have the right angular momentum. To examine the energy spread due to this circumstance we replace [2] by the limiting equations:

$$[27] \quad r\dot{\theta} = - \frac{eA(r)}{mc} \pm \frac{pt}{mr}.$$

Equation [3] expressing energy conservation still holds of course, and from [3] and [27] one readily obtains, corresponding to [7],

$$[28] \quad \frac{dr}{d\theta} = r \left\{ \left(\frac{p}{y + \Delta y} \right)^2 - 1 \right\}^{\frac{1}{2}}$$

where Δy has been written for $\pm pt/r$.

On comparing the expansions of $\{p/(y + \Delta y)\}^2$ and $\{(p + \Delta p)/y\}^2$ near $r = a$ (where $y \approx p$) it is seen that to first order the effect of the term Δy in the denominator is the same as that of a term Δp in the numerator, given by:

$$[29] \quad \frac{\Delta p}{p} = \left(\frac{\lambda \Delta E}{E} \right) = \frac{\Delta y}{y} = \frac{t}{a}.$$

Similarly to second order the equivalent Δp is given by:

$$[30] \quad \frac{\Delta p}{p} = \frac{t}{a} + \left(\frac{t}{a} \right)^2.$$

Also by considering the expansion of $\{(p + \Delta p)/(y + \Delta y)\}^2$ in conjunction with [7] it can be seen that to first order the effects of finite source width and finite counter width are additive. Thus, with a source of width t and counter of width w the energy $E \pm \Delta E$ at which the response drops to half maximum is given to first order, not by [23], but rather by:

$$[31] \quad \frac{\Delta E}{E} = \frac{1}{\lambda} \left\{ \frac{t}{a} + \frac{1}{2} \left(\frac{w}{\pi a} \right)^2 \right\}$$

which clearly shows that the limitation on source size is more stringent than the limitation on counter size.

Similarly to second order the combined effect of a finite source and a finite counter is represented by

$$[32] \quad \frac{\Delta E}{E} = (\delta_1 + \delta_2) (1 + 2\lambda\delta_2)$$

where again the left side is the proportional energy width at which the counter response drops to half maximum, and where δ_1 is written for the " $\Delta E/E$ " of [24], and δ_2 for the " $\Delta E/E$ " corresponding to the $\Delta p/p$ of [30], i.e. $\delta_2 = \{t/a + (t/a)^2\}/\lambda$. Thus we see that to second order the effect of a finite counter (δ_1) and that of a finite source (δ_2) are not strictly additive, their combined effect being rather greater than their sum.

5. EFFECT OF A FINITE z -COMPONENT OF VELOCITY

Up to this point we have limited our attention to particles whose velocities lie wholly in the median (r - θ) plane. On account of the small but finite extent of the source and counter in the z -direction some particles with a small z -component of velocity will also be counted, and this will contribute to the total spread in energy of all particles arriving at the counter. The contribution can be estimated as follows. Suppose the source extends from $z = -f$ to $z = f$ and the counter from $z = -g$ to $z = g$, then the maximum vertical distance a particle can travel and still be collected is $f + g$. While travelling this vertical distance the particle must travel a horizontal distance Ka where K is at least unity and may in fact be considerably larger, depending on the orbit. Hence

$$[33] \quad \frac{z}{v} = \frac{f + g}{Ka}$$

where v is the component of total velocity in the median plane, and is related to the kinetic energy E in that plane by:

$$[34] \quad \left(\frac{v}{c}\right)^2 = 1 - \left[\frac{m_0 c^2}{m_0 c^2 + E}\right]^2.$$

Similarly \dot{z} is related to the kinetic energy $(\Delta E)_z$ in the z -direction by:

$$[35] \quad \left(\frac{\dot{z}}{c}\right)^2 = 1 - \left[\frac{m_0 c^2}{m_0 c^2 + (\Delta E)_z}\right]^2 \approx \frac{2(\Delta E)_z}{m_0 c^2}.$$

From [33], [34], and [35]

$$[36] \quad \frac{(\Delta E)_z}{E} \approx \frac{1}{2} \left(\frac{f+g}{Ka}\right)^2 \left(\frac{m_0 c^2}{E + m_0 c^2}\right) \left(\frac{E + 2m_0 c^2}{E + m_0 c^2}\right).$$

Combining [36] and [31] we have

$$[37] \quad \left(\frac{\Delta E}{E}\right)_{\text{total}} = \frac{1}{\lambda} \left\{ \frac{t}{a} + \frac{1}{2} \left(\frac{w}{\pi a}\right)^2 + \frac{1}{2} \left(\frac{f+g}{Ka}\right)^2 \left(\frac{m_0 c^2}{E + m_0 c^2}\right) \right\}.$$

It is clear that $(\Delta E)_z/E$ can never exceed $(f+g/Ka)^2$ and that it tends to zero for large E . By a suitable field which would cause particles to spiral through many revolutions before entering the counter, K could be made large enough for the last term in [37] to be neglected even for small E . However K must not be too large because we want $\dot{z} = v(f+g)/Ka$ to be finite; for it is clearly unrealistic in a physical case to consider only particles whose motion lies *exactly* in the median plane: to have a finite number of particles entering the counter we must tolerate small z -components of velocity within the range $\pm \dot{z}$.

In this discussion we have ignored the effect of small changes of azimuthal velocity $r\dot{\theta}$ caused by the interaction of \dot{z} with H_r , which does not vanish outside the median plane (since $\text{curl } \mathbf{H} = 0$ requires $\partial H_r / \partial z = \partial H_z / \partial r$). This interaction will depend on the product of \dot{z} with H_r near the median plane, i.e., the product of two first order small quantities. Moreover, since H_r changes sign at the median plane the net effect will be a difference of such products, i.e., the difference of two second order small quantities, so its neglect is certainly justified in [37]. A similar cancellation applies to changes in \dot{z} itself caused by the interaction of $r\dot{\theta}$ with H_r .

As mentioned earlier, we offer no solution here for the general three-dimensional problem of directing particles with large z -velocities into the counter; guidance in this problem might be obtained from the discussion of Fremlin and Gooden (1) who consider a somewhat, but not altogether, similar problem in connection with cyclotrons.

6. NUMERICAL ORDERS OF MAGNITUDE

In any practicable experimental arrangement the radius of the asymptotic circle would probably be somewhere between 10 cm. and 50 cm.; for these two values of a the Tables I and II give values of H_a obtained from the formula

$$[38] \quad H_a = \frac{1}{r} \frac{d}{dr} (rA) \Big|_{r=a} = \frac{pc}{ea} = \frac{\sqrt{E^2 + 2Em_0 c^2}}{ea}.$$

This relation between kinetic energy, maximum radius, and field at maximum radius is the same as in the cyclotron: in both cases it is that for a particle of energy E moving in a circle of radius a in a uniform field H_a . For $E \ll m_0 c^2$ [38]

TABLE I
ELECTRONS
 H_a in kilogauss

a (cm.)	10	50
E (Mev.)		
0.01	0.0338	0.00675
0.1	0.111	0.0223
1.0	0.473	0.0947
10.0	3.50	0.701

TABLE II
HEAVY PARTICLES
 H_a in kilogauss

Particle	Proton or alpha-particle		Deuteron	
a (cm.)	10	50	10	50
E (Mev.)				
1	14.5	2.90	20.4	4.08
5	32.4	6.48	45.7	9.14

becomes $H_a = c(2m_0E)^{1/2}/ea$ which was adequate for calculating Table II; relativistic heavy particles could be handled only by employing fields and orbits comparable with those used in the largest cyclotrons. (Indeed even larger fields and orbits than these would be required for relativistic particles of rest mass greater than the alpha-particle's.)

From [37] we can estimate $\Delta E/E$ for the above values of a by substituting reasonable numerical values for t , w , $f + g$, and K . Let us suppose the source is about 2 mm. across and 1 cm. long, and that the dimensions of the counter window are of order 1 cm., so that $t \approx 1$ mm., $w \approx f + g \approx 1$ cm. Then for $a = 10$ cm. $\Delta E/E$ ranges from 2.5% for $K = 1$ down to 1.5% for $K \gg 1$; while for $a = 50$ cm. $\Delta E/E \approx 0.2\%$ whatever value (> 1) K may have.*

The magnitude of k_2 , which by [12] is a measure of d^2A/dr^2 (and hence of the gradient of the field in the median plane) at $r = a$, may be estimated by comparing the first and second order calculations of $\Delta E/E$. Thus the neglect of $k_2(r - a)^2$ in [19] to obtain the first order expressions [20] and [23] implies $k_2(r - a)^2 \ll \Delta E/E$. On the other hand k_2 must not be too small since for $k_2 \rightarrow 0$ the left side of [24] diverges as $-(k_2)^{-2}$, as may be seen by expanding the hyperbolic functions in [25] and substituting the resulting expression for γ back into [24]. In fact the condition that expressions [23] and [24] for $\Delta E/E$ must differ only by quantities of second or higher order smallness yields the result:

$$[39] \quad k_2 = -\frac{e}{pc} \left(\frac{d^2A}{dr^2} \right)_{r=a} = -\frac{e}{pc} \left(\frac{dH_z}{dr} \right)_{r=a} \approx \frac{1}{(\pi a)^2}.$$

*We have assumed the worst case $(\Delta E)_2/E = (f + g/Ka)^2$, i.e. $E \ll m_0c^2$.

Now from [38] $-e/\rho c$ may be expressed as $-1/aH_a$, so that [39] gives an approximate relation between the field and its gradient in the median plane at $r = a$:

$$[40] \quad \left(\frac{dH_z}{dr} \right)_{r=a} \approx - \frac{H_a}{\pi^2 a}.$$

For certain simple types of field [40] is sufficient to relate H_a to the field H_0 at the center; thus if H decreases linearly with r we find H_a must be about 90% of H_0 , and if it decreases parabolically (from a maximum H_0) H_a must be about 95% of H_0 . Of course fields which are simply described mathematically are not necessarily simple to construct physically; however it is certainly possible to construct a field which will satisfy the conditions [13]–[15]—for this is just what we have in the cyclotron.

ACKNOWLEDGMENTS

The author is indebted to Prof. R. E. Peierls and Dr. R. S. Turgel for valuable discussion in the early stages of this work, and particularly to Dr. L. G. Elliott for carefully reading the manuscript and making many helpful criticisms.

REFERENCES

1. FREMLIN, J. H. and GOODEN, J. S. Repts. Progress Phys. 13: 303. 1950.
2. GARDNER, J. W. Proc. Phys. Soc. (London), B, 62: 300. 1949.
3. MCCREA, W. H. Relativity Physics. 2nd ed. Methuen & Co. Ltd., London. 1947. Chapter VII.

AUGER TRANSITIONS IN SILVER¹

BY F. A. JOHNSON AND J. S. FOSTER

ABSTRACT

Twenty of the K Auger lines of silver have been resolved and estimates of their relative intensities obtained. Comparison with the theoretical intensities calculated by Burhop indicates that the existing theory is not quantitatively correct and that relativistic modifications offer little hope of improvement. Special attention is directed to the $K \rightarrow LL$ lines where disagreement with theory is most marked. Comparison with similar observations previously reported for gold and bismuth shows an interesting agreement in the observed ratio of the intensity of the $K \rightarrow L_{II}L_{III}$ line to that of the $K \rightarrow L_{III}L_{III}$ line, and in the ratio of the intensity of the $K \rightarrow L_{II}L_{III}$ line to that of the $K \rightarrow L_{II}L_{II}$ line.

Twenty of the K Auger lines of silver have been resolved using a high resolution 180° permanent magnet photographic spectrograph, and estimates of their relative intensities obtained. The spectrograph source was a 2 mil tungsten wire onto which Cd^{107} (6.7 hr.) had been evaporated *in vacuo*. The active cadmium was produced by proton bombardment of silver at 20 Mev. in the McGill University synchrocyclotron. The Auger electrons were recorded on Eastman X-Ray No Screen plates and the intensities of the various electron lines were obtained from the trace of a Moll recording microphotometer type A. Calibration was by means of light exposures of known relative intensities, and it was found that the photographic density of the electron lines and of the background were all within the linear region. The energies of the lines were measured with reference to the thorium A line (2).

The complete set of Auger lines is shown in Fig. 1 (a), and a microphotometer trace of the $K \rightarrow LL$ group in Fig. 1 (b). For the particular magnetic field setting, the strongest of the lines, $K \rightarrow L_{II}L_{III}$, had a ρ value of 10.94 cm. and was separated on the plate from the $K \rightarrow L_{III}L_{III}$ line by 1.13 mm. The measured energies of the lines, together with those calculated using the most recent values (4) of X-ray level energies, are listed in Table I. The measured intensities, corrected for influence of geometry on line widths, are compared with the theoretical values calculated nonrelativistically by Burhop (1) for interactions in the L subshells, and with Burhop's estimates for the interactions of the L and M shells using a plane wave approximation for the emerging electron. In addition, the integrated values calculated by Pincherle (7) are compared with the experimental values.

The experimental relative intensities of the $K \rightarrow LL$ transitions are not in accord with the nonrelativistic theory of Burhop. Relativistic effects, estimated by Massey and Burhop (5) to cause an increase of 15 to 20% in the calculated values for silver, are not likely to give agreement. The general trend of the intensities is in agreement with the experimental results of Mihelich (6) for gold and of Ellis (3) for bismuth. Especially interesting is the fact that in all three cases the ratio of the intensity of the $K \rightarrow L_{II}L_{III}$ line to that of the

¹ Manuscript received December 11, 1952.

Contribution from the Radiation Laboratory, McGill University, Montreal, Que.

TABLE I
EXPERIMENTAL AND THEORETICAL ENERGIES AND INTENSITIES FOR
THE AUGER TRANSITIONS IN SILVER

Transition	Energy (kev.)		Intensity			
	Meas. \pm 0.06	Calc.	Measured	Burhop	Meas.	Burhop Pincherle
$K \rightarrow L_I L_I$	17.70	17.88	1 \pm 0.2	1		
$K \rightarrow L_I L_{II}$	17.98	18.16	1.3 \pm 0.2	1.1		
$K \rightarrow L_I L_{III}$	18.14	18.33	1.3 \pm 0.2	2.3		
$K \rightarrow L_{II} L_{II}$	18.25	18.44	0.5 \pm 0.2	0.96	1	1
$K \rightarrow L_{II} L_{III}$	18.42	18.61	3.2 \pm 0.4	2.6		
$K \rightarrow L_{III} L_{III}$	18.61	18.79	1.8 \pm 0.2	3.2		
$K \rightarrow L_I M_I$	20.88	20.96	0.8 \pm 0.2	0.49		
$K \rightarrow L_I M_{II, III}$	21.02	21.10	0.8 \pm 0.2	1.24	0.18	0.16
$K \rightarrow L_I M_{IV, V}$	—	21.32	—	0.05		
$K \rightarrow L_{II} M_I$	21.17	21.25	0.2 \pm 0.1	0.18		
$K \rightarrow L_{II} M_{II}$	—	21.42	—	—		
$K \rightarrow L_{II} M_{II, III}$	21.31	21.38	1.6 \pm 0.3	2.5	0.45	0.30
$K \rightarrow L_{II} M_{II, III}$	21.47	21.55	1.7 \pm 0.3	—		0.49
$K \rightarrow L_{II} M_{IV, V}$	—	21.60	—	—		
$K \rightarrow L_{III} M_{IV, V}$	21.68	21.77	0.55 \pm 0.2	0.61		
$K \rightarrow L_{II} N_{II, III}$	21.85	21.91	0.3 \pm 0.2	—		
$K \rightarrow L_{III} N_{II, III}$	22.02	22.08	0.55 \pm 0.2	—		
$K \rightarrow M_I M_{II, III}$	24.11	24.18	0.18 \pm 0.1	—		
$K \rightarrow M_{II, III} M_{II, III}$	24.25	24.32	0.3 \pm 0.2	—	0.06	0.075
$K \rightarrow M_{II, III} M_{IV, V}$	24.48	24.54	\sim 0.05	—		
$K \rightarrow M_I N_{II, III}$	24.65	24.71	\sim 0.05	—		
$K \rightarrow M_{II, III} N_{IV, V}$	24.82	24.90	\sim 0.05	—		
$K \rightarrow M_{IV, V} N_{IV, V}$	25.04	25.12	$<$ 0.05	—		

$K \rightarrow L_{III} L_{III}$ line is 1.8, although only in the case of silver and bismuth is the $K \rightarrow L_I L_{III}$ line the strongest of the group. In addition, the ratio of the intensity of the $K \rightarrow L_I L_{III}$ line to that of the $K \rightarrow L_I L_I$ line is about 1.3 in the three cases. The $K \rightarrow L_I L_{II}$ line is the weakest of the group in all cases, in qualitative agreement with theory.

In the $K \rightarrow LM$ group the main discrepancy between experiment and theory is in the intensities of the $K \rightarrow L_I M_I$ and the $K \rightarrow L_I M_{II, III}$ lines. This is not surprising since the plane wave approximation is poorest for transitions involving the L_I shell (1). Experimentally it would just be possible to resolve two lines differing in energy by an amount equal to the separation of the $K \rightarrow L_{III} M_{II, III}$ and $K \rightarrow L_{II} M_{IV, V}$ lines, but where only one line is visible, it is difficult to be certain of the assignment. If the measured intensity of 1.7 was assigned to the former and this added to the intensity of 1.6 for the $K \rightarrow L_{II} M_{II, III}$ line, then the sum would be 3.3 as compared to 2.5 estimated by Burhop. This assumption that the intensity of the $K \rightarrow L_{II} M_{IV, V}$ line is small is perhaps substantiated by the agreement between the observed intensity of the $K \rightarrow L_{III} M_{IV, V}$ line and the value calculated for the combined intensity of the $K \rightarrow L_{II} M_{IV, V}$ and $K \rightarrow L_{III} M_{IV, V}$ lines. A similar argument can be used to show that the intensity of the $K \rightarrow L_{III} M_I$ line might also be small.

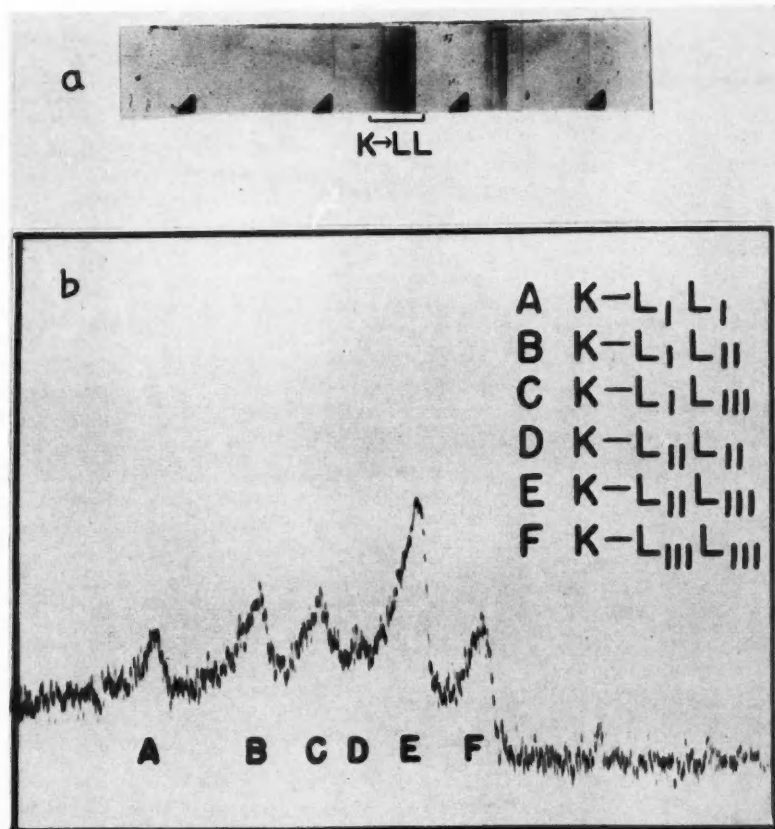
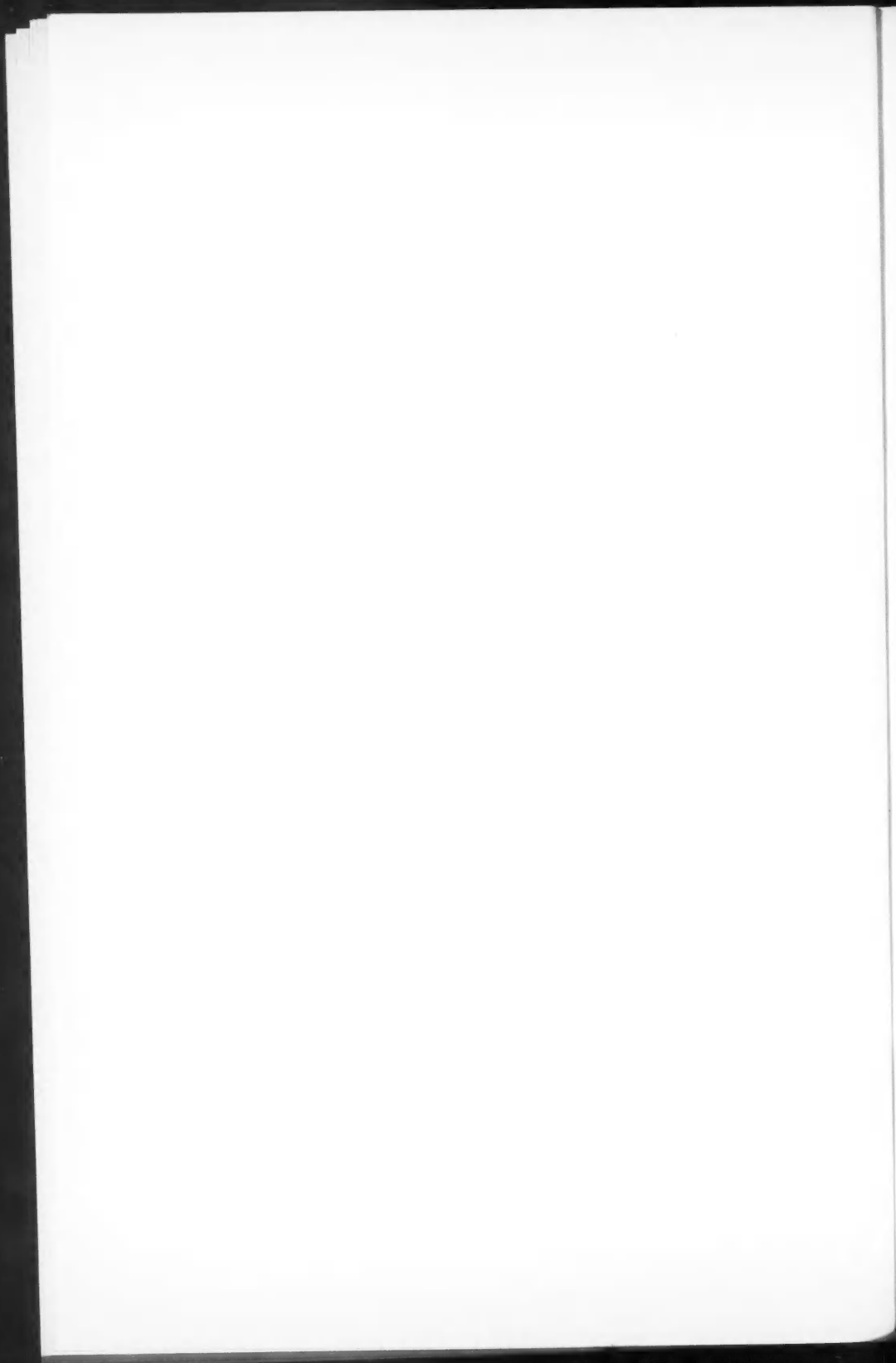


FIG. 1. (a) Reproduction of spectrograph plate showing all the Auger lines of silver; (b) microphotometer trace of $K \rightarrow LL$ Auger lines.



In order to compare the experimental results with the theoretical calculations of Pincherle, it was necessary to sum the intensities of various groups as indicated in the table. In addition, corresponding values were derived from Burhop's calculations. In all cases the intensities were normalized to that of the $K \rightarrow LL$ group as unity. It will be seen that the measured intensities of the $K \rightarrow LL$, $K \rightarrow L_I M_{I, II, III}$, and $K \rightarrow L_{II, III} M$ groups are in moderately good agreement with the estimates of Burhop, considering that his latter two values are rough. Except for the $K \rightarrow L_I M_{I, II, III}$ group, the total intensities of the groups are in good agreement with the values calculated by Pincherle. The measured intensities for all four groups follow the pattern of the less accurate measurements of Robinson and Young (8) for zirconium and molybdenum, in the same region of the periodic table.

The detailed experimental results clearly indicate that existing theory is not quantitatively correct and offer little hope that relativistic modifications in themselves will make the desired corrections. At present it is not clear whether theoretical agreement may be reached by the employment of more suitable wave functions or whether more complex phenomena must be taken into account. Burhop's calculations were made using hydrogen-like wave functions with suitably chosen effective charges. In addition it was assumed that the Auger transition involves an interaction between only two electrons. It might be expected, however, that the other electrons in the atom should have some influence on the Auger transition probabilities. In this way the transfer of energy to the final Auger electron may take place in a number of competing ways through intermediate states, with a resulting change in the transition probabilities from those calculated to date.

REFERENCES

1. BURHOP, E. H. S. Proc. Roy. Soc. (London), A, 148: 272. 1935.
2. CRAIG, H. Phys. Rev. 85: 688. 1952.
3. ELLIS, C. D. Proc. Roy. Soc. (London), A, 139: 336. 1933.
4. HILL, R. D., CHURCH, E. L., and MIHELICH, J. W. Rev. Sci. Instruments, 23: 523. 1952.
5. MASSEY, H. S. W. and BURHOP, E. H. S. Proc. Roy. Soc. (London), A, 153: 661. 1936.
6. MIHELICH, J. W. Phys. Rev. 88: 415. 1952.
7. PINCHERLE, L. Nuovo cimento, 12: 81. 1935.
8. ROBINSON, H. R. and YOUNG, C. L. Proc. Roy. Soc. (London), A, 128: 92. 1930.

RADIAL-AXIAL HEAT FLOW IN REGIONS BOUNDED INTERNALLY BY CIRCULAR CYLINDERS¹

BY J. H. BLACKWELL

ABSTRACT

Two radial-axial transient heat flow problems have been solved for regions bounded internally by circular cylinders. They are not of the simple "product-solution" type and it is considered that they may have application in other fields of physics where the Diffusion Equation applies. The problems arose during investigation into "end-effect" in cylindrical thermal-conductivity probes. The solutions are obtained by integral-transform methods, two different types of transform being used in each solution.

INTRODUCTION

The writer has recently been examining the theory of the cylindrical heat probe method (1, 6, 8) for determination of thermal conductivity and diffusivity of materials in bulk. (A discussion of the theory is to be published shortly.)

In the course of such an investigation the writer has solved several transient heat flow problems for infinite or semi-infinite regions, bounded internally by a circular cylinder, and with heat-flow in the axial as well as the radial direction. Two such solutions are reproduced below.

It is considered that the results obtained may have applications in other fields where the Diffusion Equation applies and that the combined use of different types of integral transform in the analyses, although not new (9), may be of interest. Solutions of problems of this type for regions bounded internally by circular cylinders other than the simple "product-solutions" (3, p. 284) do not appear to be available in the literature.

It may be remarked that it is essential for simple application of the cylindrical probe method that the heat-flow be treated as radial to within the limits set by experimental error. Accordingly the effect of finite cylinder length on the validity of the radial-flow theory must be investigated, so that a criterion for minimum probe-length may be established.

The problems may be described as follows:

- (1) Transient heat flow in the infinite region bounded internally by an (infinite) circular cylinder. There is constant flux of heat across a finite length of the internal boundary surface and the remainder of this surface is insulated.
- (2) Transient heat flow in the semi-infinite region bounded internally by a circular cylinder and by planes at right angles to the axis of the cylinder. There is constant flux of heat across the cylindrical boundary and the planes are maintained at zero temperature.

Case (1) is solved using a Laplace Transformation with respect to time, and an (infinite) Fourier Transformation with respect to the axial variable.

¹ Manuscript received December 12, 1952.

Contribution from the Department of Physics, University of Western Ontario, London, Ontario.

Case (2) employs a Laplace Transformation with respect to time and a finite Fourier Sine Transformation with respect to the axial variable. The analyses given are of a formal nature throughout and from the pure mathematical standpoint require verification. Verification of results obtained using a Laplace Transformation alone is more or less standardized (3, p. 367) but in the present cases, the situation is somewhat complicated by the use of another type of integral transform in the same problem. In consequence of this and since such verifications are space-consuming and of little interest to the physicist, they are omitted.

ANALYSIS—CASE (1)

We wish to solve the Heat Equation in cylindrical co-ordinates with circular symmetry, i.e.

$$[1] \quad \frac{\partial^2 \theta}{\partial \rho^2} + \frac{1}{\rho} \frac{\partial \theta}{\partial \rho} + \frac{\partial^2 \theta}{\partial z^2} = \frac{1}{h^2} \frac{\partial \theta}{\partial t}, \quad a < \rho < \infty : -\infty < z < \infty : t > 0$$

subject to:

$$[2] \quad \theta = 0, \quad t = 0, \quad a < \rho < \infty : -\infty < z < \infty$$

$$[3] \quad \begin{cases} -K \frac{\partial \theta}{\partial \rho} = Q, & \rho = a, |z| < L : t > 0 \\ = 0, & \rho = a, |z| > L : t > 0 \end{cases}$$

where

ρ, z are the radial and axial co-ordinates,

t is the time,

K, h^2 are the thermal conductivity and diffusivity of the medium,

$\theta(\rho, z, t)$ is the temperature,

Q is the heat flux (constant) across the cylindrical surface.

Firstly, we make a Fourier Transformation of equation [1] and boundary conditions with respect to 'z'. (We use the form of Fourier Transform closest to that of the standard Laplace Transform, i.e.,

$$F(\omega) = \int_{-\infty}^{\infty} f(z) e^{-i\omega z} dz,$$

$$f(z) = \frac{1}{2\pi} \int_{-\infty}^{\infty} F(\omega) e^{i\omega z} d\omega.$$

The result of this transformation is:

$$[4] \quad \frac{\partial^2 \Theta}{\partial \rho^2} + \frac{1}{\rho} \frac{\partial \Theta}{\partial \rho} - \omega^2 \Theta = \frac{1}{h^2} \frac{\partial \Theta}{\partial t} \quad a < \rho < \infty : t > 0$$

subject to:

$$[5] \quad \Theta = 0, \quad t = 0, \quad a < \rho < \infty$$

$$[6] \quad -K \frac{\partial \Theta}{\partial \rho} = \frac{2Q}{\omega} \sin L\omega, \quad \rho = a, \quad t > 0$$

where $\Theta(\rho, \omega, t)$ is the Fourier Transform of $\theta(\rho, z, t)$ and we assume

$$\lim_{|z| \rightarrow \infty} \theta, \frac{\partial \theta}{\partial z} = 0.$$

Next we make a Laplace Transformation of equation [4] and boundary conditions, with respect to 't'. We obtain

$$[7] \quad \frac{d^2 \Phi}{d\rho^2} + \frac{1}{\rho} \frac{d\Phi}{d\rho} - \omega^2 \Phi = q^2 \Phi \quad a < \rho < \infty$$

subject to:

$$[8] \quad -K \frac{d\Phi}{d\rho} = \frac{2Q}{\omega \beta} \sin L\omega \quad \rho = a$$

where $\Phi(\rho, \omega, p)$ is the Laplace Transform of $\Theta(\rho, \omega, t)$,

$$q = p^{1/2}/h.$$

The general solution of [7] subject to the implicit condition that Φ be bounded as $\rho \rightarrow \infty$ may be written down, i.e.

$$[9] \quad \Phi = AK_0(\beta\rho)$$

where $\beta = \sqrt{q^2 + \omega^2}$ and $K_0(\beta\rho)$ is the modified Bessel function of the second kind and zero order. Applying boundary condition [8] we get finally

$$[10] \quad \Phi = \frac{2Q \sin L\omega}{K\omega} \frac{K_0(\beta\rho)}{\rho\beta K_1(\beta a)}$$

where $K_1(\beta\rho)$ is the modified Bessel function of the second kind and first order.

By the Inversion Theorem of the Laplace Transformation (4, p. 72) then

$$[11] \quad \Theta = \mathcal{L}^{-1}\Phi = \frac{1}{2\pi i} \left(\frac{2Q \sin L\omega}{K\omega} \right) \int_{\gamma-i\infty}^{\gamma+i\infty} \frac{K_0(\beta\rho)}{\rho\beta K_1(\beta a)} e^{t\rho} d\rho$$

which by another well-known theorem of the Laplace Transformation (4, p. 5) may be written

$$[12] \quad \Theta = \frac{2Q \sin L\omega}{K\omega} \int_0^t \left[\frac{1}{2\pi i} \int_{\gamma-i\infty}^{\gamma+i\infty} \frac{K_0(\beta\rho)}{\beta K_1(\beta a)} e^{\lambda\rho} d\rho \right] d\lambda.$$

Consider the contour integral within the square brackets, i.e., written in full

$$I_1 = \frac{1}{2\pi i} \int_{\gamma-i\infty}^{\gamma+i\infty} \frac{K_0(\rho\sqrt{q^2 + \omega^2}) e^{\lambda\rho} d\rho}{\sqrt{q^2 + \omega^2} K_1(a\sqrt{q^2 + \omega^2})}.$$

Make the change of variable

$$p' = p + \omega^2 h^2$$

and put

$$q' = p'^{1/2}/h.$$

This change of variable does not modify shape or orientation of the contour. Then we get

$$[13] \quad I_1 = \frac{1}{2\pi i} \exp(-\omega^2 h^2 \lambda) \int_{\gamma'-i\infty}^{\gamma'+i\infty} \frac{K_0(q'\rho) e^{\lambda p'} dp'}{q' K_1(q'a)}.$$

The reduced contour integral of equation [13] may be expressed as a real infinite

integral without difficulty using standard methods (4, p. 91). It arises in the solution of the analogous radial-flow problem and has already been evaluated by Carslaw and Jaeger (3, p. 283). Inserting its value we obtain

$$[14] \quad I_1 = \frac{2h^2}{\pi} \exp(-\omega^2 h^2 \lambda) \int_0^\infty \exp(-h^2 \lambda u^2) \times \left[\frac{J_1(ua) N_0(u\rho) - N_1(ua) J_0(u\rho)}{J_1^2(ua) + N_1^2(ua)} \right] du.$$

Substituting from equation [14] into equation [12] we get

$$\theta(\rho, \omega, t) = \frac{4Qh^2 \sin L\omega}{\pi K \omega} \int_0^t \exp(-\omega^2 h^2 \lambda) \int_0^\infty \exp(-h^2 \lambda u^2) f(\rho, u) du d\lambda$$

where

$$[15] \quad f(\rho, u) = J_1(ua) N_0(u\rho) - N_1(ua) J_0(u\rho) / J_1^2(ua) + N_1^2(ua).$$

Proceeding to the inverse Fourier Transformation

$$\begin{aligned} \theta(\rho, z, t) &= \mathcal{F}^{-1} \theta \\ &= \frac{2Qh^2}{\pi^2 K} \int_{-\infty}^\infty \frac{1}{\omega} \exp(iz\omega) \sin L\omega \int_0^t \exp(-\omega^2 h^2 \lambda) \int_0^\infty \exp(-h^2 \lambda u^2) \\ &\quad \times f(\rho, u) du d\lambda d\omega \\ [16] \quad &= \frac{2Qh^2}{\pi^2 K} \int_0^\infty \frac{1}{\omega} [\sin(L+z)\omega + \sin(L-z)\omega] \int_0^t \exp(-\omega^2 h^2 \lambda) \\ &\quad \times \int_0^\infty \exp(-h^2 \lambda u^2) f(\rho, u) du d\lambda d\omega. \end{aligned}$$

Equation [16] can be simplified by performing either or both of the integrations with respect to λ and ω . The procedure to be followed depends to a certain extent on the use to be made of the solution.

It may be desired to find the approximate size of L for which the solution for a given value of $|z| < L$ (in particular, $z = 0$) differs from the corresponding radial-flow solution by less than a certain maximum error. In this case we need to perform the integration with respect to ω only. We use the standard result (2)

$$\int_0^\infty \frac{1}{x} \sin ax \exp(-x^2) dx = \frac{\pi}{2} \operatorname{erf}\left(\frac{a}{2}\right)$$

and, assuming that the order of integration may be interchanged, we obtain

$$[17] \quad \theta(\rho, z, t) = \frac{Qh^2}{\pi K} \int_0^t \int_0^\infty \left[\operatorname{erf}\left(\frac{L+z}{2h\sqrt{\lambda}}\right) + \operatorname{erf}\left(\frac{L-z}{2h\sqrt{\lambda}}\right) \right] \times \exp(-h^2 \lambda u^2) f(\rho, u) du d\lambda.$$

For convenience consider the temperature at $z = 0$

$$[18] \quad \theta(\rho, 0, t) = \frac{2Qh^2}{\pi K} \int_0^t \int_0^\infty \operatorname{erf}\left(\frac{L}{2h\sqrt{\lambda}}\right) \exp(-h^2 \lambda u^2) f(\rho, u) du d\lambda.$$

Now if $L/2h\sqrt{t}$ is large, $\operatorname{erf}(L/2h\sqrt{\lambda})$ changes very little from unity over the range of integration and we may write

$$[19] \quad \theta(\rho, 0, t) \approx \frac{1}{2} \left[1 + \operatorname{erf} \left(\frac{L}{2h\sqrt{t}} \right) \right] \left[\frac{2Qh^2}{\pi K} \int_0^t \int_0^\infty \exp(-h^2 \lambda u^2) f(\rho, u) du d\lambda \right] \\ = \frac{1}{2} \left[1 + \operatorname{erf} \left(\frac{L}{2h\sqrt{t}} \right) \right] \times \text{radial-flow solution.}$$

Hence for a given maximum departure from radial flow conditions we may determine an approximate minimum value for the quantity $L/2h\sqrt{t}$ from the tables of $\operatorname{erf}(x)$. If the orders of magnitude of h and t are known, this fixes the minimum size of L .

If desired, the integral with respect to λ in equation [17] may be expressed in terms of tabulated functions. Each part of this integral is of the form

$$I_2 = \int_0^t \operatorname{erf} \left(\frac{a}{\sqrt{\lambda}} \right) \exp(-b^2 \lambda) d\lambda \quad \text{where } a, b \text{ are real, } b > 0.$$

Integrating by parts and making an appropriate substitution in the remaining integral we get

$$I_2 = \frac{1}{b^2} \left[1 - \operatorname{erf} \left(\frac{a}{\sqrt{t}} \right) \exp(-b^2 t) - \frac{2}{\sqrt{\pi}} \int_{a/\sqrt{t}}^\infty \exp \left[- \left(\lambda^2 + \frac{a^2 b^2}{\lambda^2} \right) \right] d\lambda \right].$$

By a well-known result (5)

$$\frac{2}{\sqrt{\pi}} \int_{a/\sqrt{t}}^\infty \exp \left[- \left(\lambda^2 + \frac{a^2 b^2}{\lambda^2} \right) \right] d\lambda = \frac{1}{2} \left[\exp(2ab) \operatorname{erfc} \left(\frac{a}{\sqrt{t}} + b\sqrt{t} \right) \right. \\ \left. + \exp(-2ab) \operatorname{erfc} \left(\frac{a}{\sqrt{t}} - b\sqrt{t} \right) \right].$$

Hence I_2 is expressible in terms of tabulated functions and $\theta(\rho, z, t)$ is reduced to a single (infinite) integral.

ANALYSIS—CASE (2)

We wish to solve

$$[20] \quad \frac{\partial^2 \theta}{\partial \rho^2} + \frac{1}{\rho} \frac{\partial \theta}{\partial \rho} + \frac{\partial^2 \theta}{\partial z^2} = \frac{1}{h^2} \frac{\partial \theta}{\partial t} \quad a < \rho < \infty : 0 < z < 2L : t > 0$$

subject to:

$$[21] \quad \theta = 0, \quad t = 0, \quad a < \rho < \infty : 0 < z < 2L$$

$$[22] \quad -K \frac{\partial \theta}{\partial \rho} = Q, \quad \rho = a, \quad 0 < z < 2L : t > 0$$

$$[23] \quad \theta = 0, \quad z = 0, 2L, \quad a < \rho < \infty : t > 0$$

where the symbols are the same as in case (1).

We first make a finite Fourier Sine Transformation of equation [20] and boundary conditions with respect to 'z'. (The following form of transform and Inversion Theorem (9, p. 74) are used

$$F(n) = \int_0^{2L} f(z) \sin \frac{n\pi z}{2L} dz,$$

$$f(z) = \frac{1}{L} \sum_{n=1}^{\infty} F(n) \sin \frac{n\pi z}{2L}$$

We obtain

$$[24] \quad \frac{\partial^2 \Theta}{\partial \rho^2} + \frac{1}{\rho} \frac{\partial \Theta}{\partial \rho} - \frac{n^2 \pi^2}{4L^2} \Theta = \frac{1}{h^2} \frac{\partial \Theta}{\partial t} \quad a < \rho < \infty : t > 0$$

subject to:

$$[25] \quad \Theta = 0, \quad t = 0, \quad a < \rho < \infty$$

$$[26] \quad -K \frac{\partial \Theta}{\partial \rho} = \frac{2QL}{\pi n} \left[1 + (-1)^{n+1} \right] \quad \rho = a, \quad t > 0$$

where $\Theta(\rho, n, t)$ is the finite Fourier Sine Transform of $\theta(\rho, z, t)$.

Next we make a Laplace Transformation of equation [24] and boundary condition with respect to 't' obtaining

$$[27] \quad \frac{d^2 \Phi}{d\rho^2} + \frac{1}{\rho} \frac{d\Phi}{d\rho} - \frac{n^2 \pi^2}{4L^2} \Phi = q^2 \Phi \quad a < \rho < \infty$$

subject to:

$$[28] \quad -K \frac{d\Phi}{d\rho} = \frac{2QL}{\pi n \rho} \left[1 + (-1)^{n+1} \right] \quad \rho = a$$

where $\Phi(\rho, n, p)$ is the Laplace Transform of $\Theta(\rho, n, t)$ and

$$q = p^{1/2}/h.$$

The general solution of [27] subject to [28] and the implicit boundary condition that Φ is bounded as $\rho \rightarrow \infty$ is

$$[29] \quad \Phi = \frac{2QL}{K\pi n} \left[1 + (-1)^{n+1} \right] \frac{K_0(\beta\rho)}{\rho\beta K_1(\beta a)}$$

where

$$\beta = \sqrt{q^2 + (n^2 \pi^2 / 4L^2)}.$$

Proceeding with the Inverse Laplace Transformation as in case (1) we get

$$[30] \quad \Theta(\rho, n, t) = \frac{4Qh^2 L}{K\pi^2 n} \left[1 + (-1)^{n+1} \right] \int_0^t \exp\left(-\frac{n^2 \pi^2 h^2}{4L^2} \lambda\right) \\ \times \int_0^\infty \exp(-h^2 \lambda u^2) f(\rho, u) du d\lambda$$

where $f(\rho, u)$ has the same significance as before.

Inverting the finite Fourier Sine Transform

$$[31] \quad \theta(\rho, z, t) = \frac{1}{L} \sum_{n=1}^{\infty} \Theta(\rho, n, t) \sin \frac{n\pi z}{2L} \\ = \frac{4Qh^2}{K\pi^2} \sum_{n=1}^{\infty} \frac{1}{n} \left[1 + (-1)^{n+1} \right] \sin \frac{n\pi z}{2L} \\ \times \int_0^t \exp\left(-\frac{n^2 \pi^2 h^2}{4L^2} \lambda\right) \int_0^\infty \exp(-h^2 \lambda u^2) f(\rho, u) du d\lambda$$

$$[32] \quad = \frac{8Qh^2}{K\pi^2} \sum_{k=0}^{\infty} \frac{1}{2k+1} \sin \alpha_k z \int_0^t \exp(-\alpha_k^2 h^2 \lambda) \times \int_0^{\infty} \exp(-h^2 \lambda u^2) f(\rho, u) du d\lambda$$

where:

$$\alpha_k = \frac{1}{2L}(2k+1)\pi.$$

We may simplify this expression by performing the integration with respect to ' λ ', i.e.

$$[33] \quad \theta(\rho, z, t) = \frac{8Q}{K\pi^2} \sum_{k=0}^{\infty} \frac{1}{2k+1} \sin \alpha_k z \int_0^{\infty} \frac{1 - \exp[-h^2 t(u^2 + \alpha_k^2)]}{u^2 + \alpha_k^2} f(\rho, u) du.$$

As in case (1) we may use the solution to determine the minimum L for radial-flow conditions. We proceed as follows.

Rewrite equation [32] in the form

$$[34] \quad \theta(\rho, z, t) = \frac{8Qh^2}{K\pi^2} \int_0^t \left[\sum_{k=0}^{\infty} \frac{1}{2k+1} \sin \alpha_k z \exp(-\alpha_k^2 h^2 \lambda) \right] \times \int_0^{\infty} \exp(-h^2 \lambda u^2) f(\rho, u) du d\lambda$$

where we assume that the order of summation and integration with respect to λ may be interchanged. Taking $z = L$ for convenience, and for comparison with case (1), we get

$$[35] \quad \theta(\rho, L, t) = \frac{2Qh^2}{K\pi} \int_0^t \left[\frac{4}{\pi} \sum_{k=0}^{\infty} \frac{(-1)^k}{2k+1} \exp(-\alpha_k^2 h^2 \lambda) \right] \times \int_0^{\infty} \exp(-h^2 \lambda u^2) f(\rho, u) du d\lambda.$$

Now $\alpha_k h \sqrt{\lambda} = (2k+1)\pi h \sqrt{\lambda}/2L$ and if $\pi h \sqrt{t}/2L$ is small, the sum of the series

$$S(\lambda) = \frac{4}{\pi} \sum_{k=0}^{\infty} \frac{(-1)^k}{2k+1} \exp(-\alpha_k^2 h^2 \lambda)$$

changes very little over the range of integration from its value, unity, at $\lambda = 0$. Hence we may write, similarly to case (1),

$$\Theta(\rho, L, t) \approx \frac{1}{2}[1 + S(\lambda)] \times \text{radial-flow solution}.$$

Thus, again, we can derive a minimum value of L for a given maximum departure from radial-flow conditions since the series S is tabulated (7).

ACKNOWLEDGMENTS

The author wishes to acknowledge with gratitude the financial assistance of the Research Council of Ontario during the research of which the work reported in this paper forms part. The writer expresses his sincere thanks also for the facilities of the Physics Department, University of Western Ontario.

REFERENCES

1. BLACKWELL, J. H. and MISENER, A. D. *Proc. Phys. Soc. (London)*, A, 64: 1132. 1951.
2. CARSLAW, H. S. *Fourier's series and integrals*. 3rd ed. The Macmillan Co., Limited, London. 1930. p. 213.
3. CARSLAW, H. S. and JAEGER, J. C. *Conduction of heat in solids*. University Press, Oxford. 1947.
4. CARSLAW, H. S. and JAEGER, J. C. *Operational methods in applied mathematics*. 2nd ed. University Press, Oxford. 1947.
5. CHURCHILL, R. V. *Modern operational mathematics in engineering*. McGraw-Hill Book Company Inc., New York and London, 1944. p. 120.
6. HOOPER, F. C. and LEPPER, F. R. *Heating, Piping Air Conditioning*, 22: 129. August, 1950.
7. INGERSOLL, L. R., ZOBELL, O. J., and INGERSOLL, A. C. *Heat conduction*. McGraw-Hill Book Company Inc., New York and London. 1948. p. 255.
8. LENTZ, C. P. *Can. J. Technol.* 30: 153. 1952.
9. SNEDDON, I. N. *Fourier transforms*. McGraw-Hill Book Company Inc., New York and London. 1951.

ENERGY LOSS OF HIGHLY CHARGED PARTICLES PRODUCED BY FISSION AND BY COSMIC RAYS

III. THE LINEAR DENSITY OF DELTA RAYS. EXPERIMENTS¹

BY PIERRE DEMERS AND ZOFIA LECHNO-WASIUTYNSKA

WITH AN APPENDIX

IV. THE LINEAR DENSITY OF DELTA RAYS. THEORETICAL

BY ZOFIA LECHNO-WASIUTYNSKA

ABSTRACT

Delta rays having an energy as low as 2-5 kev. have been counted along the tracks of mesons, protons, and α rays of low velocity, allowing the identification of each. Three methods are presented and applied to determine the efficiency f of counting delta rays of various energies; measured values of f vary between 0.05% at 2 kev. and 100-180% near 50 kev. The number of grains, and the energy distribution among visible delta rays, are analyzed. A new method of determining velocity, based on the analysis of the number of grains in the delta rays, is presented. In the Appendix, the effect of relativistic corrections is computed and discussed. It is small except at large velocities where comparison with experiment is difficult.

COUNTING LOW ENERGY DELTA RAYS

1. *Low Energy Delta Rays*

The possibility of recognizing very short and low energy delta rays in our fine grain emulsions was noticed earlier (2) by observing delta rays at some 50 μ from the end of the range of α particles. This range would set an upper limit of 5 kev. on the lowest energy of delta rays that may be seen. See Appendix.

Sheets of emulsion irradiated in the summer of 1952, during ascents described elsewhere (4), provided more abundant experimental material. By examining proton and α -ray tracks recorded in them, it became clear that these low energy delta rays could be counted regularly enough to be of use in the identification of particles even over short lengths of track, and at low velocities.

For instance an α ray of 2000 μ range gives $n = 2$ delta rays per 100 μ with the accepted techniques (1), and a proton of 150 μ shows no delta ray at all. It will be seen by inspection of our curves that a 2000 μ α ray shows $n = 15$ approximately, while a proton shows three or four delta rays in the last 150 μ of its path.

The first findings were reported briefly by Demers and Lechno-Wasiutynska (5). An appendix by one of us, at the end of this paper, describes numerical calculations of the Mott-Bradt-Peters formula (1). These calculations are made assuming that all delta rays above a certain minimum energy w_{min} , for instance 5, 10, or 20 kev., are counted. Then comparison with experi-

¹ Manuscript received November 24, 1952.

Contribution of the Institut de Physique, Université de Montréal, Montreal, Que.

ment requires some assumption regarding the relation between the energy w of a delta ray and its range or its number of grains. For instance delta rays of more than two grains are supposed to have more than 10 kev., and this allows us to define an *average efficiency* in this case, as follows: (Number of delta rays found with more than two grains) \div (Number of delta rays expected with $w_{min} = 10$ kev.). The average efficiency as mentioned in the Appendix is of the order of 15 to 20% in G5, NTB, and C₂.

Here no assumption is made on the energy of the delta rays when counting them; on the contrary from the analysis described in this paper, the relation between their energy and their number of grains is arrived at. This analysis makes use of the usual range-energy relation for protons and α rays.

2. Counting Criteria

We attempt to count every recognizable delta ray. Those defined by more than one grain, or by one grain distinct from those defining the track of the particle, pose no special problem, since the background is low. However, grains pressed together in the main part of the track sometimes protrude in a singular way, and these seem to be genuine delta rays. This belief is based upon inspection of their appearance, and on the consistency of the results obtained by counting them as being delta rays. Also, if they were mere accidents or defects in the track, they would be expected to show a frequency more or less proportional to grain density or to ionization, and therefore to decrease as the range increases from the end of a proton track for instance. On the contrary their frequency follows a different law, and quite a few times a proton will not show a single delta ray in the last 150 μ of its path, while an α ray of the same ionizing power will show several in an equal length.

It is difficult to state much more precisely the criteria used in counting such delta rays; they are to a degree subjective, and this reflects in the variations between days and between observers. This matter is taken up later.

So much for the counting when delta-ray density n is low enough. At the highest values of n , the delta rays overlap and are more difficult to distinguish individually.

All our measurements were carried out in baseless sheets of our "fine grain" emulsion formula 2, discussed earlier (3).

3. Effect of Charge and Mass

Several tracks identified as protons P , and as α rays α , respectively, from their appearance, were counted in one plate. In this case the range in divisions, at which each delta ray was recognized, was noted. The integral number N of delta rays per track found from the end of the track up to a certain range R is plotted against R . One division is worth 1.12 μ of the object being examined; since the sheet expanded by 7% sidewise during processing, one division is worth 1.05 μ of the track when registered.

The plot, Fig. 1, should provide a good test of the method: P and α have the same velocity at a given range, while the charges are in the ratio of 2 to 1. Theory then requires that N values should be exactly in the ratio of the square of the charges, i.e., 4 to 1, which checks remarkably well with these experimental results, at all ranges.

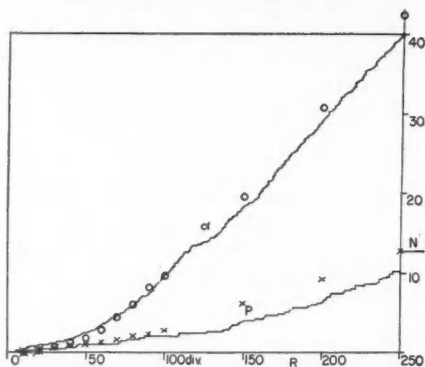


FIG. 1. Total number N of delta rays per track vs. R , counted under comparable conditions for 10 α and 5 P by P.D. (broken line), and for 10 α and 22 P by Z.L.W. (single points).

Differential plots of n vs. R show a similarly good agreement. It follows that distinction between P and α may be accomplished by the sole counting of delta rays on short segments. If the end of the track is visible, 150 μ length will provide almost certain identification. In the said series of measurements,

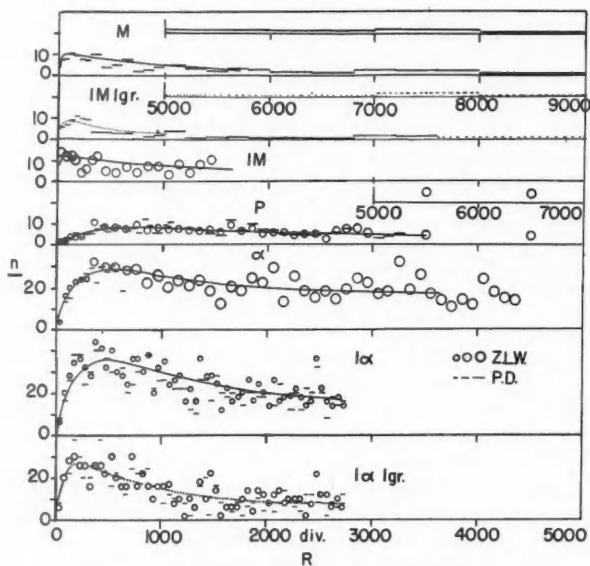


FIG. 2. Differential number n of delta rays per 100 divisions counted under various conditions of development by two observers, circles denote Z.L.W., otherwise P.D. Curves are for several α , P , and M . Lowest two curves are for a single α . Dotted line is for one-grain delta rays. Range R is in divisions; number of delta rays n is per 100 divisions in this as in all figures.

the following values of N were found by one observer in 150 μ range for P : 15, 11, 11, 8, 6 and for α : 65, 50, 48, 48, 41, 34, 33, 29, 28, 20. In 100 μ , values were as follows: P : 4, 3, 2, 1, 0; α : 22, 15, 11, 11, 10, 9, 8, 6, 5, 2. Here some 10% errors would be expected.

The differential curves of n vs. R for P and α , Fig. 2, show a maximum near 450 μ and then a slow decrease of n at larger ranges. The curve drawn for mesons, Fig. 2, shows a very sharp initial rise and a descent starting at 100 μ or even at a shorter range. This curve represents the sum of measurements on π and μ mesons combined, there being no significant difference between the two. Mesons can therefore be easily recognized by such a plot.

If the position of the maximum in the n vs. R curve could be ascertained with enough accuracy, it could be taken as a measure of the mass of the particle when $z' = 1$. In general, if z' does not vary along the path:

$$[1] \quad R_{\max}(M, z') = (M/z'^2) R_{\max}(1, 1) \sim (M/z'^2) 450 \mu.$$

Mesons can also be distinguished from P and α in the 100 μ path at the end of the range by the number of grains in the delta rays: in such a range some three delta rays with two grains or more will usually appear for a meson, and usually none and seldom one for P or α . This naturally follows from the range velocity relations.

4. Comparison with Theoretical Curves

If we compare the differential curves for P and α in Fig. 2 with the theoretical distributions, we find that the range at which the maximum occurs is best represented by choosing $w_{\min} = 8$ kev. approximately, while the absolute value at 2000 μ range leads to choosing $w_{\min} = 10$ kev.; on the other hand, the range at which the first delta appears would lead to $w_{\min} = 2$ kev.

These somewhat conflicting observations are well reconciled by assuming that the efficiency f of counting delta rays, or the proportion of delta rays theoretically formed that are seen, is a rapidly varying function of their energy, and this suggests the possibility of determining precise values of the efficiency.

EFFICIENCY OF COUNTING DELTA RAYS

1. Linear Equations Method

This first method utilizes a system of m linear equations, containing m coefficients of efficiency that are the unknowns, and the m values derived from experiment for the linear density of delta rays in as many successive segments of the tracks. Coefficients in these equations are theoretical values of the total number of delta rays N .

Firstly theoretical n vs. R curves were drawn for P , with various limits set on w : n_{1-3} represents the theoretical density for 1 kev. $< w < 3$ kev.; n_{3-5} , the same for 3 kev. $< w < 5$ kev.; and so on for n_{5-7} , n_{7-10} , $n_{10-\infty}$. From these curves, the total number expected theoretically between specified range values of the particle were computed. These range values in microns are shown in superscripts, thus: N_{1-3}^{0-20} , N_{1-3}^{20-50} , etc. Inasmuch as we may assume that the probability of seeing a delta ray depends only on the energy class

to which it belongs, and not on the velocity of the particle, we may define and use f_{1-3} as this probability for 1 to 3 kev. delta rays, f_{3-5} , for 3 to 5 kev. delta rays, etc., and write down the following set of equations, where N^{0-20} means the observed number between 0 and 20 μ , N^{20-50} , between 20 and 50 μ , etc.:

$$\begin{aligned}
 [2] \quad N^{0-20} &= N_{1-3}^{0-20} \cdot f_{1-3} \\
 N^{20-50} &= N_{1-3}^{20-50} \cdot f_{1-3} + N_{3-5}^{20-50} \cdot f_{3-5} \\
 N^{50-160} &= N_{1-3}^{50-160} \cdot f_{1-3} + N_{3-5}^{50-160} \cdot f_{3-5} + N_{5-7}^{50-160} \cdot f_{5-7} \\
 N^{160-300} &= N_{1-3}^{160-300} \cdot f_{1-3} + N_{3-5}^{160-300} \cdot f_{3-5} + N_{5-7}^{160-300} \cdot f_{5-7} + N_{7-10}^{160-300} \cdot f_{7-10} \\
 N^{300-400} &= N_{1-3}^{300-400} \cdot f_{1-3} + N_{3-5}^{300-400} \cdot f_{3-5} + N_{5-7}^{300-400} \cdot f_{5-7} + N_{7-10}^{300-400} \cdot f_{7-10} \\
 &\quad + N_{10-\infty}^{300-400} \cdot f_{10-\infty}
 \end{aligned}$$

This system is easily solved because the range limits have been so chosen as to add one class of energy and one term as we pass from one equation to the next one. The first equation is solved for f_{1-3} , and the value found used in the next equation which in turn is solved for f_{3-5} and so on.

This procedure has been applied to the average of a sum of measurements on P and also on α by multiplying every theoretical value by 4, and the results are shown in Table I. In fact, in applying it, one division of the micrometer

TABLE I
EFFICIENCY OF COUNTING (IN %) IN DIFFERENT ENERGY INTERVALS (IN KEV.)
OF THE DELTA RAYS, LINEAR EQUATIONS METHOD

	f_{1-3}	f_{3-5}	f_{5-7}	f_{7-10}	$f_{10-\infty}$	$f_{10-\infty}$ (other range intervals)
10 α rays (Z.L.W.)	0.07	2	16.8	15.9	41	41-61
10 protons (Z.L.W.)	0.42	0.54	15	30	37	37-70
10 α rays (P.D.)	0.26	0.33	45.3	—	—	—

was taken as equal to 1 instead of 1.05 μ , but this makes little difference for what follows. The first and second terms are never negligible, and the efficiencies f_{1-3} and f_{3-5} , which are derived from relatively small numbers N , have a great influence on the other efficiencies. Some better way of using the experimental data along these lines might be designed, but we thought at this point of a differential method which is probably preferable, and less laborious, as described in the next section.

The straight application of this method to further segments of P and α has led to rising values of f reaching as high as 190% at $R = 4000 \mu$. This may perhaps be attributed to the counting of spurious delta rays in these cases, or else to the fact that f at a given energy of the delta ray increases when the density of the track decreases. The results in Table I indicate a small and variable proportion of the delta rays being counted between 1 and 5 kev., and a rising efficiency tending toward unity near $w = 10$ kev.

2. 1st Differential Method

Examining the equations led us to another simpler method for calculating f from the experimental data. We write a partly relativistic equation for n :

$$[3] \quad n = (2.73 z'^2/\beta^2) \int_0^{w_{\max}} f dw/w^2, \quad w_{\max} = 2 mc^2 \beta^2 / (1 - \beta^2).$$

The value of 2.73 for the coefficient holds for $n = dN/dx$, w in kev.; then $2 mc^2 = 1021.7$ kev. This equation differs from a similar one in the Appendix in that the differential dw/w^2 is multiplied by the efficiency f ; we suppose f to depend only on w . The lower energy limit may now be $w_{\min} = 0$, since $f = 0$, at zero energy, and w_{\max} is the same as previously. In the other form of the equation f is assumed as zero below $w = w_{\min}$, and as unity between w_{\min} and w_{\max} .

Let us write a function ϕ , similar in its first expression to the function $1/K$ of Hoang (6):

$$[4] \quad \phi = n\beta^2/2.73 z'^2 = \int_0^{w_{\max}} f dw/w^2$$

which is experimentally determined from n and from the range velocity relation, as a function of β . By differentiating with respect to w_{\max} which is itself a function of β :

$$d\phi/dw_{\max} = f/w_{\max}^2.$$

The value of f refers to the energy w_{\max} . Omitting the subscript we may write:

$$[5] \quad f = w^2 d\phi/dw.$$

This equation may be applied by plotting ϕ vs. w , finding the slope of the smoothed curve passing through the points, and multiplying it by w^2 , then f values obtain. This was done for the same series of 10 α rays of Fig. 1 measured by P.D. See Fig. 3, and the following list, which shows reasonable agreement with the data of Table I for the same α rays:

1 kev.	2	3	4	5	6	7	8	9	10	12
0	0.64%	2.7	8.16	19.2	37.5	65.5	80.6	84.5	102	136

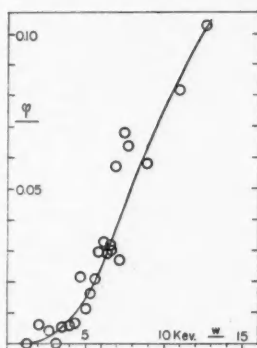


FIG. 3. First differential method of determining f , ϕ vs. w , 10 α rays of P.D. as in Fig. 1; efficiency $f = \text{slope} \times \beta^2$.

3. 2nd Differential Method

However, noting that $d(-1/w) = dw/w^2$, we may plot the data in such a way that f is read directly as a derivative:

$$[6] \quad f = d\phi/d(-1/w).$$

This second procedure was applied to the same series of 10 α rays with very similar results indeed, the differences arising only from the exact manner of fitting the curve through the points. It was also applied to several other series of measurements. See Figs. 4, 5, and 8.

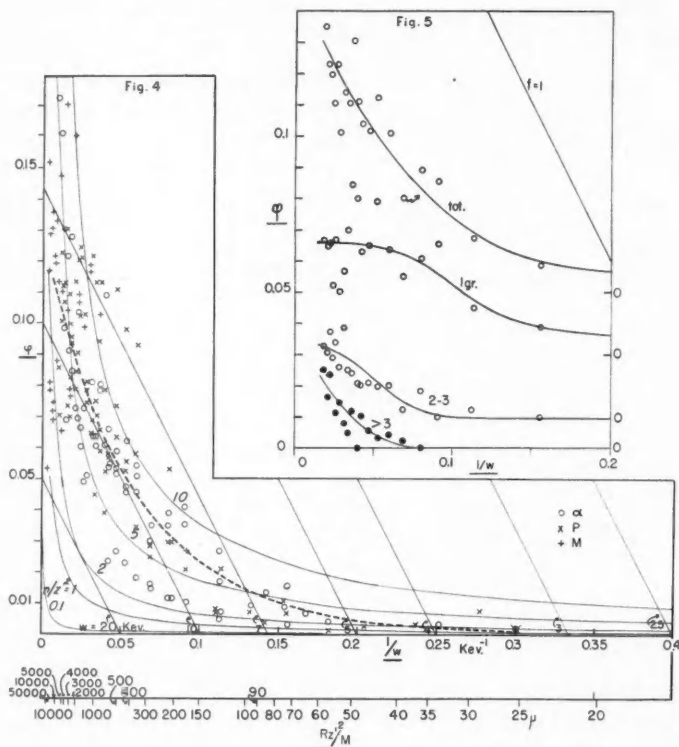


FIG. 4. Second differential method of determining f , ϕ vs. $1/w$ plot, efficiency $f = -\text{slope}$. All measurements, made by two observers, are included. About 10,000 delta rays were counted for this curve. No systematic difference appears between α , P , and M . Experimental curve shown by dotted line represents an average, better agreement is found with a closer control of conditions, as in Fig. 5, on a single α ray. The oblique straight lines with slope -1 represent $f = 1$, and various values of w_{\min} . The curves that are nearly hyperbolas represent constant values of n/z^2 . The supplementary scale in abscissae represents the range of the equivalent proton, $R z^2 / M$.

FIG. 5. Same plot for single α of Fig. 2; *tot.* for all delta rays; *1*, *2-3*, and *> 3*, for those having 1, 2 and 3, and more than 3 grains respectively. Vertical scale is displaced from one curve to the next for clarity.

For these plots the length of the segments of tracks considered was 100 divisions, or multiples thereof, so that n was naturally counted not per 100 μ , but per 100 *divisions* of 105 μ . With this practical definition of n , ϕ was written so:

$$[7] \quad \phi = n\beta^2/2.87 z^{1/2}.$$

If ϕ and $1/w$ are used as the rectangular coordinates, we may write in along the $1/w$ scale a scale of the ranges R for a particle. We may also draw two families of curves which are of interest. Suppose $f = 1$ for $w > w_{\min}$, then we have a series of straight lines of slope -1 along which a value of w_{\min} is uniquely defined. Suppose successive fixed values of n , $n = 1, n = 2, \dots$. We have a series of curves which nearly follow the law $xy = \text{constant}$. Then one pair of experimental values of n and R may be plotted without calculations on the curvilinear system of coordinates drawn. The point so chosen defines uniquely the value of w_{\min} which would agree with the data assuming $f = 1$.*

The values of f derived from the slope of the ϕ vs. $1/w$ curve are very sensitive to errors and fluctuations. Measurements on a single track give better internal agreement as seen in Fig. 5. On the whole it is fairly satisfactory that no case has been found so far which clearly required values of f greater than 1 or smaller than zero. For reasons that will become apparent later, the accuracy is good around $w = 10\text{--}20$ kev., and very little can be told from the application of this method above 50 kev. However it seems probable that f should reach a maximum of the order of unity between 40 and 100 kev., and then diminish, since a 1 Mev. delta ray would be entirely invisible, and since a 70 kev. delta ray should be long enough to emerge from the axis of the track, and dense enough in our emulsion to be recognized.

The experimental values of f are shown in Fig. 8. They agree reasonably well with those derived from the other two methods when $w < 25$ kev. In agreement with the first method the present method applied to the same data indicates values of f decidedly passing unity above 25 kev. While this matter is not entirely clear, it may be an indication that some spurious delta rays are sometimes counted. This would induce a tendency to find in the high energy tracks a constant value of n , so that the ϕ vs. $1/w$ curve would tend to follow a curve of constant n but of increasing slope. We have an equivalent explanation if we assume that f does not depend exclusively on w but that it may increase with β as discussed later. So far nothing obliges us to suspect the validity of the Mott-Bradt-Peters formula.

The values of f depend on the visibility of the delta rays as distinct from the grains along the axis of the track at the lower energies of the delta rays, and as distinct from the background of single grains and of other electron tracks at the higher energies. Indications are that the values at low energies may be somewhat greater along a track with a low grain density. On the other hand, the values at high energies may be larger when the delta rays are more numerous because confusion with a background electron is not so much to be

* Also, along one line of given w_{\min} value for which $f = 1$, we may read the n and R coordinates. The n vs. R relation so obtained corresponds to the hypothesis $f = 1$ when $w > w_{\min}$.

feared then. Moreover the relativistic corrections make the procedure outlined theoretically unfit for obtaining the true values of f at energies of the delta rays much higher than 50 kev. Taking them fully into account would be very difficult.

4. Analysis of the Number of Grains

The number of delta rays may be counted while imposing on them any criteria we please. As long as these criteria do not change the efficiency of counting the delta rays of a given energy as we pass from one segment of the track to the other, we may carry the analysis just described, and determine for such delta rays how the efficiency varies with energy w . Accordingly the data for one long α ray were plotted in several ways, Fig. 5. Curve I is for the total number of delta rays, curve II for those having only one grain, $g = 1$, curve III for two and three grains, $g = 2$ and 3, curve IV, for more than three grains, $g > 3$.

We expect f for one grain to be quite small at high enough energies, since a 50 kev. delta ray with a mean range of 15μ should very seldom be represented by only one grain. The slope of curve I should therefore be very small both at zero and at a higher energy, with an inflection point at some intermediate energy. Within experimental uncertainties, such a course agrees with the data. This agreement may be taken as a confirmation of the proper identification of the one grain delta rays.

Calling N_{th} the theoretical number expected, N' , N'' , ... the numbers in the different classes making the total observed of N ;

$$N' = f' N_{th}; N'' = f'' N_{th}; \dots N = (f' + f'' + \dots) N_{th}$$

[8]

$$f = f' + f'' + \dots$$

the over-all efficiency is the sum of the efficiencies in the component classes. This applies whether the N values are for all energies of delta rays or only for an infinitesimal energy range. Therefore the slopes of curves II, III, IV at a given abscissa should add up to that of curve I. This rule was kept in mind while fitting the various curves to the experimental points, and accordingly, the f vs. w plots in Fig. 6 verify it quite well.

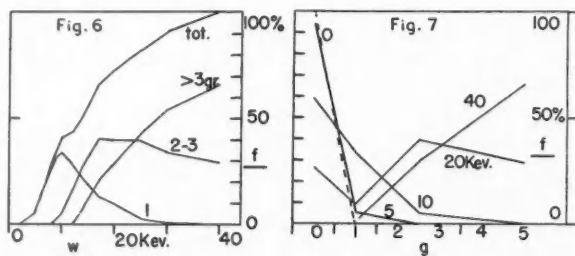


Fig. 6. f vs. w for different number of grains, derived from Fig. 5; f is the probability of seeing a delta ray of energy w counting g grains.

Fig. 7. f vs. number of grains g , for different energies w , derived from Fig. 5.

There is in curve III a suggestion of a maximum slope, and of a flattening above $w = 50$ kev., meaning that higher energies are seldom represented by two or three grains.

The f vs. w tables established for given numbers of grains g may be completed by adding a column for $g = 0$, the values of f_0 in this column being obtained by difference: $f_0 = 1 - f$. This table may be read either way, to give at a constant energy the absolute number of times the delta ray has zero, 1, 2 or 3, or more than 3 grains. For a few energies, Fig. 7 has accordingly been drawn. This differs from the usual distribution curves, in that the ordinate is not the number of cases per unit interval of the abscissae, but the total number of cases in one of four categories, represented in abscissae: 0, 1, 2 or 3, and more than 3 grains. Somewhat comparable curves have been drawn by Zajac (7) in different conditions. For 30 kev. electrons recorded in NT2A and in NT4 emulsions she found tracks measuring on the average 8μ and containing from 6 to 18 grains. No such distributions at lower energies are described in the literature. We have recorded the tracks of 50 kev. electrons accelerated in an electron diffraction installation. These tracks in one fine grain emulsion measured about 15μ and contained about 12 grains, while those of Zajac of the same energy had the same range and contained on the average 20 grains.

5. Energy Distribution of Delta Rays

If we inspect equation [3] we see that within a factor $2.73 z'^2/\beta^2$, the expression of dn/dw as a function of w is f/w^2 and does not depend on z' or on β . The energy distribution of the delta rays is therefore the same in relative value for all particles of all velocities, except that the high energy limit w_{\max} in this distribution is a growing function of β .

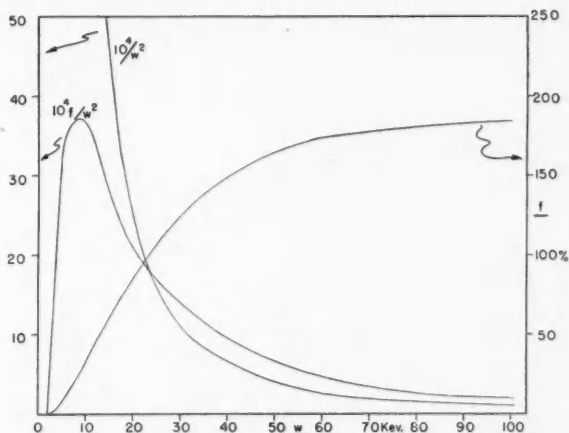


FIG. 8. Plots of f derived from Fig. 4, of $1/w^2$, and of f/w^2 vs. w ; f/w^2 is theoretically proportional to the relative number per unit energy interval dn/dw . The upper limit w_{\max} in the energy distribution curve is 5 kev. for $\beta = 0.07$, 10 for 0.1, 42 for 0.2, 68 for 0.25, and 103 for 0.3.

Fig. 8 shows f values from Fig. 4; f and f/w^2 are plotted against w . It is seen that the f/w^2 curve has a maximum at about 12 kev. and falls off more or less like $1/w$ until 90 kev. The values of f are not very certain above 25 kev., and if we assume that $f = 100\%$ above 25 kev., it means that dn/dw decreases from then on as $1/w^2$. The difference between the energy spectra at various velocities lies in the limit w_{\max} , as long as we neglect relativity corrections. The high energy tail is very low above $\beta = 0.35$ so that the area under this curve, which is equal to ϕ , is little dependent on the high energy cutoff and takes an almost constant value above $\beta = 0.35$.

This curve manifests why the experimental determination of f cannot be very precise above $w = 30$ kev. This determination is based on the variation of ϕ with w_{\max} ; at higher values of w_{\max} , ϕ is large and the method amounts to looking for a small increase in the area under the said curve at the high energy extremity, assuming that the rest of its shape remains unchanged. The best accuracy should be attained between 8 and 15 kev. near the maximum of the curve, and it is for such values of w that individual determinations of f agree best.

Suppose that f depends not only on w but also to some degree on β , for instance that a lower grain density or a higher β favors counting the low energy delta rays around 5–15 kev. This would change the shape of the energy spectrum and affect the determination of f , in such a way that f would seem too large at high energies, in agreement with observations described above.

6. Corrected Equation for the Linear Density of Delta Rays

To evaluate properly the values of n we should determine in given experimental conditions the variation of f with w , and proceed to integrate equation [3].

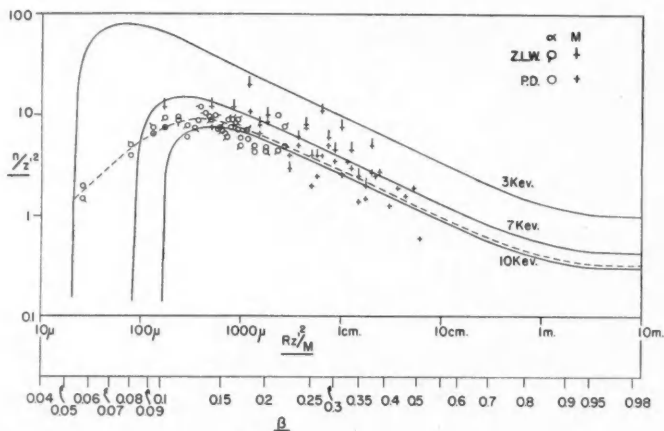


FIG. 9. Average n/z^2 vs. $R z^2/M$ curve in log log scale drawn from one α measured by Z.L.W. and by P.D., from five M , by P.D., and one M , by Z.L.W. This should be a universal function for all z' and M , as long as z' remains constant. Theoretical data assuming $f = 1$, and various values of w_{\min} are also shown.

An alternative procedure is to find the experimental values of n as a function of β for $z' = 2$ and use the equation:

$$[9] \quad n(z', \beta) = (z'^2/4) n(2, \beta).$$

The relative energy distribution of the delta rays is practically invariable above $\beta = 0.35$, so that above this velocity, n should vary quite accurately as $1/\beta^2$.

$$[10] \quad n(z', \beta) = C z'^2/\beta^2 \quad \beta > 0.35.$$

The constant C would have to be determined by measurements for instance with $z' = 2$ and $\beta \geq 0.35$. It is numerically equal to the linear density of delta rays along a relativistic proton, which is about 0.28 according to Fig. 9. The above should hold as long as f depends exclusively on w , and disregarding relativistic corrections.

Fig. 9 shows a universal curve of n vs. R derived from our measurements.

VELOCITY DETERMINATIONS

From the preceding arguments, at least for velocities β less than 0.35, a change in the velocity of the particle modifies the distribution in energy of the delta rays, and accordingly should modify their distribution in number of grains. Therefore, a study of this distribution should enable one to determine the velocity along a track, whatever be the values of z' , M , and R . Fair agreement with this rule may be seen in Fig. 10 derived from measurements on M , P , and α . In this figure the number N of delta rays are shown vs. their number of grains g , for different segments of tracks. The distribution extends to greater and greater values of g as β passes from 0.09 to 0.47, and distributions are nearly the same for different particles having the same velocity. Comparing such diagrams with the one drawn for a segment of an unknown track may

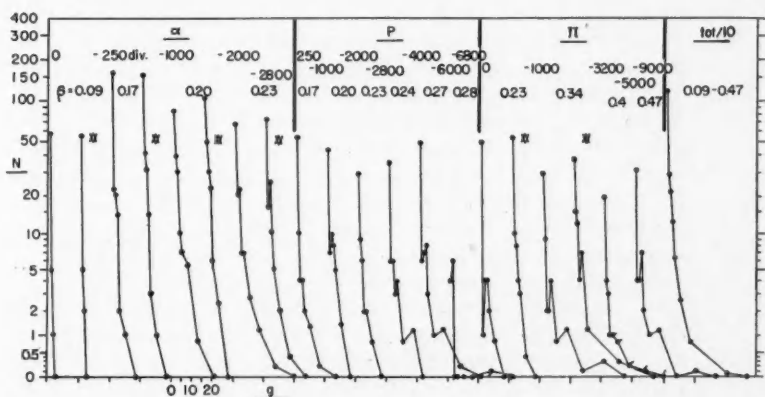


FIG. 10. Effect of velocity β on the distribution of number of delta rays N vs. number of grains g . Range intervals in divisions are shown. Two observers, Z.L.W. is denoted by an asterisk. The vertical coordinate is $\log(N+1)$. Scale of g is marked only once, it is displaced by 15 units from one distribution to the next one.

allow the determination of β . An almost equivalent rule is to determine in a population of 50 or 100 delta rays the greatest value of g to be found; this from Fig. 10 is 3 or 4 at $\beta = 0.09$, 8 to 13 at $\beta = 0.20$, and 30 at $\beta = 0.35$ to 0.5. This fast and approximate rule may be of use even above $\beta = 0.35$, since it does not depend on the general features of the distribution in number of grains, which varies little above this velocity, but upon the upper energy limit in the distribution.

CONCLUSION

From these results, we may draw a picture of the *delta-ray structure* of a track. Very many delta rays having energies near 1 or 2 kev. are formed according to theory, and despite a very low efficiency of counting, a small number of them apparently do show up in our emulsion formula 2. When visible they have one grain. Conversely when a one grain delta ray is seen, its energy, from Fig. 6, may be as low as 2 kev. or as high as 30 kev. Delta rays of 15 to 150 kev. seldom fail to show up, they have 1, 2, and mostly 3 and more grains.

The *average efficiency* defined at the beginning depends on the lowest energy w_{\min} which is assumed as being counted, and this may be chosen in a number of different ways, since a given number of grains, such as 2, may represent quite different energies as seen in Fig. 7.

Despite some more or less subjective features the counting of low energy delta rays may yield quite reliable results if some care is taken to make conditions comparable for different observers, as seen from a comparison in Fig. 2. The *identification* of the particles, especially when mass, charge, and velocity are low, may be provided by the present method, used either alone or in conjunction with other methods based on the appearance, the grain density or the optical density of the track, and angular scattering.

The *variation of the efficiency* of counting delta rays has been shown to depend mostly on the energy of the delta rays, but it may also depend to some degree on the grain density of the track, and on the linear density of the delta rays.

To sum up the discussion of the calculations in the Appendix and of the experiments in this paper, the *linear density* of delta rays along a track at low velocities, $\beta < 0.35$, and low charges of the particle, depends strongly on the values of the efficiency. At high velocities, the relativistic corrections may have a small visible influence. At low velocities and high charges, the important factor is electron capture, of which no full study has been made yet.

Counting the delta rays when their density is more than about 60 per 100 μ is very difficult and not very certain. It seems that some other method might be preferable, taking advantage of the statistical features of the delta ray distribution in space. *Photometry* is indicated then, or an equivalent thereof. We have tried for instance counting the grains in elements at different distances from the axis, with fairly reliable results. These matters will be taken up in another article.

ACKNOWLEDGMENTS

We thank Miss Solange Boucher who did part of the searching of the plates. We also thank the National Research Council and Canadian Industries Limited, for grants that made this work possible.

REFERENCES

1. BRADT, H. and PETERS, B. Phys. Rev. 74: 1828. 1948.
2. DEMERS, P. Phys. Rev. 78: 320. 1950.
3. DEMERS, P. Can. J. Phys. 31: 78. 1953.
4. DEMERS, P. Can. J. Phys. 31: 366. 1953.
5. DEMERS, P. and LECHNO-WASIUTYNSKA, Z. Compt. rend. 235: 474. 1952.
6. HOANG, T. F. Thesis, Paris, France. 1950.
7. ZAJAC, B. Ph.D. Thesis, Edinburgh, Scotland. 1950.

APPENDIX

1. Introduction

Mott (4) wrote down a relativistic expression for the linear density of delta rays, based on the Rutherford scattering formula. Bradt and Peters (2) published a revision of this expression, where the path length is written down explicitly in the laboratory coordinates. In a later paper (3), they thank J. Ashkin for supplying them with this revised expression, which is as follows. In it dn or d^2N/dx is the number of delta rays found per unit length, for an energy interval dw of the delta rays.

$$[1] \quad d^2N/dx = (2\pi \mathcal{N} e^4 z'^2 / mc^2 \beta^2) (dw/w^2) \times$$

$$\{1 - (1 - \beta^2)w/2mc^2 + (\pi z' \beta / 137)[(1 - \beta^2)w/2mc^2 \beta^2]^{\frac{1}{2}}[1 - (1 - \beta^2)w/2mc^2 \beta^2]\}$$

N = total number of delta rays.

n = number per unit length dN/dx .

x = length of path not in cm., but in units of 100 microns = 0.1 mm.

$\mathcal{N} = \sum (\text{number of atoms per cc.})_i z_i$, for all atoms i present = number of electrons per cc. of the emulsion used, taken here as 10^{24} . It is in fact nearer to $1.07 \cdot 10^{24}$ in concentrated emulsions.

$e = 4.8 \cdot 10^{-10}$ e.s.u.

z' = atomic number of the particle supposed to be completely ionized.

Otherwise z'_{eff} should be used.

mc^2 = rest energy of the electron, 510.7 kev. or $0.818 \cdot 10^{-6}$ ergs.

β = velocity of the particle.

w = energy of the delta ray in kev. or in ergs.

All terms past the first one inside the brace are relativistic. The integrated form with the kev. as a unit for w is:

$$[2] \quad n = dN/dx = \left| \begin{array}{l} -2.5512 z'^2 / \beta^2 w - 2.4977 \cdot 10^{-3} (1 - \beta^2) z'^2 \log_e w / \beta^2 \\ -3.6612 \cdot 10^{-3} (1 - \beta^2)^{\frac{1}{2}} z'^3 / \beta^2 w^{\frac{1}{2}} - 3.5843 \cdot 10^{-6} (1 - \beta^2)^{\frac{1}{2}} z'^3 w^{\frac{1}{2}} / \beta^4 \end{array} \right| \frac{w_{\text{max}}}{w_{\text{min}}}$$

The value of w_{min} is taken usually between 5 and 20 kev. according to the range of the shortest delta rays visible. The upper limit w_{max} is the maximum energy of a knock-on electron. Bhabha (1) has written down a general expression for this:

$$[3] \quad w_{\text{max}} = 2mc^2(E^2 - M^2c^4)/(m^2c^4 + M^2c^4 + 2mc^2E).$$

An excellent approximation, good within 5% for a meson, 1% for a proton, and better still for heavier ions, is, as we have found,

$$[4] \quad w_{\max} = 2mc^2\beta^2/(1 - \beta^2) \quad \beta \leq 0.99.$$

The relativistic correction on w_{\max} makes little difference on the calculated value of n , for any value of β ; the uncorrected value of w_{\max} is $2mc^2\beta^2$.

2. Results

Fig. A1 contains the results for n derived from accurate numerical computation according to the above, with $w_{\min} = 5$ kev. (n on the left scale). The

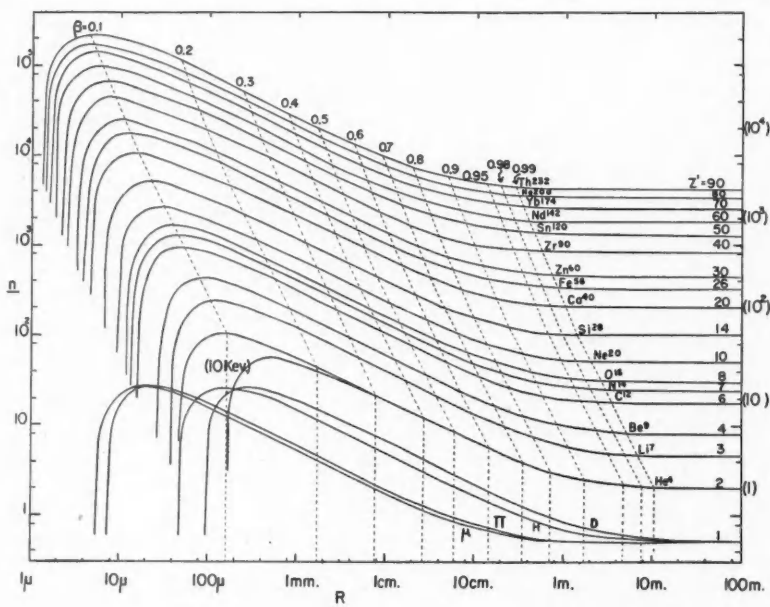


FIG. A1. Absolute densities n in number per 100 μ , vs. range R in emulsion, for $N = 10^{24}$ electrons per cc., add 7% for concentrated emulsions containing about $1.07 \cdot 10^{24}$ electrons per cc. For $w_{\min} = 5$ kev., n scale on the left; for $w_{\min} = 10$ kev., n scale on the right, and read only above $\beta = 0.35$; at lower β values, the other curves are parallel to the one drawn for α rays marked (10 kev.). Intersections of dotted lines with the curves mark the ranges for different β values, except for D , π , and μ . Charge of the ion z' is assumed constant, neglecting electron capture.

differences between such accurate values of n and those obtained when relativistic corrections are neglected are greatest when $\beta \sim 0.5$ (see Fig. A2), but even then they amount to less than 5% when $z' < 30$, and they would be practically invisible in Fig. A1. The same curves for $\beta > 0.35$ may be used with the n scale on the left, to read off values of n when $w_{\min} = 10$ kev. The scale of ranges has been calculated from data of Rotblat (5) and of Smith (6).

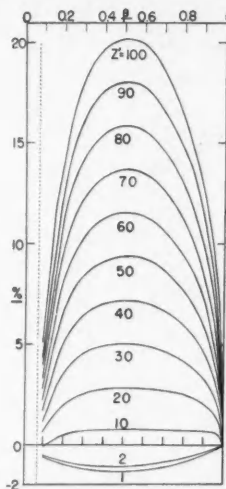


FIG. A2. Relative values in percentage of the correction brought about by the relativistic terms in [1] to the value of n , when $w_{\min} = 5$ kev., for several z' and β values.

No account has been taken of electron capture, which reduces the effective charge when $\beta < \beta_{\text{crit}} = z'/137$. This would lower the maximum value of n and visibly alter the shape of the curve up to a range passing somewhat that shown for $\beta = \beta_{\text{crit}}$, for z' between 5 and 30. For much higher charges, nearly the whole curve would have to be revised, but this will not be attempted here, as no satisfactory theory of the details of electron capture exists.

At high velocities, the value of n tends to a low constant value and shows no true minimum, like ionizing power (7). The absolute values are 5 to 10 times those found in C₂, NTB (2), and in G5, while those for $w_{\min} = 10$ kev. approximately agree at average velocities with those found in our fine grain emulsion formula 2.

One influence of the relativistic terms might perhaps be put in evidence, if it becomes possible to count the most energetic delta rays having nearly the energy w_{\max} produced by a fast particle. If the complete expression for dn/dw is written down, for $w = w_{\max}$ it is seen to be of the form $(1/w^2)(1 - \beta^2)$, the second factor comprises a relativistic correction equal to $-\beta^2$, which means that for $\beta = 0.3$, there are 9% fewer rays than expected otherwise, for $\beta = 0.7$ the correction is -49%, and for $\beta = 0.9$, it is -81%. This correction is very large; however, the presence of the term $1/w^2$ shows that very few rays of the highest energies may be expected anyhow, which renders the experimental verification very difficult.

ACKNOWLEDGMENTS

I thank Prof. P. Demers for his help and suggestions. This work was carried out with the assistance of grants from the National Research Council, and from Canadian Industries Limited.

REFERENCES

1. BHABHA, H. J. Proc. Roy. Soc. (London), A, 164: 269. 1938.
2. BRADT, H. and PETERS, B. Phys. Rev. 74: 1828. 1948.
3. BRADT, H. and PETERS, B. Colston papers. Butterworth Scientific Publications, London. 1949. p. 5.
4. MOTT, N. F. Proc. Roy. Soc. (London), A, 124: 425. 1929.
5. ROTBLAT, J. Nature, 167: 550. 1951.
6. SMITH, P. Phys. Rev. 71: 32. 1947.
7. VOJVODIC, L. Bristol Conference. 1951.

THEORY OF THE ELECTROMAGNETIC VACUUM¹

(Preliminary Report)

BY F. A. KAEMPFER

ABSTRACT

It is shown that, if one assumes Dirac's electrodynamics to be the correct description of the electromagnetic field at the absolute zero of temperature, the electromagnetic vacuum ("the Dirac sea") can be considered as a nonviscous fluid, in which pressure waves ("sound") travel with velocity c , and in which with rising temperature excitations appear as particles analogous to the excitations ("phonons" and "rotons") in ordinary nonviscous fluids at low temperatures. It is suggested that photons be considered as vortex-free excitations and charged particles as vortex excitations of the fluid representing the electromagnetic vacuum. Some evidence which supports this suggestion is given.

Dirac (1) has recently proposed a new formulation of electrodynamics, in which the well-known relations between electromagnetic fields and potentials are maintained:

$$[1] \quad \mathbf{E} = -\text{grad } \phi - \frac{1}{c} \frac{\partial \mathbf{A}}{\partial t}; \quad \mathbf{H} = \text{curl } \mathbf{A}$$

but in which the gauge of the potentials is fixed such that

$$[2] \quad \phi^2 = A^2 + \kappa^2; \quad \kappa = \frac{mc^2}{e}.$$

The potentials appear then as a four-vector which has everywhere the same direction as the velocity four-vector of small test charges immersed in the electromagnetic field.

We shall now take this idea seriously and adopt the point of view that Dirac's theory is the correct description of the electromagnetic field at the absolute zero of temperature. If especially no electric charges are present, we expect then the state of the electromagnetic vacuum at the absolute zero of temperature to be described correctly by the conditions that no fields shall be present:

$$[3] \quad \frac{1}{c} \frac{\partial \mathbf{A}}{\partial t} + \text{grad } \phi = 0; \quad \text{curl } \mathbf{A} = 0.$$

We expand now

$$[4] \quad \phi = \sqrt{\kappa^2 + A^2} = \kappa + \frac{1}{2\kappa} A^2 + \dots,$$

i.e. we intend to consider only fields which are so weak that test charges immersed in the fields will only obtain velocities $v \ll c$. Then the vacuum equations [3] can be written:

$$[5] \quad \frac{1}{c} \frac{\partial \mathbf{A}}{\partial t} + \frac{1}{2\kappa} \text{grad } (A^2) = 0; \quad \text{curl } \mathbf{A} = 0.$$

¹ Manuscript received January 12, 1953.
Contribution from the Department of Physics, University of British Columbia, Vancouver, B.C.

The remarkable fact now is that these equations are identical with the Bernoulli equations for an incompressible nonviscous fluid in absence of vortex motions:

$$[6] \quad \frac{\partial \mathbf{v}}{\partial t} + \frac{1}{2} \text{grad} (\mathbf{v}^2) = 0; \quad \text{curl } \mathbf{v} = 0$$

provided we identify

$$[7] \quad \mathbf{A} = \frac{\kappa}{c} \mathbf{v} = \frac{mc}{e} \mathbf{v}$$

which is just the relation proposed by Dirac.

We may therefore safely adopt the following point of view:

The electromagnetic vacuum at the absolute zero of temperature can be described as an incompressible nonviscous fluid, characterized by the classical equations [6]. Upon increase in temperature, motions of the vacuum liquid will be excited in complete analogy to the excitations observed in liquid Helium II. We shall tentatively identify the longitudinal excitations of the vacuum fluid (phonons) with the photon gas of black-body radiation, and the vortex excitations of the vacuum fluid (rotons) with the appearance of electrons. It is readily seen that the phonons excited in the vacuum fluid fulfill indeed the requirements necessary to identify them with the photons of black-body radiation. As is well known (Landau (4), Kronig and Thellung (3)) the longitudinal excitations of a nonviscous fluid contribute in second approximation to the energy of the system the amount

$$[8] \quad E^{(2)} = \frac{1}{2} \hbar \sum_{\mathbf{k}} c_0 k (2N_{\mathbf{k}} + 1)$$

where $E^{(2)}$ are the eigenvalues of the Hamiltonian

$$[9] \quad \mathcal{H}^{(2)} = \int H^{(2)} dV; \quad H^{(2)} = \frac{1}{2} (\mathbf{v}_\rho \mathbf{v});$$

c_0 is the velocity of sound in the fluid, and $\hbar k$ is the amount of momentum represented by a phonon of frequency $\omega_k = c_0 k$. It is seen that $E^{(2)}$ is identical with the energy of black-body radiation, provided we assume that the velocity of sound in the vacuum fluid is equal to the velocity of light. This high velocity of "sound" in the fluid is a further indication of the fact that the vacuum fluid is virtually incompressible.

The excitation of vortex motions in the fluid presents a more difficult problem since a rigorous Hamiltonian formulation of vortex theory has not yet been found. However, from the analogy to the theory of vortex excitations in ordinary nonviscous fluids as established by Landau (4) we may draw already some rather far-reaching conclusions.

The energy contributed by a vortex excitation of linear momentum P is, according to Landau,

$$[10] \quad \epsilon = \epsilon_0 + \frac{1}{2\mu} P^2$$

which is formally identical with the contribution to the energy by an electron appearing in the vacuum fluid, provided we can identify (Kramers (2))

$$[11] \quad \epsilon_0 = mc^2; \quad \mu = m.$$

Existence of vortex motion implies that

$$[12] \quad \oint (\mathbf{v} \cdot d\mathbf{s}) \neq 0.$$

Because of

$$[7] \quad \mathbf{v} = \frac{e}{mc} \mathbf{A}$$

this means that excitation of a vortex motion in the vacuum fluid means also

$$[13] \quad \oint (\mathbf{A} \cdot d\mathbf{s}) = \iint (\text{curl } \mathbf{A})_n dS = \iint \mathbf{H}_n dS \neq 0$$

which shows that vortex excitations in the vacuum fluid will become sources of a magnetic field. Now because of the relation

$$[4] \quad \phi = \kappa + \frac{1}{2\kappa} \mathbf{A}^2$$

this magnetic field will give rise to an electric field as well. In the stationary case we shall have

$$[14] \quad \mathbf{E} = -\text{grad } \phi = -\frac{1}{2\kappa} \text{grad } (\mathbf{A}^2)$$

and

$$[15] \quad \text{div } \mathbf{E} = -\frac{1}{2\kappa} \nabla^2 (\mathbf{A}^2).$$

This corresponds to a source of electric field of charge density

$$[16] \quad \rho = -\frac{1}{8\pi\kappa} \nabla^2 (\mathbf{A}^2).$$

In other words: the vortex excitations of the vacuum fluid will be sources of a magnetic field and consequently of an electric field. Thus the rotons of the vacuum fluid will appear as particles which are carriers of electric charge and magnetic moment. The author believes that future investigations will show these rotons to be identical with electrons.

In conclusion of this preliminary report, which is necessarily of a somewhat tentative nature, it might be worth noting that Landau and Khalatnikov (5) have calculated the very small viscosity of Helium II on the theory that it is caused by phonon-phonon interactions which appear in higher order terms of the Hamiltonian. If the analogy of the vacuum fluid to liquid Helium II is complete we should expect the vacuum fluid to have a small viscosity as well. This would allow then for the propagation of transverse pressure waves in the vacuum fluid. The author believes that these transverse phonons are identical with neutrinos and he hopes to report further on this matter in subsequent publications.

ACKNOWLEDGMENT

The author feels deeply grateful for the stimulations received through the work of Landau, Dirac, and H. A. Kramers.

REFERENCES

1. DIRAC, P. A. M. Proc. Roy. Soc. (London), A, 209: 291. 1951.
2. KRAMERS, H. A. Physica, 18: 653. 1952.
3. KRONIG, R. and THELLUNG, A. Physica, 18: 749. 1952.
4. LANDAU, L. D. J. Phys. (U.S.S.R.), 5: 71. 1941.
5. LANDAU, L. D. and KHALATNIKOV, I. M. J. Exptl. Theoret. Phys. (U.S.S.R.), 19: 637, 909. 1949.

THE PHYSICAL MEANING OF AUXILIARY CONDITIONS IN THE THEORY OF GRAVITATIONAL WAVES¹

By F. A. KAEMPFFER

ABSTRACT

The conditions are examined which are necessary to reduce the gravitational field equations in first approximation to a set of ordinary wave equations. These conditions are evaluated for the case of the gravitational field produced by an accelerated particle, and it is shown that they restrict the consideration to observers whose radius vector towards the source of the field is perpendicular to the vector of acceleration of the particle at the retarded time.

Einstein (2) has shown that it is possible to integrate his general field equations

$$[1] \quad G_{ik} = -\kappa(M_{ik} - \frac{1}{2}g_{ik}M)$$

in first approximation, if the right-hand side can be treated as a perturbation which will cause only small deviations γ_{ik} from the pseudo-euclidean metric δ_{ik} , such that if one carries out the substitution

$$[2] \quad \begin{aligned} g_{ik} &= \delta_{ik} + \gamma_{ik}; \delta_{11} = \delta_{22} = \delta_{33} = -1; \delta_{44} = +1; \delta_{il}\delta^{kl} = \delta_i^k = \begin{cases} 0; i \neq k \\ 1; i = k \end{cases} \\ g^{ik} &= \delta^{ik} + \gamma^{ik}; \delta^{11} = \delta^{22} = \delta^{33} = -1; \delta^{44} = +1; \end{aligned}$$

on the left-hand side, and if all terms of higher than first order in γ_{ik} are neglected, the resulting equations will describe in good approximation the metric field g_{ik} produced by gravitating matter, which is characterized by the energy-momentum tensor M_{ik} . Explicitly one obtains in this way

$$[3] \quad \square^2 \gamma_{ik} + \frac{\partial}{\partial x^i} \left(\frac{\partial \gamma_k^s}{\partial x^s} - \frac{1}{2} \frac{\partial \gamma_s^s}{\partial x^k} \right) + \frac{\partial}{\partial x^k} \left(\frac{\partial \gamma_i^s}{\partial x^s} - \frac{1}{2} \frac{\partial \gamma_s^s}{\partial x^i} \right) = 2\kappa(M_{ik} - \frac{1}{2}\delta_{ik}M)$$

and since according to a theorem by Hilbert (3) it is always possible to find an infinitesimal transformation of the coordinates which will make

$$[4] \quad \frac{\partial \gamma_k^s}{\partial x^s} - \frac{1}{2} \frac{\partial \gamma_s^s}{\partial x^k} = 0,$$

the field equations can be reduced to the well-known wave equations

$$[5] \quad \square^2 \gamma_{ik} = 2\kappa(M_{ik} - \frac{1}{2}\delta_{ik}M)$$

which, for given M_{ik} , can always be solved by retarded potentials. Equations of the type [5] will be called hereafter "ordinary" wave equations, and their solutions "ordinary" retarded potentials, in order to distinguish them from the more complicated type [3], which cannot be interpreted in terms of an analogy to the electromagnetic potentials produced by electric charges and currents.

¹ Manuscript received December 22, 1952.
Contribution from the Department of Physics, The University of British Columbia, Vancouver, B.C.

It was the purpose of the work reported in this paper to investigate what the state of motion of an observer relative to the source of the metric field must be, in order that he may be able to observe ordinary gravitational waves.

It is seen by inspection of equations [3] that the necessary conditions imposed on the coordinates of an observer, who wishes to observe ordinary gravitational waves, are

$$[6] \quad \frac{\partial}{\partial x^i} \left(\frac{\partial \gamma_k^s}{\partial x^s} - \frac{1}{2} \frac{\partial \gamma_s^s}{\partial x^k} \right) + \frac{\partial}{\partial x^k} \left(\frac{\partial \gamma_i^s}{\partial x^s} - \frac{1}{2} \frac{\partial \gamma_s^s}{\partial x^i} \right) = 0.$$

These conditions are weaker than the conditions [4] which are sufficient but not necessary in order to reduce equations [3] to ordinary wave equations. It is convenient to introduce new field variables ψ_k^s by

$$[7] \quad \psi_k^s = \gamma_k^s - \frac{1}{2} \gamma_r^r \delta_k^s$$

which allow the conditions [6] to be written in the simpler form

$$[8] \quad \frac{\partial}{\partial x^i} \frac{\partial \psi_k^s}{\partial x^s} + \frac{\partial}{\partial x^k} \frac{\partial \psi_i^s}{\partial x^s} = 0$$

and which solve the equations

$$[9] \quad \square^2 \psi_k^s = 2\kappa M_k^s.$$

Take as an example the metric field produced by a particle of mass m moving along a world-line described by the coordinates $z^\mu(s)$, where s is the proper time of the particle. The tensor M_k^s has in this case the form

$$[10] \quad M_k^s = m \frac{dz^s}{ds} \frac{dz_k}{ds}$$

and the solutions of the wave equations [9] are ordinary retarded potentials, which read in a notation introduced by Dirac (1)

$$[11] \quad \psi_k^s(x^\mu) = \frac{\kappa}{2\pi} \int_{-\infty}^{s'} M_k^s(s) \delta\{(x^\mu - z^\mu)(x_\mu - z_\mu)\} ds; \bar{s} < s' < \bar{\bar{s}}$$

where s' is a proper time between the retarded and the advanced proper times \bar{s} and $\bar{\bar{s}}$, \bar{s} and $\bar{\bar{s}}$ being the two solutions of the equation

$$[12] \quad \{x^\mu - z^\mu(s)\} \{x_\mu - z_\mu(s)\} = 0$$

corresponding to $x_4 - z_4(\bar{s}) > 0$ and $x_4 - z_4(\bar{\bar{s}}) < 0$ respectively. The explicit evaluation of the conditions [8] can be carried out most conveniently by using the identity of Dirac

$$[13] \quad \frac{\partial}{\partial x^i} \int_{-\infty}^{s'} M_k^s(s) \delta\{(x^\mu - z^\mu)(x_\mu - z_\mu)\} ds = \int_{-\infty}^{s'} \frac{d}{ds} \left[\frac{M_k^s(s) (x_i - z_i)}{\frac{dz^\mu}{ds} (x_\mu - z_\mu)} \right] \\ \times \delta\{(x^\mu - z^\mu)(x_\mu - z_\mu)\} ds$$

which has to be applied twice for each of the two terms, and which yields by straightforward calculation using the expression [10] for $M_k^s(s)$:

$$\begin{aligned}
 [14] \quad & \left\{ \frac{dz^r}{ds} (x_r - z_r) \frac{dz^\mu}{ds} (x^\mu - z^\mu) \right\}^{-1} \left[\frac{dz^r}{ds} (x_r - z_r) \left\{ \frac{d^3 z_k}{ds^3} (x_i - z_i) + \frac{d^3 z_i}{ds^3} (x_k - z_k) \right. \right. \\
 & - \frac{d^2 z_k}{ds^2} \frac{dz_i}{ds} - \frac{d^2 z_i}{ds^2} \frac{dz_k}{ds} \left. \right\} + \left\{ \frac{dz^r}{ds} \frac{dz_r}{ds} - \frac{d^2 z^r}{ds^2} (x_r - z_r) \right\} \left\{ \frac{d^2 z_k}{ds^2} (x_i - z_i) \right. \\
 & \left. \left. + \frac{d^2 z_i}{ds^2} (x_k - z_k) \right\} \right] = 0
 \end{aligned}$$

where all coordinates z_μ have to be taken at the retarded time \bar{s} . One may therefore multiply this condition by $(x^i - z^i)$ and $(x^k - z^k)$ successively, use the definition [12], and reduce it thus after some relabelling of summation indices to the simple form

$$[15] \quad \frac{d^2 z_k}{ds^2} (x^k - z^k) = 0 \text{ at } s = \bar{s}.$$

This then is the condition which the coordinates x^k of the observer must fulfill with respect to the coordinates z^k of the particle, in order that the effect of the particle on the metric field can be recorded as an ordinary gravitational wave. If the velocity of the particle is restricted to values $v \ll c$, and if the three-dimensional vectors \mathbf{a} and \mathbf{r} of the acceleration of the particle and of the distance between observer and particle respectively are introduced, then equation [15] may be written neglecting terms of higher than first order in v/c :

$$[16] \quad (\mathbf{a} \cdot \mathbf{r}) = 0,$$

which means that the gravitational effect of an accelerated particle is observed as an ordinary gravitational wave only if the acceleration at the retarded time is perpendicular to the radius vector from the observer to the particle at that time. Thus the gravitational field of an oscillating mass will consist of ordinary (transverse) waves only in the plane perpendicular to the direction of its motion, while the (longitudinal) waves emitted in the direction of the motion, when recorded by an observer at rest with respect to the center of motion, are of the rather complicated type which solve the equations [3], and for which no simple solutions in terms of ordinary retarded potentials can be found.

It is readily seen after a similar calculation that the stronger conditions [4], which read expressed in terms of the variables ψ_k^i

$$[17] \quad \frac{\partial \psi_k^i}{\partial x^i} = 0,$$

and which since Hilbert (3) are employed throughout the literature on this subject, imply

$$[18] \quad \frac{d^2 z_k}{ds^2} = 0 \text{ at } s = \bar{s}.$$

This means that only such observers are considered whose state of acceleration is the same as that of the source at the retarded time, and who will then be able to record ordinary gravitational waves. This is hardly the type of observer that could be realized in an actual experiment.

REFERENCES

1. DIRAC, P. A. M. Proc. Roy. Soc. (London), A, 167: 151. 1938.
2. EINSTEIN, A. Sitzber. kgl. preuss. Akad. Wiss., 831. 1915.
3. HILBERT, D. Math. Ann. 92: 1. 1924.

THE ABSORPTION DUE TO CARBON MONOXIDE IN THE INFRARED SOLAR SPECTRUM¹

BY J. L. LOCKE AND L. HERZBERG

ABSTRACT

New tracings of the absorption bands due to carbon monoxide in the 4.7μ and 2.4μ regions of the solar spectrum were obtained with a spectrometer of high resolving power. From the observed absorption intensity at 4.7μ the abundance of carbon monoxide in the earth's atmosphere over Ottawa was found, during spring and fall 1952, to vary between 0.1 and 0.2 cm-atm. Similar observations, made at other stations, were re-evaluated with the laboratory data used at Ottawa. The values for the carbon monoxide abundance in the earth's atmosphere at different geographical locations, determined in this way, were found to be within the limits of the values obtained at Ottawa. Absorption lines due to solar carbon monoxide in the 4.7μ region of the spectrum were resolved. Their intensity relative to the intensity of the solar carbon monoxide absorption in the 2.4μ region of the spectrum was found to be in agreement with expectations based on the theoretical curves of growth for solar absorption lines.

INTRODUCTION

Absorption due to carbon monoxide occurs in the infrared solar spectrum at 4.7μ and 2.4μ . The absorption at 4.7μ was discovered by Migeotte (6), working at Columbus, Ohio, and identified as the 1-0 (fundamental) vibration-rotation band of telluric carbon monoxide. The same band was also observed by Shaw, Chapman, Howard, and Oxholm (13) at the same station, and by Migeotte and Neven (7, 8) at the Jungfraujoch, Switzerland. The intensity of the absorption band, as observed by Shaw and his co-workers (13), did not vary during the time of observation, and was estimated by Goldberg, McMath, Mohler, and Pierce (3) from the published tracings to correspond to a concentration of carbon monoxide in the earth's atmosphere of 0.5 cm-atm. Migeotte (6), and Migeotte and Neven (7) found that the intensity of the band varied by a factor 3 or 4 during the observations. The band has also been found by Adel (1) on old tracings taken by him at Flagstaff, Ariz., in 1940.

The absorption at 2.4μ was discovered by Goldberg, McMath, Mohler, and Pierce (3) in observations made at Lake Angelus and at Mount Wilson. The absorption lines were found to belong to the 2-0, 3-1, 4-2, and 5-3 (first overtone) rotation-vibration bands of carbon monoxide, and to be of solar origin. After re-examination of the tracings obtained by Shaw and his co-workers (13) in the 4.7μ region, Goldberg and his co-workers (3) pointed out that the intensity of the absorption due to solar carbon monoxide in the region of the fundamental vibration was apparently much smaller than might have been expected from the intensity observed in the region of the overtone. Also, the intensity of the overtone band due to telluric carbon monoxide, as observed at Lake Angelus and Mount Wilson, seemed to suggest a much lower abundance of terrestrial carbon monoxide over these stations than the abundance estimated from the observations of the fundamental band at Columbus.

¹ Manuscript received January 5, 1953.
Vol. 2, No. 13, Contributions from the Dominion Observatory, Ottawa, Canada.

Goldberg and his co-workers (3) suggested the possibility that carbon monoxide was localized in certain regions over the earth's surface.

It therefore seemed desirable to investigate the carbon monoxide absorption in the solar spectrum at another geographical location and, if possible, in both the fundamental and first overtone regions at approximately the same time. Such a program was initiated at the Dominion Observatory in the spring of 1952 (5).

A similar program of observations was undertaken by Shaw and Howard (14) at Columbus, Ohio. These authors investigated the absorption due to telluric carbon monoxide in the first overtone band as well as in the fundamental. The abundance was determined from the observations in both the fundamental and first overtone bands and found to be 0.09 and 0.10 cm-atm. respectively. Further, new lines, attributed to solar carbon monoxide, were found in the region of the fundamental vibration.

In the present paper a report is given of the observations in the 4.7μ and 2.4μ regions of the solar spectrum obtained at Ottawa during spring and fall, 1952. The carbon monoxide concentration over Ottawa is determined on the basis of new curves of growth obtained in the laboratory. The geographical distribution of this atmospheric constituent is discussed, taking into account all the published data, and an explanation is given for the apparent inconsistencies in the relative intensities of the fundamental and first overtone bands.

APPARATUS

The observations were made with the recently constructed high dispersion spectrograph placed at the focus of the 80 ft. horizontal solar telescope of the Dominion Observatory at Ottawa.

The spectrograph consists of a plane grating with collimator and camera mirrors of 20 ft. focal length. When the instrument is used in the infrared beyond the photographic region the spectrum is scanned by rotating the grating, and the light is chopped at 1080 cycles per second before entering the first slit. The detector output is fed into a Wilson type amplifier (4), and recorded by a Brown strip chart recorder.

In the 4.7μ region the spectra were obtained in the first order of a 5000 line/inch grating, using a lead telluride detector refrigerated with liquid nitrogen. The wave length region of interest was isolated by a Poloroid C3 infrared filter. The observations in the 2.4μ region were made in the first order of a 14,400 line/inch grating with a lead sulphide detector, overlapping orders being eliminated by glass filters.

In the case of the solar spectra, in both the 4.7μ and the 2.4μ regions, an equivalent slit width of less than 0.15 cm.^{-1} was used. On the tracings taken at 4.7μ , lines differing by 0.18 cm.^{-1} were well separated.

The necessary laboratory spectra were obtained with a Nernst filament as light source, and an absorption cell of length 10 cm. with rock salt windows. The laboratory tracings of the 4.7μ region were taken with equivalent slit widths of 0.25 cm.^{-1} and less, those in the 2.4μ region with an equivalent slit width of 0.15 cm.^{-1} .

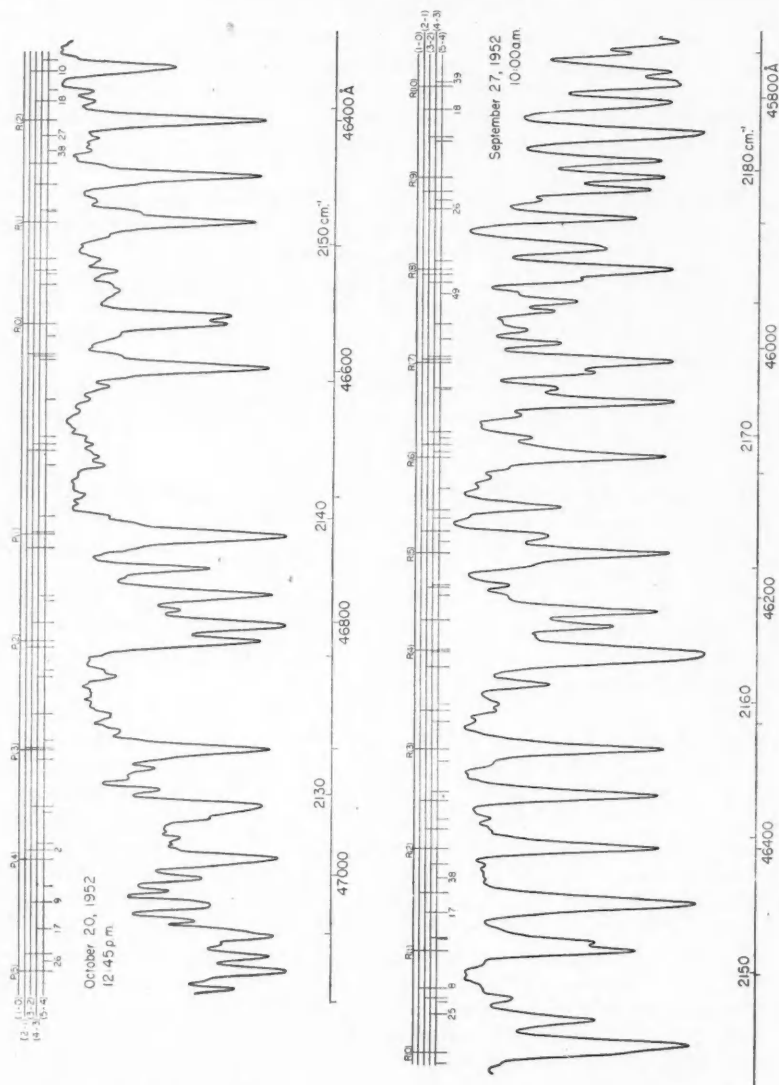


[Figure to be viewed broadside.]

FIG. 1. Portions of the 4.7μ region in the solar spectrum, containing *P*- and *R*-branches of the 1-0 band, and *R*-branches of the 2-1, 3-2, 4-3, and 5-4 bands of carbon monoxide. The computed positions of the lines expected in the region are indicated at the top; they are identified by the values of the rotational quantum number J'' . The lines of the 1-0 band are almost entirely of terrestrial origin; those of the other bands are due solely to absorption in the solar atmosphere.

For the wave length determination in the 4.7μ region the overlapping 8th order of the Fraunhofer spectrum at 6000\AA was used as comparison spectrum. In the 2.4μ region wave length standards were taken from the McMath-Hulbert Observatory Atlas (9). The accuracy of both methods employed was satisfactory for the purpose of identification of the observed lines.

OBSERVATIONS

The first tracings of the 4.7μ region of the solar spectrum, obtained at Ottawa in June, 1952, are very similar in over-all appearance to those published by Shaw, Chapman, Howard, and Oxholm (13). They show the series of strong absorption lines identified by Migeotte (6) as lines of the *P*- and *R*-branches of the 1-0 band of the CO molecule. The intensity distribution (intensity maximum at about $J = 7$) is in agreement with the earlier observations. It corresponds to a temperature of about 300°K ., indicating that the absorption takes place in the terrestrial and not in the solar atmosphere.

On later tracings, obtained on very clear days in the fall, a great number of additional weak and narrow lines appear which had been obscured on the earlier tracings by the then very strong absorption due to atmospheric water vapor. Portions of such tracings are reproduced in Fig. 1. Amongst these new lines a search was made for carbon monoxide lines of solar origin, the frequencies of which can be computed with the molecular constants of Plyler, Benedict, and Silverman (12). The positions of the computed lines are indicated in Fig. 1 above the reproductions of the recordings. Inspection of the figure shows that all the predicted lines of the 2-1, 3-2, 4-3, and 5-4 bands can be identified in the spectrum, except those which fall in regions of strong absorption of different origin. A sufficient number of good coincidences between observed and computed frequencies is found to consider the presence of these bands as established. The 2-1, 3-2, 4-3, and 5-4 bands correspond to transitions between excited vibrational levels of the molecule, and can occur, in absorption, only at temperatures well above that of the terrestrial atmosphere. They therefore must be of solar origin. However, unlike the solar lines observed in the 2.4μ region, they do not appear enhanced in tracings of the solar limb spectrum.

In the tracings of the 2.4μ region of the solar spectrum obtained at Ottawa, a great number of lines of the 2-0, 3-1, 4-2, and 5-3 bands of carbon monoxide are readily observed. These are the bands discovered by Goldberg and his co-workers (3), and found by them to be of solar origin. The enhancement of these lines in the spectrum of the solar limb was confirmed. The same lines were found to appear with considerably higher intensity in tracings taken with the slit over the large sunspot of June 30, 1952 (Fig. 4).

The tracings obtained at Ottawa of the spectral region of the first overtone band are very similar to those obtained at Mt. Wilson and reproduced in the Atlas (9). The absorption due to telluric carbon monoxide should contribute mainly to the intensities of the lines of the 2-0 band with low J values. Only a few of these lines, notably *P*(3), *P*(1), and *R*(3), are not obscured by strong

lines of origin other than carbon monoxide. Since these lines are very weak, and, in fact, weaker than the solar carbon monoxide lines of high J values, the presence of telluric absorption in this region is not immediately apparent.

THE ABUNDANCE OF CARBON MONOXIDE IN THE EARTH'S ATMOSPHERE

All the lines of the fundamental rotation-vibration band of carbon monoxide appearing in the solar spectrum are to some extent overlapped by lines of different origin. The $R(3)$ line appears to be the line most free of such blending, and its equivalent width therefore was chosen as a measure of the atmospheric carbon monoxide content.

The equivalent width is defined as

$$[1] \quad W = \int_{-\infty}^{+\infty} \left(1 - \frac{I_\nu}{I_0} \right) d\nu$$

where I_0 and I_ν are the intensities at frequency ν before and after passage through the absorbing gas. The advantage of using the equivalent width as a measure of intensity, rather than, for instance, the integrated optical depth, lies in the fact that the equivalent width is independent of any distortion of the line profile due to insufficient resolution.

The equivalent width W of the line $R(3)$ was therefore determined on a number of tracings of the solar spectrum obtained on different days at different solar altitudes. The values for $W_{R(3)}$ measured on one day's tracings were plotted, on a logarithmic scale, against the length of absorption path as computed from the sun's altitude. The curve of growth so obtained can be

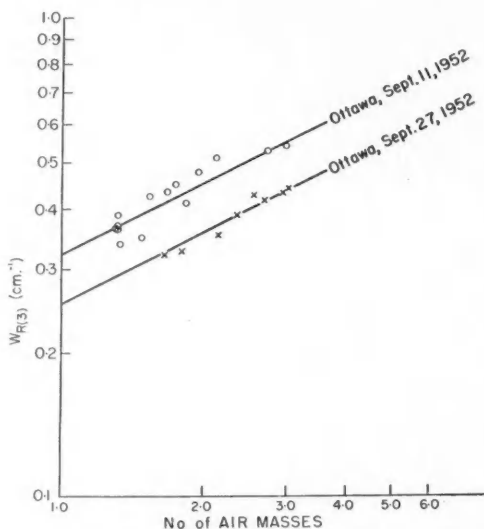


FIG. 2. Curves of growth for the $R(3)$ line of the fundamental (1-0) rotation-vibration band of telluric carbon monoxide observed in the solar spectrum.

represented by a straight line of slope one-half. $W_{R(3)}$ therefore is proportional to the square root of the length of absorption path. Examples of curves of growth obtained on two representative observing days are given in Fig. 2.

In order to find the abundance of carbon monoxide in the earth's atmosphere from observations of the equivalent width of the line $R(3)$ of the fundamental vibration band in the solar spectrum, the curve of growth was determined under various known conditions in the laboratory.

The equivalent width of a line depends (at constant total pressure) on the product of its absorption coefficient and the number of molecules in the absorption path. A curve of growth for any line can be obtained in the laboratory by measuring its equivalent width for different numbers of absorbing molecules, i.e. for different path lengths l and, within limits, for different partial pressures p of the absorbing gas. In the case of a line belonging to a molecular band, like the one under consideration, it is also possible to vary the absorption coefficient by using different lines of the band, assuming that the line width is not dependent on the rotational quantum number. This can be done because the intensity distribution in a band depends only on the temperature and the molecular constants, and, in this case, can be computed theoretically, since for carbon monoxide the molecular constants are known with sufficient accuracy. Fig. 3 shows three curves of growth for the lines of

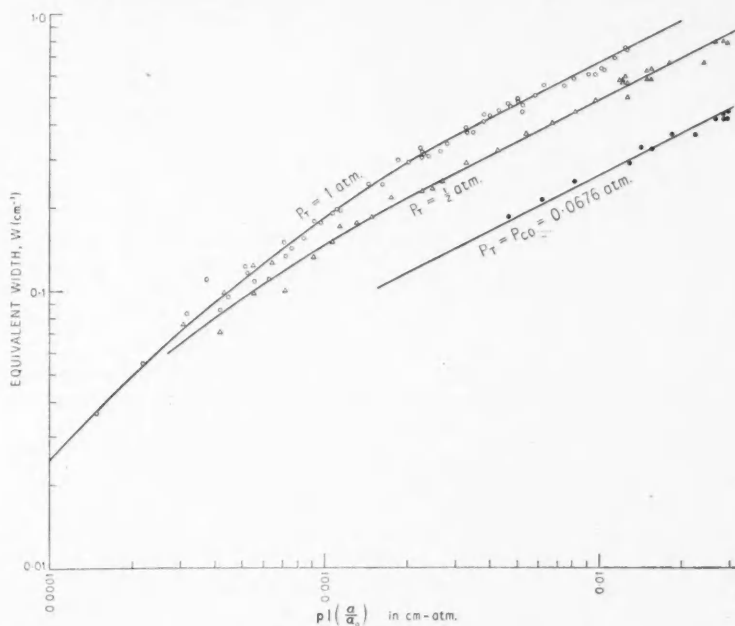


FIG. 3. Curves of growth for the lines of the fundamental (1-0) rotation-vibration band, determined in the laboratory.

the fundamental band, one obtained with pure carbon monoxide in the absorption cell, the two others with carbon monoxide and air at a total pressure P_T equal to one-half and one atmosphere respectively. In this representation the equivalent widths of suitable lines are plotted against the values of $pl(\alpha/\alpha_0)$. Here the values (α/α_0) are the relative intensities of the lines within the band, and were taken from Penner's (10) computed tables of line intensities for carbon monoxide. The length l of the absorption path was always 10 cm. The pressure p of the carbon monoxide contained in the absorption cell was 0.0676 atm. in the experiments with the pure gas, and varied from approximately 0.006 to 0.07 atm. in the experiments with mixtures of carbon monoxide and air.

The experimentally determined curves of growth have, for small equivalent widths, a linear portion which is given by

$$[2] \quad W = pl \left(\frac{\alpha}{\alpha_0} \right) \cdot \alpha_0$$

(see for instance van de Hulst (16)). This portion of the curves of growth gives directly the integrated absorption coefficient of the whole band, $\alpha_0 = 245 \text{ cm.}^{-1}$ per cm-atm. at 300°K . This is in good agreement with the value $\alpha_0 = 237 \text{ cm.}^{-1}$ per cm-atm. at 300°K ., which was obtained, with a different method, by Penner and Weber (11).

For larger equivalent widths there is a transition of the curves of growth to the form given by

$$[3] \quad W = \left[pl \left(\frac{\alpha}{\alpha_0} \right) \alpha_0 \cdot \frac{\gamma}{\pi} \right]^{1/2}$$

where γ is the collision damping constant. This is the "square root portion" of the curve of growth where pressure broadening of the line is important.

The constant γ , accounting for the effects of both self-broadening and foreign gas broadening, determines directly the half-width $\Delta\nu$ of the line according to the relation

$$[4] \quad \Delta\nu = \frac{\gamma}{2\pi}$$

From the curve of growth for absorption lines of pure carbon monoxide the half-width due to self-broadening alone is found to be $\Delta\nu = 0.21 \text{ cm.}^{-1}$ per atmosphere.

The half-width due to broadening by air can be determined, using mixtures of carbon monoxide and air. However the partial pressures of carbon monoxide must be low enough that the number of collisions between carbon monoxide molecules, and consequently the self-broadening, is negligibly small. The curves given in Fig. 3, obtained with carbon monoxide and air at total pressures of one-half and one atmosphere respectively, fulfill this condition. This is borne out by the fact that the different groups of points, obtained with different partial pressures of carbon monoxide, lie all on the same smooth curve, and not on separate curves corresponding to different combinations of self-broaden-

ing and foreign-gas broadening. The half-width for carbon monoxide lines broadened by air, as determined from the curves of growth, is $\Delta\nu = 0.092 \text{ cm.}^{-1}$ per atmosphere total pressure.

As discussed earlier the equivalent width of the line $R(3)$ of the fundamental vibration-rotation band of carbon monoxide, when observed in the solar spectrum, varies with the square root of the length of absorption path. The observed portion of the curve of growth thus corresponds to relation [3] above, which contains the pressure broadening constant γ . In order to determine the abundance of carbon monoxide from the observed curve of growth for the line $R(3)$ it is therefore necessary to know the effective total pressure at which the line is formed. If most of the atmospheric carbon monoxide were concentrated near ground level the effective total pressure would be approximately the ground level pressure; if the concentration should fall off exponentially with height the effective total pressure for lines of low J value would be approximately half the ground level pressure (16). The case that most of the carbon monoxide is concentrated in a layer high up in the atmosphere is excluded simply by the observation that the equivalent width of the lines observed at the Jungfrauoch (3580 m.) is considerably smaller than that of the lines observed at Ottawa and at Columbus. A further argument to this effect, based on the observed relative intensities of the fundamental and first overtone bands, will be presented below.

With sufficiently high resolution the effective total pressure can be found directly by comparing the half-widths of the lines observed in the solar spectrum with the half-widths of the lines obtained in the laboratory using carbon monoxide in air at different total pressures. Sufficiently narrow slits can be used with the Ottawa instrument to make this test quite sensitive. It was found that on Oct. 24, 1952, when such an investigation was made, the half-width of the lines in the solar spectrum approximated quite closely that of the lines obtained in the laboratory at one-half atmosphere total pressure. Thus it appears likely that the carbon monoxide, like the major constituents of the atmosphere, decreases exponentially with height.

Therefore, the determinations of the carbon monoxide abundance in the atmosphere over Ottawa were based on the curve of growth obtained in the laboratory at one-half atmosphere total pressure. The results for different observing days are given in Table I.

TABLE I
ATMOSPHERIC CO CONTENT (OTTAWA)

1952, June 2	0.13 cm-atm. at 300°K.	1952, Sept. 27	0.09 cm-atm. at 300°K.
Sept. 11	0.15	29	0.18
20	0.09	30	0.13
22	0.11	Oct. 4	0.12
23	0.13	9	0.13
25	0.14	20	0.14
26	0.11	24	0.11

Bates and Witherspoon (2), discussing the chemical processes affecting the balance of carbon monoxide in the earth's atmosphere, have suggested that

combustion is the main source of this constituent. Thus, since Ottawa is situated close to the northern boundary of the densely populated part of the North American continent, the carbon monoxide abundance in the air might be affected by the prevailing wind directions. Indeed, the sharp drop in abundance which occurred between Sept. 11 and Sept. 20 coincided with the movement of very substantial polar air masses in a southerly direction. But the attempt to correlate generally the observed variations of the atmospheric carbon monoxide content with meteorological data led to inconclusive results.

It should be mentioned that day to day variations in the vertical distribution of a fixed quantity of carbon monoxide would appear as changes in the abundance if, as done here, all the abundance computations were based on the same laboratory curve of growth. It is not likely that such an effect, though it may be present, could completely account for the variations shown by the values given in Table I.

The carbon monoxide abundances published for different observing stations have not all been made with the same assumptions concerning the distribution with height. Since presumably the distribution with height is everywhere the same, these values cannot be used for a discussion of the geographical variation of the atmospheric carbon monoxide content. The published data have therefore been re-evaluated assuming an exponential variation with height, as was done in the evaluation of the Ottawa data. The computations were based on laboratory curves of growth for total pressures equal to half the ground level pressure at the station concerned.

A value for the abundance of carbon monoxide in the atmosphere over Columbus, Ohio, was obtained from the curve of growth for the line $R(2)$ of the fundamental vibration-rotation band in the solar spectrum, published by Shaw and Howard (14). The carbon monoxide content of the atmosphere over Columbus, Ohio, was found to be 0.15 cm-atm. The difference between this value and the value 0.09 cm-atm. given by Shaw and Howard appears quite reasonable, since the latter was determined from a laboratory curve of growth obtained with a mixture of carbon monoxide and nitrogen at a total pressure of approximately one atmosphere.

Similarly, from a spectrum published by Migeotte and Neven (8), the carbon monoxide abundance over the Jungfraujoch was found to be 0.08 cm-atm. The sea level value derived from this is 0.12 cm-atm.

A new value also has been determined for Mt. Wilson on the basis of observations made in the region of the fundamental rotation-vibration band. Professor Mohler (private communication) recently has determined the equivalent width of the $R(3)$ line of the fundamental rotation-vibration band at Mt. Wilson (1450 m.) and found it to be $W = 0.26 \text{ cm.}^{-1}$ for one air mass. The abundance of carbon monoxide over Mt. Wilson computed from this value is 0.11 cm-atm. This corresponds to a sea level value of 0.13 cm-atm.

Shaw and Howard (14), in addition to their observations of the fundamental band, have made a close study also of the absorption due to terrestrial carbon monoxide in the spectral region of the first overtone vibration-rotation band. The absorption lines in the latter spectral region are relatively weak (equivalent

width of $P(6)$ approximately 0.015 cm.^{-1}). They lie on the portion of the curve of growth (see Fig. 2) where pressure broadening is of no importance and where, therefore, the equivalent width is independent of the effective total pressure at which the absorption takes place. The carbon monoxide abundance determined from the observed equivalent width of the lines in the first overtone band will therefore have the same value regardless of the carbon monoxide distribution with height. This is quite different from the case of the much stronger lines of the fundamental band, the equivalent width of which varies linearly with the effective total pressure of the absorption column. From the lines in the first overtone band Shaw and Howard have determined the abundance of carbon monoxide in the earth's atmosphere over Columbus, Ohio, to be 0.1 cm-atm. Within its accuracy this value is in good agreement with the value 0.15 cm-atm. , obtained from observations in the region of the fundamental vibration, assuming exponential decrease with height, i.e. an effective total pressure of 0.5 atm. If the atmospheric carbon monoxide were concentrated at a height where the total pressure is much lower than 0.5 atm. , the assumption of an effective total pressure of 0.5 atm. would have introduced a considerable error into the abundance determination from the absorption in the region of the fundamental band. The good agreement of the values for the abundance obtained from observations in the two spectral regions therefore serves as an additional argument to exclude the possibility that the carbon monoxide might be concentrated in a layer in the upper atmosphere.

The value 0.15 cm-atm. for the carbon monoxide abundance over Columbus, Ohio, and the sea level values 0.12 cm-atm. and 0.13 cm-atm. for the geographical locations of the Jungfraujoch and Mt. Wilson respectively are all within the limits of the values obtained for Ottawa (Table I). It therefore can be stated that there is no evidence so far for a significant variation of the carbon monoxide abundance of the earth's atmosphere with geographical location.

INTERPRETATION OF THE RELATIVELY LOW INTENSITIES OF THE SOLAR CARBON MONOXIDE BANDS IN THE 4.7μ REGION

Goldberg and his co-workers (3), in their investigations of the carbon monoxide absorption in the 2.4μ region of the solar spectrum, have found that the relative intensities of the whole bands as well as the intensity distributions within the single bands correspond to a temperature of the absorbing gas of about 4300° K. The observed lines are weak and if produced in a solar layer of this temperature should have profiles which are determined entirely by Doppler broadening. The curves of growth for Doppler broadened lines differ considerably from curves of growth for the pressure broadened lines discussed in the preceding section. The main characteristic of curves of growth for Doppler broadened lines is that, after an initial linear rise, they bend off sharply and become practically horizontal. This means that after the equivalent width has reached a certain value an increase in the number of absorbing molecules or in the absorption coefficient has practically no effect on the equivalent width.

The following discussion is based on the theoretical curves of growth of Menzel and Unsöld (17). It is assumed that the Doppler velocity is entirely thermal and has the value of 1.6 km. per sec., corresponding to a temperature of 4300° K. The damping constant γ is assumed to be small; for lines of the intensities to be considered the exact value is of no importance.

The carbon monoxide absorption lines in the region of the overtone vibration, as measured on the spectra of the center of the solar disk obtained at Ottawa, have equivalent widths $W < 0.02 \text{ cm.}^{-1}$. They lie on the initial, linear, portion of the curve of growth corresponding to a Doppler velocity of 1.6 km. per sec. The number N of carbon monoxide molecules per unit volume of the solar atmosphere can therefore be computed from the relation

$$[5] \quad W = N\alpha.$$

With the tabulated absorption coefficients α of Penner (10), the abundance of carbon monoxide above the photosphere at the center of the disk is found to be 4.0×10^{19} molecules per cm.^2 . This value is somewhat higher than the

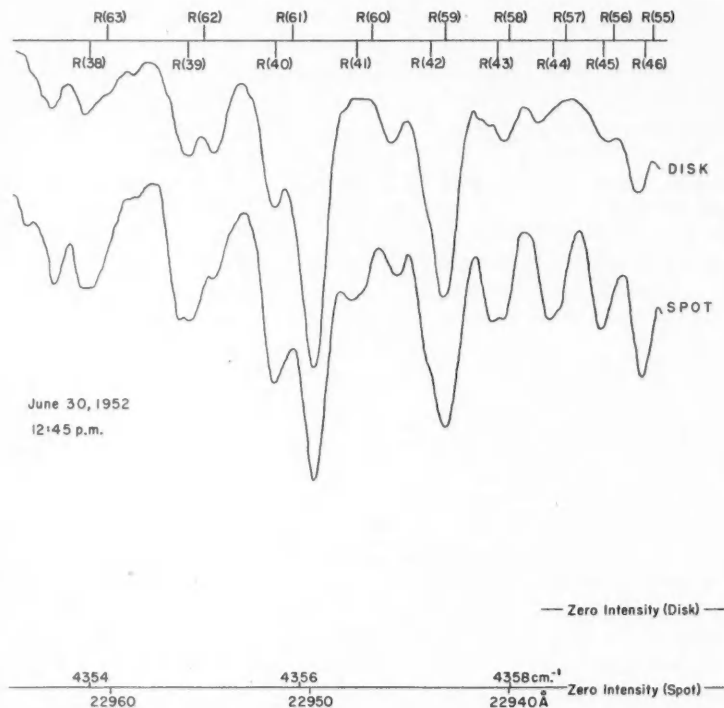


FIG. 4. Comparison of the spectrum of a sunspot with that of an undisturbed region of the disk. The reproduced portions of the spectra contain the lines near the head of the 2-0 band of the CO molecule. The computed positions of the lines are indicated at the top of the figure.

value 1.1×10^{19} molecules per cm^2 given by Goldberg and his co-workers (3). The difference may, at least in part, be due to a difference in the values of the absorption coefficients used.

In the spectrum of the large sunspot of June 30, 1952, a portion of which is reproduced in Fig. 4, the lines of the 2-0 band are enhanced by about a factor 7 relative to the lines observed in the spectrum of an undisturbed region. This corresponds, on the basis of the adopted curve of growth, to an abundance ratio of the order of 100:1, in satisfactory agreement with Russell's (15) theoretical value of 160:1.

The solar carbon monoxide lines observed in the spectral region of the fundamental vibration have equivalent widths of the order of 0.03 cm^{-1} , i.e. only about three times the equivalent widths of corresponding lines in the region of the first overtone vibration. This appears to be extremely low, considering that the absorption coefficients of the lines in the region of the fundamental vibration are about 40 times as large as those of the lines in the region of the first overtone. The explanation for the small difference in the observed intensities is to be found in the fact that, as explained above, the equivalent width for Doppler broadened lines, after reaching a certain value, increases only very slowly with increasing absorption coefficient. The equivalent width of the most intense lines in the region of the fundamental vibration, computed for the known carbon monoxide abundance on the basis of the curve of growth, is about 0.03 cm^{-1} . This is in very good agreement with the observations.

The fact that the lines in the region of the fundamental vibration are not found enhanced, when observed in the spectrum of the solar limb, can be explained in a similar way. The lines lie on the portion of the curve of growth where the equivalent width has become insensitive to increases in the number of absorbing molecules.

ACKNOWLEDGMENTS

The authors wish to thank Dr. G. Herzberg for the loan of the lead telluride detector, obtained through the kindness of Dr. R. A. Smith of the Telecommunications Research Establishment, Great Malvern, England. They would like also to thank Professors Shaw and Howard for making their papers available to them prior to publication. The helpful discussions with Dr. J. A. Rottenberg and the general assistance of Mr. R. M. Small are greatly appreciated.

It is a pleasure to thank the Dominion Astronomer, Dr. C. S. Beals, for many helpful suggestions during the construction of the equipment and for his active interest in and continued support of the work in solar physics.

REFERENCES

1. ADEL, A. *Sky and Telescope*, 12: 12. 1952.
2. BATES, D. R. and WITHERSPOON, A. E. *Monthly Notices Roy. Astron. Soc.* 112: 101. 1952.
3. GOLDBERG, L., McMATH, R. R., MOHLER, O. C., and PIERCE, A. K. *Phys. Rev.* 85: 140, 481. 1952.
4. KUIPER, G. P., WILSON, W., and CASHMAN, R. J. *Astrophys. J.* 106: 246. 1947.
5. LOCKE, J. L. and HERZBERG, L. Report presented to the Joint Meeting of the A.A.S. and the A.S.P., June, 1952.

6. MIGEOTTE, M. *Phys. Rev.* 76: 1108. 1949.
7. MIGEOTTE, M. and NEVEN, L. *Physica*, 16: 123. 1950.
8. MIGEOTTE, M. and NEVEN, L. *Zwanzig Jahre Hochalpine Forschungsstation Jungfraujoch*. 1951.
9. MOHLER, O. C., PIERCE, A. K., McMATH, R. R., and GOLDBERG, L. *Photometric atlas of the near infra-red solar spectrum*. University of Michigan Press, Ann Arbor, Mich. 1950.
10. PENNER, S. S. *Wave number and intensity tables for carbon monoxide*. Guggenheim Jet Propulsion Center, California Institute of Technology. 1952.
11. PENNER, S. S. and WEBER, D. *J. Chem. Phys.* 19: 807. 1951.
12. PLYLER, E. K., BENEDICT, W. S., and SILVERMAN, S. *J. Chem. Phys.* 20: 175. 1952.
13. SHAW, J. H., CHAPMAN, R. M., HOWARD, J. N., and OXBOLM, M. L. *Astrophys. J.* 113: 268. 1951.
14. SHAW, J. H. and HOWARD, J. N. *Phys. Rev.* 87: 380, 679. 1952.
15. RUSSELL, H. N. *Astrophys. J.* 79: 317. 1934.
16. VAN DE HULST, H. C. *Ann. Astrophys.* 8: 12. 1945.
17. UNSÖLD, A. *Physik der Sternatmosphären*. Julius Springer, Berlin. 1938. p. 264.

THE MASS SPECTROMETER DETERMINATION OF THE HALF-LIFE OF Kr^{85} ¹

BY R. K. WANLESS² AND H. G. THODE

ABSTRACT

The half-life of Kr^{85} has been redetermined using the high precision mass spectrometer method. Several samples of krypton gas extracted from fission product material have been investigated over a period of seven years. The half-life of Kr^{85} has been found to be 10.27 ± 0.18 years.

Prior to 1945 the only Kr^{85} isomer known had a 4.5 hr. half-life, an activity first noted by Snell (3) in 1937 while studying the d, p reaction on Kr. In 1945 Hoagland and Sugarman (2) found an activity with a minimum half-life of 10 years when investigating the gaseous activities in fission products. They were able to show that this was due to an isotope of krypton and assigned it either to Kr^{85} or Kr^{87} . Thode and Graham (4) of the Canadian Atomic Energy Project independently discovered a long-lived isotope of krypton during investigation of gaseous fission products with a mass spectrometer. Their results showed the definite existence of a long-lived isotope of krypton at mass 85 and hence an isomer of the known 4.5 hr. krypton of that mass. The mass spectrometer work also indicated that the fission yield of this isomer was about 25% of the total yield of the 85 mass chain. By following the decrease of this isotope over a period of a few months Thode and Graham were able to show that it decayed with a half-life of about 9.4 years. With this additional information the uncertainty in the mass assignment of the activity reported by Hoagland and Sugarman was removed and the 10 year activity was attributed to Kr^{85} .

The early mass spectrometer determinations were not too precise since measurements were made on samples that had only decayed a short time. However, with these samples almost seven years old it has been possible to redetermine the half-life of Kr^{85} with improved accuracy. The results obtained are reported below.

Half-life measurements by the mass spectrometer method involve the determination of the concentration of the radioactive isotope relative to a stable isotope after various time intervals. These measurements are most accurate when the elapsed time between two isotope ratio determinations is of the order of the half-life of the isotope being investigated, which in the case of Kr^{85} is approximately ten years. In the work reported here the Kr^{85} concentration was determined relative to both the stable isotope Kr^{84} and the stable isotope Kr^{86} , thus eliminating any mass discrimination that may be inherent in the mass spectrometer. The equation $N = N_0 e^{-\lambda t}$, where N is the concen-

¹ Manuscript received January 9, 1953.

Contribution from Departments of Physics and Chemistry, Hamilton College, McMaster University, Hamilton, Ont.

² Holder of a National Research Council Studentship 1951-52 and of a National Cancer Institute Fellowship 1952-53.

tration at time t , N_0 the concentration at zero time, and λ the disintegration constant, was used in the determination. By substituting the mass spectrometer ratios $\text{Kr}^{85}/\text{Kr}^{84}$ and $\text{Kr}^{85}/\text{Kr}^{86}$, obtained after different time intervals, for N/N_0 , the half-life may be calculated from the relation $T_{1/2} = 0.6931/\lambda$. The ratios $\text{Kr}^{85}/\text{Kr}^{84}$ and $\text{Kr}^{85}/\text{Kr}^{86}$ obtained in 1946 were substituted for N_0 in all the calculations.

A few uranium disks irradiated in 1945 were available in this laboratory. Two of these were dissolved and the fission gases extracted using the techniques developed by Arrol, Chackett, and Epstein (1). Since there are indications that small variations in fission yields can and do occur depending on irradiation conditions it was felt that a more reliable result could be obtained if the same gas studied in 1946 were re-analyzed. A sample of the original gas was, therefore, purified in a calcium furnace and the small amount (< 0.001 cc.) of gas remaining was analyzed in both the krypton and xenon mass ranges. The results of this determination are included in Table II as run No. 7.

Table I gives the relative mass spectrometer abundance data for the krypton isotopes obtained for sample L in 1946 and 1952. The decrease in the Kr^{85} abundance over a period of nearly seven years is readily apparent.

TABLE I
ABUNDANCE DATA FOR ISOTOPES OF FISSION PRODUCT KRYPTON
SAMPLE L DETERMINED WITH A 180 DEGREE
MASS SPECTROMETER

Mass unit	1946 Atom %	1952 Atom %
83	14.25 ± 0.04	14.55 ± 0.01
84	26.76 ± 0.01	27.50 ± 0.01
85	7.43 ± 0.01	4.85 ± 0.01
86	51.52 ± 0.04	53.09 ± 0.02

The half-life results obtained from seven different mass spectrometer runs made on samples F , K , and L are given in Table II. Uranium samples F and K were irradiated at the same time (1945) and in adjacent positions to sample L ,

TABLE II
 Kr^{85} HALF-LIFE FROM MASS SPECTROMETER ABUNDANCE DATA

Run No.	Sample	Elapsed time (in days)	$\text{Kr}^{85} T_{1/2}$ (in years) Calculated from:		Average
			$\text{Kr}^{85}/\text{Kr}^{84}$	$\text{Kr}^{85}/\text{Kr}^{86}$	
1	F	2027	9.95	10.11	10.03
2	K	2167	10.53	10.38	10.46
3	K	2168	10.64	10.39	10.52
4	K	2176	10.44	10.42	10.43
5	K	2176	10.34	10.09	10.22
6	K	2176	10.20	9.98	10.09
7	L	2439	10.19	10.13	10.16
Average					$10.27 \pm 0.18^* \text{ yr.}$

* Standard deviation.

which was investigated first in 1946. It is, therefore, reasonable to assume similar irradiation conditions for the three uranium samples. The results of run 7, given in Table II, are, of course, not dependent on this assumption. The Kr^{85} half-life determined from the average of these results was found to be 10.27 ± 0.18 years.

As mentioned above the purified gas from disk *L* was analyzed in both the krypton and xenon mass ranges. Tables III and IV compare the stable krypton and xenon isotope abundances determined in 1946 and 1952. The percentage differences shown indicate agreement within 1% which is indeed remarkable

TABLE III

COMPARISON OF ABUNDANCE DATA FOR STABLE ISOTOPES OF FISSION PRODUCT
KRYPTON SAMPLE *L* DETERMINED WITH A 180 DEGREE MASS SPECTROMETER

Mass unit	1946 Atom %	1952 Atom %	% Difference
83	15.40 ± 0.04	15.29 ± 0.01	-0.71
84	28.92 ± 0.01	28.90 ± 0.01	-0.07
86	55.68 ± 0.04	55.80 ± 0.02	+0.20

TABLE IV

COMPARISON OF ABUNDANCE DATA FOR ISOTOPES OF FISSION PRODUCT XENON
SAMPLE *L* DETERMINED WITH A 180 DEGREE MASS SPECTROMETER

Mass unit	1946 Atom %	1952 Atom %	% Difference
131	13.38 ± 0.04	13.39 ± 0.01	+0.07
132	20.09 ± 0.04	20.01 ± 0.01	-0.40
134	35.76 ± 0.04	36.00 ± 0.02	+0.67
136	30.77 ± 0.04	30.63 ± 0.02	-0.45

in view of the fact that the mass spectrometer has been completely rebuilt in the interval. We can, therefore, have considerable confidence in the isotope ratios obtained in 1946 which are used together with the more recent values to determine the half-life of Kr^{85} . The mass spectrometer is now equipped with a vibrating reed electrometer and automatic recording, hence more precise determinations are possible.

We wish to thank the National Research Council and The Atomic Energy of Canada Limited for their financial assistance.

REFERENCES

1. ARROL, W. J., CHACKETT, K. F., and EPSTEIN, S. Can. J. Research, B, 27:757. 1949.
2. HOAGLAND, E. J. and SUGARMAN, N. National Nuclear Energy Series. Division IV. Volume 9. Part V. McGraw-Hill Book Company Inc., New York and London. 1951. p. 635.
3. SNELL, A. H. Phys. Rev. 52:1007. 1937.
4. THODE, H. G. and GRAHAM, R. L. Report MX-129. National Research Council. April, 1945; Can. J. Research, A, 25: 1. 1947.

WAVE GUIDE ARRAYS WITH SYMMETRICAL CONDUCTANCE FUNCTIONS¹

By H. D. GRIFFITHS

ABSTRACT

Design formulae for nonresonant slotted wave guide arrays with a symmetrical conductance function are given. Methods are outlined for the calculation of the patterns from the asymmetrical near-field distributions produced by symmetrical arrays.

For some scanning applications it is required to switch a beam into one of two positions. This may be accomplished by the use of a nonresonant slotted wave guide array. Nonresonant arrays have a radiation pattern in which the main beam is at an angle to the array normal. This angle is generally called the squint angle. If an array with uniform slot spacing is fed alternately from either end, two beams that are symmetrically disposed with respect to the normal are produced. In order that the two beams be identical with respect to beam width and side-lobe levels, the slot conductances must be symmetrical with respect to the center line of the array. The near field from this symmetrical array is not symmetrical, the maximum amplitude being nearer the input end. Formulae for the near field in terms of a given conductance distribution, and methods of evaluating the radiation pattern, are given in this paper.

The tilting of the beam with respect to the normal in nonresonant arrays arises from the nonresonant slot spacing. The slots are usually spaced a little more than a half wave length apart, and alternate slots are given a phase reversal by mechanical means (4). The total phase change between slots is therefore

$$\left(\frac{2\pi d}{\lambda_g} - \pi \right)$$

where λ_g is the guide wave length, and d is the slot spacing.

The squint angle θ is then given by

$$[1] \quad \sin \theta = \frac{\lambda}{\lambda_g} - \frac{\lambda}{2d}$$

where λ is the free-space wave length.

Long nonresonant slotted arrays are usually designed on the assumption that the amount of power radiated by each slot is small compared to the power remaining in the guide. The power radiated by the slot is then given by the incident power times the normalized slot conductance. Since the array is usually terminated in a matched load, the guide remains substantially matched along its entire length. To a first approximation an array of discrete elements may be replaced by one which radiates continuously along its entire length. The power radiated per unit length is then given by:

¹ Manuscript received December 20, 1952.

Contribution from the Radio and Electrical Engineering Division, National Research Laboratories, Ottawa, Canada. Issued as N.R.C. No. 2957.

$$[2] \quad P(y) = g(y) P_0(y)$$

where $P(y)$ is the radiated power per unit length, $g(y)$ is the normalized conductance per unit length, and $P_0(y)$ is the power in the guide at y .

The power in the guide at any point, neglecting ohmic losses, must equal the input power less that which has been radiated, i.e.,

$$[3] \quad P_0(y) = 1 - \int_{-a}^y P(y) dy$$

where $-a$ and a are the boundaries of the array, and the input power is taken as unity.

Substituting Equation [2] in Equation [3] and differentiating with respect to y , one obtains

$$\frac{P'(y)}{P(y)} - \frac{g'(y)}{g(y)} + g(y) = 0.$$

After integrating over the limits $-a$ to y and noting that for unit power input

$$P(-a) = g(-a),$$

then

$$[4] \quad P(y) = g(y) \exp \left[- \int_{-a}^y g(y) dy \right].$$

The total power radiated determines the efficiency of the array, i.e.,

$$[5] \quad \eta = 1 - P_0(a) = 1 - \frac{P(a)}{g(a)} = 1 - \exp \left[- \int_{-a}^a g(y) dy \right].$$

For switching purposes it is often convenient to substitute a short circuit for the matched load. This substitution has no noticeable effect on the far-field pattern other than to produce another lobe with a squint angle of the same magnitude but opposite in sign to that of the main beam. The ratio of the power in this lobe to that in the main beam is very nearly the same as the ratio of the power that would have been dissipated in the matched load to that at the input to the array. If the efficiency is high, the voltage standing wave ratio at the input to the array is not noticeably affected by the change.

RADIATION PATTERNS FROM SYMMETRICAL ARRAYS

The radiation pattern of a linear aperture $-a \leq y \leq a$ with a near-field distribution $f(y)$ is given by the Fourier transform of $f(y)$, i.e.,

$$[6] \quad |R(\theta)| = \left| \int_{-a}^a f(y) \exp(j\beta y/a) dy \right|$$

in which $\beta = (2\pi a/\lambda) \sin \theta$. θ is the angle between line of sight and the normal to the array, and $f(y)$ is proportional to $[P(y)]^{1/2}$.

The addition of a linear phase change along the aperture will tilt the beam with respect to the array normal, i.e., it will produce a squint angle but the pattern will be unchanged if the phase change is small. The near-field distribution $f(y)$ produced by a symmetrical function $g(y)$ will be asymmetrical, since the power incident on the slots near the load end is much less than that at the input. An asymmetrical function may always be expressed as the sum

of an even and an odd function. Even and odd symmetry is preserved under Fourier transformation; however, odd real functions lead to odd imaginary transforms (1). If $G_e(u)$ is the transform of $f_{\text{even}}(y)$ and $jG_o(u)$ is the transform of $f_{\text{odd}}(y)$, then the far-field pattern is given by

$$|R(\theta)| = [G_e^2(u) + G_o^2(u)]^{\frac{1}{2}}$$

The radiation pattern from a symmetrical $g(y)$ is therefore symmetrical although the field distribution is asymmetrical. The pattern will have shoulders rather than discrete side lobes and will have no nulls.

A direct integration of Equation [6] with values for $f(y)$ calculated from Equation [4] is often very difficult if not impossible. Two approximate methods for evaluating the radiation pattern are available however. The first method is that of approximating the field by simple functions, whose transform can either be looked up in a table of transforms or can be calculated. A convenient function is an asymmetrical triangle. The radiation pattern from an asymmetrical triangle with apex at $y = c$ is given by

$$[7] \quad |R(\theta)| = \frac{2}{(1 - \gamma^2)\beta^2} [2 + (\gamma^2 - 1) \sin^2 \beta - 2 \cos \beta \cos \beta \gamma - 2 \gamma \sin \beta \sin \beta \gamma]^{\frac{1}{2}}$$

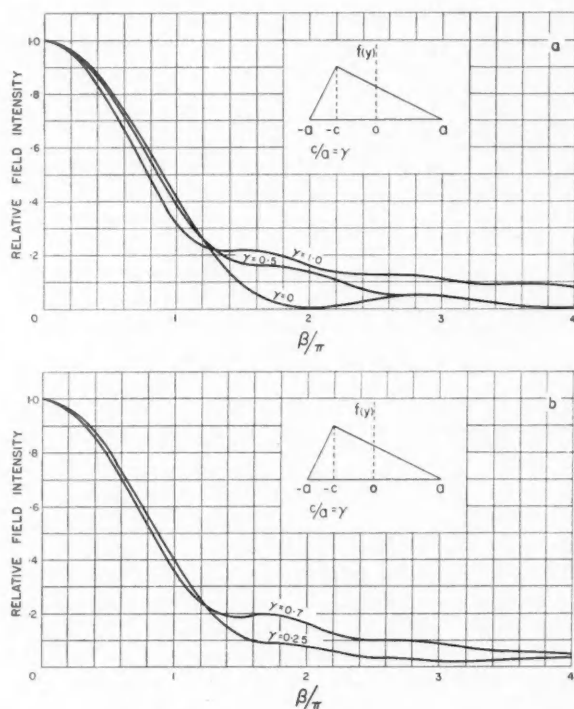


FIG. 1(a) and (b). Radiation pattern from an asymmetrical-triangle near-field distribution.

in which $\beta = (2\pi a/\lambda) \sin \theta$, $\gamma = c/a$, $-a \leq y \leq a$. For the symmetrical case, i.e., $\gamma = 0$, Equation [7] reduces to

$$[7a] \quad |R(\theta)| = \frac{2}{\beta^2} (1 - \cos \beta)$$

and for the extreme case, $\gamma = 1$,

$$[7b] \quad |R(\theta)| = \frac{1}{\beta} \left[1 - \frac{\sin 2\beta}{\beta} + \frac{\sin^2 \beta}{\beta^2} \right]^{\frac{1}{2}}.$$

The latter is obtained by a limiting process. Figs. 1(a) and 1(b) are plots of Equation [7] for different values of γ .

The second approximation to the pattern is given by the following procedure. Consider that the field $f(y)$ is produced by a number of isotropic sources evenly spaced along the aperture and with amplitudes given by the value of $f(y)$ at the location of each of the sources. On each of the sources is superimposed a linear aperture with a uniform or symmetrical triangle near-field distribution and with a length equal to the spacing between the sources. The distant pattern is then given by the product of the pattern from the sources and the pattern from the subaperture. This method is discussed by Spencer (3). The larger the number of sources, of course, the more accurate is the approximation.

The following are examples of the calculation of patterns arising from specific $g(y)$.

Example I

The simplest choice for $g(y)$ is $g(y) = K$, a constant. Then from Equations [4], [5], and [6],

$$P(y) = K \exp [-K(y+a)],$$

$$\eta = 1 - \exp [-2aK],$$

$$R(\theta) = \frac{aK/2}{[\beta^2 + (aK/2)^2]^{\frac{1}{2}}} \left[\frac{\cos aK - \cos 2\beta}{\cos aK - 1} \right]^{\frac{1}{2}}.$$

Fig. 2 is a plot of $R(\theta)$ for $\eta = 0.95$. $R(\theta)$ is normalized to unity for $\theta = 0$.

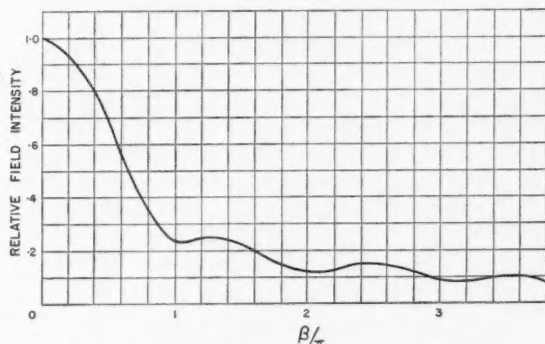


FIG. 2. Radiation pattern from $g(y) = K$, a constant.

This pattern would not be satisfactory for most practical purposes owing to the large amplitude of the shoulders.

Example II

A better choice for $g(y)$ would be $g(y) = K \cos(\pi y/2a)$, since the amount of power radiated by the initial slots would be reduced and hence the shoulders on the pattern would be lower. From Equations [4] and [5]

$$P(y) = K \cos(\pi y/2a) \exp[(-2aK/\pi)(1 + \sin \pi y/2a)],$$

$$\eta = 1 - \exp(-4aK/\pi).$$

The radiation pattern from $f(y)$ can be found by substitution of $f(y) = [P(y)]^{1/2}$ in Equation [6]. However, this results in a difficult integration. Instead of this procedure, patterns were obtained by the asymmetrical triangle and the subaperture approximations.

$f(y)$ for $\eta = 0.95$, and the asymmetrical triangle approximation to it are shown in Fig. 3. The asymmetrical triangle has a maximum at a point corre-

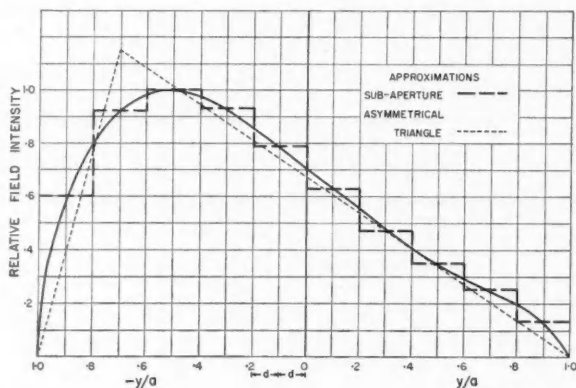


FIG. 3. Near field from a symmetrical array with $g(y) = K \cos(\pi y/2a)$.

sponding to $\gamma = 0.7$. The radiation pattern from this near-field distribution is shown in Fig. 1(b). Also, in Fig. 3 the aperture has been divided into 10 equal subapertures of width $2d$. An isotropic source is considered to be located at the center of each subaperture, the first pair of sources being located at $\pm d$, the second $\pm 3d$, etc.

The pattern of the sources is given by

$$|R(\omega)| = |(A_{-1} \exp(-j\omega) + A_{-2} \exp(-j3\omega) \dots + A_1 \exp(j\omega) + A_2 \exp(j3\omega) + \dots)|$$

where $\omega = (2\pi d/\lambda) \sin \theta$ and A_i is the amplitude of $f(y)$ at each of the sources. Expanding into trigonometric functions, we have

$$|R(\omega)| = \left| \sum_{i=1}^5 (A_i + A_{-i}) \cos(2i-1)\omega + j(A_i - A_{-i}) \sin(2i-1)\omega \right|.$$

For an aperture of width $2d$, a uniform field gives a radiation pattern proportional to $(\sin \omega)/\omega$. Then the pattern from $f(y)$ is given approximately by

$$|R(\theta)| = \left| \frac{\sin(\beta/10)}{\beta/10} \sum_{i=1}^5 (A_i + A_{-i}) \cos(2i-1)(\beta/10) + j(A_i - A_{-i}) \sin(2i-1)(\beta/10) \right|$$

since $d = a/10$, $\omega = \beta/10$, $\beta = (2\pi a/\lambda) \sin \theta$.

Fig. 4 is a plot of the radiation pattern obtained in this way.

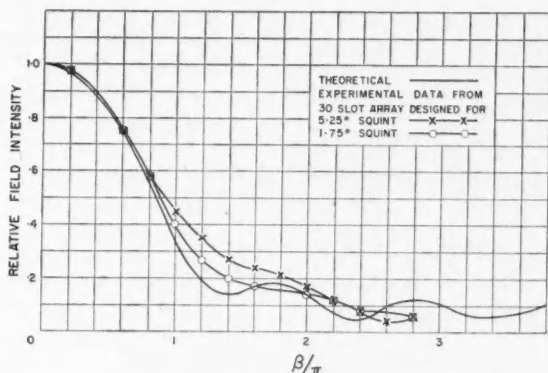


FIG. 4. Experimental and theoretical radiation patterns from a symmetrical array with $g(y) = \cos(\pi y/2a)$.

Example III

From an examination of Figs. 1(a) and 1(b), patterns with lower amplitude shoulders can be obtained by shifting the peak amplitude so as to make it more symmetrical. This could be accomplished by increasing the taper of the conductance distribution. Let

$$g(y) = K \cos^2(\pi y/2a).$$

Then from Equations [4] and [5]

$$\eta = 1 - \exp(-aK),$$

$$f(y) = \cos(\pi y/2a) \exp\{(-K/4)[y + (a/\pi) \sin(\pi y/a)]\}$$

leaving out irrelevant factors. Fig. 5 is a plot of $f(y)$ for $\eta = 0.95$. The radiation pattern from the asymmetrical triangle approximation, $\gamma = 0.5$, is given in Fig. 1(a).

A very close approximation is the chord approximation shown dotted in Fig. 5. The aperture is divided into nine subapertures each with a symmetrical triangle near-field distribution. The approximate pattern calculated as in Example II is given by

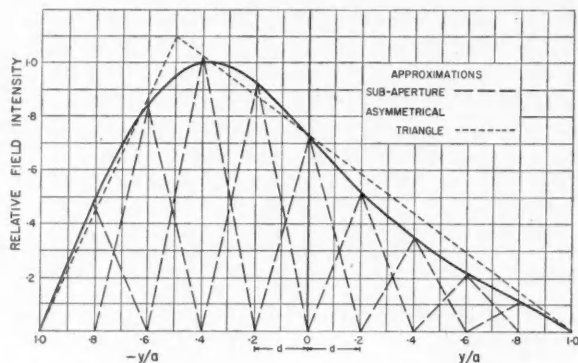


FIG. 5. Near field from a symmetrical array with $g(y) = K \cos^2(\pi y/2a)$.

$$|R(\theta)| = \left| \frac{2}{(\beta/5)^2} \left(1 - \cos \frac{\beta}{5} \right) \left[A_0 + \sum_{i=1}^4 (A_i + A_{-i}) \cos \frac{i\beta}{5} + j(A_i - A_{-i}) \sin \frac{i\beta}{5} \right] \right|$$

in which A_i is the amplitude of the field at the center of each subaperture, and $\beta = (2\pi a/\lambda) \sin \theta$.

Fig. 6 is a plot of $R(\theta)$.

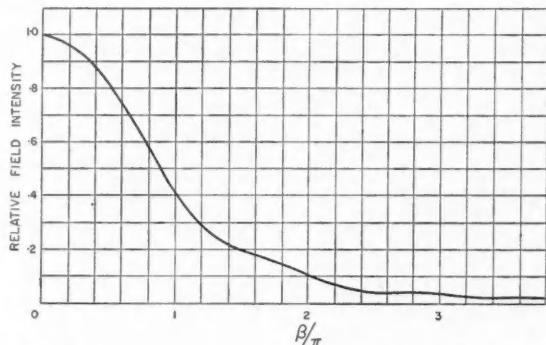


FIG. 6. Radiation pattern from a symmetrical array with $g(y) = K \cos^2(\pi y/2a)$.

COMPARISON OF APPROXIMATE PATTERNS

At this point the patterns obtained from the simple asymmetrical triangle approximation and the more elaborate subaperture method should be compared. It will be noted that the radiation patterns from both the cosine and the cosine squared symmetrical conductance arrays as obtained from the two approximations differ chiefly in the structure of the side lobes. It would appear that for practical purposes little is to be gained by using the more elaborate approximation.

VARIATION OF THE PATTERN WITH THE EFFICIENCY OF THE ARRAY

Some idea of the variation of the radiation pattern from symmetrical arrays with the efficiency may be obtained from the change in the position of the maximum of the near-field as the efficiency is varied. Increasing the efficiency makes the pattern more asymmetrical since the slots near the input have to radiate more power. This is borne out by finding the maximum of $f(y)$ in the usual way.

For $g(y) = K \cos(\pi y/2a)$, the maximum field occurs when

$$\frac{y}{a} = -\frac{2}{\pi} \sin^{-1} \left\{ \left[1 + \left(\frac{\pi}{4aK} \right)^2 \right]^{\frac{1}{2}} - \frac{\pi}{4aK} \right\}.$$

For $g(y) = K \cos^2(\pi y/2a)$, the maximum field occurs when

$$\frac{y}{a} = -\frac{2}{\pi} \left| \cos^{-1} \left[\frac{2}{\sqrt{3}} \frac{\pi}{aK} \sinh \frac{\phi}{3} \right]^{\frac{1}{2}} \right|,$$

in which $\sinh \phi = 3\sqrt{3} aK/2\pi$.

An estimate of the effect of the asymmetry may be obtained by comparing the patterns in Figs. 1(a) and (b) for the different values of the maxima as given in Table I.

TABLE I
POSITION OF NEAR-FIELD MAXIMUM

$g(y)$	η	K	y/a for maximum field
$K \cos \frac{\pi y}{2a}$	0.95	$\frac{3\pi}{4a}$	-0.51
	0.99	$\frac{2.3\pi}{2a}$	-0.596
$K \cos^2 \frac{\pi y}{2a}$	0.95	$\frac{3}{a}$	-0.37
	0.99	$\frac{4.6}{a}$	-0.45

EXPERIMENTAL WORK

Two experimental arrays made at the National Research Council show what happens to the patterns when arrays are designed on the basis of the simple theory outlined but the wave guide is not matched throughout its length. If the efficiency of an array is made high and the number of slots small, the normalized conductance of the slots is not small compared to unity. In addition, if the squint angle desired is small, the slots are near resonant spacing so that the slot admittances tend to add up in phase. The experimental arrays were designed with approximately thirty slots, the center slots having conductances as high as 0.2. The squint angles were 1.75 degrees and 5.25 degrees. The symmetrical conductance function chosen was $g(y) = K \cos(\pi y/2a)$ with K adjusted to give an efficiency of 95%.

The experimental patterns from the two arrays are shown in Fig. 4. The measured beam widths agree very closely with that obtained from the approxi-

mate patterns but the squint angle was larger than that predicted by Equation [1]. For the 5.25 degree array the measured value was 5.7 degrees and for the 1.75 degree array, 2 degrees. This can be explained by noting that the phase change between two points on a mismatched line is different from the phase change on a matched line. It was found that by making the slot length greater than the resonant length, the negative susceptance added at the slot tends to reduce the squint angle. Care must be taken not to increase the slot length too much or the conductance will decrease considerably. This can be seen from published curves of conductance and susceptance of slots in the broad face of the rectangular wave guide (4).

The mismatch that arises at any point along the guide may be obtained from a plot on the Smith admittance chart (2). Such a plot gives the input admittance to the array very closely. A design procedure for short arrays with symmetrical conductance functions, taking into account the mismatch has not been worked out up to the present.

REFERENCES

1. RAMSAY, J. F. *Marconi Rev.* 10: 41. 1947.
2. SMITH, P. H. *Electronics*, 17: 130. 1944.
3. SPENCER, R. C. *Mass. Inst. Technol., Radiation Lab. Rept.* 762-1. 1946.
4. WATSON, W. H. *J. Inst. Elec. Engrs. (London)*, Pt. III, A, 93: 747. 1946.

FERROMAGNETISM AND ORDER IN NICKEL MANGANESE ALLOYS¹

By G. R. PIERCY² AND E. R. MORGAN³

ABSTRACT

An investigation of ferromagnetism in nickel manganese alloys containing up to 40 atomic per cent manganese has been carried out. Twenty alloys within this composition range were subjected to heat treatments such that the atomic arrangement within the alloys varied from disorder to a high degree of long range order.

The degree of order of Ni_3Mn calculated from measured saturation magnetization using the atomic model of ferromagnetism was consistent with the value calculated from the ratio of measured integrated intensity of the (110) X-ray diffraction superlattice line to that of line (111).

The relationship between saturation magnetization and concentration for the disordered alloys can be explained adequately by the existence of short range order. A value of 3.4 Bohr magnetons for the effective magnetic moment of manganese atoms in a nickel lattice was deduced.

A. INTRODUCTION

The atomic model (6) of ferromagnetism has been used by many investigators to explain ferromagnetism and antiferromagnetism in ferrites and metallic alloys. This model is based on the work of Heisenberg (5), employing a Heitler-London treatment in which the electrons are near their respective atoms, with the further simplification of limiting the orientation of the magnetic moments of the atoms to either of two parallel directions. It is particularly adaptable to the case of ordered alloys.

An interesting application of the atomic model to an ordered alloy is the interpretation of the change of saturation magnetization with increasing manganese content in nickel manganese alloys. It was found by Kaya and Kussmann (7) that the saturation magnetization increases with manganese concentration up to 8%* manganese and then decreases again. The results of Kaya and Kussmann for the values of saturation magnetization extrapolated to 0°K. are shown in Fig. 1. At low manganese concentrations there are few Mn-Mn interactions and therefore it may be concluded from the initial slope of the curve that the Mn-Ni interaction must be positive. This interaction results in the magnetic moments of the manganese atoms being oriented in the same direction as those of the nickel atoms. With perfect order in the lattice, there will be no Mn-Mn interactions up to 25% manganese. One would therefore expect that for an ordered lattice below 25% manganese, the saturation magnetization would lie on the tangent shown as a dotted line in

¹ Manuscript received December 9, 1952.

² Contribution from University of British Columbia, Vancouver, B.C.

³ Formerly N.R.C. Bursary holder at University of British Columbia, Vancouver, B.C. Now Athlone Fellow at Department of Metallurgy, University of Birmingham, England.

⁴ Formerly Research Associate at University of British Columbia, Vancouver, B.C. Now Research Engineer, Metallurgical Department, Scientific Laboratory, Ford Motor Company, Dearborn, Michigan.

*All percentages referred to in this paper are in terms of atom per cent.

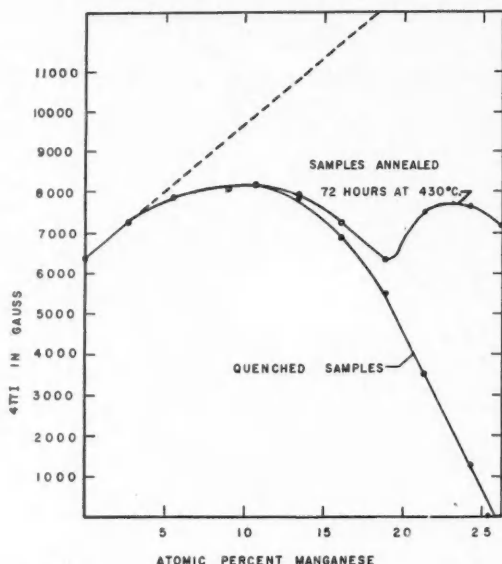


FIG. 1. Values of saturation magnetization (Kaya and Kussmann (7)), extrapolated to 0°K., versus atom per cent manganese.

Fig. 1. From the curve for the ordered alloys in Fig. 1, it is seen that long range order begins at approximately twenty per cent manganese. The value of saturation magnetization for the ordered alloy of 25% manganese is not as high as the theoretical value, which, for a fully ordered alloy, would correspond to a point on the dotted tangent. Other investigators have obtained higher values than Kaya and Kussmann for saturation magnetization of Ni_3Mn , but their heat treatments differed considerably and no values were as high as the theoretical value. The existence of long range order in Ni_3Mn has been demonstrated by resistivity measurements, and by the observation of X-ray diffraction superlattice lines using monochromatic iron radiation in an evacuated camera (1). The superlattice lines have also been seen by neutron diffraction (9).

Using the atomic model of ferromagnetism, it should be possible to calculate the degree of order of Ni_3Mn from measurements of the difference between the experimental value of saturation magnetization and the theoretical value on the dotted tangent of Fig. 1. The value of the effective magnetic moment of a manganese atom in a nickel lattice can be found from the slope of the tangent.

B. EXPERIMENTAL DETAILS

Twenty alloys were made covering the range 0 to 40% manganese. Fisher nickel powder, the chief impurities of which were 0.1% Fe and less than 0.1% Co, and electrolytic manganese (99.9% Mn), donated by the Electromanganese

Corporation, were used as base materials. The oxide on the surface of the metal was reduced by heating the metals for 10 min. at 600°C. under a hydrogen atmosphere before melting. All alloys were melted in alundum crucibles by high frequency induction and chill cast into a cold brass mold under a purified argon atmosphere. Each ingot was homogenized at 1000°C. for five days under argon. X-ray powder and magnetic balance samples were heat treated in evacuated Pyrex or Vycor tubes containing pure manganese in order to reduce the sublimation of manganese from the alloy. It was shown by subsequent chemical analysis that none of the heat treatments changed the composition of the magnetic balance samples. The magnetic balance, which utilized a field of 3000 ± 100 oersteds, was of the Fereday type (4) based upon null point reading and a restoring force supplied by a torsion head twisting the suspension.

Two preliminary heat treatments were given. Alloys with 15.3, 19.9, 23.7, and 32.1% manganese were annealed at 380, 400, 420, and 450°C. to find the annealing temperature which produced maximum magnetization within a reasonable time. The work of Thompson (11), and Sykes and Jones (10), had shown that large order domains are produced by annealing the sample just below the critical ordering temperature of 520°C. To find the length of annealing time necessary to produce large order domains, samples of an alloy with 23.7% manganese were annealed for different periods at 490°C., followed by 400 hr. at 420°C. The saturation magnetization was measured at the end of the heat treatment.

From the results of the preliminary experiments, the following heat treatments were selected for the final investigation:

A. Two hours at 800°C. followed by a water quench. This treatment resulted in a well annealed disordered alloy.

B. Two weeks at 420°C. plus one week at 400°C. This treatment resulted in an alloy having a high degree of order at 400°C., but a small domain size.

C. Sixteen hours at 555°C., plus 250 hr. at 490°C., plus 260 hr. at 420°C., followed by 260 hr. at 400°C. Annealing at 490°C. increased the size of the order domains; annealing at 420°C. and finally at 400°C. produced a high degree of order within the domains.

The saturation magnetization was measured on all samples at 293, 200, and 90°K. X-ray diffraction patterns were obtained using a Straumanis type camera. The integrated intensities of the (110) and (111) lines were measured for the alloy containing 25% manganese after this alloy had been subjected to heat treatment C. A Philips goniometer with the Geiger counter oscillating across the line was used for these intensity measurements.

C. EXPERIMENTAL RESULTS

Graphs depicting the results of the preliminary heat treatments are shown in Figs. 2 and 3. It is seen from Fig. 2 that the saturation magnetization increases with annealing time at 420°C. up to a period of two weeks, and from Fig. 3 that 200 hr. at 490°C. is sufficient to produce large order domains.

Results for the values of saturation magnetization extrapolated to 0°K. are shown in Fig. 4. From the slope of the dotted tangent to this curve after,

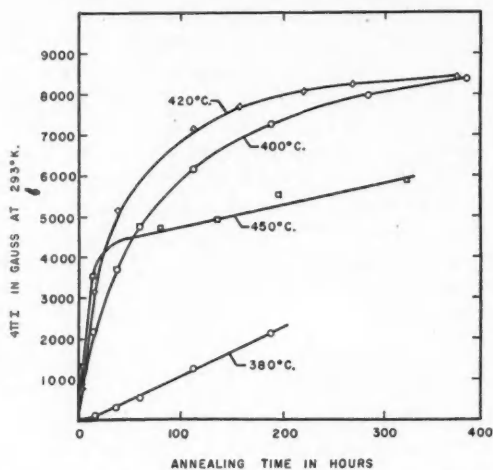


FIG. 2. Change in saturation magnetization of 23.7% Mn alloy with annealing time. All measurements made at room temperature.

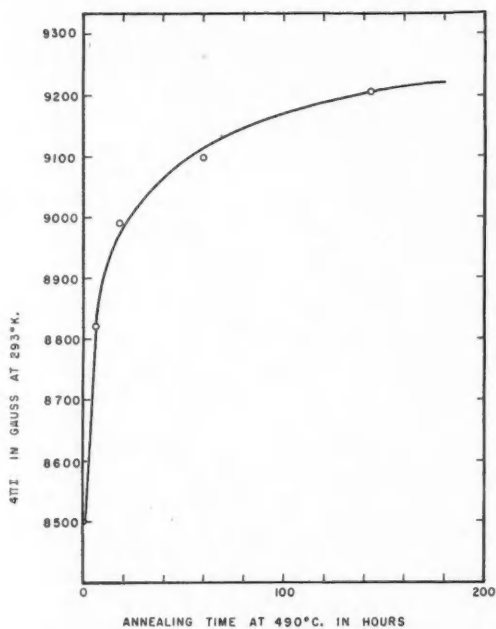


FIG. 3. Change in saturation magnetization of 23.7% Mn alloy with annealing time at 490°C. and a subsequent anneal of 400 hr. at 420°C. All measurements made at room temperature.

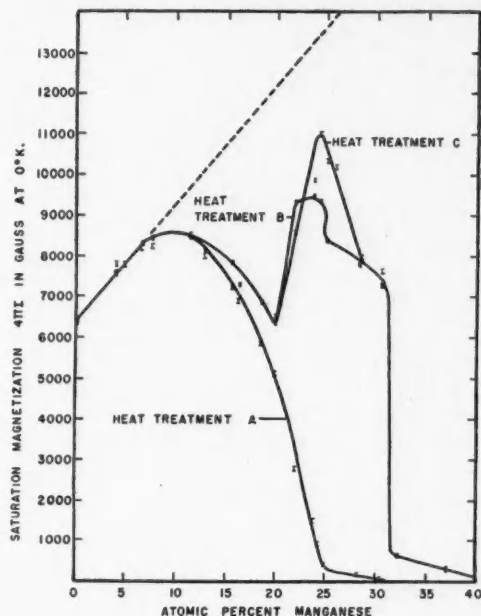


FIG. 4. Values of saturation magnetization extrapolated to 0°K. for heat treatments A, B, and C.

correction to give saturation magnetization per atom, it was found that the effective magnetic moment of the manganese atoms in a nickel lattice was 3.4 Bohr magnetons. This value is in agreement with the values of the magnetic moment of manganese in other alloys (2).

The tail above 25% manganese in the curve of saturation magnetization against concentration for the quenched alloys is probably due to the slow quenching rate since the Vycor tubes were not broken when they were quenched in water. The curve according to Kaya and Kussmann, shown in Fig. 1, has no tail.

D. DISCUSSION OF RESULTS

To explain the drop in saturation magnetization to zero at 25% manganese for the quenched alloys, it is necessary to assume that the manganese atoms retain five of their 3*d* electrons and give the rest to the 3*d* shell of the nickel atoms. From the value obtained for the effective magnetic moment of the manganese atom, it is apparent that each manganese atom will give 1.6 electrons to the 3*d* shell of the nickel atoms. The 3*d* shell of the nickel atoms will therefore become filled at approximately twenty-seven per cent manganese.

Carr (3), in a recent paper, gives the following explanation for the curve of saturation magnetization against composition for the quenched alloy:

"For a disordered alloy with an appreciable percentage of manganese atoms, the Mn-Mn interaction begins to outweigh the weaker Mn-Ni interaction, and one eventually finds that the manganese spins start to cancel one another. The bending over of the curve should occur for a relatively small fraction of manganese. Beyond this point, the magnetic moment is derived principally from the nickel ions and diminishes with increasing manganese content because of the replacement of nickel and the filling up of the nickel 3*d* shell".

In his theory Carr assumes that the magnetization in the range just below 25% manganese is produced by the nickel atoms alone. If this is true, then, in order for the magnetization to fall to zero at 25% manganese, the curve of saturation magnetization versus per cent manganese should approach zero with a slope equal to $-6400/25 = -256$, using the units on Fig. 4. The actual slope is -960 . This discrepancy can be eliminated by assuming that the manganese atoms contribute to the magnetism up to 25% manganese, and that above this concentration all the magnetic moments of the manganese atoms have orientations such that they are paired and cancel each other. These conditions can arise in either of two ways, by assuming that the strength of the Mn-Mn interaction is such that it finally overpowers the Mn-Ni interaction at 25% manganese, or by assuming that local order exists and tends to keep the manganese atoms from becoming nearest neighbors in the quenched alloys. The degree of order will then be such that below 25% manganese there are insufficient Mn-Mn interactions to make the contribution of the manganese atoms to the magnetic moment of the alloy equal to zero. Of these two assumptions, the latter is preferable for the following reasons:

1. If it is assumed that the manganese atoms keep five of their 3*d* electrons and give the rest to the 3*d* shell of the nickel atoms, it can be shown (8), using the atomic model of ferromagnetism, that the first explanation will give a value for the slope of the curve at 25% manganese that is only one half of the experimental value.

2. The Mn-Mn interaction should outweigh the Mn-Ni interaction at a manganese concentration lower than 25% because the strength of the Mn-Ni interaction becomes weaker as the 3*d* shell of the nickel atoms becomes filled.

3. Some degree of short range order is present in all alloys.

4. The saturation is the same for quenched and annealed alloys up to 9% manganese. The Curie temperature is the same for quenched and annealed alloys up to 17% manganese (7). Because the annealed alloys will be ordered, then the quenched alloys will also be ordered if their magnetization and Curie temperature are the same.

The maximum in saturation magnetization for the ordered alloys occurs at a concentration of less than 25% manganese because the alloy is not completely ordered. An incompletely ordered alloy at 25% manganese must have some of its manganese atoms in face center sites with resultant antiparallel orientation of their magnetic moments. However, an incompletely ordered alloy containing less than 25% manganese may be disordered only to the extent of having nickel atoms in manganese sites, and therefore no manganese atoms with antiparallel spin moments.

The drop in magnetization of Ni_3Mn from the ordered value of 13400 to the value of 8380 after heat treatment *B* can be explained by assuming that the magnetic moment of a manganese atom of one orientation will cancel the moment of a manganese atom of antiparallel orientation. To account for the magnetic moment found experimentally in heat treatment *B* using this assumption, it is necessary to have $\frac{1}{2}(13400 - 8380)/13400$ of the manganese atoms with moments of antiparallel orientation. Therefore, these atoms must occupy face center positions, which leads to an order parameter of $S = 0.81$ from the Bragg and Williams long range order theory. The parameter obtained after heat treatment *C*, calculated in a similar manner, was $S = 0.88$.

The ratio of the intensities of the (110) and (111) X-ray diffraction lines for the 25% manganese alloy after heat treatment *C* was:

$$\frac{32 \pm 7.3}{4280 \pm 23} = 0.0075 \pm 0.0016.$$

If it is assumed that the domain size is very large, then the theoretical ratio of intensities of the (110) and (111) planes will be $[(4S - 1)/3]^2 (0.0123)$ where the first term is the structure amplitude factor calculated in terms of S , and the second term includes factors for the multiplicity of planes, polarization, temperature, absorption, and the Lorentz factor. Equating these two values of intensity ratio leads to the solution $S = 0.84 \pm 0.07$. This value for S compares favorably with that found from the magnetization of Ni_3Mn after treatment *C*.

E. SUMMARY

The results of this magnetic and X-ray investigation of nickel manganese alloys show that the relationship between saturation magnetization and concentration can be explained for the ordered alloys by using the atomic model of ferromagnetism. Application of this model produces a value for the order parameter of Ni_3Mn that is in agreement with the order parameter calculated from the intensity of the superlattice lines. To explain the change in saturation magnetization with concentration for the quenched alloys it is necessary to assume that some of the $3d$ electrons from the manganese atoms go into the $3d$ shells of the nickel atoms. Once this assumption has been made, the relationship between saturation magnetization and composition can be most satisfactorily explained by the existence of short range order. The value of the effective magnetic moment of a manganese atom in a nickel lattice was found to be 3.4 Bohr magnetons.

F. ACKNOWLEDGMENTS

The authors wish to thank Mr. R. G. Butters for the chemical analyses; Mr. A. C. Affleck for the construction of the equipment; and Prof. F. A. Forward, Head of the Department of Mining and Metallurgy at the University of British Columbia, for the use of the laboratory and equipment. Mr. G. R. Piercy wishes to acknowledge financial assistance from the National Research Council while this work was being carried out.

REFERENCES

1. AVERBACH, B. L. J. Applied Phys. 22: 1088. 1951.
2. BOZORTH, R. M. Ferromagnetism. D. Van Nostrand Company, Inc., New York, 1951.
p. 335.
3. CARR, W. J. Phys. Rev. 85: 590. 1952.
4. FEREDAY, R. A. Proc. Phys. Soc. (London), 46: 214. 1934.
5. HEISENBERG, W. Z. Physik, 49: 619. 1928.
6. ISING, E. Z. Physik, 31: 253. 1935.
7. KAYA, S. and KUSSMANN, A. Z. Physik, 72: 293. 1931.
8. PIERCY, G. R. Thesis, University of British Columbia. 1952.
9. SHULL, C. G. and SIEGEL, S. Phys. Rev. 75: 1008. 1949.
10. SYKES, C. and JONES, F. W. Proc. Roy. Soc. (London), A, 166: 376. 1938.
11. THOMPSON, N. Proc. Phys. Soc. (London), 52: 217. 1940.

THE MEASUREMENT OF ENERGIES AND INTENSITIES OF γ -RAYS WITH A PAIR SPECTROMETER¹

BY B. B. KINSEY AND G. A. BARTHOLOMEW

ABSTRACT

The performance of a pair spectrometer of the Walker and McDaniel type is discussed from both a theoretical and an experimental point of view. It is shown that the energy of the γ -ray may be measured to a first approximation by the product of the distance between the inner edges of the slits which define the coincidence counters and the highest value of the magnetic field at which coincidences are found. A more accurate value of the energy of the γ -ray may be obtained by adding a small correction, called the "toe" correction, to the result so obtained. The magnitude of this correction is dependent on the γ -ray energy and on the width of the slits and is obtained from calculations of the shape of the coincidence peak based on the Bethe-Heitler formula. The correction depends very little on the length of the slits or on the thickness of the radiator. The relation between the calculated correction and the slit width has been examined experimentally. It is shown that the ultimate accuracy in energy measurement depends on the homogeneity of the magnetic field and on the error involved in the calculated toe correction. The latter error can be minimized by using very narrow slits and may be eliminated by plotting the value of magnetic field at the upper limit of the coincidence spectrum against the slit width and extrapolating the curve so obtained to zero slit width. The uncertainty in the magnetic field of the present instrument introduces a possible systematic error of about 0.05%. Measured values of the energies of a number of neutron capture γ -rays are compared with the values derived from the energy balance in (*d*, *p*) reactions. The results are in good agreement (within 0.1%).

The relative counting efficiency as a function of energy is calculated theoretically and found to be in good agreement with experiment from 2.75 to 7.4 Mev. Above 7.4 Mev. no good method of checking the theoretical efficiency has been found. The absolute value of the counting efficiency at 2.75 and 7.38 Mev. has been measured by an ionization chamber method and is found to be in rough agreement with theoretical estimates.

1. INTRODUCTION

Walker and McDaniel have shown that their pair spectrometer (22) is a very suitable instrument for the study of γ -radiation of energy of a few million electron-volts. In this spectrometer, pairs are produced in a foil of high atomic number placed with its plane parallel to the direction of a magnetic field and perpendicular to that of the incident γ -radiation. Walker and McDaniel have shown that, in a magnetic field of suitable strength, when the energy is sufficiently high, a large area of the foil will contribute to the coincidence counting rate recorded by counters placed in the plane of the radiator. A homogeneous γ -ray appears as a peak in the curve obtained when the coincidence counting rate is plotted as a function of the strength of the magnetic field. The product of the value of the magnetic field at the coincidence peak and the mean distance between the centers of the counters determines approximately the energy of the γ -ray. The counting efficiency of the pair spectrometer decreases very rapidly with decreasing γ -ray energy and consequently this instrument is unsuitable for the study of γ -rays with energies between 3 Mev. and the threshold at 1 Mev., unless they are exceptionally strong.

¹ Manuscript received December 31, 1952.

Contribution from the Physics Division, Atomic Energy of Canada Limited, Chalk River, Ontario. Issued as A.E.C.L. No. 42.

Compared with spectrometers using the Compton or the photoelectric process, the pair spectrometer is a very insensitive instrument and good use can be made of it only when strong sources of γ -radiation are available. To increase the sensitivity, Walker and McDaniel employed several counters mounted side by side and connected in an elaborate coincidence circuit.

In the apparatus described in this paper, only two counters have been employed mainly for the sake of simplicity, but the accuracy has been greatly increased by the use of precision slits in front of the counters. A detailed theoretical and experimental analysis of the behavior of this pair spectrometer is given and it is shown how it can be applied to the accurate measurement of γ -ray energies.

2. THEORETICAL

2.1 Measurement of γ -Ray Energy

In the method of Walker and McDaniel, the γ -ray energies are computed from the product of the mean distance between the counters and the value of the magnetic field, and, therefore, the accuracy of their spectrometer as an absolute instrument is limited by the ratio of the widths of the apertures of the counters to the distance separating them.

It will be shown below that a much more accurate measurement of the energy of a γ -ray can be obtained by using the product of the upper limit of the magnetic field required to produce coincidences and the distance separating the inner edges of the two slits used to define the effective areas of the counters.

The shape of the coincidence peak obtained experimentally for a single homogeneous γ -ray is shown diagrammatically in Fig. 1. The curve exhibits a sharp and approximately linear cutoff PQ which passes into a tail QR towards higher magnetic fields. The counting rate in the tail decreases linearly* with

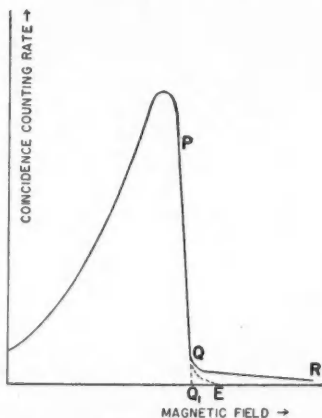


FIG. 1. Shape of coincidence peak (diagrammatic). Q_1 is the end point of the peak obtained by extrapolation; E is the position of the true end point.

*In practice with the present apparatus a small ghost peak also appears superposed on this tail. The peak is produced by scattering from the frame supporting the slits. See Ref. (12).

increasing field strength and the end point occurs at a field which is much higher than that of the peak of the spectrum. We have found that the greater part of this tail is due to the scattering of electrons from the walls of the vacuum chamber. It will be shown below that, in the absence of scattering, one would expect nevertheless to find a genuine tail, QE . The value of the magnetic field above which no coincidence should occur, therefore, lies above the observed upper limit Q of the linear cutoff and is hidden by the tail due to scattering. The position of the true upper limit, E , therefore, cannot be determined by direct measurement.

The geometry of the apparatus is shown diagrammatically in Fig. 2 in which the radiator and the slits, S_+ , S_- , defining the effective area of the counters,

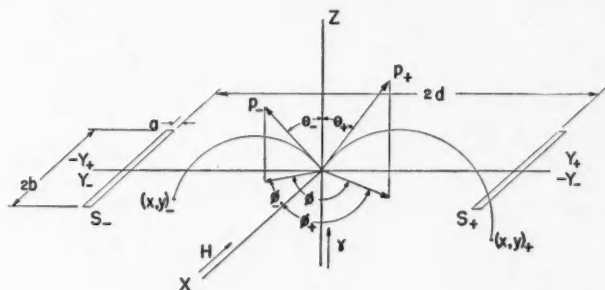


FIG. 2.

are in the XY plane, the magnetic field is directed along the (negative) X -axis, and the γ -ray beam is parallel to the Z -axis. Consider an electron pair produced at the origin. Let the momentum vectors p_+ , p_- for the positron and the electron have polar angles θ_+ and θ_- , and azimuthal angles ϕ_+ and ϕ_- , and let the angle between the planes containing the γ -ray and the vectors p_+ and p_- be $\phi = \phi_+ + \phi_-$, the positive Y -axis lying to the right for the positron and to the left for the electron.

It may be shown that the co-ordinates of the end point of the trajectory of the positron in the XY plane are given by the (relativistic) equations:

$$[1] \quad y_+ = \frac{2p_+c}{eH} \cos \theta_+,$$

$$[2] \quad x_+ = \frac{2p_+c}{eH} \sin \theta_+ \cos \phi_+ \cot^{-1} (\tan \theta_+ \sin \phi_+)$$

where e is the electronic charge in electrostatic units, H is the strength of the magnetic field in gauss, and c is the velocity of light. Similar equations apply for the electron.

The energy relation which holds at the upper limit E may be obtained from Equation 1.

We have: $y_+ + y_- = (2c/eH) \cdot (p_+ \cos \theta_+ + p_- \cos \theta_-)$.

From this equation it is clear that:

$$eH < \frac{2c(p_+ + p_-)}{y_+ + y_-}.$$

For coincidences to occur, the trajectories must pass through the slits, and the minimum value of $y_+ + y_-$ is then the distance $2d$, the distance between the inner edges of the slits. Therefore, there is a maximum value of the field strength, H_0 , above which no coincidences will be observed, where:

$$H_0 = \frac{c(p_+ + p_-)_{\max}}{de}.$$

To find the condition for $(p_+ + p_-)$ to be a maximum, we use the expression for the total momentum of the components of a pair:

$$c(p_+ + p_-) = (E_+^2 - m_0^2 c^4)^{\frac{1}{2}} + (E_-^2 - m_0^2 c^4)^{\frac{1}{2}}$$

where m_0 is the rest mass of the electron, E_+ and E_- are the total electron energies, and their sum, $E_+ + E_- = k$, is the γ -ray energy.* The expression for the sum of the momenta is a maximum when:

$$E_+ = E_- = k/2$$

and therefore when:

$$p_+ = p_-.$$

Hence the maximum value of the field strength, H_0 , for which coincidences can be recorded, is given by:

$$[3] \quad H_0 = 2 p_0 c / de$$

where p_0 is the momentum corresponding to a symmetrical division of the γ -ray energy. Consequently when H is near H_0 , coincidences are produced only by pairs of which both components are emitted nearly normally from the center of the radiator.

Since the electric vector of the γ -radiation has no component in the direction of incidence, the number of pair components produced near this direction is vanishingly small. It is to be expected, therefore, that the coincidence counting rate should increase first very slowly and then more rapidly as the magnetic field is decreased below the critical value H_0 . It follows that the linear portion of the upper edge of the peak (Fig. 1), when extrapolated, cuts the axis of abscissae at a point below H_0 . There must, therefore, be a genuine tail to the coincidence peak, which, in practice, is not observed because of the scattered electrons previously mentioned.

Now the energy of the γ -ray is given by:

$$k = 2(p_0^2 c^2 + m_0^2 c^4)^{\frac{1}{2}}.$$

Hence, using Equation [3], k may be expressed in terms of H_0 and d :

$$[4] \quad k = eH_0 d S(\chi)$$

*These expressions take no account of the energy imparted to the nucleus in recoil. Since the momentum communicated is of the order of $m_0 c$ (5), this energy is negligible even in the lightest elements.

$$\begin{aligned} \text{where} \quad S(\chi) &= [1 - (2\chi)^2]^{-\frac{1}{2}} = 1 + 2\chi^2 + 6\chi^4 + 20\chi^6 + \dots \\ [5] \quad \text{and } \chi &= m_0 c^2 / k, \end{aligned}$$

and where m_0 is the rest mass of the electron. Equation [4] is the required expression giving the γ -ray energy in terms of the quantities d and H_0 .

As already pointed out, the field H_0 , corresponding to the end point, E , of the coincidence spectrum, cannot be determined directly. A reliable quantity, which can be obtained by direct measurement, is the field strength H_1 at the point Q_1 (Fig. 1), obtained by extrapolating the linear slope of the coincidence peak. The true γ -ray energy can then be obtained by adding the small correction, Δk :

$$[6] \quad k = eH_1 d S(\chi) + \Delta k.$$

Hereafter, Δk will be called the 'toe correction'.

Experimentally the value of the field H_1 is determined from a measurement of the corresponding frequency, f_1 , of the proton magnetic resonance in an aqueous solution of manganese sulphate. This quantity is given by the equation:

$$2\pi f_1 = gH_1$$

where g is the gyromagnetic ratio of the proton. Equation [6] then becomes:

$$k = 2\pi e f_1 d S(\chi) / g + \Delta k.$$

Expressing k in Mev. and f_1 in megacycles per second,

$$[7] \quad k = 2\pi \cdot 10^{-14} \cdot f_1 c d S(\chi) / g + \Delta k.$$

For g we use the value* obtained by Thomas, Driscoll, and Hipple (20), viz. $2.67523 \pm 0.00006 \times 10^4$ per sec. per gauss. For c we use (2) the value $2.99790 \pm 0.00001 \times 10^{10}$ cm. per sec. Equation [7] then becomes:

$$[8] \quad k = (0.0704103 \pm 0.0000016) f_1 d S(\chi) + \Delta k$$

where, as before, k is in Mev., f_1 in Mc. per sec., and d in cm.

The toe correction Δk was obtained (§2.4) from a calculation (§2.2) of the shape of the coincidence peak; it is a function of the γ -ray energy and of the ratio of the widths of the slits to the distance separating them. If the latter ratio is 1.0%, Δk is about 0.3% of the γ -ray energy. Theoretical curves for Δk are given in Fig. 9. The experimental verification of these curves will be discussed in §3.3.

2.2 Calculation of the Peak Shape

A calculation of the shape of a coincidence peak at different γ -ray energies is necessary in order to obtain the toe correction and the energy variation of the counting efficiency, which is defined as the ratio of the peak coincidence counting rate to the γ -ray intensity. The energy variation could be obtained by actual

*A paramagnetic salt is used to decrease the relaxation time of the protons in the magnetic resonance and the paramagnetic ions must increase the strength of the magnetic field applied to the protons above that existing outside the water solution. In the conditions which apply in our measurements we have not been able to detect this effect and we conclude that it cannot be much greater than the limits of error given in the above value of g . No correction for diamagnetic effects (19) has been applied since this value of g was obtained by measurements in water, and the uncorrected result is the one required for the measurement of an external magnetic field.

measurements of the counting rate for a number of homogeneous γ -rays of known energy and intensity, but there are very few γ -rays with energies above 3 Mev. suitable for this purpose. The counting efficiency as a function of energy was therefore obtained theoretically by calculating the peak shape at a number of energies and the result was subsequently checked where possible by comparison with experiment. The calculation of the peak shape also gives the resolution of the spectrometer.

The basis of the peak shape calculation is the Bethe-Heitler formula (8) for the differential cross section for pair production:

$$\begin{aligned}
 d\sigma = & -\frac{Z^2}{137} \cdot \frac{e^4}{2\pi} \frac{p_+ p_- c^2 dE_+ \sin\theta_+ \sin\theta_- d\theta_+ d\theta_- d\phi}{k^3 q^4} \\
 & \times \left[\frac{p_+^2 c^2 \sin^2\theta_+ (4E_-^2 - q^2)}{(E_+ - p_+ c \cos\theta_+)^2} + \frac{p_-^2 c^2 \sin^2\theta_- (4E_+^2 - q^2)}{(E_- - p_- c \cos\theta_-)^2} \right. \\
 & + \frac{2p_+ p_- c^2 \sin\theta_+ \sin\theta_- \cos\phi}{(E_+ - p_+ c \cos\theta_+)(E_- - p_- c \cos\theta_-)} \times (4E_+ E_- + q^2 - 2k^2) \\
 & \left. - \frac{2k^2(p_+^2 c^2 \sin^2\theta_+ + p_-^2 c^2 \sin^2\theta_-)}{(E_+ - p_+ c \cos\theta_+)(E_- - p_- c \cos\theta_-)} \right], \\
 q^2 = & k^2 + (p_+ c)^2 + (p_- c)^2 + 2p_+ p_- c^2 \sin\theta_+ \sin\theta_- \cos\phi \\
 [9] \quad & + 2p_+ p_- c^2 \cos\theta_+ \cos\theta_- - 2k(p_+ c \cos\theta_+ + p_- c \cos\theta_-)
 \end{aligned}$$

in which p_+ , p_- , θ_+ , θ_- , and ϕ are defined in Fig. 2, E_+ and E_- are the energies of the positron and electron, k is the γ -ray energy, and the other symbols have their usual meanings.

The formula is valid provided that $(Z/137) \ll 1$ and provided that the γ -ray energy is not so high that screening (which has been neglected) becomes important. For reasons of intensity, it has been necessary to use gold and lead radiators for which the first condition does not hold. Although it is known that in heavy elements the total pair cross section does not differ much from that given by this formula, experiment has shown that both the variation of the differential cross section with the energy of one of the pair components and the angular distribution do differ appreciably. For example, it follows from Equation [9] that the energy distribution of the positron reaches a maximum at half the γ -ray energy, but experiment shows that in heavy elements this distribution rises with the positron energy, reaching a maximum just short of the γ -ray energy less $2m_0 c^2$. The angular distribution at low energies has been studied experimentally by Simons and Zuber (17), by Groshev and Franck (5,6), and by Groshev (4). The most thorough investigation seems to have been made by the latter, who found that while the mean angles θ agree for light elements with those predicted from Equation [9], in the heavier elements they increase linearly with atomic number, the average value of θ_+ increasing more rapidly than that of θ_- . This result appears to be in agreement with the theoretical work of Jaeger and Hulme (9).

A more exact expression for the differential cross section at high energies, but one that is less amenable to computation, has been given recently by Maximon and Bethe (14).

The calculation of the peak shape involves an integration of Equation [9] between limits which are determined by the magnetic field and the geometry of the instrument. Approximations must be made since an exact calculation would be extremely difficult and laborious even by modern computing methods. The basic calculation of the peak shape is outlined below in §2.2.1, corrections for slit geometry are described in §2.2.2, and in §2.2.3 the validity of the approximations made in the calculation are discussed.

2.2.1 Basic Calculation

It follows from Equations [1] and [2] that the conditions for both components of a pair to pass through the slits are:

$$[10] \quad d < \frac{2p+c}{eH} \cos\theta_+ < d + a$$

where, to anticipate an assumption made below, the radiator is assumed to be a point midway between the slits, and:

$$[11] \quad 0 < \frac{2p+c}{eH} \sin\theta_+ \cos\phi_+ \cot^{-1}(\tan\theta_+ \sin\phi_+) < b,$$

and similar expressions for the electron. Here a is the width, and $2b$ the length of a slit; all other symbols have already been defined. Expression [10] is strictly true for infinitely thin slits and it will be shown below that when the thickness is taken into account, the upper limit in [10] is a function of ϕ_+ . Therefore, expressions [10] and [11] define the limits of integration for slits of zero thickness.

Even with this simplification an exact integration of Equation [9] is very difficult. One complication arises from the fact that the variable ϕ of Equation [9] must be replaced by ϕ_+ and ϕ_- and a second difficulty is that the limit of integration for θ_+ is a function of the angle ϕ_+ . Both these difficulties are removed by assuming that the slit length, $2b$, is infinite, for then expression [11] ceases to be a condition for obtaining coincidences. This means that coincidences will be obtained regardless of the angles ϕ_+ and ϕ_- and therefore also regardless of the angle ϕ . In these conditions the limits of integration of ϕ are simply 0 and 2π .

In the first approximation, then, we make the following assumptions:

- (1) the slits are infinitely long;
 - (2) the jaws of the slits are infinitely thin;
- and in addition:
- (3) the radiator is confined to a point midway between the slits;
 - (4) the radiator is thin enough for the pairs produced in it to traverse it without scattering or retardation.

With these assumptions it is not difficult to calculate the peak shape with sufficient accuracy to give the relative counting efficiency and the resolution of the spectrometer at high energies and the magnitude of the toe correction at all energies. At low γ -ray energies the error introduced by the first two assump-

tions becomes important and the finite length and thickness of the slits must be taken into account in order to obtain a sufficiently accurate estimate of the relative counting efficiency. However, these, and other assumptions introduced later, permit us to make only a rough estimate of the absolute counting efficiency.

For a point radiator midway between the slits, (assumption (3)), only those pairs are of interest for which the energy is shared equally or nearly equally. Then $p_+ = p_- = p_0$, and $k = 2 p_0 c S(\chi)$, and Equation [9] may be written in the simplified form:

$$\begin{aligned}
 d\sigma &= -\frac{C}{k^3} dE_+ d\theta_+ d\theta_- d\phi f(\theta_+, \theta_-, \phi, k), \\
 f &= \frac{\sin\theta_+ \sin\theta_-}{Q^2} \left[\frac{\sin^2\theta_+(S^2 - Q/2)}{(S - \cos\theta_+)^2} + \frac{\sin^2\theta_-(S^2 - Q/2)}{(S - \cos\theta_-)^2} \right. \\
 [12] \quad &\quad \left. - \frac{2 \sin\theta_+ \sin\theta_- \cos\phi (S^2 - Q/2)}{(S - \cos\theta_+)(S - \cos\theta_-)} - \frac{2S^2(\sin^2\theta_+ + \sin^2\theta_-)}{(S - \cos\theta_+)(S - \cos\theta_-)} \right], \\
 C &= Z^2 e^4 / (2\pi \cdot 137), \\
 Q &= 1 + \sin\theta_+ \sin\theta_- \cos\phi + 2(S - \cos\theta_+)(S - \cos\theta_-) - \cos\theta_+ \cos\theta_-.
 \end{aligned}$$

The integration of the function f , Equation [12], between the limits $\phi = 0$ and $\phi = 2\pi$ is possible analytically. However, if this procedure is adopted it is not possible to make the correction for finite slit length (§2.2.2 below) which is required for the calculation of the counting efficiency for low energy γ -rays. For the present purpose, a crude, but nevertheless sufficiently accurate, integration with respect to ϕ was made by first carrying out the integration of the function f with respect to the remaining variables, θ_+ , θ_- , and E_+ , for the two cases $\phi = 0$ and $\phi = \pi$, averaging the results, and multiplying by 2π . In other words, it was assumed that a sufficient approximation* to the exact integration over ϕ is given by:

$$[13] \quad 2\pi \times \frac{1}{2} [I(0) + I(\pi)]$$

where

$$I(\phi) = \iiint f d\theta_+ d\theta_- dE_+.$$

The restriction of the angle ϕ to the values 0 and π introduces a simplification to the function f , Equation [12], which may now be written:

$$\begin{aligned}
 f(\theta_+, \theta_-, \phi = \frac{0}{\pi}, k) &= -\frac{\sin\theta_+ \sin\theta_-}{Q^2} \times \\
 [14] \quad &\left[(Q/2 - S^2) \left\{ \frac{\sin\theta_+}{S - \cos\theta_+} \mp \frac{\sin\theta_-}{S - \cos\theta_-} \right\}^2 + \frac{2S^2(\sin^2\theta_+ + \sin^2\theta_-)}{(S - \cos\theta_+)(S - \cos\theta_-)} \right], \\
 Q &= 1 - \cos(\theta_+ \pm \theta_-) + 2(S - \cos\theta_+)(S - \cos\theta_-).
 \end{aligned}$$

*This approximation would certainly not lead to correct results if the function I , Equation [13], did not vary monotonically between $\phi = 0$ and $\phi = \pi$. This was tested by plotting the function f , Equation [12], as a function of ϕ for a number of fixed values of θ_+ and θ_- . It was found to increase monotonically from $\phi = 0$ to $\phi = \pi$ for all values of θ_+ and θ_- , except in the region where θ_+ was equal to or almost equal to θ_- . Since this region is small, it is safe to assume that the function I , Equation [13], increases monotonically between $\phi = 0$ and $\phi = \pi$.

This function is symmetrical between θ_+ and θ_- and for the purposes of graphical integration may be plotted as a contour map with these variables as rectangular co-ordinates. Fig. 3 shows the distribution of f for 10.8 Mev. and for 2.75 Mev.

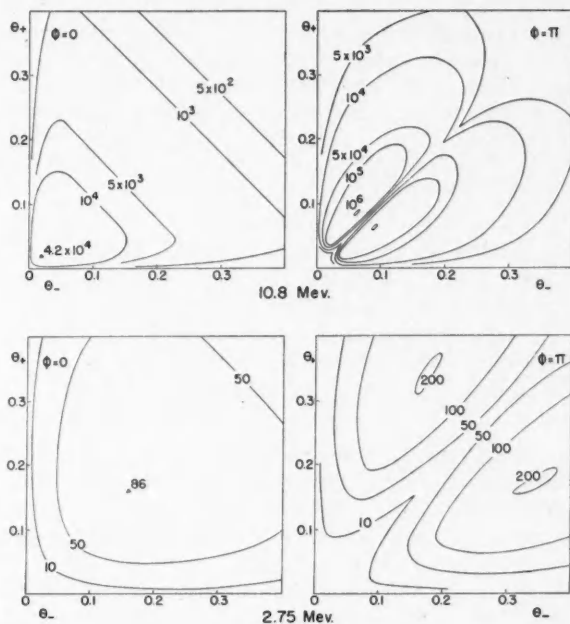


FIG. 3. Contour diagrams of the function f (Equation [19]). Above: 10.8 Mev.; below: 2.75 Mev.

It will be seen that the probability of pair emission is much greater when the components are emitted on opposite sides of the incident direction, a conclusion which has been demonstrated experimentally by Groshev (6). It has been found by numerical computation that the position of these contours is independent of small changes in the division of the energy. One such contour map can be used therefore for calculations involving small departures from symmetrical division.

It has been shown that, for a given γ -ray energy, k , there is a maximum field, H_0 , for which coincidences can be recorded (Equation [3]). Under these conditions both components of the pair must have the momentum p_0 . When the field strength is fixed at some value, H , less than H_0 , there is a limited range of values for the momenta for which coincidences are possible. For electrons of very high energy the momentum is proportional to the energy, and, therefore, to the extent to which this relativistic relation is true, the momenta of the components of a pair may be represented by the expressions:

$$p_+ = p_0 (1 \pm z); \quad p_- = p_0 (1 \mp z)$$

where z is the fraction which measures the deviation from equal division of the

energy of the γ -ray. For the present purpose, where only small deviations from symmetrical division are required, these expressions are sufficiently accurate. The maximum deviation from symmetrical division for which coincidences are possible occurs when the diameter of the orbit of the component with lower momentum, $p_0(1-z)$, is just equal to d , half the distance between the inner edges of the slits. Such an electron is projected normally from the radiator and just touches the inner edge of a slit. Its momentum is proportional to Hd , and since p_0 is proportional to H_0d , it follows that for a field strength H , the maximum deviation from symmetrical division of the γ -ray energy is given by:

$$1 - z = H/H_0$$

or

$$z = w, \text{ where } w = (H_0 - H)/H_0.$$

Therefore, coincidences can only occur for values of z in the range $0 < z < w$.

We must now consider the range of angles, θ_+ and θ_- , available to the components of a pair which are projected from a central point-radiator and whose momenta, p_+ and p_- , lie within the range limited by a given field displacement, w . From expression [10] the ranges of the angles θ_+ and θ_- are:

$$\cos \theta_+ = \frac{eH}{2p_+c} y_+, \quad \cos \theta_- = \frac{eH}{2p_-c} y_-$$

when y_+ and y_- take the limiting values d and $d+a$. The upper and lower limits of these angles will be called α_2 and α_1 respectively, for the orbit with higher momentum; and β_2 and β_1 for the orbit with the lower momentum. The values of these limiting angles are calculated and listed in the Appendix (§5.1); they are functions of w , z , and $\delta = a/d$.

The probability of the two components of a pair being produced within a given angular element $d\theta_+$ and $d\theta_-$ is given by the differential cross section formula, Equation [12]. For a given momentum division, the probability of recording a coincidence will be proportional to the volume contained beneath the surface of the function, f , between the two pairs of limiting angles. The quantity

$$[15] \quad I(w, \delta, k, z, \phi = \pi) = 2 \int_{\alpha_1}^{\alpha_2} \int_{\beta_1}^{\beta_2} f(\theta_+, \theta_-, k, \phi = \pi) d\theta_+ d\theta_-,$$

therefore, is proportional to the probability of producing a coincidence at a given field strength, defined by w , for an azimuthal angle $\phi = \pi$, and for a given ratio of the momenta specified by z , which must, however, lie in the range $0 < z < w$. The factor of 2 takes into account the fact that either the one or the other component of the pair can have the lower momentum. A similar expression applies for the function $I(w, \delta, k, z, \phi = 0)$. Using the approximation of Equation [13], the total number of coincidences, for given w , is proportional to:

$$[16] \quad I(w, \delta, k) = \frac{1}{2} \times 2\pi \sum \int_0^w \left[2 \int_{\alpha_1}^{\alpha_2} \int_{\beta_1}^{\beta_2} f(\theta_+, \theta_-, k, \phi) d\theta_+ d\theta_- \right] dz$$

where the summation over the angle ϕ means that the integrals for $\phi = 0$ and for $\phi = \pi$ are added together.

To a sufficient approximation the differential relation between the energy of a component of a pair and its momentum is given by:

$$dE = \frac{1}{2} k/S^2 dz$$

and from Equation [12] the cross section for the production of a coincidence is proportional to:

$$\frac{C}{2k^2 S^2} I(w, \delta, k).$$

Hence, when one photon is incident on a radiator of unit area and thickness W gm. per sq. cm., the probability of producing a coincidence is:

$$[17] \quad P(w, \delta, k) = \frac{WN_0}{A} \cdot \frac{Z^2 r_0^2}{4\pi \cdot 137} \cdot \frac{\chi^2}{S^2} \cdot I(w, \delta, k).$$

In this expression, N_0 is Avogadro's number; A is the atomic weight of the radiator; r_0 is the electronic radius, e^2/m_0c^2 ; and χ is m_0c^2/k as before.

To the degree that the approximations used above are true, the factor $I(w, \delta, k)$ determines the shape of the coincidence peak, and the maximum value of this quantity, when multiplied by χ^2/S^2 , determines the energy dependence of the counting efficiency.

The numerical values of the integrals $I(w, \delta, k, z)$ with respect to $d\theta_z$ and $d\theta_{-}$ in Equation [15] were obtained by a graphical method with $\delta = 0.018$ and for a considerable number of fixed values of w and z differing by 0.002. The integration with respect to z in Equation [16] was then performed by making the appropriate summations of the terms with constant w . These calculations were carried out for the four γ -ray energies 2.75, 5.0, 8.0, and 10.8 Mev.

2.2.2 Corrections for Slit Thickness and Slit Length

If the thickness* of the slits is of the same order as the width, a little consideration will show that the angular range, into which the electrons must be projected to pass into the slits, is reduced. The angular limits of Equation [15], therefore, require modification, and these modifications are discussed in the Appendix (§5.2).

Fig. 4 shows examples of the theoretical curves for the shape of the coincidence peaks at 2.75 and 10.8 Mev., calculated for the nominal resolution $(a/d) = 0.018$. The curves for the two values of ϕ are plotted separately; the dotted lines are the uncorrected curves; the full lines are the curves obtained with the slit thickness correction. The heavy full line represents the sum of the corrected curves for $\phi = 0$ and $\phi = \pi$. It will be noted that the slit thickness correction is important at 2.75 Mev. and quite small at 10.8 Mev. Fig. 4 also shows that the contribution to the coincidence counting rate, due to pairs for which $\phi = 0$, is very small for the higher γ -ray energy.

The finite length of the slits restricts the range of the azimuthal angle into which a positron or electron, with a given polar angle, must be emitted in order that it may subsequently enter the slit. (The following discussion which is

*The jaws of the slits must be thick enough to stop all electrons incident on them. In practice the thickness must be equivalent to the range of the electrons with about three quarters of the maximum γ -ray energy. In the present instrument we employ gold slits with a thickness of 1.5 mm.

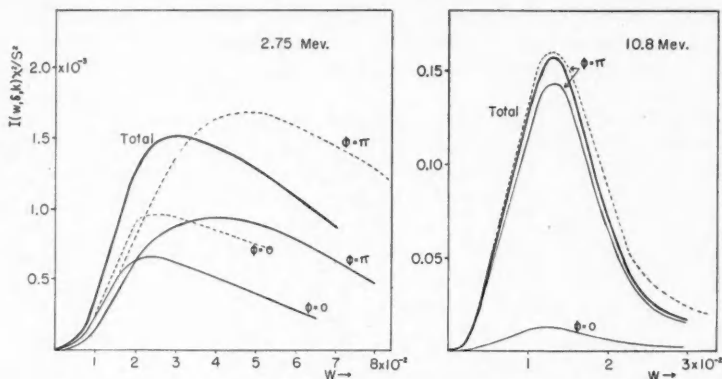


FIG. 4. Theoretical shape of coincidence curve for $\delta = 0.018$ at 2.75 Mev. and at 10.8 Mev. showing effect of slit thickness. Dotted lines: uncorrected. Full lines: corrected for slit thickness. The heavy lines represent the sum of the contributions for $\phi = 0$ and $\phi = \pi$.

given for positrons applies equally well to electrons.) For a slit separation $2d$ and a slit length $2b$ the minimum angle ϕ_+ permitted for a given angle θ_+ is given by the relation:

$$[18] \quad \tan \theta_+ \cos \phi_+ \cot^{-1}(\tan \theta_+ \sin \phi_+) = b/d$$

which is derived from Equations [1] and [2]. A plot of this function applicable to the case of the present spectrometer ($d = 11.34$ cm., $2b = 7.62$ cm.) is given in Fig. 5. It can be seen that positrons which are ejected with $\theta_+ < 0.21$ radian will enter the slits for all values of ϕ . Therefore, when computing the angular integrations of Equation [12], no error is introduced by the assumption that the

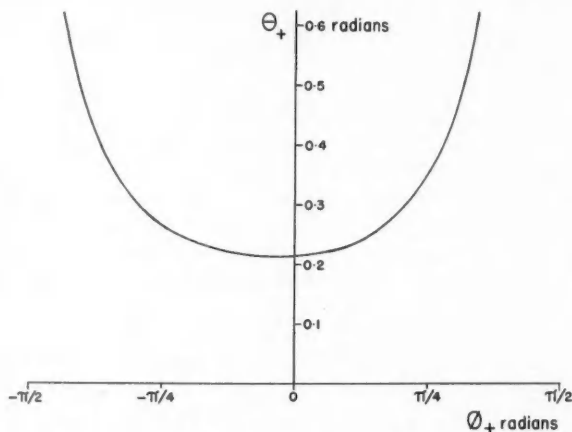


FIG. 5. Relation between θ_+ and the minimum value of ϕ_+ (Equation [18]).

slits are infinitely long in that part of the graphical integration of the contours of Fig. 3 which extends over the range $0 < \theta < 0.21$ radian. At high energies (above 5 Mev.) the integral of the differential cross section over this range of θ includes the greater part of the total cross section for pair formation and only an insignificant contribution is made to the maximum of the coincidence peak by pairs with $\theta_+ > 0.21$ radian. At 2.75 Mev., however, important contributions to the peak of the curve are made by components of pairs projected with angles above the critical angle. It follows that the correction for finite slit length, like that for slit thickness, is important at low energies and becomes less important as the energy increases.

The problem of estimating the correction for slit length is simplified by the fact that the integrations were carried out at only the two values $\phi = 0$ and $\phi = \pi$. Under these conditions the momentum vectors p_+ and p_- and the incident γ -ray lie in a plane. Only one of the azimuthal angles, say ϕ_+ , is required to describe the orientation of this plane with respect to the direction of the magnetic field. As pointed out above, when θ_+ and θ_- are both less than 0.21 radian, coincidences can be recorded for all orientations of the plane, i.e., for any value of ϕ_+ in the range $0 \leq \phi_+ \leq 2\pi$. When one or both of the polar angles exceeds 0.21, the range of ϕ_+ is reduced and the probability of obtaining a coincidence is decreased. The magnitude of the decrease is roughly proportional to the range of ϕ_+ excluded, and is different for each increment of area of the contour diagram (Fig. 3) employed in the graphical integration.

The effect of the slit length correction on the peak shape at 2.75 Mev. is shown in Fig. 6. The full line is the uncorrected curve and is identical with the curve

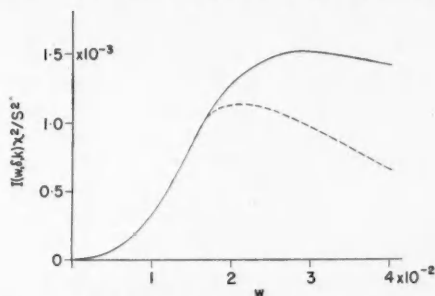


FIG. 6. Effect of slit length correction on the peak shape for 2.75 Mev. Full line: corrected for slit thickness. Dotted line: corrected for slit thickness and slit length.

marked "total" in Fig. 4. The dotted line is the corrected curve. It will be seen that the correction reduces the peak height by about 25% and makes the peak much sharper. It has no appreciable effect on the slope of the linear edge of the peak. The correction was calculated in detail only at 2.75 Mev.; a rough estimate of the correction for 5 Mev. is 6% at the peak maximum. The correction becomes negligible at higher energies.

2.2.3 Validity of the Calculations

The approximation represented by Expression [13] requires discussion. Though their heights may differ for the limiting cases $\phi = 0$ and $\phi = \pi$, the theoretical

curves of Fig. 4 have similar shapes. It follows that any combination of these curves will have similar properties and, in particular, the curve obtained by averaging these two cases will not be a poor approximation for that obtained from the exact integration with respect to ϕ . It follows that the peak shape calculated using the approximation [13] will give good values for the resolution and for the toe correction. It does not follow, however, that the peak heights obtained by the approximate method are the same at all γ -ray energies as those which might be obtained from an exact integration, or that the ratio of these quantities is independent of energy. This latter assumption, however, is necessary for the calculation of the counting efficiency as a function of γ -ray energy.

These calculations moreover were made on the assumptions (1) that the radiator was confined to an infinitesimal area midway between the slits, and (2) that the radiator was thin enough that scattering and retardation of the electron pairs in it could be ignored. The validity of these assumptions must now be considered in their application to an experimental arrangement.

(1) *Finite Area of the Radiator*

Let us first consider the influence of an extension of the radiator in the equatorial plane of the magnetic field on the counting rate measured at the peak of the coincidence curve. In their original communication, Walker and McDaniel showed that for relativistic electrons all parts of such a radiator should contribute to the peak coincidence counting rate. This property arises from the proportionality which exists between the momenta and the energy of relativistic electrons. However, the momenta of electrons, in the energy range of interest here, are not exactly proportional to their energy, and this limits the length of radiator which can be effective in producing coincidences. Two factors have to be considered: the length of radiator which is effective, and the extent to which the counting rate calculations can be applied to this length in view of the fact that they are strictly applicable only to the case where pairs are emitted from the center of the radiator.

The length of the radiator which is effective in producing coincidences depends on the γ -ray energy and on $w = (H_0 - H)/H_0$, the displacement of the magnetic field relative to the end point. It may be shown that the maximum length, L , is given by the expression:

$$[19] \quad L = \frac{2d}{1-w} \cdot \left[1 + \frac{(2\chi)^2 (1-w)^2}{w(2-w)} \right]^{-\frac{1}{2}}.$$

As w tends to zero, i.e., as the field H approaches the maximum value H_0 , the effective length of the radiator is reduced and only the central portion contributes to the coincidence counting rate. In our present instrument, the length of the radiator illuminated by γ -radiation is equal to about one-third of the distance between the slits. From Equation [19] it follows that the whole length is effective at all γ -ray energies above 2.75 Mev. provided w is greater than 1%. Now, as may be seen by re-examination of Fig. 4 (where $\delta = a/d = 0.018$), the position of the coincidence peak is given approximately by $w = \delta$. It follows, therefore, that the minimum width of slit, a , for the whole length of radiator to be effective

at the peak, for γ -ray energies equal to or greater than 2.75 Mev., is determined by $a/d = 1\%$.

As already pointed out, the permissible range in the division of the γ -ray energy between the components of a pair is determined by the relative field strength w . For a small radiator, centrally placed between the slits, the pairs which contribute to the coincidence counting rate at the peak (and therefore at small values of w) must always divide the γ -ray energy approximately equally. However, at the edge of a radiator with a length equal to one third of the distance between the slits, the energy ratio will be approximately two to one. The contours of the differential cross section of Fig. 3 are not applicable under these conditions. Numerical calculations, based on Equation [9], show that, although the height of the contours is not changed appreciably, the valley between them is shifted from the 45° angle to another for which the tangent is approximately equal to the ratio of the energy division. We have not attempted to calculate the peak shape contributed by pairs ejected from the ends of a long radiator, but we have found experimentally, for slits for which $\delta = 0.018$, that equal areas from different parts of the radiator contribute approximately equally to the peak height and that both the position and the shape of the peak are very little affected by the origin of the source of the pairs.

It follows that Equation [17], in regard to the height of the peak, is applicable to an extended radiator, provided that the width of the slits is great enough that the effective length of the radiator at the lowest γ -ray energy is not less than the length actually illuminated.

(2) Thickness of the Radiator

In deriving Equation [17] it was assumed that: (i) there was no retardation of the pair particles in traversing the radiator, and (ii), multiple scattering had little effect on their angular distribution as they were projected from the radiator. If these two assumptions hold, the peak height must be proportional to the thickness of the radiator. It may be shown that, if the thickness of the radiator is small enough to satisfy (ii), the effect of (i) is negligible.

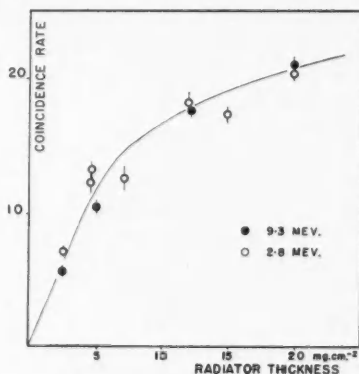


FIG. 7. Variation of peak coincidence counting rate with the thickness of the radiator.

Multiple scattering has the effect of broadening the natural angular distribution of pair formation; it will be important only when the average angle of scattering is of the order of the angle corresponding to the high points in the contour map of Fig. 3. Both angles vary inversely with the energy and therefore the radiator thickness at which multiple scattering becomes important is independent of the energy. This is demonstrated in Fig. 7 in which the peak coincidence counting rate for two γ -rays of different energies is plotted against the thickness of the gold radiator. The peak counting rate at first increases linearly with the thickness and finally approaches a saturation value. Subsequent increase in the thickness results in impaired resolution caused by a broadening of the coincidence peak without change in height.

Fig. 7 shows that saturation is reached at a thickness near 20 mgm. per sq. cm. Most of our measurements have been made with a gold radiator with a thickness of 5 mgm. per sq. cm. for which Equation [17], therefore, should be applicable. It follows that the retardation can be neglected, for the mean retardation in the radiator is then only about 5 kev., which is very small compared with the width of a coincidence peak.

2.3 Resolution

The resolution of the spectrometer was not studied in detail theoretically since it is a quantity which can be easily investigated by experiment.

The shape of the coincidence peak was calculated for a number of different slit widths at an energy of 8 Mev. In these calculations the corrections for slit thickness and slit length were not applied because, at this energy, their effect would be small. The results are shown in Fig. 8, the ordinates being normalized to give the same maximum coincidence rate at the peak. Fig. 8 shows that, as the width of the slits is reduced, the linear upper edge of the peak moves towards the limiting field H_0 and its slope becomes steeper. The resolving power of the instrument, i.e., the width of the peak at half maximum, does not decrease

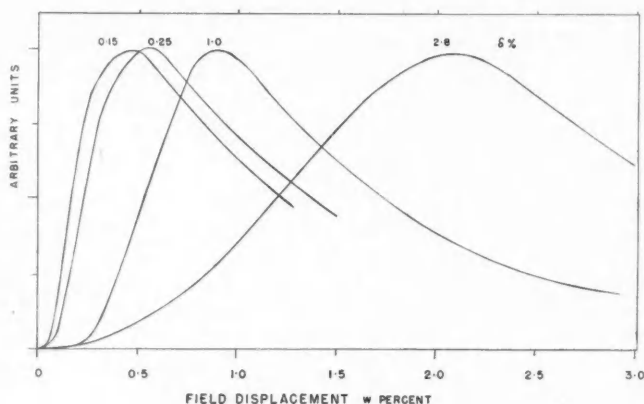


FIG. 8. Theoretical peak shapes for 8 Mev.

indefinitely with the slit width as in other kinds of spectrometers. For wide slits, the peak width is proportional to the width of the slits. However, as the width of the slits is reduced, the peak width tends to a finite value. At 8 Mev., this minimum width is 70 kev.

The calculations (with $\delta = 0.018$), previously discussed, show that the peak width is essentially independent of the γ -ray energy.

2.4 Toe Correction

The toe correction is obtained directly from the calculated curve of the coincidence peak; its value is equal to the difference between the field at the end point and the point where the linear upper edge of the peak, when extrapolated, meets the axis of abscissae.

The value of the toe correction is determined entirely by those electron pairs which contribute to the steep linear edge of the coincidence peak. In a practical design of spectrometer in which the radiator is of large area, these pairs are ejected from the region of the radiator midway between the slits and follow trajectories for which θ_+ and θ_- are near zero. Electrons which follow other orbits or which are affected by retardation in the radiator can only produce coincidences at lower values of the magnetic field. Therefore, the value of the toe correction will be largely independent of the area and thickness of the radiator, and of the slit length and thickness, and will be a function only of the γ -ray energy and the slit width. That the toe correction is practically independent of slit thickness and length is apparent from Figs. 4 and 6. The theoretical value of the toe correction should, therefore, be reliable and not subject to errors introduced by the simplifying assumptions involved in the calculation of Equation [17]. It follows also that accurate energy measurements can be made using thick radiators when the maximum counting rate is required at the sacrifice of resolving power.

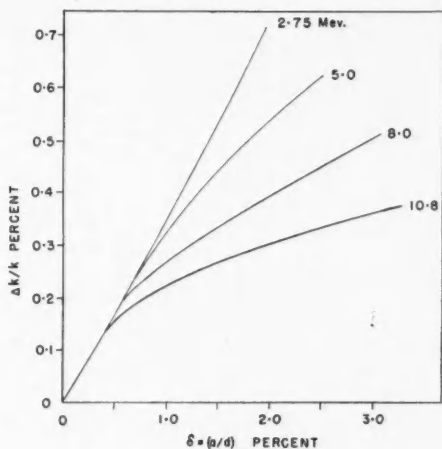


FIG. 9. Theoretical toe corrections.

The value of Δk was obtained from calculated curves of the peak shape in which the effect of the length and thickness of the slits was neglected. The results for a number of different energies are given in Fig. 9 in which Δk , expressed as a fraction of the γ -ray energy, is plotted against δ . This figure shows that initially the toe correction increases linearly with δ and that the point at which the linearity fails depends on the energy. In the range $0 < \delta < 0.005$, the curves are linear for all energies up to 10 Mev. In this range of δ , the pairs responsible for the linear upper edge of the coincidence peak are produced at angles which are always less than those corresponding to the maxima in the contours of Fig. 3. The deviations from linearity in the toe correction curves occur when pairs, which are emitted in the directions of the high points of Fig. 3, contribute to the observed coincidence counting rate.

The slope (0.3) of the linear portion of the toe correction curve seems to depend very little on the shape of the angular distribution of pair formation. Calculations of the toe correction to be expected for an artificial angular distribution, which had a maximum in the forward direction and was gaussian with respect to the angles θ_+ and θ_- , produced curves very similar to those of Fig. 9. The angular distribution was adjusted to give a maximum differential cross section in the direction of the incident γ -ray and normalized so that the total cross section and the mean angle of emission varied with the energy in the same way as the pair formation cross section. For small angles this differential cross section varies very little with θ_{\pm} and the fact that the slope of the linear toe correction in this case is so similar to that of our original calculations, in which the cross section is zero in the forward direction, indicates that the slope is nearly independent of the angular distribution which is chosen.*

2.5 Relative Counting Efficiency

The peak counting efficiency is proportional to the maximum value of $P(w, \delta, k)$ with respect to w (Equation 17). The energy dependence of the counting efficiency is contained in the factor

$$I(w, \delta, k) \cdot (\chi^2/S^2)$$

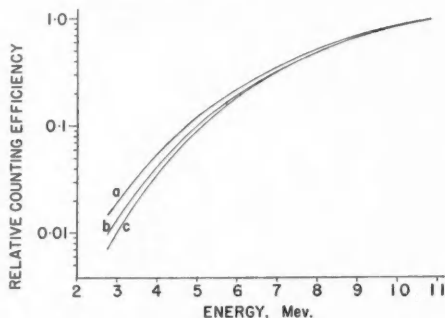


FIG. 10. Theoretical efficiency curves: (a) uncorrected, (b) corrected for slit thickness, (c) corrected for both slit thickness and length.

*We are much indebted to Dr. J. D. Jackson for making this calculation, and for discussion of the results.

of Equation [17]. Maximum values of this factor, with and without the correction for slit thickness and slit length, for an apparatus with slits 2 mm. thick and 2 mm. wide ($\delta = 0.018$), are listed in Table I. It is evident that the counting efficiency rises extremely rapidly with energy—nearly as the fifth power at 3 Mev. This effect is the result of the rapid increase of the heights of the contours of Fig. 3 and the shift in the position of the maxima toward the origin as the energy increases. The results of Table I are plotted in Fig. 10 after normalization to unit efficiency at 10.8 Mev. This figure shows the effect of the corrections for slit geometry.

TABLE I
RELATIVE COUNTING EFFICIENCY FOR $\delta = 0.018$

k (Mev.)	Maximum value of $I(w, \delta, k) \cdot (\chi^2/S^2)$		
	Uncorrected	Corrected for slit thickness only	Corrected for slit length and thickness
2.75	0.00255	0.00152	0.00111
5.0	0.0216	0.0158	0.0148
8.0	0.092	0.076	0.076
10.8	0.176	0.156	0.156

3. EXPERIMENTAL

3.1 Experimental Arrangement

The experimental arrangement of the spectrometer is shown diagrammatically in Fig. 11. A more detailed drawing is shown in Fig. 12. The horizontal pole faces

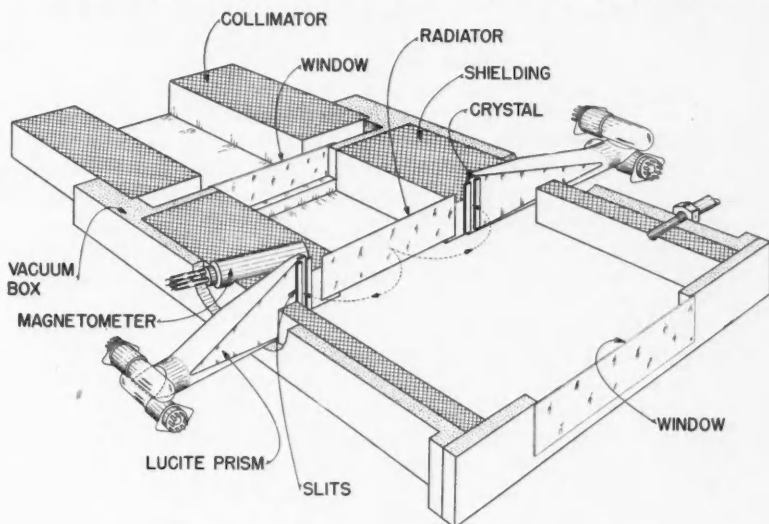


FIG. 11. Diagrammatic sketch of the pair spectrometer.

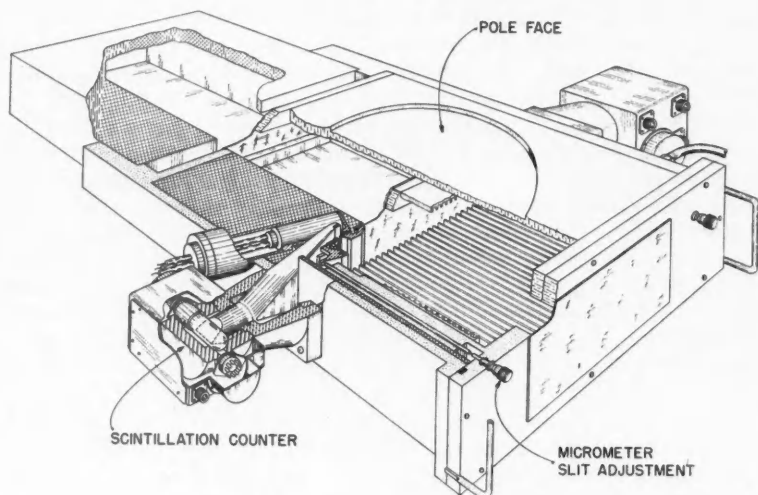


FIG. 12. Detailed drawing of the pair spectrometer.

of the electromagnet are 12 in. in diameter and 5 in. apart. An evacuated rectangular chamber is mounted between the pole faces. The γ -ray beam passes into and out of the chamber through thin beryllium-copper windows. The radiator is placed centrally in the vacuum chamber with its plane vertical. It is mounted on an aluminum frame (shown in Fig. 12) to which are attached the fixed inner jaws of the slits which define the entrance to the counters. In the final model of the spectrometer, the jaws were made of gold 3 in. long, $\frac{1}{4}$ in. wide, and 1.5 mm. thick. The adjustable outer jaws of the slits move in slots and are separately controlled by micrometer adjustments outside the vacuum system. The inside surfaces of the walls of the compartment in which the electron pairs move are lined with slotted sheets of polystyrene, shown in Fig. 12, to reduce the effects of scattering. The compartment of the vacuum chamber nearest the source of γ -rays is lined with thick lead blocks to shield the crystal counters. The spectrometer is evacuated with a mechanical pump.

The pair components are detected by two stilbene crystals, $3\frac{1}{2}$ in. \times $\frac{1}{4}$ in. \times $\frac{1}{8}$ in., each of which is cemented to a light guide, terminating in a 60° prism which is viewed by two IP21 photomultiplier tubes connected in parallel. The photomultiplier tubes, which are situated outside the vacuum chamber, are enclosed in thick steel containers which reduce the strength of the magnetic field within them to a few gauss, a field which has no detectable influence on the counting rate. The pulses produced by the two multipliers are fed to cathode followers and fast amplifiers (cutoff at 200 Mc. per sec.), and thence to a mixing circuit, operating at a coincidence resolving time of 2.5×10^{-8} sec.

In the earlier model of the pair spectrometer, the magnetic field was stabilized by control of the magnet current and the value of the magnetic field was

measured from the frequency of the proton resonance, using a super-regenerative circuit. Automatic operation was obtained by altering the magnetic field step by step according to a pre-arranged program. The values of the magnetic field at each step were not measured automatically. They depended to some extent on the magnetic history and were determined over the same cycle of operations, before and after each run.

The apparatus has since been much improved by allowing the proton resonance to control the magnetic field. In the present instrument, the useful range of frequency of the proton resonance is 2.8 to 16 Mc. per sec. In the range 2 to 4 Mc. per sec., the proton resonance frequency is the fundamental frequency of an oscillator of high stability, adjustable over this frequency range by tuning a motor-driven variable condenser. From 4 to 8 Mc. per sec., and from 8 to 16 Mc. per sec., the proton resonance frequency is the second or the fourth harmonic of this oscillator.

For automatic operation, the coincidences are counted at values of the magnetic field corresponding to a predetermined set of proton resonance frequencies. These frequencies are the harmonics of the pulses produced when the oscillations of a 100 kc. crystal-controlled oscillator are squared off, sharpened, and reduced in frequency by a scale-of-two circuit. By successive divisions of two, any submultiple of the original frequency of 100 kc. per sec. can be obtained, the lowest frequency used being 1.5625 or $100/2^6$ kc. per sec.

As the proton resonance frequency is changed, the magnetic field changes correspondingly. The proton resonance frequency is allowed to heterodyne with the harmonics of the reduced crystal-controlled frequency; the heterodyne frequency is detected in a mixing circuit connected to an audio-frequency amplifier tuned to 390 cycles per sec., which, after rectification, provides current to operate a relay. As the proton resonance oscillator frequency is shifted, the relay is operated twice at each tuning point, i.e., when the proton frequency passes 390 cycles per sec. above or below the frequency of a harmonic of the crystal oscillator. Every second operation of the relay is made to stop the motor shifting the proton resonance and to start coincidence counting. At the end of the counting interval, the result is printed automatically, power is supplied to the tuning motor, and another cycle of events is started. By adjustment of the degree of the subdivision of the frequency of the crystal oscillator, the frequency interval between the coincidence counting positions can be adjusted, in factors of two, to any of seven values between 1.5625 and 100 kc. per sec. Since the magnetic field follows any change in the frequency of the proton resonance which controls and stabilizes it, the value of the magnetic field, at the position for coincidence counting, is quite independent of magnetic hysteresis, and is fixed in terms of a harmonic or subharmonic of the frequency of the crystal oscillator.

3.2 Accuracy of Energy Measurement

From Equation [8] it is clear that the accuracy of measurement of the γ -ray energy k depends on: the distance, d , between the slits; the frequency, f_1 , corresponding to the extrapolated end point of a coincidence peak; and the toe correction, Δk .

3.2.1 The Distance d

The error in the measurement of the distance d is very small. In our improved apparatus, the mean value of $2d$ is 22.674 ± 0.001 cm. and the slits are parallel to each other such that the distances between corresponding ends are equal to within 0.0007 in. Changes in the ambient temperature of the room produce a negligible uncertainty in this quantity. Two possible sources of error need to be considered which are connected with the dimension d :

(1) An error will arise if the edges of the slits are not parallel to the direction of the magnetic field. In the present apparatus this angle, ζ , is certainly less than one-quarter of one degree; the error in the energy measurement is $\frac{1}{2}\zeta^2$ and is therefore not greater than 0.001%.

(2) An error will occur if the radiator is not coplanar with the slits, Equation [8] having been calculated on the assumption that the two are coplanar. There are two difficulties in the realization of this condition. (i) The slits are of finite thickness and this makes the effective position of the slits relative to the radiator uncertain. (ii) It is difficult to construct an accurately plane radiator from a thin metallic foil over an area of about 10 sq. in. These difficulties, however, are not serious for, as pointed out above, the energy measurement involves only pair components emitted near the center of the radiator and if the latter is displaced in a direction normal to its surface by an amount h , the distance d is changed effectively only by an amount h^2/d . Even if h is 1 mm., this error is less than 0.01%. Therefore the accurate location of the radiator is not important and also the effect of the thickness of the slits can be neglected.

3.2.2 The Frequency f_1

The errors in the determination of the frequency f_1 required in Equation [8] fall into two groups: (1) those associated with the determination of the extrapolated end point of the peak and (2) those associated with the measurement of frequency.

3.2.2.1 The Extrapolated End Point

There is a statistical error associated with the experimental points on the linear upper edge of the coincidence peak. This error depends on the counting rate produced by the γ -ray and the time allowed for counting; when these quantities are fixed, the amount of the error is independent of the γ -ray energy, and for exceptionally strong γ -rays, the energy equivalent of this error may be as low as 2 or 3 kev.

The level of the counting rate to which the linear upper edge is to be extrapolated may be uncertain. If no other γ -rays with similar energy exist in the spectrum being examined, the correct result is obtained by extrapolation of the linear upper edge of the peak to zero counting rate. However, if the coincidence peak is superposed on a continuous background or on the tail of a neighboring peak, the extrapolation must be made to a level below the background by the amount of the scattering tail of the peak being studied. This is about 5% of the peak height. The error committed in omitting this procedure varies directly with the slope of the upper edge and may be appreciable for large slit widths. In fact, since the frequency displacement between the upper limit and the peak

is roughly given by δ , the error involved in ignoring this effect, in our present instrument, is roughly 0.05δ . For 3 mm. slits, this error may amount to 0.1% .

3.2.2.2 The Frequency Measurement

The coincidence counting rate is plotted against the frequency of the proton oscillator. This is determined from a simple function of the natural frequency of the crystal calibrating oscillator, viz., $m/2^n$, where m and n are integers. It is necessary to apply three corrections to this frequency. (a) In deriving Equation [8] it was assumed that the magnetic field is uniform. Consequently, a correction must be applied to allow for lack of uniformity. (b) A correction must be applied to the nominal frequency of the crystal-controlled oscillator. (c) A small correction arises from the heterodyne method of field control.

(a) Since all parts of the radiator contribute to the coincidence counting rate, the pairs produced may follow a number of widely different trajectories. However, to determine the energy of a γ -ray using Equation [8], it is only necessary to know the average value of the field over the orbits of pairs which produce coincidences contributing to the linear upper edge of the coincidence peak. As pointed out in §2.4, these pairs are emitted from the central region of the radiator with small polar angles θ . Their trajectories, therefore, are parallel or nearly parallel to the equatorial plane.*

In the present apparatus the reduction in the field strength which normally occurs near the edges of the pole faces has been purposely overcorrected. In the equatorial plane, the maximum positive deviation of the field from the value measured at the center was about 0.24% . Near the pole faces and near the periphery the deviation was nearly 1% .

Using a relation due to Hartree (7), the difference $(H_a - H_c)$, between the average field (H_a) over a trajectory and that at the axis of the magnet (H_c) was obtained for a representative number of semicircular orbits lying parallel to the equatorial plane. The average of these values of $(H_a - H_c)$ is the required correction to be made for field inhomogeneity, when referred to the value of the field at the center (H_c) . This average value was found to be 0.12% of H_c at the field corresponding to 9 Mev., and 0.19% at the field corresponding to 3 Mev. A value of $(H_a - H_c)$ suitable for all energy measurements is $0.15 \pm 0.04\%$.

The location of the search coil in its standard position in the well (Fig. 11) corresponds to the maximum of the magnetic field in the radial direction, and for this reason, the field (H_s) measured by the search coil is independent of small displacements of the coil in the well. The difference $(H_s - H_c)$ was measured accurately and found to be $0.24 \pm 0.02\%$. The variation of this number with field strength was found to be negligible. The difference $(H_a - H_s) = -0.09 \pm 0.05\%$ refers the averaged value of the field to that measured at the search coil, and is the correction required.

In the foregoing, we have assumed that the value of the magnetic field at the search coil is given exactly by the proton resonance frequency. However, when the proton frequency is used to stabilize the magnetic field through an electronic regulator, the magnetic field at the search coil may not correspond exactly

*This can be seen by solving Equations [1] and [2] for x_z .

to the proton resonance. Exact adjustment is easily made by the usual method of centering the proton signal on a cathode-ray tube. In the present apparatus we have examined the accuracy of this adjustment by a simultaneous measurement of the field strength at the center of the magnet with a subsidiary proton resonance magnetometer. It was found that the accuracy of this adjustment was always within 0.01%.

(b) The frequency of the crystal oscillator was nominally 100 kc. per sec. The actual frequency was determined by comparison with the frequency of the radio station WWV, using a heterodyne method. It was found to be greater than the nominal frequency by $0.245 \pm 0.002\%$.

(c) It has been pointed out in §3.1 that the automatic operation of this apparatus is designed so that the tuning motor is stopped at the second of the two tuning points obtained when an harmonic of the reduced frequency of the crystal oscillator and of the proton oscillator differ by that of the tuned amplifier. It is therefore necessary to add or to subtract a small correction depending on the frequency of this amplifier, according to whether the proton resonance is increasing or decreasing between the intervals of coincidence counting. In the range of 2 to 4 Mc. per sec., the proton resonance frequency is equal to that of the oscillator, and the frequency correction, therefore, is the frequency of the tuned amplifier, viz., 390 cycles per sec. At higher frequencies, the proton frequency is the second or fourth harmonic of the oscillator, and the frequency correction, therefore, is two or four times that of the audio amplifier. The tuning of the latter is sharp, and the uncertainty in the proton oscillator frequency caused by the relay circuits stopping the tuning near, but not exactly at, the heterodyne points can be neglected.

3.2.3 The Toe Correction

The error possibly involved in the toe correction is important because the magnitude of this correction is usually much greater than the errors associated with the frequency measurements. As will be shown below, the theoretical curves given in Fig. 9 are well corroborated by experiment, at least over the linear portion of that figure. If a toe correction lies on this linear portion, its magnitude is certainly correct to 10%. Beyond the linear portion, the possible error in the toe correction is equal to the accuracy with which the theoretical toe corrections can be verified by experiment. It will be shown below that this lies between 2 and 10 kev.

3.3 Measurement of the Toe Correction

The toe correction, Δk , can be determined experimentally by plotting the upper limit of the coincidence peak as a function of the slit width. As the slit width approaches zero, the value of H_1 approaches the limiting value, H_0 . In practice, however, owing to the fact that the peak counting rates decrease rapidly with decreasing slit widths and with decreasing γ -ray energy, such upper limit measurements can be made only for exceptionally strong high-energy γ -rays.

The upper limits were measured for different values of the slit width for the strong magnesium (10) γ -ray at 3.95 Mev. and for several strong γ -rays be-

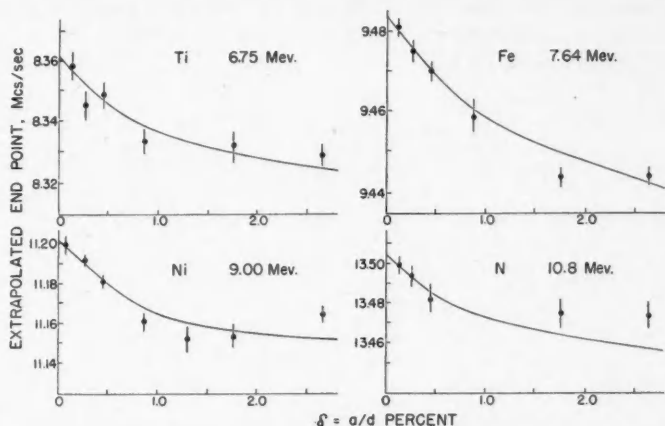


FIG. 13. Experimental values of the extrapolated end point plotted against the slit width. The full lines are theoretical curves interpolated from Fig. 9.

tween 6.75 and 10.8 Mev. Some of the results are shown in Fig. 13, in which the upper limits are plotted as ordinates and the slit widths (in terms of δ) as abscissae. The full lines, which were obtained from the calculated toe correction curves of Fig. 9, have been adjusted on the ordinate scale to give the best fit for low values of δ . For every γ -ray examined, there is an initial linear decrease in the measured upper limit, the slope being in agreement with that expected theoretically (0.3). The value of the frequency corresponding to the true end point, H_0 , of the coincidence spectrum, is determined by the intercepts of these curves with the axis of ordinates, and the toe correction by the difference between any other ordinate and this value. By plotting the upper limit for low values of δ and extrapolating linearly the results obtained to zero δ , the true end point can be obtained without using the toe correction.

From Fig. 13, we estimate that the linear portions of the theoretical curves of Fig. 9 give the value of the toe correction to within 10%. This error is usually less than the statistical error of measurement of the upper limit. For $\delta > 0.5\%$, the maximum error in the calculated toe correction may vary from 2 kev. at $\delta = 0.5\%$ to about 10 kev. at $\delta = 3\%$. In a rough way we have been able to check that the error in the toe correction is not greater than these values by measuring the energies of the cascaded γ -rays produced when a neutron is captured in Si^{28} (11). The majority of the captures in that isotope produce a γ -ray (M) leading to the excited state at 4.93 Mev.; this is followed by the emission of a second γ -ray (K) leading directly from that state to the ground state. The sum of the transition energies of these two γ -rays must be equal to that of the direct transition to the ground state, a much weaker γ -ray (B), but one that can be measured with some precision. If there were no errors in the toe corrections and if there were no nonlinear errors in the magnetic field measurements, these two quantities would be equal within the statistical error

of measurement. The results obtained with $\delta = 0.018$ are shown in Table II in which the transition energy is equal to the γ -ray energy plus the recoil energy of the nucleus emitting the γ -ray.

TABLE II
ENERGIES OF CASCADED γ -RAYS IN Si^{29} .
THE ERRORS IN THE LAST COLUMN ARE STATISTICAL ERRORS ONLY

γ -Ray	k_1 (kev.)	Δk (kev.)	k (kev.)	Nuclear recoil energy (kev.)	Transition energy (kev.)
K	4908 ± 3	25	4933 ± 3	0	4933 ± 3
M	3519 ± 6	21	3540 ± 6	0	3540 ± 6
$K + M$					8473 ± 7
B	8439 ± 2	28	8467 ± 2	1	8468 ± 2

It will be seen that the sum of the transition energies corresponding to the γ -rays K and M is equal to that of B to within a relatively large statistical error, arising mainly from the difficulty of measuring the upper limit of the γ -ray M in the presence of a background of unresolved radiations. This agreement shows that no serious error is committed in using the calculated toe corrections.

The conclusion of §2.4, that the upper limit should be sensibly independent of the thickness of the radiator, was verified using the 7.6 Mev. γ -ray from iron. The upper limits obtained with the usual radiator, 5 mgm. per sq. cm., were the same within the statistical error of measurement, about 0.04%, as those obtained with another, about 50 mgm. per sq. cm. With this γ -ray we also found that the toe correction, as expected, was independent of the slit length.

3.4 Comparison with Other Energy Measurements

In Table III we list the results of some careful measurements of neutron capture γ -rays made recently with the improved apparatus. These new results supersede similar measurements already published (10, 11). The first column gives the nucleus responsible for the γ -radiation; the second, the value of δ ; the third, the toe correction obtained from the curves of Fig. 9. The fourth column lists the γ -ray energy; the error in this column is made up of the items listed in the next column: (1), the error due to the uncertainty in the inhomogeneity of the magnetic field, viz., 0.05%; (2), the statistical error of the determination of the upper limit; and (3), an estimate of the probable error in the toe correction. The figures in the sixth column are the transition energies, i.e. the γ -ray energy plus the energy of the nuclear recoil, and with the exception of the first figure, the seventh column contains the transition energy deduced from the addition of the binding energy of the deuteron, obtained by Mobley and Laubenstein (15) (2.226 ± 0.003 Mev.), to the highest Q -value obtained in the (d, p) reaction (18, 21). The first figure in Column 7 is a γ -ray measurement made with a magnetic lens spectrometer. The results are generally in good agreement.

TABLE III
COMPARISON OF SOME ENERGY MEASUREMENTS

Source	δ , %	Δk , kev.	k , kev.	Error in kev.			Transition energy in kev.		
				(1)	(2)	(3)	Present work	From reaction energies	Ref.
Na ²⁴	1.8	18	2751 \pm 5	1.3	3	3	2753 \pm 5	2755 \pm 5	23
	2.7	22	2756 \pm 6	1.3	4	5			
C ¹³	0.9	15	4951 \pm 5	2.5	2.5	3	4949 \pm 6	4942 \pm 6	18
	1.8	25	4945 \pm 7	2.5	5	4			
Be ¹⁰	0.45	11	6812 \pm 5	3.4	4	1	6816 \pm 6	6811 \pm 8	18
	0.9	19	6816 \pm 7	3.4	4	4			
Al ²⁸	0.45	12	7722 \pm 5	4	3	1	7724 \pm 6	7720 \pm 10	18
	0.9	20	7724 \pm 7	4	3	4			
Si ²⁹	1.8	28	8467 \pm 8	4	3	6	8468 \pm 8	8472 \pm 8	18
Si ³⁰	1.8	30	10599 \pm 11	5.2	5	8	10601 \pm 11	10614 \pm 13	21
N ¹⁵	0.9	24	10828 \pm 9	5.5	4	4	10832 \pm 8	10841 \pm 9	18

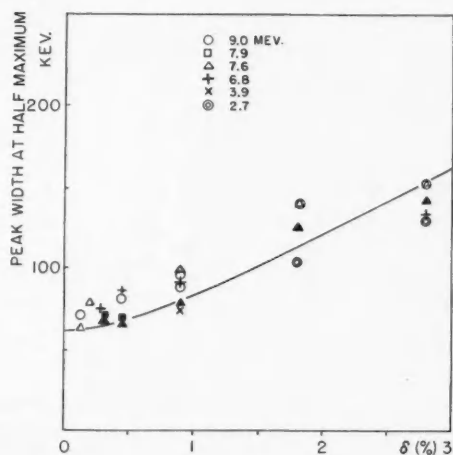


FIG. 14. Widths of coincidence peaks at half maximum plotted as a function of the slit width. The full line is obtained from the widths of the curves calculated at 8 Mev. (Fig. 8). Open points, slit length 7.6 cm.; full points, slit length 2.8 cm.

3.5 Experimental Width and Shape of the Coincidence Peak

Experimental values of the width of coincidence peaks are plotted in Fig. 14 for different values of the slit width. In this figure, the full points are those obtained with a slit length of $2b = 2.8$ cm., the others being obtained with $2b = 7.6$ cm. The smooth curve is the width of the coincidence peak calculated

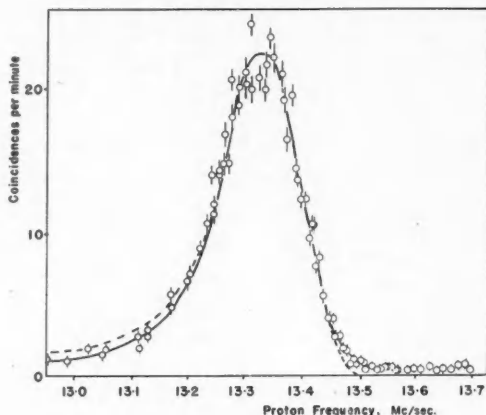


FIG. 15. Comparison of theoretical and experimental coincidence peaks for 10.8 Mev. and $\delta = 0.018$ (nitrogen γ -ray). The abscissae give the strength of the magnetic field, in units of the proton resonance frequency; the broken line is the calculated curve.

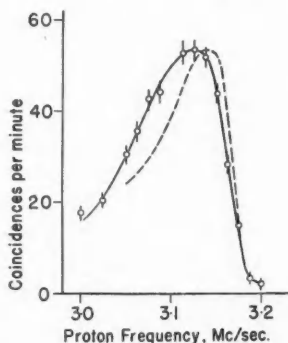


FIG. 16. Comparison of theoretical and experimental coincidence peaks for 2.75 Mev. and $\delta = 0.018$ (Na^{24} γ -ray). The abscissae give the strength of the magnetic field, in units of the proton resonance frequency; the broken line is the calculated curve, corrected for slit thickness and length.

at 8 Mev. It will be seen that the experimental results agree well with the theoretical curve and verify the conclusion reached in §2.3 that the width is independent of energy. There is an indication that the peak widths tend to decrease as the slits are shortened. A similar small decrease in width is found if the area of the radiator is contracted.

Fig. 15 shows the theoretical curve for the shape of a coincidence peak fitted at the peak and at the upper limit to the early experimental results obtained for the 10.83 Mev. capture γ -ray emitted by nitrogen. There is remarkably good agreement. In Fig. 16 we have plotted the recent experimental points for the 2.75 Mev. γ -ray from Na^{24} and compared it with the theoretical curve, which,

again, is fitted at the peak and at the upper limit. The agreement here is less satisfactory; the discrepancy at low frequencies is probably caused by the approximations used in making the corrections for slit thickness and slit length.

3.6 Experimental Determination of the Counting Efficiency

An experimental test of the counting efficiency curve of Fig. 10 is difficult to make with precision for no radioactive materials exist which produce γ -rays of known intensity with energies above that of the 2.75 Mev. γ -ray of Na^{24} . Neutron capture γ -rays have therefore been used, and we have attempted to determine the relative counting efficiencies of those few capture γ -rays for which the necessary absolute intensities are approximately known. The method consists in comparing the peak counting rates of these γ -rays using samples in which weighed amounts of the materials have been mixed together. If, then, the neutron capture cross sections are known, the ratio of the counting efficiencies of the spectrometer can be deduced from the ratio of the peak coincidence counting rates.

In making such measurements, we have to consider the possible effect of counting losses in the photomultipliers. It is not possible to use so high a voltage on the photomultipliers that even 90% of the pairs are counted without introducing a large random coincidence rate due to noise. Instead, it is convenient to record only 80 to 90% of the total coincidence rate. It is found that this fraction is independent of the γ -ray energy, the characteristic counting rate curve (counting rate plotted against photomultiplier voltage) for the sodium 2.75 Mev. γ -ray being very similar to that due to the nickel 9.0 Mev. γ -ray.

Let σ and N be respectively the thermal neutron capture cross section and the number of atoms of the sample material exposed to the field of view of the spectrometer. Let ϵ be the counting efficiency, i.e., the number of coincidences produced per photon incident on the radiator, T_s the mean transmission coefficient in the sample material, T the transmission coefficient in the neutron filters and other materials between the sample and the spectrometer, and P the absolute intensity of the γ -ray in photons per capture. Then the ratio of the peak counting rates, q_1 and q_2 , of two γ -rays to be compared, is given by:

$$[20] \quad \frac{q_1}{q_2} = \frac{N_1 \sigma_1 \epsilon_1 T_{s1} T_1 P_1}{N_2 \sigma_2 \epsilon_2 T_{s2} T_2 P_2}.$$

The transmission, T , is easily calculated and in our present arrangement lies between 0.85 and 0.92 throughout the range between 2.75 and 11 Mev. The self-absorption, T_s , is also readily calculated, and except for the heavy elements, does not change much with energy.* Thus the ratio of the efficiencies may be determined, knowing the products, $N\sigma$, and the approximate values for the intensities, P .

It is convenient to determine the efficiency relative to that at 2.75 Mev., at the lower end of the energy scale, by making use of the γ -ray emitted in the radioactive decay of Na^{24} for it is well known that one photon of this energy is

*Strictly, the variation of the neutron flux along the length of the sample should be taken into account in calculating the ratio of the coefficients, T_s , but calculation shows that it has a negligible effect.

emitted in every disintegration of Na^{24} . If the material which emits the γ -ray to be studied is mixed with a sodium salt, a comparison of the peak counting rate of this γ -ray with that of the sodium γ -ray will give the efficiency relative to 2.75 Mev., provided that the mixture has been irradiated in a constant neutron flux for a sufficient time for the Na^{24} activity to attain radioactive equilibrium with the neutrons producing it.

In the derivation of Equation [20] we have assumed that thermal neutrons only are responsible for the production of the γ -radiation and that the capture cross sections refer to neutrons of these energies. In sodium, and in all the elements used for comparison measurements, resonance activation is negligible, and so the intensities of the capture radiations will certainly be proportional to the thermal neutron capture cross sections.

Direct comparisons of the intensity of neutron capture radiations with that of Na^{24} are difficult to make because the low energy of the latter entails a low peak counting rate, even when kilogram quantities of a sodium compound are used. We have therefore compared only the 9.0 Mev. nickel capture γ -ray directly with sodium. The other elements were compared with nickel, for nickel has a high cross section (4.8 barns), produces a strong coincidence peak near 9 Mev., and relatively few coincidences below this energy (12).

For some comparisons, we mixed the sample material with nickel sesquioxide, Ni_2O_3 . In others, involving weakly absorbing materials, we found it more convenient to use nickel sheets, either with one sheet stuck to the front of the sample and one behind it, or with sheets of nickel sandwiched between slabs of the material to be examined. We made a direct test of the reliability of this method in the case of silicon. When nickel oxide was mixed with silicic acid, and when sheets of nickel were stuck to the front and back ends of the container, the ratios of the quantities ($P\epsilon$) for selected γ -rays from silicon and nickel were found to be identical within the limits of experimental error.

The nickel-sodium ratio was determined from a comparison of the coincidence peaks of the 2.75 Mev. γ -ray with that of the 9.0 Mev. nickel γ -ray using an intimate mixture of a few grams of nickel sesquioxide with a kilogram of sodium fluoride. The prompt γ -radiation due to capture in the vicinity of 2.75 Mev. was studied immediately after installation of the sample and before an appreciable amount of Na^{24} activity had developed. No coincidence peaks above a continuous unresolved background due to capture radiation could be detected in the immediate vicinity of 2.75 Mev. After allowing 24 hr. to elapse for the Na^{24} activity to approach equilibrium with the neutron flux, the 2.75 Mev. peak was plotted. After subtraction of the continuous background, the results at each point in the curve were corrected to infinite irradiation time. As a check, the sodium peak was also plotted immediately after the pile was shut down. The capture cross sections of nickel and of sodium were taken to be 4.8 and 0.54 barns.* Using Equation [20], the results of these measurements gave:

$$[21] \quad \epsilon(9.0) \cdot P/\epsilon(2.75) = 24.4 \pm 1.0$$

*L. Yaffe, private communication. This cross section, which is higher than usually quoted, was obtained recently by an activation method. It is based on a gold cross section of 93 barns and is probably more accurate than those obtained by pile oscillator methods; cf. Pomerance (16).

where P refers to the absolute intensity of the 9.0 Mev. nickel γ -ray. This result does not give directly the efficiency at 9.0 Mev., for the quantity P , in the case of nickel, is not accurately known.

The γ -ray spectra emitted by most elements on neutron capture are too complicated to allow an estimate of P for individual γ -rays and that quantity can only be established when one γ -ray is emitted per capture, or when one strong γ -ray is associated with a few weak ones. The two lead isotopes Pb^{206} and Pb^{207} emit homogeneous γ -rays with energies at 6.73 Mev. and 7.38 Mev. respectively, but only the capture cross section of Pb^{207} is known with sufficient accuracy. Beryllium and carbon produce strong γ -rays with energies of 6.8 Mev. and 4.9 Mev., respectively, and the intensities of these radiations are known to be respectively about 0.75 and 0.70 photon per capture. Furthermore, upper limits for the intensities of the 6.75 Mev. γ -ray from titanium, the 9.0 Mev. γ -ray from nickel, and the 9.3 Mev. γ -ray from iron can be deduced from the capture γ -ray spectra. The efficiencies were measured relatively to the value of ϵP for the nickel γ -ray, and the efficiencies relative to that of the sodium γ -ray were then obtained by multiplying the result by 24.4, Equation [21]. These efficiencies are independent of both P (for nickel) and the value chosen for the nickel cross section. The results are listed in Table IV and plotted in Fig. 17, in which the smooth curve is the fully corrected theoretical curve of Fig. 10,

TABLE IV
MEASURED COUNTING EFFICIENCIES RELATIVE TO THAT AT 2.75 MEV.

Target element	Energy h of γ -ray (Mev.)	Thermal neutron capture cross section	P	$\epsilon(h)/\epsilon(2.75)$
C	4.95	4.5 mb.	0.7	8.9
Ti	6.76	5.6 b.	0.53	38.5
Be	6.81	9.0 mb.	0.75	38.7
Pb	7.38	156 mb.	1.0	49
Ni	9.00	4.5 b.	< 0.55	> 47
Fe ⁵⁴	9.30	2.3 b.	< 0.65	> 57

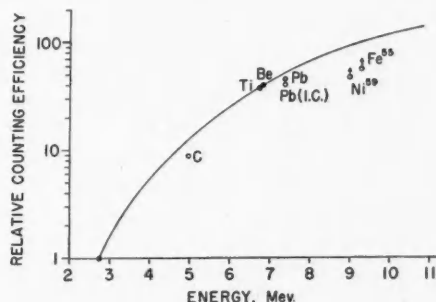


FIG. 17. Experimental counting efficiencies relative to that at 2.75 Mev. The smooth curve is the fully corrected theoretical curve of Fig. 10.

adjusted to unit efficiency at 2.75 Mev. To make these results comparable with the calculated curve, they have all been obtained with $\delta = 0.018$.

The carbon result was obtained by sandwiching nickel sheets (8 mgm. per sq. cm.) between thin disks of graphite, one sheet at either end and two between each disk. The beryllium measurement was made in a similar way, using slabs of exceptionally pure sintered beryllium oxide. Of these two results, that due to carbon is the least satisfactory because of the uncertainty in the value of its capture cross section.

The titanium measurement was made using a mixture of titanium dioxide and nickel sesquioxide. The titanium spectrum consists essentially of two strong γ -rays of comparable intensity and with energies of 6.41 Mev. and 6.76 Mev. and very little other high energy radiation. Since the greater part of the titanium capture cross section (95%) is due to capture of neutrons in Ti^{48} , and assuming that there is no cascade of low energy γ -rays which have escaped detection by the pair spectrometer, it follows that the sum of the values of P for these two γ -rays must be nearly unity. Assuming that this sum is 90% of the neutron capture rate in natural titanium, the value of P for the 6.76 Mev. γ -ray is found to be 0.53. It will be seen that the titanium and beryllium results are in good agreement.

The result for the lead radiation given in Table IV was obtained using a mixture of Pb_3O_4 and nickel sesquioxide. The capture cross section given in the table is the contribution (1) of Pb^{207} to the total capture cross section of natural lead, and, in the absence of any other γ -ray known to be emitted when neutrons are captured by that isotope, the absolute intensity is assumed to be unity.

The counting efficiency for lead radiation has also been measured by a direct method, in which the intensity of the beam of lead radiation was obtained from the ionization current produced in a thick walled ionization chamber. The ionization chamber was calibrated with a radium source, using the figures published by Laurence (13). The intensity of the γ -ray beam, in photons per sq. cm. per sec., was deduced from the ionization current using the figures given by Fowler, Lauritsen, and Lauritsen (3). The absolute counting efficiency of the spectrometer at 7.38 Mev. was deduced from these results after correcting for the presence of the capture radiation produced by Pb^{206} . A similar measurement was made with a source of about 1000 curies of Na^{24} , the ionization current observed being corrected for the effect of the 1.38 Mev. γ -ray. The ratio of the efficiency at 7.38 Mev. relative to that at 2.75 Mev. was 42, in good agreement with the previous result.

Above 8 Mev. we have found no satisfactory way to measure the counting efficiency of the spectrometer. We have determined a minimum value for the efficiency at 9.3 Mev., assuming that the three capture γ -rays ascribed to Fe^{55} (12) are the only γ -rays emitted by that nucleus, and knowing the contribution of Fe^{54} to the total capture cross section of iron. A similar method has been employed to obtain the minimum efficiency at 9 Mev., using the capture γ -rays from Ni^{59} .

We estimate that the probable error in the measured efficiencies near 7 Mev.

relative to that at 2.75 Mev. is about 10%. The efficiency near 5 Mev. is less certain; it may be in error by some 20%. In view of the agreement between the experimental results and the theoretical curve in this energy range, we use that curve as the basis of intensity measurement at all energies.

3.7 Consistency of Intensity Measurements

Some information on the validity of the empirical counting efficiency curve can be obtained by a study of the total energy emitted in neutron capture. If there is no production of long lived isomers, and if internal conversion is negligible, the total energy radiated in neutron capture must be equal to the neutron binding energy of the product nucleus. Let k , be the energy of a γ -ray, r , and let P_r be its intensity, in photons per capture. Then $\sum_r k_r P_r = B$, where B is the neutron binding energy of the product nucleus. Remembering that the pair spectrometer will not detect γ -rays with energies much below 2.5 Mev., it follows that the sums of the products of the energies and intensities of the observed γ -rays must be less than the binding energy B , or

$$[22] \quad S = \sum_r (k_r P_r) / B \leq 1.$$

This equation can be applied only to γ -rays which can be separately resolved. The spectrum produced by neutron capture in most of the lighter elements, however, consists of a series of discrete γ -rays superposed on a continuous background* of unresolved radiation. Equation [22] may be modified to take account of the latter. Let $\nu(k)$ be the number of photons emitted per capture per unit energy range. Then Equation [22] becomes

$$[23] \quad S' = \int_{k_m}^{\infty} \nu(k) k / B dk \leq 1$$

where k_m is the lower limit of the energy range of the measurements.

Let $q(k)$ be the coincidence counting rate corresponding to an energy k . Evidently, $q(k)$ is derived from only those γ -rays for which the energy k' is greater than k . By definition of the counting efficiency ϵ , the peak coincidence counting rate produced by γ -rays of energy k' is proportional to $\nu(k') \epsilon(k')$. The contribution to the counting rate, at energy k , therefore, is given by:

$$q(k) = \text{const.} \int_k^{\infty} \nu(k') \epsilon(k') f(k' - k, k) dk'$$

where the function, $f(k' - k, k)$, traces the shape of the coincidence curve for a homogeneous γ -ray of energy k' , and has the value unity at the peak. To a sufficient approximation, $\epsilon(k') = \epsilon(k)$; if, then, $\nu(k)$ does not vary appreciably over a range of k of the order of the width of a coincidence peak, we can write $\nu(k') = \nu(k)$, and:

$$q(k) = \text{const.} \nu(k) \epsilon(k) A$$

*The continuous background is certainly due to unresolved γ -rays, very little of which generally comes from sources other than the sample. This can be demonstrated by withdrawing the sample. An elementary calculation shows that Compton degraded radiation from the sample is negligible. An additional contribution to this background is produced by unwanted coincidences between an electron or positron entering one counter and annihilation radiation or bremsstrahlung produced in the slit facing the other counter. The effect is difficult to measure; at 8 Mev. it seems to produce a broad peak, about 1 Mev. wide with a maximum at the position of the genuine coincidence peak and about 1% of its height.

where A , the area under a coincidence peak of unit height, is known to be nearly independent of the energy (cf. Fig. 14). The constant in this equation contains the transmission coefficients which appear in Equation [20]. If $q(k_0)$ is the counting rate produced by a homogeneous γ -ray k_0 in the same spectrum, for which the absolute intensity P_0 has been measured by the nickel comparison method,

$$q_0 = \text{const. } \epsilon(k_0) P_0,$$

where the constant has the same numerical value. Thus, $\nu(k)$ can be found from the ratio:

$$[24] \quad \frac{q(k)}{q(k_0)} = \frac{\epsilon(k)}{\epsilon(k_0)} \cdot \frac{T_s(k) T(k)}{T_s(k_0) T(k_0)} \cdot \frac{\nu(k) A}{P_0}.$$

After calculating, from this equation, the corrected γ -ray spectrum, $\nu(k)$, we determined the fraction S' (Equation [23]) for the capture γ -ray spectra emitted by a number of different elements. Some early results, already published (10, 11), were recalculated on the basis of the efficiency curve of Fig. 17 and these results together with those obtained from some new measurements are listed in Table V.

TABLE V

OBSERVED FRACTION OF THE TOTAL ENERGY RADIATED IN NEUTRON CAPTURE RADIATION. THE NEUTRON BINDING ENERGIES MARKED BY ASTERISKS ARE MEAN VALUES CALCULATED WITH THE AID OF RECENT CROSS SECTION MEASUREMENTS OBTAINED BY POMERANCE (16)

Element	σ , barns	δ , %	A , Mev.	B , Mev.	k_m , Mev.	S'
Mg	0.059	1.8	0.18	8.9 *	2.6	0.99
Al	0.212	0.9	0.15	7.7	2.5	0.78
Si	0.13	1.8	0.18	8.5 *	2.5	1.44
P	0.19	1.8	0.18	7.9	2.5	0.66
S	0.49	1.8	0.18	8.6	2.7	0.76
Cl	32.7	1.8	0.18	8.5	3.3	0.26
K	1.89	2.7	0.20	7.8	3.0	0.48
Ca	0.40	1.8	0.18	8.4	2.6	0.80
Ti	5.6	0.9	0.15	8.1	2.4	1.02
V	4.7	0.9	0.15	7.2	2.6	0.82
Cr	2.90	0.9	0.15	9.65*	2.8	0.73
Mn	12.6	0.9	0.15	7.25	3.5	0.64
Fe	2.43	0.9	0.15	7.7 *	3.0	0.78
Co	34.8	0.9	0.15	7.5	2.5	0.67
Ni	4.80	0.9	0.15	9.1 *	3.4	0.95
Cu	3.59	0.9	0.15	7.9	3.4	0.67
Zn	1.06	0.9	0.15	8.0	2.8	0.60

Apart from the error introduced by the counting efficiency curve, the greatest source of error in the determination of the fraction S' is the value of the area A , which has been assumed to be independent of the γ -ray energy. Owing to the complexity of neutron capture radiation we have not been able to measure the area under coincidence peaks at intermediate energies and we have been obliged therefore to use the area under the 9 Mev. nickel coincidence peak. The quantity taken for A may be too small by as much as 20% since we were not able to

estimate the contribution from the unwanted coincidences due to the annihilation and bremsstrahlung effect previously mentioned.

Except for silicon and chlorine the values of S' listed in Table V are those to be expected. The chlorine discrepancy has been discussed elsewhere (11); the high value for silicon was obtained after making a large correction for the measured background radiation generated in the bismuth block and in the collimators and it is possible that the discrepancy for this element is due partly to the difficulty of making a satisfactory correction for this effect. The low value obtained for potassium is to be expected in view of the large amount of low energy radiation emitted by that element.

3.8 Counting Efficiency Curves for Other Slit Widths

The peak coincidence counting rate, for small slit widths, increases very rapidly with increasing width, at first nearly as the cube and then less rapidly. This is shown in Fig. 18 in which the experimental points follow the general trend of the broken line, obtained from the peak shape calculation at 8 Mev.

The ratio of the peak coincidence counting rates to that for 2 mm. is plotted as a function of the energy in Fig. 19. The results for 2.75 Mev., which have been carefully made under very good conditions, show a significant departure

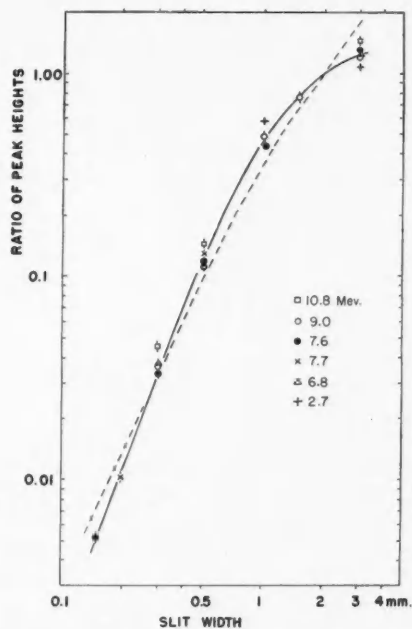


FIG. 18. Full line: experimental ratios of the peak coincidence counting rate to that obtained with 2 mm. slits as a function of the slit width. Broken line: from calculations made at 8 Mev.

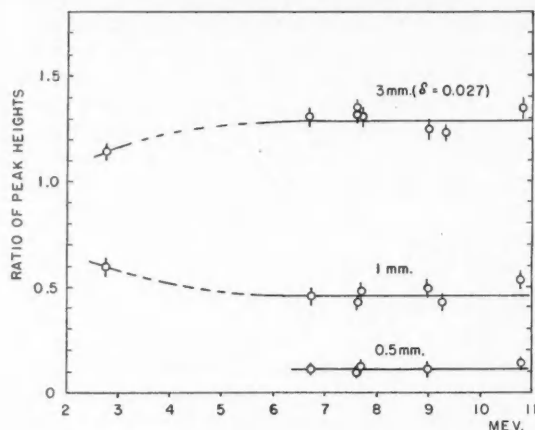


FIG. 19. Ratio of the peak coincidence counting rate to that obtained with 2 mm. slits ($\delta = 0.018$) as a function of the γ -ray energy.

from the constant values obtained at higher energy. Therefore, the use of the efficiency curve at any slit width other than that appropriate to Fig. 17 will lead to errors at low energies.

3.9 Absolute Counting Efficiency

As already described, the absolute counting efficiency of the spectrometer has been measured at 2.75 and at 7.38 Mev., the strength of the γ -ray beam near the radiator being measured with a thick-walled ionization chamber. In Table VI the measured peak counting rate per photon incident on unit area of the

TABLE VI
ABSOLUTE PEAK COUNTING EFFICIENCY IN COINCIDENCES PER PHOTON INCIDENT ON THE RADIATOR

Energy, Mev.	Calculated from Equation [13]	Measured
2.75	4.6×10^{-9}	2.6×10^{-9}
7.38	2.4×10^{-7}	1.1×10^{-7}

radiator is compared with an interpolation of the results of Table I. In these measurements, the slits were 2.86 cm. long, the slit width was defined by $\delta = 0.018$, and the gold radiator thickness was 4.7 mgm. per sq. cm. It will be seen that the calculated efficiencies are rather higher than those determined experimentally. This is to be expected from the crude method of integration employed (Equation [13]). It is evident that the absolute efficiency of the spectrometer is indeed very low and it is obvious from Table VI that this instrument can be used successfully only when exceptionally strong sources of γ -radiation are available.

4. ACKNOWLEDGMENTS

We are greatly indebted to Dr. J. D. Jackson for checking some of our calculations of the counting efficiency, and for numerous discussions on the theoretical aspects of the pair spectrometer; to Mr. G. Likely for theoretical calculations and for the simplification of the formula of Equation [9]; and to the staff of the computing section for help in numerical computations. We are also much indebted to Mr. W. H. Walker for help in the development of the apparatus in its early stages; to Mr. J. W. Gregory for the design of the electromagnet and for supervision of its construction; to Mr. W. McAlpin for the design of the vacuum chamber and slit system of the improved spectrometer; to Mr. R. R. MacLanders for technical help; and to Mr. G. J. R. MacLusky for design of some electronic apparatus.

5. APPENDIX

5.1 Limiting Angles for Slits of Zero Thickness

It has been shown that the range of polar angles available to the components of a pair which can produce a coincidence from a point radiator midway between the slits is given by:

$$[1] \quad \cos \theta = \frac{eH}{2pc} y$$

in which y can take any value between d and $d + a$ and the momentum p is restricted by the relation $0 < z < w$, where $z = |(p - p_0)/p_0|$ is the fractional momentum displacement and $w = (H_0 - H)/H_0$ is the fractional displacement of the magnetic field. At the upper limit of the field for which coincidences can be obtained,

$$[3] \quad p_0 = \frac{eH_0}{2c} d.$$

Combining these equations:

$$\cos \theta = \frac{H}{H_0} \frac{p_0}{p} \frac{y}{d} = \frac{(1 - w) y}{(1 \pm z) d}$$

in which the plus sign refers to the pair component with higher momentum and the minus sign to the component with lower momentum. By substituting the limits of y we obtain the limiting values of $\cos \theta$ for the two components. Let α_1 and α_2 be the lower and upper limits of θ for the high momentum component and β_1 and β_2 those for the low momentum component. Then ignoring terms of second order:

$$[25] \quad \begin{aligned} \cos \alpha_1 &= 1 - w - z + \delta, \\ \cos \alpha_2 &= 1 - w - z, \\ \cos \beta_1 &= 1 - w + z + \delta, \\ \cos \beta_2 &= 1 - w + z. \end{aligned}$$

Values of the cosine which are greater than unity have no meaning and therefore, in Table VII the angular limits are classified according to the range of w per-

TABLE VII
LIMITS OF INTEGRATION

w	α_1	α_2	β_1	β_2
$z < w < (\delta - z)$	0	B	0	D
$(\delta - z) < w < (\delta + z)$	0	B	C	D
$(\delta + z) < w$	A	B	C	D

mitted by fixed values of z and δ . For the sake of brevity we use the notation:

$$A = \cos^{-1}(1 - w - z + \delta), \quad B = \cos^{-1}(1 - w - z),$$

$$C = \cos^{-1}(1 - w + z + \delta), \quad D = \cos^{-1}(1 - w + z).$$

5.2 Limiting Angles for Slits of Finite Thickness

Consider the projection on the Y - Z plane of a trajectory with $\phi_+ < \pi/2$ (Fig. 20). It is clear that while the lower limit for y remains equal to d as before,

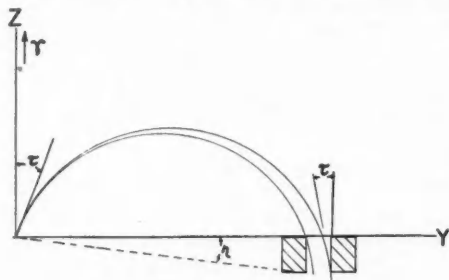


FIG. 20.

the upper limit now becomes $(d + a - d\eta\tau)$ approximately, where τ is the angle between the Z -axis and the component of momentum in the Y - Z plane for the trajectory which just grazes the outer edge of the slit and η is the angle subtended by the thickness of the slit at the origin. For the high momentum component, the equations corresponding to Equation [25] in §5.1 then become:

$$\cos \alpha'_1 = 1 - w - z + \delta - \eta\tau,$$

$$\cos \alpha'_2 = 1 - w - z$$

where the primes indicate the new limiting angles. The angle τ is given by the relation:

$$\tan \tau = \sin \phi_+ \tan \alpha'_1$$

where ϕ_+ is the azimuthal angle referred to in Fig. 2. Since we are concerned only with particles projected at small angles to the γ -ray direction, we can write:

$$\tau = \alpha'_1 \sin \phi_+.$$

The presence of ϕ in this equation presents serious difficulties, which may be removed only by considering the special case in which $\phi_+ = \pm \pi/2$. For $\phi_+ = \pi/2$,

$$\begin{aligned}\tau &= \alpha'_1, \\ \cos \alpha'_1 &= 1 - w - z + \delta - \eta \alpha'_1, \\ \cos \alpha'_2 &= 1 - w - z, \text{ etc.}\end{aligned}$$

whence new limits are given approximately by the equations:

$$\begin{aligned}\alpha'_1 &= \alpha_1 + \eta, & \beta'_1 &= \beta_1 + \eta, \\ \alpha'_2 &= \alpha_2, & \beta'_2 &= \beta_2,\end{aligned}$$

in which the lower limits have been increased by the angle η , the upper limits remaining unchanged. If the positron is emitted when $\phi_+ = -\pi/2$, a little consideration will show that the lower limits now remain unchanged, while the upper limits are increased by the angle η . It follows that the integral of Equation [15] for slits of finite thickness should be replaced by:

$$\begin{aligned}[26] \quad \phi &= \pi: \frac{1}{2} \left[\int_{\alpha_1+\eta}^{\alpha_1} \int_{\beta_1+\eta}^{\beta_1} f d\theta_+ d\theta_- + \int_{\alpha_1}^{\alpha_1-\eta} \int_{\beta_1}^{\beta_1-\eta} f d\theta_+ d\theta_- \right], \\ \phi &= 0: \frac{1}{2} \left[\int_{\alpha_1+\eta}^{\alpha_1} \int_{\beta_1}^{\beta_1-\eta} f d\theta_+ d\theta_- + \int_{\alpha_1}^{\alpha_1-\eta} \int_{\beta_1+\eta}^{\beta_1} f d\theta_+ d\theta_- \right],\end{aligned}$$

where the α 's and β 's are given in Table VII, and where it is understood that the lower limits of integration are zero when the corresponding limits are zero in Table VII.

The error introduced in the correction term $\eta\tau$, by setting $\tau = \alpha'_1$, is largest at small values of w , for in this region of field strength, the main contribution to the coincidence counting rate comes from pairs projected with polar angles less than the critical angle 0.21 radian. At larger values of w the important contribution to the counting rate is made by pairs projected into angles greater than 0.21 radian, and, in this case, the assumption that $\phi_+ = \pm \pi/2$ is a better approximation. The error in the calculated peak shape due to this approximation will therefore be small at low values of w (because the correction $\eta\alpha'$ is small), greatest at intermediate values, and small again at large values of w . Since the peak coincidence counting rate appears at rather low values of w for all γ -ray energies, this approximation does not lead to a large error in the calculated counting efficiency curve.

REFERENCES

1. AITKEN, K. L., LITTLER, D. J., LOCKETT, E. E., and PALMER, G. H. *Proc. Phys. Soc. (London)*, A, 65: 761. 1952.
2. DUMOND, J. W. M. and COHEN, E. R. *Phys. Rev.* 82: 555. 1951.
3. FOWLER, W. A., LAURITSEN, C. C., and LAURITSEN, T. *Revs. Modern Phys.* 20: 236. 1948.
4. GROSHV, L. V. *J. Phys. (U.S.S.R.)*, 5: 115. 1941.
5. GROSHV, L. V. and FRANK, I. M. *Compt. rend. acad. sci. U.S.S.R.* 20: 273. 1938.
6. GROSHV, L. V. and FRANK, I. M. *Compt. rend. acad. sci. U.S.S.R.* 24: 239. 1941.
7. HARTREE, W. *Proc. Cambridge Phil. Soc.* 21: 746. 1923.
8. HEITLER, W. *The quantum theory of radiation.* Oxford at the Clarendon Press. 1944.
9. JAEGER, J. C. and HULME, H. R. *Proc. Roy. Soc. (London)*, A, 153: 443. 1935.
10. KINSEY, B. B., BARTHOLOMEW, G. A., and WALKER, W. H. *Phys. Rev.* 83: 519. 1951.
11. KINSEY, B. B., BARTHOLOMEW, G. A., and WALKER, W. H. *Phys. Rev.* 85: 1012. 1952.
12. KINSEY, B. B. and BARTHOLOMEW, G. A. *Phys. Rev.* 89: 375. 1953.
13. LAURENCE, G. C. *Can. J. Research*, A, 15: 67. 1937.
14. MAXIMON, L. C. and BETHE, H. A. *Phys. Rev.* 87: 156. 1952.
15. MOBLEY, R. C. and LAUBENSTEIN, R. A. *Phys. Rev.* 80: 309. 1950.
16. POMERANCE, H. *Phys. Rev.* 83: 641. 1951; 88: 412. 1952.

17. SIMONS, L. and ZUBER, K. Proc. Roy. Soc. (London), A, 159: 383. 1937.
18. STRAIT, E. N., VAN PATTTER, D. M., BUECHNER, W. W., and SPERDUTO, A. Phys. Rev. 81: 747. 1951.
19. THOMAS, H. A. Phys. Rev. 80: 901. 1950.
20. THOMAS, H. A., DRISCOLL, R. L., and HIPPLE, J. A. Phys. Rev. 78: 787. 1950.
21. VAN PATTTER, D. M., SPERDUTO, A., ENDT, P. M., BUECHNER, W. W., and ENGE, H. A. Phys. Rev. 85: 142. 1952.
22. WALKER, R. L. and MCDANIEL, B. D. Phys. Rev. 74: 315. 1948.
23. WOLFSON, J. L. Phys. Rev. 78: 176. 1950.

AN ISOLATING POTENTIAL COMPARATOR¹

By T. M. DAUPHINEE

ABSTRACT

A circuit is described by which electromotive forces can be compared accurately without making any direct electrical connection between them. A double-pole, double-throw chopper, having a condenser connected between the vibrating contacts, is used with a galvanometer or electronic amplifier to indicate any inequality between the e.m.f.'s without allowing any net flow of current between the circuits. Polystyrene condensers and mechanically driven choppers are used to minimize leakage and pickup problems.

Potentiometric measurements may be made through this "isolating potential comparator" to $\pm 0.1 \mu\text{v}$. The error due to potential difference between the circuits is about 10^{-6} of the difference for 100 ohm circuits. An analysis of the method is given and optimum condenser and galvanometer characteristics determined. Magnitude and elimination of errors are discussed.

The comparator is suitable for measurement or control of e.m.f. differences between thermocouples which are electrically connected through the tips. It also has many applications in resistance measurement and resistance thermometry.

INTRODUCTION

There are many occasions in Physics when one wishes to make an accurate comparison of two e.m.f.'s or potential differences but is unable to do so because the sources cannot be connected directly into the same measuring circuit. This problem occurs whenever the two e.m.f.'s arise at different parts of the same electrical network and some known or unknown potential difference is maintained between them by other circuit connections. For instance, we cannot, by present techniques, make a direct measurement of the difference in e.m.f. of two thermocouples which are connected at the tips to the same piece of metal or to one another, even when this difference is relatively small and constant or slowly varying. Nor can we make a direct comparison of the voltage drops across two potential lead resistors when they are connected in series, although this would greatly simplify resistance measurements where lead resistance is a significant factor as in resistance thermometry (2).

We can, however, compare our two e.m.f.'s or potential differences indirectly by the use of some intermediate e.m.f. which can be compared directly with either one. In practice, the intermediate e.m.f. usually has the form of some manually adjusted measuring instrument such as a potentiometer, but anything that can be made to take on exactly the same voltage as the first of the e.m.f.'s to be compared and hold it long enough for comparison to be made with the other will do equally well. Moreover, we only require a null indicator for equality between the two circuits because it is always possible to insert in one potential lead a known e.m.f. which may be adjusted until the indicator reads zero.

Present methods of meeting this problem are slow and frequently require considerable voltage or current stability (3). They are, therefore, funda-

¹ Manuscript received January 2, 1953.

Contribution from the Division of Physics, National Research Council, Ottawa, Canada.
Issued as N.R.C. No. 2965.

mentally unsuited for any measurement where the two e.m.f.'s are varying quantities, since the errors introduced are essentially proportional to the length of time required to make the measurement and the rate of change of the e.m.f.'s being compared.

In the following pages a new method is described by which the effective period of comparison may be reduced to a few hundredths of a second. Comparison of two e.m.f.'s at an appreciable potential difference from one another may then be made with almost the same facility and accuracy as if they were connected together into the same potentiometer circuit.

METHOD

Reduction of the time constants of the apparatus has been accomplished by making two basic changes. The manually adjusted intermediate e.m.f. is replaced by the voltage across a large condenser, and the usual manual switching mechanism is replaced by a mechanically driven double-pole, double-throw chopper (vibrator converter). The condenser is connected between the vibrating contacts which are of the break-before-make type. The basic circuit is shown in Fig. 1. The process is as follows.

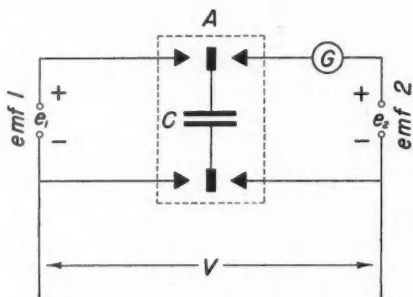


FIG. 1. The isolating potential comparator circuit.

Operation of the chopper connects the condenser first to e.m.f. 1, causing it to charge to voltage e_1 . The chopper contacts now open, and then close on the other side, connecting the condenser *with the same polarity* to e.m.f. 2 through the galvanometer G . If e_1 is equal to e_2 the total e.m.f. around the loop is zero and no current flows. However, if e_1 is *not* equal to e_2 the condenser charges or discharges through the galvanometer until it has the value e_2 . The condenser is then transferred back to e.m.f. 1, and the whole process is repeated many times a second. The net result of the inequality between e_1 and e_2 is that a series of current pulses *always in the same direction* passes through the galvanometer which thus behaves as a null indicator. Since there is no time during the cycle when a direct connection exists between the two circuits, it is possible to maintain appreciable potential differences between them without affecting the balance. At balance, there is no current flowing in any of the potential leads and the resistance of these leads is completely eliminated from

the result as in all true potentiometric comparisons. We have called the electrical loop through the choppers, the galvanometer, and the two e.m.f.'s an "isolating potential comparator."

In an actual circuit, conditions will be slightly different from the ideal conditions of the foregoing discussion. The sources of e.m.f., the galvanometer, and the chopper will have some resistance and charging and discharging of the condenser will have associated time constants. However, the basic concepts of the discussion are not affected, while at balance there is no net current flow and resistance is not a factor.

DISCUSSION

Let us consider the characteristics of operation we might expect from an "isolating potential comparator" with a view to determining the optimum operating conditions.*

The Change in Condenser Voltage

When the chopper contacts are closed on the side of e_2 ,

$$[1] \quad i_2 = C d\epsilon/dt = -(\epsilon - e_2)/R_2.$$

Integrating and using conditions $\epsilon = e_1$ at $t = 0$, $\epsilon = e_2$ at $t = t_2$ (e_2 constant),

$$[2] \quad e_2 - e_2 = (\epsilon_1 - e_2) \exp(-t_2/R_2C).$$

Similarly,

$$[3] \quad e_1 - e_1 = (\epsilon_2 - e_1) \exp(-t_1/R_1C).$$

Therefore,

$$[4] \quad \Delta\epsilon = \epsilon_1 - \epsilon_2 = \frac{\Delta e(1 - \exp(-t_1/R_1C))(1 - \exp(-t_2/R_2C))}{1 - \exp(-t_1/R_1C - t_2/R_2C)}.$$

Equation [4] may also be put in the more useful form

$$[5] \quad \Delta\epsilon = 2\Delta e / \left(\coth \frac{t_1}{2R_1C} + \coth \frac{t_2}{2R_2C} \right).$$

Galvanometer Current

The current I_g being transferred through the galvanometer is

$$[6] \quad I_g = fC\Delta\epsilon = 2fC\Delta e / \left(\coth \frac{t_1}{2R_1C} + \coth \frac{t_2}{2R_2C} \right).$$

If R_1 and R_2 are fixed and t_1 and t_2 are variable (but $t_1 + t_2$ constant), the sensitivity has a maximum when

$$[7] \quad \sinh \frac{t_1}{2R_1C} / \sinh \frac{t_2}{2R_2C} = \sqrt{\frac{R_2}{R_1}}.$$

* The following symbols have been used throughout the discussion: e_1, e_2 , the e.m.f.'s to be compared; $\Delta e = e_1 - e_2$; f , the chopper frequency; t_1, t_2 , the length of time the condenser is connected to e_1 or e_2 ; $T = t_1 + t_2$, total closed time of the chopper (per cycle); $\alpha = T \times 1/f$ = proportion of time that chopper contacts are closed; C , capacity of the condensers; ϵ , voltage across the condenser; ϵ_1 , voltage across the condenser after connection to e_1 but before connection to e_2 ; ϵ_2 , voltage across the condenser after connection to e_2 but before connection to e_1 ; $\Delta\epsilon = \epsilon_1 - \epsilon_2$, voltage swing of the condenser; i_1, i_2 , current while connected to e_1, e_2 ; R_1, R_2 , resistance of the circuit (including galvanometer and chopper) when connected to e_1 or e_2 .

If t_1 and t_2 are fixed and R_1 and R_2 variable (R constant), the maximum occurs when

$$[8] \quad \sinh \frac{t_1}{2R_1C} / \sinh \frac{t_2}{2R_2C} = R_2 \sqrt{t_1} / R_1 \sqrt{t_2}.$$

If both resistance and time can be varied, the greatest sensitivity occurs for greatest unbalance between the two sides. (See Fig. 2 (a, b, c).)

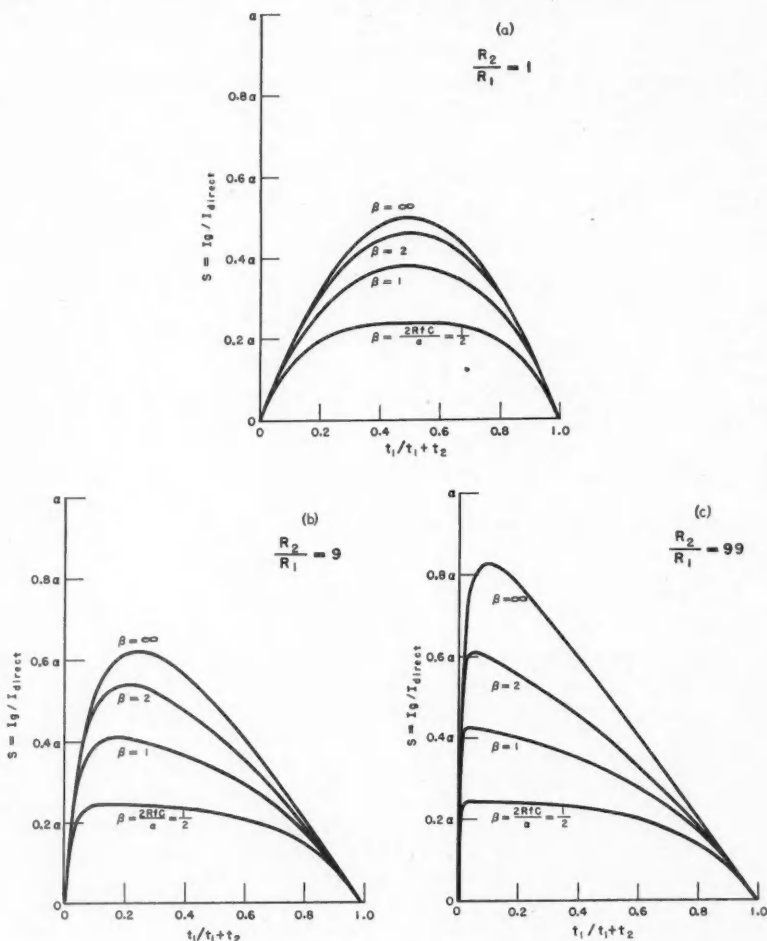


FIG. 2. The effect of resistance, time distribution, and capacity on galvanometer sensitivity as calculated from equation [6]:

(a) $R_2/R_1 = 1$,

(b) $R_2/R_1 = 9$,

(c) $R_2/R_1 = 99$.

The ratio, S , of sensitivity through the chopper circuit to sensitivity through a direct connection is

$$[9] \quad S = \frac{I_g}{I_{\text{direct}}} = 2RfC / \left(\coth \frac{t_1}{2R_1C} + \coth \frac{t_2}{2R_2C} \right)$$

if we assume the chopper circuit resistance may be neglected. In the case where $R_1 = R_2$ and $t_1 = t_2 = \alpha/2f$ equation [9] becomes

$$[10-a] \quad S = RfC \tanh \frac{\alpha}{2RfC}$$

and approximately 75% of maximum response is given by the condition

$$[10-b] \quad 2RfC = \alpha$$

with

$$[10-c] \quad S \approx 3\alpha/8.$$

For a 100 ohm circuit with $\alpha = \frac{2}{3}$ and $f = 40$ c.p.s. the required value of C as given by equation [10-b] is $83 \mu f$. In this case the sensitivity is approximately one quarter of that obtained with a direct connection. Actually, a galvanometer with different damping characteristics is now required since the effective resistance of the circuit is increased to about $4R$.

For convenience in studying the effect of resistance, time distribution, and condenser size, the sensitivity is plotted as a function of resistance, time, and capacity in Figs. 2 (a, b, c).

The Effect of Rate of Change of e.m.f.'s

If e_1 and e_2 are varying at the same rate, namely de/dt , the discharge current I_d through the galvanometer will be approximately

$$[11] \quad I_d \approx \frac{1}{2} C \cdot de/dt$$

while the current arising from a given minimum unbalance, Δe_m , is given by

$$[12] \quad I_g \approx 3\alpha\Delta e_m/8R \approx \frac{3}{4}fC\Delta e_m$$

(for the case where $2RfC = \alpha$, $R_1 = R_2$, and $t_1 = t_2$). The maximum permissible value for de/dt if the error does not exceed Δe_m is

$$[13] \quad \frac{de}{dt_{\text{max}}} = \frac{3}{2}f \Delta e_m.$$

For $C > \alpha/2Rf$ the permissible rate of variation is less while for $C < \alpha/2Rf$ it is slightly increased.

Equation [13] indicates that in a balance requiring 10 sec. to complete ($f = 40$ c.p.s.) the values of e_1 and e_2 may vary by about 600 times the permissible error of the difference measurement during the measuring period. In terms of thermocouple thermometry, it would in principle be possible to measure a constant difference in temperature between two points on a piece of metal to 0.1°C . while the temperature of the piece was changing by 360°C . per min.

The Effect of Circuit Imperfections

The preceding discussion assumes that the condenser is a perfect one and this is, of course, not the case. It may let appreciable current leak through, or fail to discharge completely and immediately. About half of any leakage current passes through the galvanometer and this must be less than the current flowing for the smallest significant unbalance Δe_m . This will be true if

$$[14] \quad R_c > 2 \times 10^n R,$$

that is, if

$$[15] \quad R_c C > 10^n \alpha / f,$$

where R_c is the leak resistance of the condenser and n is the number of significant figures required for e_1 and e_2 . At 40 c.p.s. the condenser leak resistance must be at least 20,000 megohm-microfarads to get six significant figures. Paper condensers have a nominal resistance around 8000 megohm-microfarads, enough for about five figure accuracy, but 10 or 25 D.C.W.V. polystyrene condensers are now available with leak resistances greater than 250,000 megohm-microfarads, sufficient for seven figures without correction.

The most serious objection to paper condensers arises from their inability to charge or discharge completely as soon as a new voltage is applied. Charge which has built up within the dielectric material leaks off slowly after the initial pulse of current, and greatly hampers precision readings. Polystyrene condensers do not suffer from this disability and are highly desirable wherever five figures or more are required.

An effect which must not be overlooked is caused by stray capacity to ground (C_g) of the condensers, their lead wires, and the vibrating contacts of the chopper. With each transit the potential of this part of the circuit is changed by any potential difference (V) which exists between corresponding contacts on the two sides. Stray capacity causes leakage from one side of the chopper to the other, introducing an error which could be as much as

$$[16] \quad \Delta e = 8 R f C_g V / 3.$$

For a 100 ohm circuit with $f = 40$ c.p.s. and $C_g = 100$ pf.

$$[17] \quad \Delta e \approx 10^{-6} V$$

but a first order correction can easily be made.

The Effect of a-c. Pickup

In almost all practical circuits there will be a few microvolts (often considerably more) of a-c. mains frequency pickup. A chopper driven synchronously with the mains may rectify this pickup, while a nonsynchronous chopper gives beats with mains frequency or its harmonics. However, it should not be difficult to find frequencies giving beats too rapid for the galvanometer to follow (about five per second, or more).

Variations of the Circuit

When the potential difference between the circuits is constant but larger than the e.m.f.'s to be compared, the effect of capacity to ground can be re-

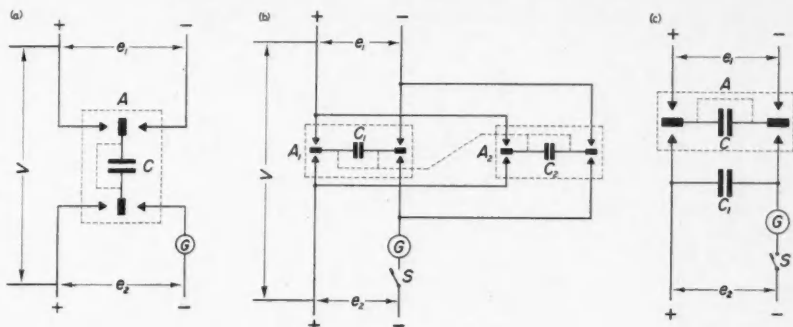


FIG. 3. Variations of the isolating potential comparator circuit:
 (a) Circuit for V large but constant.
 (b) Circuit utilizing two chopper units in parallel for doubled sensitivity.
 (c) Circuit for use when large resistances can be grouped on one side.

duced by use of the circuit of Fig. (3-a). The condenser is connected between corresponding points on the two circuits, which must be joined by some other connection of reasonably low resistance.

The available sensitivity of the circuit may be doubled by the use of two condenser and two chopper units operating synchronously and 180° out of phase (Fig. 3-b). One condenser charges on one side while the other discharges on the other and then the two exchange positions. Since the effective open circuit time of the galvanometer is halved by this connection, somewhat less difficulty with a-c. pickup would be expected.

If high resistance elements occur in the circuits there is a definite advantage in grouping them all on one side of the chopper. Sensitivity practically equal to that for direct connection may then be obtained if condensers matched to the low resistance side of the circuit are used, as in Fig. 3-c, (C_1 being on the high resistance side). The effect of capacity to ground and condenser leakage is then comparable to that for a balanced circuit with the resistance on each side equal to that of e_1 .

EXPERIMENTAL

A wiring diagram of the circuit used to test the characteristics of the isolating potential comparator is shown in Fig. 4. Two potentiometers P_1 and P_2 (Rubicon Type B) represented the sources of e.m.f. e_1 and e_2 while a third potentiometer P_3 (also Type B) maintained any desired potential difference (V) between the two circuits. The contacts of chopper A were adjusted to give a short period in each transit when both moving contacts were open circuited. A polystyrene dielectric condenser C was connected between the moving contacts and indication was provided by a high sensitivity galvanometer, G. Switches S_1 , S_2 , and S_3 were copper knife switches while switch S was an all copper, push button type switch with lockdown and release mechanism.

The condenser C used for these tests consisted of from two to ten $10\ \mu\text{f.}$, 10 D.C.W.V., polystyrene dielectric condensers in metal cans. Each $10\ \mu\text{f.}$

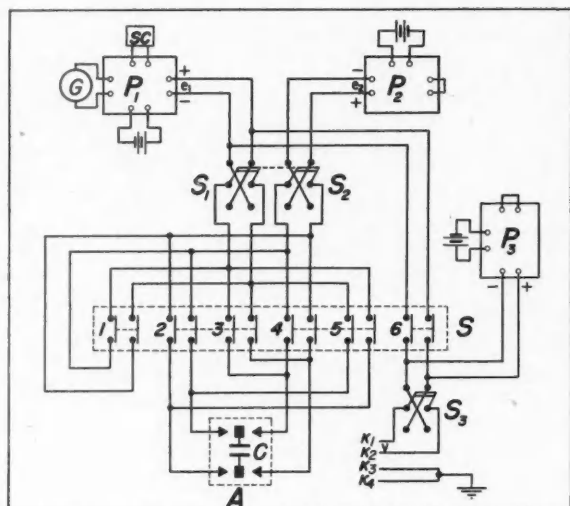


FIG. 4. The circuit used to investigate the properties of the isolating potential comparator.

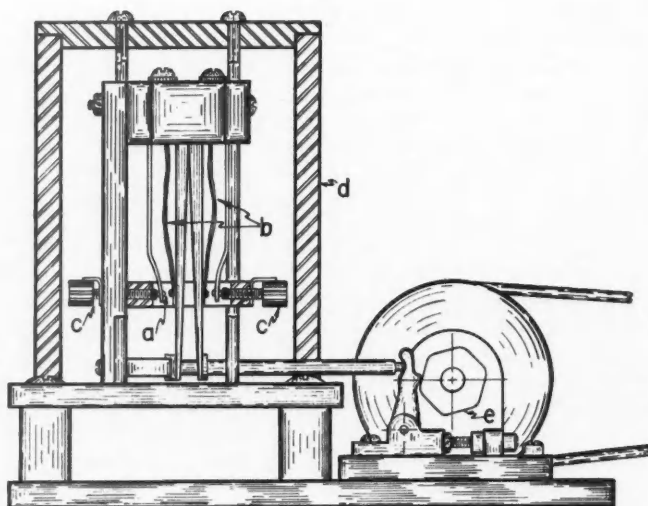


FIG. 5. The chopper.

condenser was roughly $3\frac{1}{4}$ in. \times $2\frac{1}{4}$ in. \times $4\frac{3}{4}$ in.* in size and was mounted on 2 in. bakelite feet to reduce capacity to ground.

Construction details of the chopper are shown in Fig. 5. Two double throw sections of the type shown were driven by the same cam and a second chopper, driven from the same shaft, could be used as a demodulator for an electronic amplifier. The chopper circuit was all copper with the exception of gold contacts (*a*). Flexible copper braid (*b*) gave electrical connection with the moving contacts. Drive was provided by cam, follower (*f*), and pushrod (*g*). The contacts were set (to give $t_1 = t_2$) by means of screws (*c*). The whole contact unit was covered by a soft iron magnetic shield (*d*) which also helped to maintain thermal equilibrium.

Galvanometer Sensitivity

Comparisons of galvanometer sensitivity with direct connection and with the chopper circuit are shown in Fig. 6 and the effect of variation of capacity is shown in Fig. 7. It will be noted from Fig. 6 that careful setting of the chop-

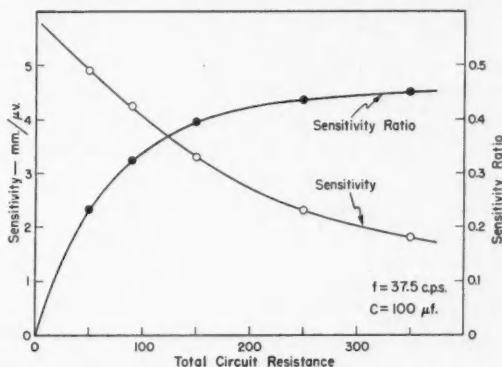


FIG. 6. The effect of total circuit resistance on galvanometer sensitivity. The circles represent galvanometer sensitivity when used with the isolating potential circuit. The dots represent the ratio of sensitivity through this circuit to sensitivity in direct connection.

pers has achieved a sensitivity ratio of 0.45 which corresponds to 10% transit time.

A good check of the reliability of the sensitivity equation

$$[10-a] \quad S = RfC \tanh \frac{\alpha}{2RfC}$$

is shown in Fig. 7 by the excellent agreement between the actual measured values and the solid line which represents an equivalent equation.

Galvanometer sensitivity was doubled when two choppers and two condensers were used (Fig. 3-b) provided that sufficient condensers were available to satisfy the equation

* Somewhat smaller polystyrene condensers are now available commercially at approximately one dollar per microfarad.

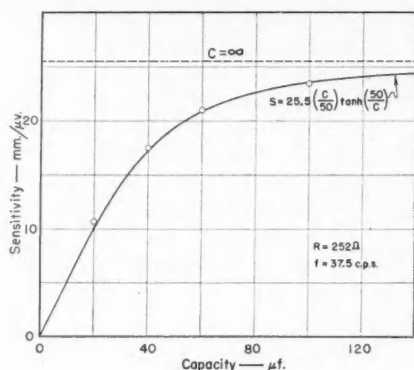


FIG. 7. The effect of capacity on galvanometer sensitivity. The circles represent measured values for 37.5 c.p.s. on a 252 ohm circuit with 32 ohm unbalance between the two sides. The solid line is an equation in the form of [10-a] with constants determined from the measurements.

[10-b]

$$2 RfC = \alpha$$

for both choppers. Considerably smoother operation and less pickup resulted from this connection. However, no great benefit resulted from splitting the capacitance when the capacity available was already too small to satisfy [10-b].

Accuracy with Small Potential Difference

The accuracy for small potential difference between the circuits was determined by making a balance with direct connection and then transferring the connections to the chopper circuit. A new balance was then made or the unbalance determined by galvanometer deflection.

Once thermal equilibrium was reached in the chopper, settings were accurate without correction to at least 2 parts in 10^7 or $0.1 \mu\text{v.}$, whichever was greater. Ground connections which did not create a potential difference between the two sides had a barely detectable effect on the balance (about $0.01 \mu\text{v.}$).

The Effect of a Potential Difference Between the Circuits

The effect of potential difference was determined by making a balance and then applying a voltage (P_s) between various points on the two circuits and observing, either by rebalancing or by deflection, the discrepancy created.

Two representative sets of readings illustrating the variation of P.D. error and current transferred under different conditions are shown in Fig. 8. The P.D. error does not approach zero for $R = 0$ because of the sensitivity limitation arising from the finite value of C , but may be kept below 10^{-6} of the P.D. for circuit resistances below 100 ohms. Calculation of the effective capacity to ground from the current transferred gives a value around 100 pf. This is quite reasonable since no great pains were taken to reduce capacitive effects in the chopper. Grounding the condenser cans resulted in a great increase in error current while a 30% increase resulted from grounding the base of the chopper. For large circuit resistance the error is roughly pro-

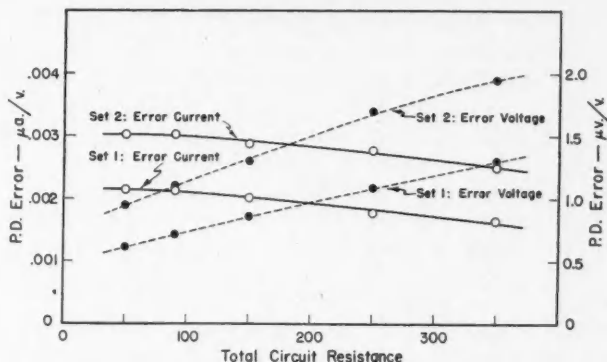


FIG. 8. The error caused by a difference in potential (V) between the two sides of the circuit. In the second set of measurements the base of the chopper was grounded and slightly less care was taken to reduce capacitive effects.

portional to frequency. Changing the points at which the P.D. was applied had negligible effect.

The Effect of a-c. Pickup

A-c. pickup caused large regular galvanometer swings whenever the beat with the mains frequency (60 c.p.s. and some subharmonics and harmonics) had a period greater than about one second. However, no difficulty was encountered in locating frequencies where the beat was too fast for the galvanometer to follow. Most of the measurements described here were carried out at or near 38 c.p.s. Somewhat more care in frequency selection was required for electronic amplifiers. However, an amplifier built in this laboratory has been used with the input circuit of Fig. 9 for null detection down to $0.05 \mu\text{V}$., and some commercial amplifiers and recording potentiometers can be used in place of the galvanometer although special input filtering or the circuit of Fig. (3-c) may be needed.

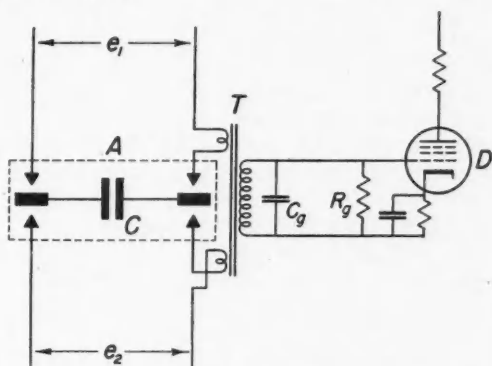


FIG. 9. An input circuit used with an electronic amplifier.

Approximate Limits of Less Refined Equipment

Several preliminary sets of equipment were tried. Some limits of performance are given as a guide where maximum precision is not required.

Case 1. Paper condensers and two Leeds and Northrup type 3338-10 converters (magnetic drive) used as chopper.

When the converters were driven at mains frequency the balance agreed with direct measurements to about $\pm 50 \mu\text{v}$. The error was quite strongly a function of the size of loops in the lead wires and of nearby transformers, etc. If the converters were driven at about 70 c.p.s. with the driving transformer at a distance the balance could usually be made to $\pm 2 \mu\text{v}$. on a 200 ohm circuit. Error from potential difference was 2×10^{-6} of the P.D.

Case 2. Paper condensers and a mechanically driven 38 c.p.s. chopper of the vibrating reed type—gold contacts.

If the paper condensers were never given more than a few millivolts charge, balances could be taken to $\pm 0.2 \mu\text{v}$. If the condensers were subjected to higher voltages minutes or even hours were required before they stabilized once more. The effect of potential difference was roughly the same as in the final apparatus. Condenser leakage and delayed discharging limited balances to five figures at best, but four figure balances were in most cases quite satisfactory above a few microvolts minimum balance. Cooling the condensers to increase leak resistance only aggravated slow discharge and charge problems while heating to accelerate discharge reduced the leak resistance seriously.

Summary of Results

The results of these measurements are summarized below. Accuracies listed are minimum ones which should ultimately be exceeded and apply to chopper frequencies around 40 c.p.s.

1. Galvanometer sensitivity is approximately one third of sensitivity for direct connection where $2RfC = \alpha$, and in general is consistent with equation [10-a]

$$S = RfC \tanh (\alpha/2RfC).$$

This sensitivity may be doubled by using two choppers and two condensers with 180° phase difference.

2. When the P.D. is small, comparisons may be made to $\pm 0.1 \mu\text{v}$., or 2×10^{-7} of the reading, whichever is greater.

3. A potential difference between the circuits creates a leakage current through the chopper and the error is roughly proportional to frequency and circuit resistance. The error may be held below $10^{-6} \times \text{P.D.}$ (without correction) for circuit resistances less than 100 ohms.

4. The effect of a-c. pickup can be practically eliminated for galvanometer detectors by using mechanically driven choppers at the proper frequency.

5. A-c. amplification is feasible but not all commercial amplifiers are suitable.

6. Leak resistance and delayed discharge are insignificant if polystyrene condensers are used. Paper condensers are sufficient for four to five figure accuracy.

APPLICATIONS

The "isolating potential comparator" has several applications in research and other fields. It appears particularly suitable for the comparison of thermocouples (3) and for the measurement and control of temperature differences in metallic bodies. By using the circuit of Fig. 10 the difference in e.m.f. of two

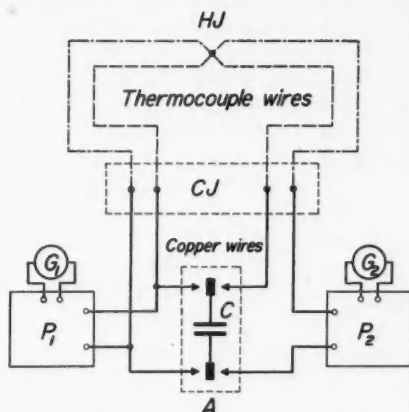


FIG. 10. A circuit for comparing thermocouples of the same type.

couples can be measured directly with one potentiometer while the whole e.m.f. is read with another. In many cases the potentiometers need only be read to the number of significant figures required of the difference and con-

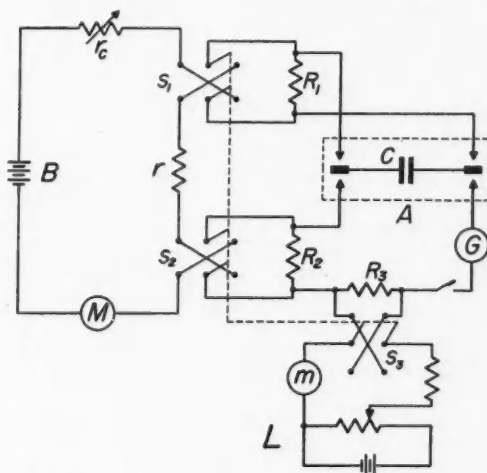


FIG. 11. A circuit for comparing standard resistors.

siderable heating rates will be permissible provided that the *difference* is constant or varying slowly. Thermocouples may be welded to the metal to ensure thermal contact.

The circuit of Fig. 11 has been used in this laboratory to make direct measurements of the difference in resistance between standard resistors of the same nominal value (1 ohm or 10 ohm). A current is passed through the two resistors (R_1, R_2) which are connected in series and the current through R_2 is then adjusted until the galvanometer gives no deflection or reversal. The difference in resistance may then be calculated (to about 1%) from the meter readings and the value of R_3 . The results of a set of measurements on 1 ohm standards are shown in Fig. 12. All deviations shown in this figure are within the uncertainty of temperature measurement alone.

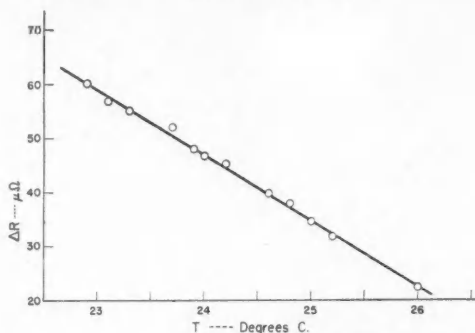


FIG. 12. The results of a series of difference measurements on a pair of 1 ohm standard resistors. ΔR is the difference in resistance of the two resistors as measured using the circuit of Fig. 11.

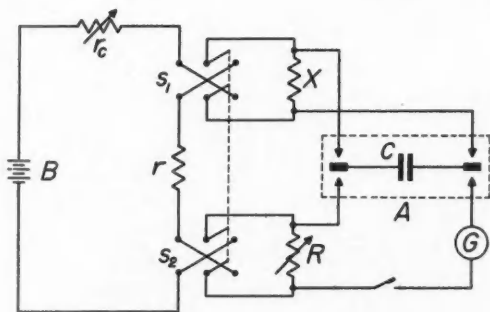


FIG. 13. A circuit suitable for resistance thermometry.

The simpler circuit of Fig. 13 may be used to compare a variable (calibrated) potential lead resistor (R) with an unknown resistor (X), say a four-lead resistance thermometer. A null is obtained in this case when the resistances between the potential leads are exactly equal. It will be noted that in this

example, as well as the preceding one, the desired result is obtained by a single balance, is completely independent of lead resistances, and does not require either high resistance ratio arms or a commutator (1, 4).

CONCLUSION

A circuit has been described and tested with which it is possible to make a precise comparison of two e.m.f.'s even when an appreciable potential difference is maintained between them by other circuit connections. The accuracy of comparison is in many cases comparable to what can be achieved by direct connection.

The circuit has distinct advantages over conventional procedures in several quite important aspects of experimental physics. In particular it presents the possibility of a combined potentiometric and bridge approach to the problem of measurement and comparison of resistances, by avoiding the stability requirements of the potentiometric method without at the same time requiring the ratio arms or potential lead current of a bridge.

Further work on the applications of this circuit to physical measurements is proceeding and will be reported later.

REFERENCES

1. MUELLER, E. F. *Bur. Standards Bull.* 13: 547. 1916-1917.
2. MUELLER, E. F. *Temperature, its measurement and control in science and industry.* Reinhold Publishing Corporation, New York. 1941. pp. 162-179.
3. ROESSER, W. F. and WENSEL, H. T. *J. Research Natl. Bur. Standards*, 14: 247. 1935.
4. SMITH, F. E. *Phil. Mag.* 24: 541. 1912.

COMPTON ELECTRON SUPPRESSION IN THE GAMMA-RAY SPECTRA OF Ra (B + C), Co⁶⁰, AND Ta¹⁸² ¹

BY R. M. PEARCE² AND K. C. MANN

ABSTRACT

A method of suppression of the Compton electron background present in photoelectron spectra is described. The method employs an anticoincidence element which eliminates Compton electron pulses in the spectrometer detector counter and leaves photoelectron pulses unaffected. The technique has been applied to the photoelectron spectra of Co⁶⁰, Ta¹⁸², and Ra (B + C). Evidence is presented for a previously unreported 1.01 Mev. gamma-ray transition in Ta¹⁸². The spectrum of Ra (B + C) is compared with the spectra reported by Ellis and by Latyshev. Some of the new transitions found by Latyshev are confirmed. Other gamma-rays not reported by other workers are presented here.

INTRODUCTION

The assignment of energy levels to radioactive nuclei depends primarily upon the detection and measurement of gamma-ray transitions. Where the gamma-ray spectrum is complex, the determination of the level sequence is very difficult. In such cases, coincidence measurements are not easy to interpret, and one must rely to a large extent upon accurate energy and intensity determinations in postulating a decay scheme. Thus the detection of relatively weak transitions of the "cross-over" or "linking" type can provide additional supporting evidence for the proposed scheme.

Gamma-ray energies are usually measured by measuring the energies of photoelectrons ejected from a thin "radiator" or "converter" of some high *Z* material. In the majority of cases, the gamma-rays are accompanied by primary beta particles and conversion electrons which have intensities greater by several orders of magnitude than the intensity of the desired photoelectrons. To avoid such an excessive background, it is customary to remove all primary electrons by placing between the source and the radiator an "absorber" of some low *Z* material the thickness of which is determined by the energy of the primaries. The thin radiator is still for all practical purposes the only source of photoelectrons because of the strong dependence of photoelectric cross-section upon *Z*.

Unfortunately, this practice replaces one background by another. Compton electrons, originating in the thick absorber and to a much lesser extent in the radiator, provide a continuous background upon which the photoelectrons are superimposed. The shape and magnitude of this background depends upon the distribution of the gamma-rays present, upon the baffling used, and upon the size and shape of the source holder. This background is always much less intense than the primary electron background would be and it has no distractions such as conversion lines. Yet it can be very troublesome whenever the experimenter is looking for low intensity photoelectron peaks in the region

¹ Manuscript received December 26, 1952.

Contribution from the Department of Physics, The University of British Columbia, Vancouver, B.C.

² Now with the Atomic Energy of Canada Ltd., Chalk River, Ont.

of the maximum of the Compton electron continuum. It may easily require prohibitively long counting times to reduce the standard deviation of the background count to values less than the photoelectron line height, particularly where the latter is small.

This paper describes a method whereby a considerable suppression of the Compton electron background has been achieved with essentially no loss of photoelectron intensity. In the arrangement used, most of the Compton electrons produce coincident pulses in two counters, one at the source end and one at the detector end of a thin-lens beta-ray spectrometer. Photoelectrons produce counts at the detector counter only. An anticoincidence element blanks the Compton pulses and leaves the photoelectron pulses undisturbed. With some sources, it has been found possible to suppress as much as 90% of the Compton electron counts in the most troublesome part of the spectrum. The details of the method are given in the following sections together with the results of this method when applied to the gamma-ray spectra of Ra (B + C), Co⁶⁰, and Ta¹⁸².

EXPERIMENTAL

The spectrometer used was of the thin-lens type, described elsewhere (2), with the difference that type 5819 photomultipliers were used in place of G.M. counters. The photomultipliers were shielded from the spectrometer focusing field by mild steel cylinders of $\frac{1}{4}$ in. wall thickness. Mild steel end plates were attached with light-tight gaskets. Suitable window openings were provided in the end plates nearest the spectrometer, while the other end plates carried the cable connections and preamplifiers matched to the impedance of the output cable. Anthracene crystal phosphors were used as scintillators. The spectrometer was arranged so that the width at half intensity of an undistorted photoelectron peak was 4% in momentum.

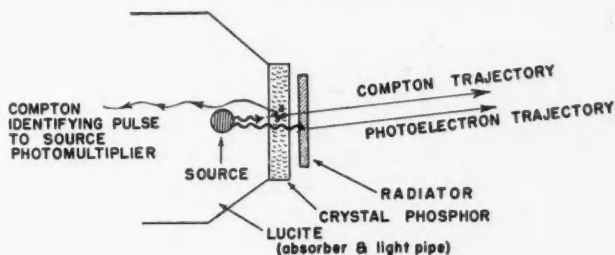


FIG. 1. Schematic diagram of source holder.

Fig. 1 shows a schematic diagram of the source holder. The radioactive source, in the form of a thin wire or cylinder approximately 1 mm. in diameter and 1 cm. long, was mounted in a lucite rod about 1 in. in length in the spectrometer source position, the lucite providing optical coupling to the cathode of the photomultiplier which will be referred to as the source counter. The lucite as well performs the function of the absorber in the conventional arrangement.

The crystal phosphor was a flake of anthracene 1 mm. thick attached to the lucite with Canada balsam. The sloping shoulders of the lucite were designed to give the best optical coupling between the phosphor and the photocathode. The lucite also served as the vacuum seal for the spectrometer, so that the anthracene and the radiator (cemented to the phosphor with a light wax) were inside the vacuum system. In this connection, it was found that continued operation for six weeks was possible before evaporation seriously affected the anthracene. The lucite between the source and the crystal was of sufficient thickness to block any primary electrons from entering the spectrometer.

With this arrangement, all Compton electrons (except those originating within the radiator) which enter the spectrometer in such a direction as to be focused at the detector must pass through the anthracene flake where they leave identifying pulses in the source counter. The efficiency of the anthracene flake for detection of fast beta-particles was tested by a direct comparison with a thin-walled beta counter with the same geometry using a source of RaE which has a single beta group with a maximum energy of about 1.18 Mev. With a thickness of 1 mm. the anthracene flake gave the same counting rate as the beta counter which was assumed to have an efficiency of 100% for all electrons entering its sensitive volume. It was then assumed that all Compton electrons originating in the lucite absorber which produce a pulse at the detector counter also produce a pulse at the source counter.

It is expected that some Compton electrons, focused and detected in the spectrometer, will not produce coincident pulses in the source counter. These might be generated (a) in the radiator itself or (b) in a thin outermost segment of the anthracene of thickness less than a few ionizing mean-free-paths. This represents one of the limitations of the method for no further separation of Compton and photoelectrons is possible once they have left the source assembly without leaving an identifying pulse. Effect (a) may be reduced in magnitude by reducing the radiator thickness but this in turn reduces the photoelectron count.

The detector counter for focused electrons was a second photomultiplier using a somewhat thicker anthracene crystal. This crystal also was inside the vacuum system, being mounted on a small lucite plug which formed the vacuum seal. The detector photomultiplier was butted against the lucite and optically coupled to it with a transparent jelly.

The proximity of the radioactive source to the source photomultiplier resulted in a very high counting rate at the source counter. In typical operation with a 0.5 millicurie source of Ra (B + C), this amounted to 2×10^6 counts per second. The speed of the electronic circuits thus puts a limit on the strength of the sources that may profitably be used. With the circuits used in this investigation, a 1 millicurie source appears to be about the limit. It is also important to assure that no primary electrons reach the anthracene flake since many of these might be in true coincidence with the photoelectrons from the radiator. The action of the anticoincidence element would then limit the photoelectron response as well as the Compton electron counts.

It might well be expected that some undesirable anticoincidence blanking should occur whenever two gamma-rays are emitted by the source in cascade. Thus photoelectrons from one might be blanked by Compton electrons from the other. However, because of the geometry and the low conversion efficiencies of the radiator and the absorber for Compton and photoelectron events, this effect is negligible as indicated in Fig. 4 for the two cascade gamma-rays of Co^{60} .

The total source-radiator distance is determined essentially by the required absorber thickness plus the 1 mm. anthracene flake. For a Ra (B + C) source, the total separation was about 3 mm. as compared to about 2 mm. in the conventional arrangement, the difference being necessary because of the small lucite density. This increase results in little, if any, loss in photoelectron peak height because of the relatively large sizes of source and radiator and the anisotropy of the photoelectron emission.

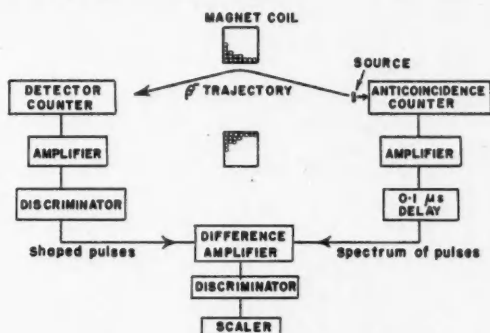


FIG. 2. Block diagram of anticoincidence arrangement.

Fig. 2 shows a block diagram of the arrangement used. The detector head amplifier is a feed-back amplifier (4) with an observed rise-time of $0.1 \mu\text{sec.}$ and a maximum output of 120 volts. The output stage is a cathode follower leading to the discriminator shown in the detector channel. Shaped pulses (approximately 2 volts in amplitude and $0.20 \mu\text{sec.}$ in duration) from the discriminator go to the difference amplifier.

The source amplifier has a gain of approximately 50 and all pulses are limited to 2 volts by the final tube, thus preventing the difference amplifier from overloading. The voltage on the source photomultiplier and the over-all gain of the following amplifier stages combined to produce a spectrum of pulses extending into the noise region. Occasional noise pulses may be limited by the source amplifier but their number is believed to be small. The limited pulses are approximately $0.20 \mu\text{sec.}$ in duration. The rise-time of this amplifier is $0.04 \mu\text{sec.}$; and the insensitive time after receiving a pulse as large as 1 volt was estimated to be $0.2 \mu\text{sec.}$ The pulses in the source channel are delayed $0.1 \mu\text{sec.}$ to allow the discriminator in the detector channel to fire. This delay is provided by three feet of RG/65 U cable with a characteristic impedance of 1000 ohms. To match this impedance, the output stage of the source pre-amplifier is an amplifier stage with a 1000-ohm plate load.

The spectrum of pulses from the source counter go to the difference amplifier where they are subtracted from the discriminator pulses coming from the detector channel. Those output pulses from the difference amplifier which retain their full magnitude are then accepted by the discriminator of a commercial scaling unit and recorded.

Tests were conducted to determine how serious was the accidental suppression of true photoelectron pulses at the detector due to the large counting rate in the detector channel. It was estimated that with a 0.5 millicurie source of Ra (B + C) approximately 5% of the photoelectron pulses were accidentally blanked, while with a 1.0 millicurie source of Ta¹⁸², the loss rose to 10%.

COMPTON SUPPRESSION EFFICIENCY

Fig. 3 shows the effectiveness of the method for the suppression of the Compton background as a function of electron energy with sources of Ta¹⁸²

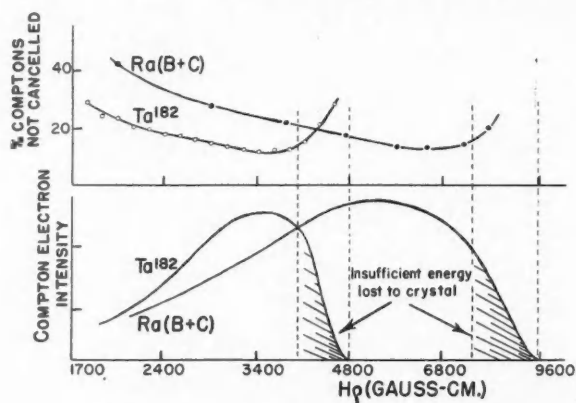


FIG. 3. Compton electron suppression efficiency. (Logarithmic abscissa.)

and Ra (B + C). The fraction of the Compton electrons *not* suppressed was obtained at each spectrometer setting by taking counts with and without voltage on the source photomultiplier. Such spectrometer settings were adjusted as well as possible to lie between known photoelectron peaks. It will be noted that the method is most effective in the region of the spectrum where the Compton electron intensity is a maximum. Poorer suppression is evident at the high and low energy ends of the distribution. In these regions, the Compton electron count is low so that the effect is not troublesome.

The poorer performance with high energy electrons can be explained if we consider the probable points of origin of the Compton electrons. The highest energy electrons are most probably those resulting from head-on collisions between photons and electrons taking place either in the radiator or in the outermost layer of the phosphor. Such electrons would be expected either to produce no pulses at all in the source counter (if they originate in the radiator), or to produce pulses of the order of thermal noise (if they originate in the

insensitive outermost layer of the phosphor). To register in the source counter, an electron must lose some minimum energy ΔE in the phosphor, where ΔE is probably in the neighborhood of 50 kev. for a 50% chance of cancellation (see Fig. 3). If E_{\max} represents the maximum energy of the Compton distribution, then all electrons recorded at the detector counter of energy greater than $(E_{\max} - \Delta E)$ will therefore produce no detectable count in the source counter, and hence will not be cancelled by the anticoincidence network. E_{\max} is greater in Ra (B + C) than it is in Ta¹⁸². For this reason, Compton electron suppression remains effective over a larger energy interval in the spectrum of Ra (B + C). Similarly, the poorer suppression efficiency at the low energy end may be ascribed to large angle Compton electron scattering from the source holder, baffles, etc., at such positions where the electrons do not pass through the anticoincidence crystal, and to large angle scattering from the insensitive outermost layer of the crystal itself.

RESULTS

(A) Co⁶⁰

The photoelectron spectrum of a 0.5 millicurie source of Co⁶⁰ taken with and without Compton electron suppression is shown in Fig. 4. As was expected,

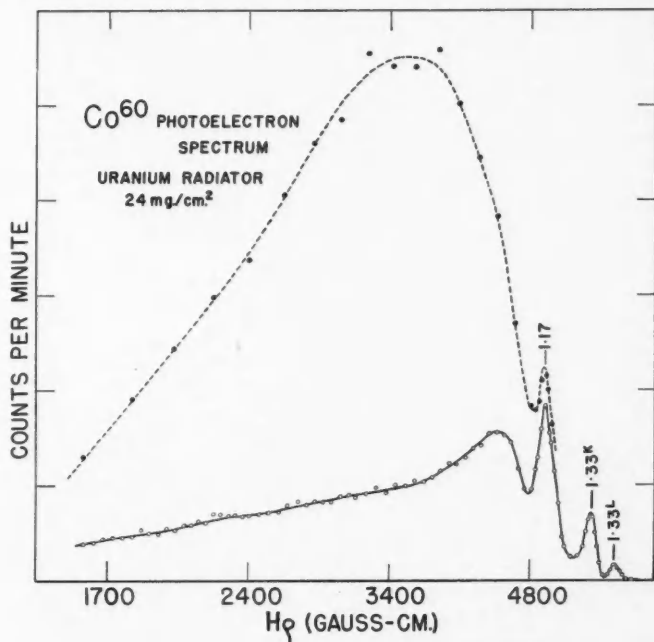


FIG. 4. Photoelectron spectrum of Co⁶⁰. (Logarithmic abscissa.) Broken curve—zero voltage on source photomultiplier. Solid curve—Compton electron suppression. (Statistical uncertainty is $4 \times$ circle diameters.) The ordinate scale markers represent units of 100 counts per min.

only the two well-known (8, 10) lines at 1.17 and 1.33 Mev. were found. No evidence appeared for any weak gamma-ray transitions. The well-defined hump lying just below the 1.17 Mev. photoelectron peak in the suppressed spectrum is caused by the coincidence of the rapidly falling Compton electron distribution and the rising inefficiency curve. Such humps seem to be characteristic of this method of suppression. Fortunately they are much broader than photoelectron peaks and there is little danger of confusing the two.

(B) Ta^{182}

Fig. 5(a) shows the photoelectron spectrum of a 1.0 millicurie source of Ta^{182} with and without Compton electron suppression. This nucleus has been

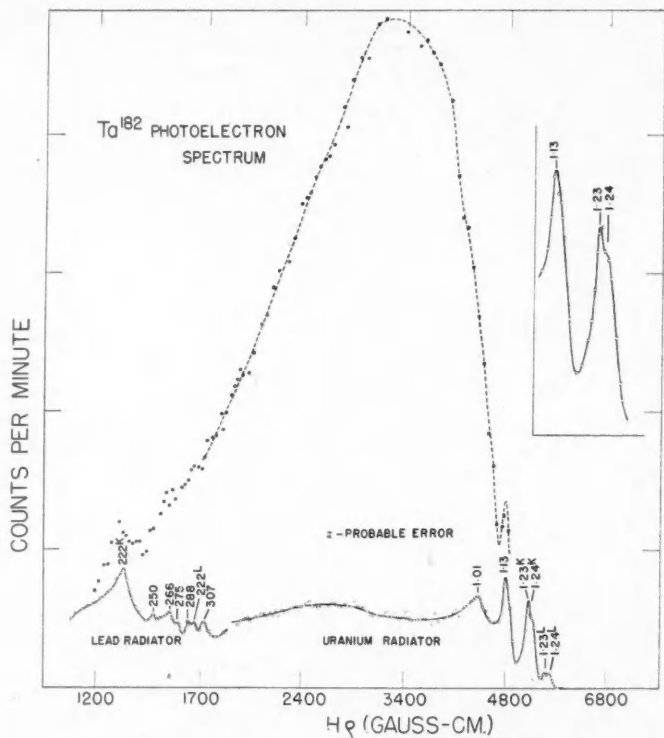


FIG. 5(a). Photoelectron spectrum of Ta^{182} . (Logarithmic abscissa.) Broken curve—zero voltage on source photomultiplier. Solid curve—Compton electron suppression. (Lead radiator 25 mgm. per cm.²; uranium radiator 24 mgm. per cm.²) The ordinate scale markers represent units of 100 counts per min.

the subject of many investigations by other workers (1, 5, 12) and the agreement as to detail is not very satisfactory. Most workers agree, however, that the gamma-rays of Ta^{182} fall into two main groups; a low energy group lying below 350 kev. and a high energy group of gamma-rays clustered about 1 Mev.

A recent report by O'Meara (11) is not in agreement with this distribution. He reports having found evidence of 14 additional gamma-rays between 300 kev. and 1.1 Mev.

The prominent 222 kev. transition found here has been identified by other workers as have the 250 kev., the 226 kev., and the 288 kev. lines allowing an uncertainty of 5 kev. in the comparison with other work. Admittedly, the spectrometer used in this investigation does not have the resolution nor the low energy performance to be very reliable in this region of the spectrum, so that the authors do not wish to overemphasize the importance of this agreement. It is to be noted however that in the high energy region three strong gamma-rays are evident, in good agreement with the work of Beach, Peacock, and Wilkinson (1) who quote values of 1.133, 1.219, and 1.237 Mev. The energies found in this investigation are 1.13, 1.23, and 1.24 Mev. In addition, a new transition corresponding to a gamma-ray energy of 1.01 ± 0.01 Mev. appeared. This peak is superimposed almost exactly upon the Compton elec-

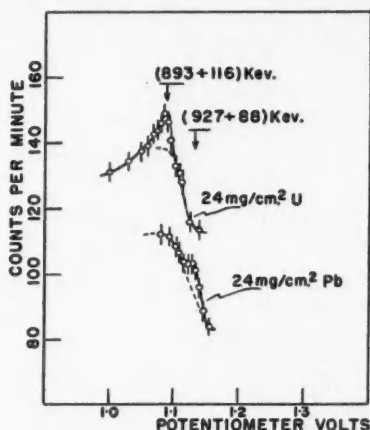


FIG. 5(b). The photoelectron spectrum of Ta^{182} in the region of the 1.01 Mev. photoelectron peak. The abscissa represents the focusing current reference voltage and so is proportional to electron momentum. The first number in the brackets is the electron energy, the second being the appropriate K -shell binding energy of the radiator used.

tron hump previously noted in the Co^{60} spectrum. In order to make certain that this peak was not spurious, this part of the spectrum was re-run using a lead radiator in place of the uranium radiator. (See Fig. 5(b).) The peak in question shifted to the right by exactly the difference in K -shell binding energy between lead and uranium. None of the gamma-rays reported by O'Meara (11) produced detectable photoelectron peaks.

(C) $Ra (B + C)$

Fig. 6 shows the conventional spectrum of a 1.0 millicurie source of $Ra (B + C)$ (upper curve) previously reported in this journal (9). Also plotted (lower curve) is a normalized spectrum taken with 0.5 millicuries of $Ra (B + C)$

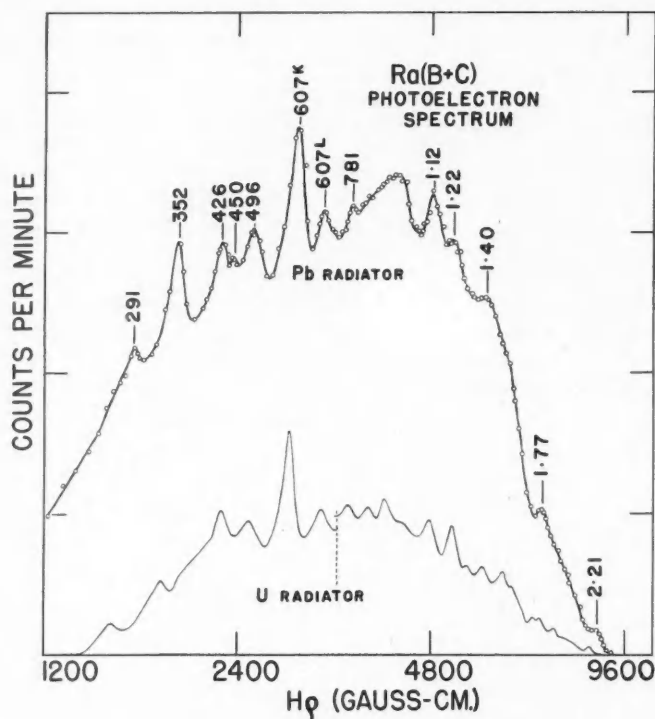


FIG. 6. Photoelectron spectrum of Ra (B + C). (Logarithmic abscissa.) Upper curve—conventional photoelectron spectrum taken with lead radiator 50 mgm. per cm.² See Reference (9). Lower curve—Compton electron suppression spectrum taken with uranium radiator 24 mgm. per cm.² and 40 mgm. per cm.² The ordinate scale markers represent units of 250 counts per min.

using the Compton suppression technique. The ordinates of the lower curve have been multiplied by two to correct for source strength differences. The vertical dotted line represents a change of radiator thickness: below the line, the radiator thickness was 24 mgm. per cm.² and above it the thickness was 40 mgm. per cm.² The radiator used for the upper curve was a lead foil of thickness 50 mgm. per cm.² In Fig. 7 the Compton suppressed spectrum is shown in detail on a larger scale for clarity. All peaks are very distinct since sufficient counts were taken at each point to ensure a very low statistical uncertainty. For example the probable error of all points taken on weaker peaks above 1.0 Mev. is contained within the circle diameters.

It will be seen that the spectrum taken this way reveals the presence of a number of gamma-ray transitions that were not evident from the earlier results obtained in this laboratory. Several gamma-rays reported by Latyshev (6, 7) and his associates are confirmed here, while still others have been found

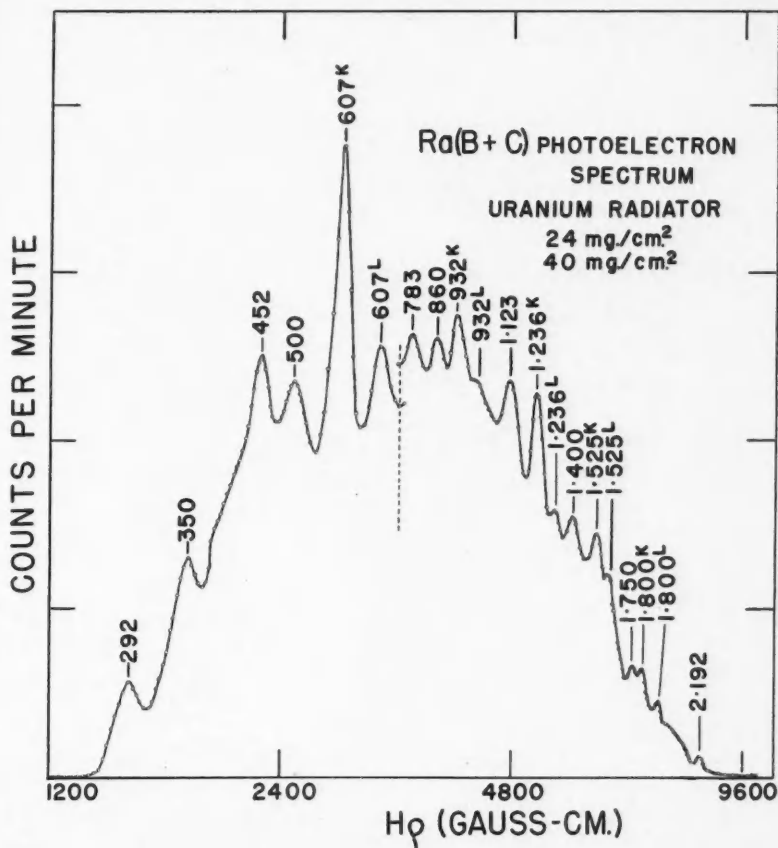


FIG. 7. Photoelectron spectrum of Ra (B + C) with Compton electron suppression. Below broken vertical line 24 mgm. per cm.² uranium radiator; above vertical line 40 mgm. per cm.² uranium radiator. (Logarithmic abscissa.) Statistical uncertainty above 1.0 Mev. is less than the circle radius. The ordinate scale markers represent units of 50 counts per min.

that have not been reported either by Latyshev or Ellis (3). Since Latyshev's results were obtained largely from internal electron pair measurements, Ellis's result largely from the measurement of internal conversion electron energies, and the present results from photoelectron measurements, the differences can perhaps be attributed to the different probabilities and selection rules governing the three nuclear events. Table I shows a comparison of the results from the three laboratories.

No attempt has been made to compare relative intensities from the data presented here. The usual method of doing so is to plot $N/H\rho$ vs. $H\rho$ and to compare the areas under the photoelectron peaks. These comparative areas

TABLE I
GAMMA-RAY ENERGIES (MEV.) OF RA (B + C)

i.c.—internal conversion
i.p.—internal electron pairs
p.e.—photoelectrons

Uncertainties in the energies quoted in the third column are estimated to be approximately 0.5%.

Ellis and co-workers	Latyshev and co-workers	Present investigation
0.0529 i.c.		
0.2406 i.c.		
0.2571 i.c.		
0.2937 i.c.		0.292 p.e.
0.3499 i.c.		0.350 p.e.
0.4260 p.e.		
		0.452 p.e.
0.4980 p.e.		0.500 p.e.
0.6067 i.c.	0.606 i.c.	0.607 p.e.
0.766 i.c.	0.766 i.c.	
		0.783 p.e.
		0.860 p.e.
		0.932 p.e.
0.933 i.c.	0.933 i.c.	
	1.11 i.p.	
1.120 i.c.	1.120 i.c.	1.123 p.e.
	1.21 i.p.	
1.238 i.c.	1.234 i.c.	1.236 p.e.
1.379 i.c.	1.370 i.c.	
	1.39 i.p.	1.400 p.e.
1.414 i.c.	1.414 i.c.	
	1.52 i.p.	1.525 p.e.
	1.62 i.p.	
	1.75 i.p.	1.750 p.e.
1.761 i.c.	1.761 i.c.	
	1.82 i.p.	1.800 p.e.
	2.09 i.p.	
2.193 i.c.	2.20 i.p. + i.c.	2.192 p.e.

in turn must be corrected for the known variation of photoelectric cross-section with energy. This method cannot be applied unless a reasonably trustworthy residual Compton electron background can be drawn. This might be obtained by re-running the spectrum with the radiator replaced by a Compton electron "equivalent" since much of the residual background arises in the radiator itself. Tentative attempts to do this were not too satisfactory. A background can be obtained in this way but it seems necessary to normalize it so that it is consistent with the photoelectron curve. This procedure involves a great deal of guesswork because of the large number of closely spaced photoelectron peaks in this spectrum. A small error in normalization introduces a large error in the area ratios. Therefore the authors did not feel justified in presenting a list of relative intensities whose accuracy was so suspect.

In conclusion, it appears that the method of suppression of the Compton electron distribution described here can prove to be a useful aid in the detection and measurement of relatively weak gamma-ray transitions. This is particularly true where there is present in the decay scheme a strong high energy gamma-ray whose Compton electron distribution tends to mask weak lower energy photoelectron peaks.

ACKNOWLEDGMENTS

This investigation has been generously supported by the National Research Council of Canada through a Grant-in-Aid of Research to K.C.M. and this support is gratefully acknowledged. One of us (R.M.P.) is indebted to the National Research Council for the award of a Fellowship. We also wish to express our appreciation to the British Columbia Cancer Research Institute who placed at our disposal the radium source used in this investigation.

REFERENCES

1. BEACH, L. A., PEACOCK, C. L., and WILKINSON, R. G. *Phys. Rev.* 76: 1585. 1949.
2. DEUTSCH, M., ELLIOTT, L. G., and EVANS, R. *Rev. Sci. Instruments*, 15: 7. 1944.
3. ELLIS, C. D. *Proc. Roy. Soc. (London)*, A, 138: 318. 1932; 143: 350. 1934.
4. ELMORE, W. C. and SANDS, M. *Electronics*. McGraw-Hill Book Company, Inc., New York and London. 1949. p. 60.
5. GODDARD, C. H. and COOK, C. S. *Phys. Rev.* 76: 1419. 1949.
6. LATYSHEV, G. D. *Revs. Modern Phys.* 19: 132. 1947.
7. LATYSHEV, G. D., KOMPANEETZ, A. F., BORISOV, N. P., and GUCAK, J. H. *J. Phys. (U.S.S.R.)*, 3: 251. 1940.
8. LIND, D. A., BROWN, J. H., and DuMOND, J. W. M. *Phys. Rev.* 76: 591. 1949.
9. MANN, K. C., and OZEROFF, M. J. *Can. J. Research*, A, 27: 164. 1949.
10. MILLER, L. C. and CURTISS, L. F. *Bur. Standards J. Research*, 38: 359. 1947.
11. O'MEARA, F. E. *Phys. Rev.* 79: 1032. 1950.
12. RALL, W. and WILKINSON, R. G. *Phys. Rev.* 71: 321. 1947.

NOTE ON THE RESONANCE METHOD OF MEASURING THE RATIO OF THE SPECIFIC HEATS OF A GAS, C_p/C_v ¹

BY HAROLD W. WOOLLEY

ABSTRACT

Experimental results of Clark and Katz and of Katz, Leverton, and Woods obtained in a resonance method for determining the ratio of specific heats C_p/C_v have been recomputed with an improved formula for the mass effect of the gas. Improved agreement with values based on spectroscopic and PVT data is obtained for nitrogen, argon, carbon dioxide, nitrous oxide, and sulphur dioxide.

In examining the agreement between the ratio of specific heats based on theory (spectroscopic plus PVT) and on experiment as given by the resonance method of Clark and Katz (8, 9, 10, 11, 17), the magnitude and nature of a discrepancy has led to an examination of the experimental method and the calculation procedure used for it.

One formula used in their extensive computation procedure is not correct, and affects their earlier results appreciably. In much of the later work the additional correction required is negligibly small.

The particular difficulty is in the correction to the mass of the moving system to include the effective mass of the gas. The gas is evenly divided into two equal cylindrical spaces at either end of an oscillating piston. They evidently considered the gas as participating to an extent of 50% in the motion, as they took the effective mass of the gas as equal to the amount of gas in a single end volume. A correct analysis shows that the effective mass of the gas is essentially two-thirds as much, in rather good approximation.

While there is 50% participation in the motion in the sense of the velocities as such, the influence upon the motion is more properly analyzed in terms of kinetic energy, such as might enter into a Hamiltonian for the system. With velocity varying approximately linearly with distance from the end of the cylinder, the distribution of the kinetic energy of interest varies approximately quadratically with distance, so that the integral supplies a factor of one-third. The combined effective mass of the two volumes of gas is then approximately two-thirds of the mass for one of them.* The effective mass of the piston is approximately $m + \frac{2}{3}m_p$, so that the correction factor Λ of Clark and Katz for the mass ratio is

$$[1] \quad \Lambda = 1 + 2 m_p/3m.$$

A more exact correction for the effective mass of the gas will now be derived.

It may be noted that for a limited range of variation of pressure and specific volume in the neighborhood of the values P_0 and V_0 , the actual dependence between pressure and volume under adiabatic conditions is given well by

$$[2] \quad PV^\alpha = P_0 V_0^\alpha$$

¹ Manuscript received January 19, 1953.

Contribution from the National Bureau of Standards, Washington, D.C.

*After completing the more elaborate analysis which follows, a paper by Koehler (18) was read mentioning the $\frac{1}{3}$ factor but not pointing out its omission by Clark and Katz.

where α , the isentropic expansion coefficient, is given by

$$[3] \quad \alpha = -\frac{V}{P} \left(\frac{\partial P}{\partial V} \right)_s = -\gamma \frac{V}{P} \left(\frac{\partial P}{\partial V} \right)_T.$$

It is equal to γG^{-1} in the notation of Clark and Katz.

If the neutral or average position of each part of the gas is indicated by x , its distance along the cylinder from a stationary end, and if the instantaneous displacement in the same direction from that average position is indicated by ξ , taken to be a function of x and time only, then the ratio between the local instantaneous specific volume and the average specific volume, V/V_0 , is given by $1 + \partial\xi/\partial x$, if displacements in all other directions are disregarded. Any small variations in pressure of the gas related to purely longitudinal motion follow the equation

$$[4] \quad P = P_0 (1 + \partial\xi/\partial x)^{-\alpha}$$

so that

$$[5] \quad \partial P/\partial x = -\alpha P_0 (1 + \partial\xi/\partial x)^{-\alpha-1} \partial^2\xi/\partial x^2$$

and to the approximation in which terms proportional to the first power of the displacement are sufficiently accurate (implying small relative variations in pressure)

$$[6] \quad \partial P/\partial x = -\alpha P_0 \partial^2\xi/\partial x^2.$$

The net force on a small mass of the gas between x and $x + \delta x$ is

$$[7] \quad \delta P a = -M_0 V_0^{-1} \delta x a \partial^2\xi/\partial t^2$$

where a is the cross-sectional area of the cylinder, $M_0 V_0^{-1}$ is the density of the gas, and δP is an increment in pressure between the position x and $x + \delta x$ in the gas. Thus

$$[8] \quad \partial P/\partial x = -M_0 V_0^{-1} \partial^2\xi/\partial t^2$$

so that

$$[9] \quad \alpha P_0 V_0 M^{-1} \partial^2\xi/\partial x^2 = \partial^2\xi/\partial t^2$$

is the governing equation. This is the equation for the transmission of sound with the velocity $c = [\alpha P_0 V_0 M^{-1}]^{1/2}$.

For a condition of simple resonance in the cylinder, a usable solution of the equation is

$$[10] \quad \xi = A \sin \frac{2\pi x}{\lambda} \cos \frac{2\pi ct}{\lambda}$$

with $x = 0$ at a stationary end of the cylinder. If the length of the gas chamber is L , conditions at the piston boundary are given by

$$[11] \quad \xi = A \sin \frac{2\pi L}{\lambda} \cos \frac{2\pi ct}{\lambda},$$

$$[12] \quad \frac{\partial \xi}{\partial x} = \frac{2\pi}{\lambda} A \cos \frac{2\pi L}{\lambda} \cos \frac{2\pi ct}{\lambda},$$

and

$$[13] \quad \frac{\partial^2 \xi}{\partial t^2} = -\frac{4\pi^2 c^2}{\lambda^2} A \sin \frac{2\pi L}{\lambda} \cos \frac{2\pi ct}{\lambda}.$$

To the accuracy of linear terms, the pressure in the gas is

$$[14] \quad P = P_0(1 - \alpha \partial \xi / \partial x)$$

so that the excess of pressure on the piston wall over and above the average value, P_0 , is

$$[15] \quad P - P_0 \approx -P_0 \alpha \frac{\partial \xi}{\partial x} = -P_0 \alpha \frac{2\pi}{\lambda} A \cos \frac{2\pi L}{\lambda} \cos \frac{2\pi ct}{\lambda}.$$

As the pressure on the other end of the piston deviates oppositely from the average value, the net force on the piston is

$$[16] \quad -2aP_0 \alpha \frac{2\pi}{\lambda} A \cos \frac{2\pi L}{\lambda} \cos \frac{2\pi ct}{\lambda}.$$

Equating this to the product of mass times acceleration for the piston,

$$[17] \quad m \frac{\partial^2 \xi}{\partial t^2} = -\frac{4m\pi^2 c^2}{\lambda^2} A \sin \frac{2\pi L}{\lambda} \cos \frac{2\pi ct}{\lambda},$$

which with $2\pi c/\lambda = \omega$ and $m_g = LaM_0V_0^{-1}$, and the formula for c^2 , leads to

$$[18] \quad \alpha = \frac{mL}{2aP_0} \omega^2 \frac{\lambda}{2\pi L} \tan \frac{2\pi L}{\lambda}$$

with

$$[19] \quad 2m_g/m = \frac{2\pi L}{\lambda} \tan \frac{2\pi L}{\lambda}.$$

By combining these two relations, the result becomes

$$[20] \quad \gamma = \alpha G = \frac{mL\omega^2}{2aP_0} \left[1 + \frac{2}{3} \frac{m_g}{m} + \frac{4}{45} \left(\frac{m_g}{m} \right)^2 - \frac{8}{189} \left(\frac{m_g}{m} \right)^3 \right] G = \frac{mL\omega^2}{2aP_0} \Lambda G.$$

The quantity in the brackets is the appropriate Λ factor, using the terminology of Clark and Katz, and should replace their value of $1 + m_g/m$ for this quantity.

Recomputed values of γ for various gases based on the measurements of Clark and Katz are listed in the final column of Tables I to V. The initial column gives the pressure in atmospheres, the columns following give, respectively, γ and Λ as reported originally and the improved value of Λ from equation 20. A value for γ^0 at zero pressure based on spectroscopic data is listed in parentheses. A graphical comparison of their results with values computed from P - V - T and spectroscopic data is shown in regard to α rather than γ because of the smaller dependence on the P - V - T data. In most cases, the quality of agreement is quite comparable on the two bases. The uncertainty in PV is not large enough to modify Λ significantly, so the new values for Λ might be regarded as essentially correct. In Figs. 1 to 5, original and recalculated experi-

mental values of $\alpha = -\gamma \frac{V}{P} \left(\frac{dP}{dV} \right)_T$ are shown with theoretical curves so

obtained. Some of the gases treated by Clark and Katz are omitted here because of the minute change of the results due to the smallness of the mass of the gas relative to the mass of the piston.

TABLE I
NITROGEN (23°C.)

Press., atm.	γ_{old}	Λ_{old}	Λ_{new}	γ_{new}
0				(1.3996)
0.9984	1.4028	1.00084	1.00056	1.4024
3.668	1.4083	1.00307	1.00205	1.4069
5.389	1.4128	1.00452	1.00302	1.4107
6.751	1.4162	1.00566	1.00378	1.4136
8.056	1.4175	1.00675	1.00450	1.4143
10.516	1.4240	1.00881	1.00588	1.4199
13.032	1.4310	1.01092	1.00729	1.4259
15.659	1.4335	1.01313	1.00877	1.4273
21.219	1.4465	1.01777	1.01188	1.4381
25.929	1.4581	1.02171	1.01452	1.4478

TABLE II
ARGON (24.2°C.)

Press., atm	γ_{old}	Λ_{old}	Λ_{new}	γ_{new}
0				(1.6667)
0.9886	1.6685	1.00117	1.00078	1.6678
2.256	1.6747	1.00268	1.00179	1.6732
4.783	1.6840	1.00569	1.00380	1.6808
6.722	1.6909	1.00800	1.00534	1.6864
8.741	1.6977	1.01042	1.00696	1.6919
10.719	1.7055	1.01279	1.00854	1.6983
12.698	1.7115	1.01517	1.01013	1.7030
14.704	1.7178	1.01759	1.01175	1.7079
16.670	1.7248	1.01996	1.01334	1.7136
18.658	1.7325	1.02237	1.01496	1.7199
20.688	1.7403	1.02483	1.01661	1.7263

TABLE III
CARBON DIOXIDE (23.8°C.)

Press., atm.	γ_{old}	Λ_{old}	Λ_{new}	γ_{new}
0				(1.2891)
0.9917	1.2996	1.00130	1.00083	1.2990
2.273	1.3075	1.00301	1.00201	1.3062
4.240	1.3190	1.00567	1.00378	1.3165
6.119	1.3335	1.00826	1.00551	1.3299
8.130	1.3489	1.01110	1.00741	1.3440
10.103	1.3640	1.01394	1.00931	1.3578
12.054	1.3805	1.01683	1.01125	1.3729
12.101	1.3820	1.01683	1.01125	1.3744
13.991	1.3995	1.01976	1.01321	1.3905
16.121	1.4201	1.02307	1.01543	1.4095
18.071	1.4436	1.02619	1.01752	1.4314
20.036	1.4661	1.02941	1.01968	1.4522
21.840	1.4891	1.03245	1.02173	1.4736
22.223	1.4956	1.03311	1.02217	1.4798

TABLE IV
 NITROUS OXIDE (25.1°C. and 25.3°C.)

Press., atm.	γ_{old}	Δ_{old}	Δ_{new}	γ_{new}
25.1°C.				
0				(1.2736)
0.9987	1.2847	1.00135	1.00090	1.2841
2.224	1.292	1.00303	1.00202	1.291
4.334	1.308	1.00597	1.00398	1.305
6.157	1.322	1.00858	1.00573	1.318
8.208	1.339	1.01158	1.00773	1.334
11.439	1.368	1.01648	1.01101	1.361
14.641	1.400	1.02169	1.01450	1.390
17.952	1.438	1.02707	1.01811	1.425
21.384	1.483	1.03312	1.02218	1.467
23.769	1.519	1.03756	1.02517	1.501
26.942	1.574	1.04376	1.02934	1.552
31.354	1.664	1.05315	1.03568	1.636
25.3°C.				
1.4017	1.2795	1.0007	1.0005	1.2792
1.6944	1.2811	1.0009	1.0006	1.2807
1.8877	1.2813	1.0010	1.0007	1.2809
2.3101	1.2845	1.0013	1.0009	1.2840
2.6944	1.2884	1.0015	1.0010	1.2878
2.9757	1.2906	1.0016	1.0011	1.2900
3.6897	1.2954	1.0025	1.0017	1.2944
4.8104	1.3061	1.0033	1.0022	1.3047
5.3356	1.3152	1.0037	1.0025	1.3136

 TABLE V
 SULPHUR DIOXIDE (25.1°C.)

Press., atm.	γ_{old}	Δ_{old}	Δ_{new}	γ_{new}
0				(1.2638)
0.9970	1.2833	1.00192	1.00128	1.2825
2.241	1.3154	1.00440	1.00294	1.3135
2.8705	1.3354	1.00570	1.00380	1.3329
3.641	1.3594	1.00733	1.00489	1.3561

Table I and Fig. 1 give results for γ and α , respectively, for nitrogen, Table II and Fig. 2 for argon, Table III and Fig. 3 for carbon dioxide, Table IV and Fig. 4 for nitrous oxide, Table V and Fig. 5 for sulphur dioxide. In Figs. 1, 2, and 3 the curves were calculated using $B^{(0)}(\tau)$ and $C^{(0)}(\tau)$ for 6-12 Lennard-Jones potentials for nonpolar gases as functions of $\tau = kT/\epsilon$. For Figs. 1 and 2 the second virial coefficient B was taken as $b_2 B^{(0)}(\tau_2)$, with $b_2 = 2\pi N r_0^3/3$. For Fig. 3 the second virial coefficient for carbon dioxide was taken as $B = \beta + b_2 B^{(0)}(\tau_2)$. For the curves in each of these three figures, the third virial coefficient was taken as $C = b_3^2[C^{(0)}(\tau_3) - 4(B^{(0)}(\tau_3))^2] + 4B^2$ as given in Reference (30). For nitrous oxide and sulphur dioxide, no force law parameters previously chosen appear to be based on all available P - V - T data. A treatment of the P - V - T data is therefore included for each of these gases. The straight lines in Fig. 4 show the initial dependence (limiting slope at zero pressure) of α on

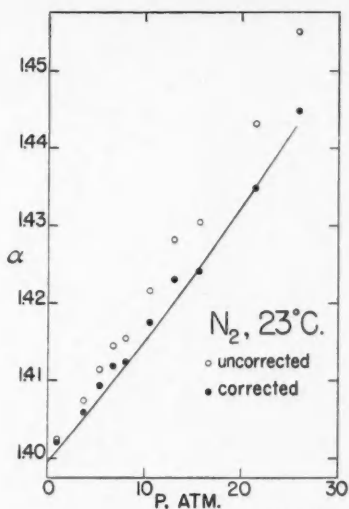


FIG. 1. Values of $\alpha = -\gamma \frac{V}{P} \left(\frac{\partial P}{\partial V} \right)_T$ for nitrogen at 23°C. Curve calculated with $C_p^0/R = 3.5028$, $b_2 = 63$ cc. per mole, $\epsilon_2/k = 95.42^\circ\text{K}$, $b_3 = 61.7$ cc. per mole, and $\epsilon_3/k = 97.7^\circ\text{K}$.

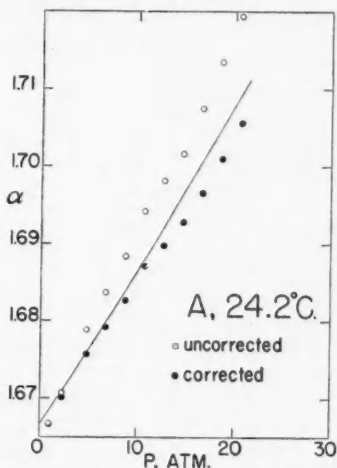


FIG. 2. Values of $\alpha = -\gamma \frac{V}{P} \left(\frac{\partial P}{\partial V} \right)_T$ for argon at 24.2°C. Curve calculated with $C_p^0/R = 2.5$, $b_2 = 49.804$ cc. per mole, $\epsilon_2/k = 119.75^\circ\text{K}$, $b_3 = 50.89$ cc. per mole, and $\epsilon_3/k = 118.6^\circ\text{K}$.

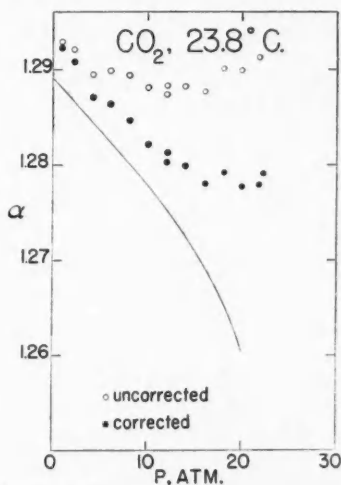


FIG. 3. Values of $\alpha = -\gamma \frac{V}{P} \left(\frac{\partial P}{\partial V} \right)_T$ for carbon dioxide at 23.8°C. Curve calculated with $C_p^0/R = 4.459$, $\beta = 34.25$ cc. per mole, $b_2 = 23.45$ cc. per mole, $\epsilon_2/k = 521^\circ\text{K}$, $b_3 = 79.5$ cc. per mole, and $\epsilon_3/k = 226^\circ\text{K}$.

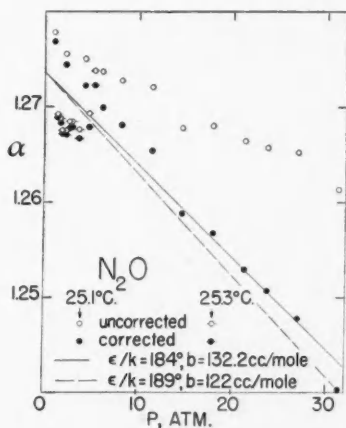


FIG. 4. Values of $\alpha = -\gamma \frac{V}{P} \left(\frac{\partial P}{\partial V} \right)_T$ for nitrous oxide near 25.1°C.

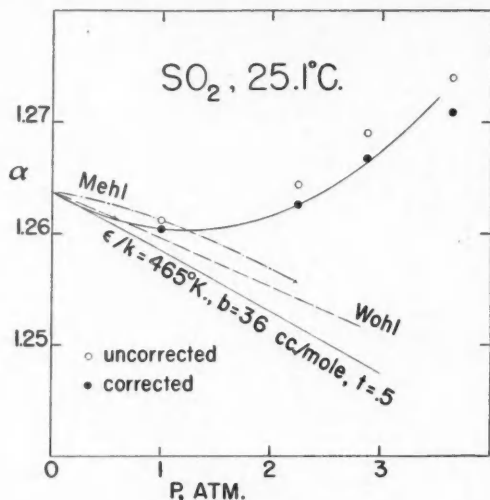


FIG. 5. Values of $\alpha = -\gamma_P \left(\frac{\partial P}{\partial V} \right)_T$ for sulphur dioxide at 25.1°C. A parabola is shown representing the experimental points and agreeing in initial slope with the theoretical line for a polar gas based on second virial data.

pressure for nitrous oxide at 25.1°C. consistent with two possible sets of parameter values to be discussed in connection with Fig. 6. The dashed line corresponds to the parameters given by Hirschfelder, Bird, and Spotz (14).

In Fig. 5, the nearly straight solid line represents a dependence of α on pressure consistent with the 6-12 Stockmayer force law parameters selected on the basis of second virial data shown in Fig. 7. Also, in Fig. 5, a parabola is shown representing the corrected experimental values of α beginning at the spectroscopic value at zero pressure and agreeing in initial slope with the theoretical line based on the second virial alone.

Fig. 6 shows the comparison between experimental second virials for nitrous oxide (2, 6, 7, 16, 19, 23, 24) and theoretical curves for the two choices of Lennard-Jones parameters shown in Fig. 4. One experimental value for B by Batuecas (3) is far from the others and has been omitted. The trend of the extensive set of values of Johnston and Weimer (16) is indicated by the part of their data shown here. The slope remains approximately as indicated over a range toward lower temperature even though their data are out of line with the results of other observers in the range of the figure. A third curve, near these latter data, is still able to give the same fit in Fig. 4 as the continuous curve, because of the flexibility in the choice of parameters allowed by the data. The calculations for these graphs for nitrous oxide have been made on the basis of Lennard-Jones potentials, as an estimate of polar effects using the small experimental dipole moment (26) shows the nonpolar treatment to be adequate to the accuracy appropriate for virial coefficients.

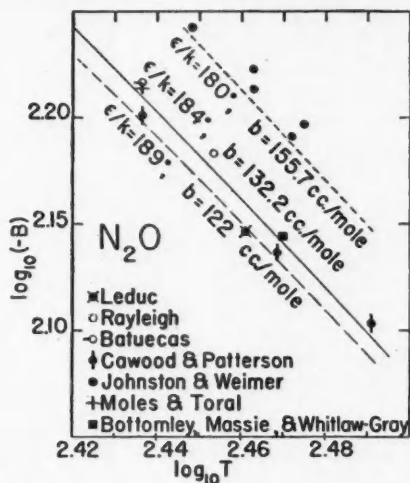


FIG. 6. Second virial data for nitrous oxide as fitted with a 6-12 Lennard-Jones potential (2, 3, 6, 7, 16, 19, 23, 24).

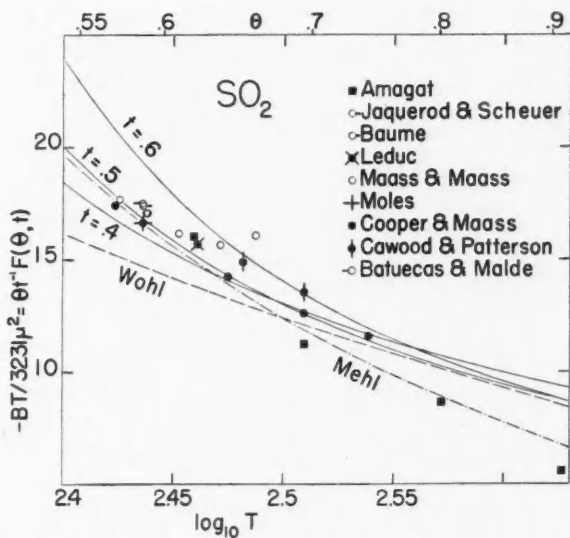


FIG. 7. Second virial data for sulphur dioxide as fitted with a 6-12 Stockmayer potential with $t = 0.5$ (1, 4, 5, 7, 12, 15, 19, 20, 22).

Fig. 7 shows the approximate fit obtained for the experimental second virial for sulphur dioxide (1, 4, 5, 7, 12, 15, 19, 20, 22) using a theoretical curve with $t = 0.5$ and fitting by a modification of Rowlinson's method (25). t here

represents $\frac{\pi}{3} \frac{N\mu^2}{\sqrt{2} b_0 \epsilon}$, a parameter depending on the dipole moment μ . Lateral

displacement of the theoretical curves vs. $\theta = kT/\epsilon$ for $t = 0.4, 0.5$, and 0.6 using experimental points obtained from the second virials with the experimental value of the dipole moment permits the selection of the best value of t and the best value of ϵ_2/k . The dipole moment used, 1.61 Debye units (31), differs only slightly from the better values 1.60 (27) and 1.59 (13). The quality of fit with equations of state that have been proposed for sulphur dioxide is also shown (21, 28, 29).

As a general comment on the quality of agreement between the values of α obtained by the resonance method and values computed using *PVT* values, discrepancies still remaining are likely to be due in part at least to the neglect of higher virial coefficients in estimating the *PVT* effects and to some inaccuracy in the virial coefficients used.

REFERENCES

1. AMAGAT, E. H. *Compt. rend.* 73: 185. 1871.
2. BATUECAS, T. *J. chim. phys.* 20: 308. 1923.
3. BATUECAS, T. *J. chim. phys.* 28: 572. 1931.
4. BATUECAS, T. and MALDE, G. G. *Anales real soc. espan. fis. y quim.* B, 46: 517. 1950.
5. BAUME, G. *J. chem. phys.* 6: 1. 1908.
6. BOTTOMLEY, G. A., MASSIE, D. S., and WHYTLAW-GRAY, R. *Proc. Roy. Soc. (London)*, A, 200: 201. 1950.
7. CAWOOD, W. and PATTERSON, H. S. *J. Chem. Soc.* 619. 1933.
8. CLARK, A. L. and KATZ, L. *Can. J. Research*, A, 18: 23. 1940.
9. CLARK, A. L. and KATZ, L. *Can. J. Research*, A, 18: 39. 1940.
10. CLARK, A. L. and KATZ, L. *Can. J. Research*, A, 19: 111. 1941.
11. CLARK, A. L. and KATZ, L. *Can. J. Research*, A, 21: 1. 1943.
12. COOPER, D. LEB. and MAASS, O. *Can. J. Research*, 4: 495. 1931.
13. CRABLE, G. F. and SMITH, W. V. *J. Chem. Phys.* 19: 502. 1951.
14. HIRSCHFELDER, J. O., BIRD, R. B., and SPOTZ, E. L. *Chem. Revs.* 44: 205. 1949.
15. JAQUEROD, A. and SCHEUER, O. *Compt. rend.* 140: 1384. 1905.
16. JOHNSTON, H. L. and WEIMER, H. R. *J. Am. Chem. Soc.* 56: 625. 1934.
17. KATZ, L., LEVERTON, W. F., and WOODS, S. B. *Can. J. Research*, A, 27: 34. 1949.
18. KOEHLER, W. F. *J. Chem. Phys.* 18: 465. 1950.
19. LEDUC, A. *Ann. chim. et phys.* (Ser. 8), 19: 441. 1910.
20. MAASS, C. E. and MAASS, O. *J. Am. Chem. Soc.* 50: 1352. 1928.
21. MEHL, W. *Bull. Intern. Inst. Refrig.* A, 15: 33. 1934.
22. MOLES, E. *Rec. trav. chim.* 48: 868. 1929.
23. MOLES, E. and TORAL, T. *Monatsh.* 69: 342. 1936.
24. RAYLEIGH, LORD. *Trans. Roy. Soc. (London)*, 204: 351. 1905.
25. ROWLINSON, J. S. *Trans. Faraday Soc.* 45: 974. 1949.
26. SHULMAN, R. G., DAILEY, B. P., and TOWNES, C. H. *Phys. Rev.* 78: 145. 1950.
27. SMITS, A., MOERMAN, N. F., and PATHUIS, J. C. *Z. physik. Chem.* B, 35: 60. 1936.
28. WOHL, A. *Z. physik. Chem.* 99: 207. 1921.
29. WOHL, K. *Z. physik. Chem.* 133: 328. 1928.
30. WOOLLEY, H. W. *Natl. Bur. Standards Rept.* 1491. 1952. Also, *J. Chem. Phys.* 21: 236. 1953.
31. ZAHN, C. T. *Phys. Rev.* 27: 455. 1926.

THE DETERMINATION OF URANIUM AND THORIUM IN ORES¹

By G. G. EICHHOLZ, J. W. HILBORN, AND C. McMAHON

ABSTRACT

The application of various physical methods to the assay of uranium and thorium in ores is discussed. It is shown how it is possible to determine their uranium and thorium content by means of simultaneous measurement of their beta and gamma activities. Simple working equations are derived which permit this determination to be carried out irrespective of the equilibrium condition of the uranium in the sample. Suitable experimental equipment is described briefly and some typical experimental results are presented.

1. INTRODUCTION

The increasing attention paid in recent years to exploration for radioactive mineral deposits and to extraction of uranium and thorium from various ores has underlined the need for a simple and precise method for determining the uranium and thorium content of mineral samples consistent with a minimum of handling of the samples and suitable for routine analysis. To appreciate the problem in its proper context it is best to survey briefly the various methods available. No consideration will be given here to purely chemical analytical methods as these have been described in detail elsewhere (22, 33, 34) and, owing to the preparatory treatment of the samples, do not fully meet the limitations imposed above. On large numbers of prospectors' samples, for instance, individual chemical assays would be undertaken only as a last resort.

Spectrographic methods (8), so far, have largely proved incapable of providing analyses of the required accuracy owing to the complexity of the spectra involved and the effects of interfering elements. X-ray fluorescence methods (13) are still in their infancy. They have been applied successfully to the analysis of lighter elements (2) but the extension of this method to the heavy elements has proved difficult owing to the low intensity of the fluorescence produced and the difficulty of correcting for the presence of other heavy elements which may seriously affect the intensity distribution. The fluorimetric method has been applied successfully to the determination of uranium over the range of 0.0005 to 2.0% U_3O_8 (46). It has not been applied to the determination of thorium in ores and the preparation of samples calls for solution, dilution, and final fusing of the sample.

Radiometric methods which depend on the nuclear radiations emitted by uranium and thorium and their decay products have been applied most widely as they call for a relatively small amount of equipment and can be modified for the detection of uranium and thorium in a variety of circumstances. Most of the work done has been concerned primarily with uranium and its decay products, and in the following sections emphasis will be placed on the assay of uranium. Similar considerations apply to thorium, unless stated otherwise.

¹ Manuscript received October 6, 1952.

Contribution from the Radioactivity Division, Mines Branch, Department of Mines and Technical Surveys, Ottawa.

Most of the practical problems associated with the assaying of radioactive ores are due to the diverse properties and origins of the radiations emitted by minerals containing uranium and thorium and their various decay products. Table I contains collected data on the uranium family and Table II on the thorium

TABLE I
URANIUM SERIES (MAIN SEQUENCE ONLY)

Name	Isotope	Half life	Principal emission energies in Mev.		
			Alpha	Beta	Gamma
UI	U 238	4.5×10^9 y.	4.18	—	—
UX ₁	Th 234	24.1 d.	—	0.2,0.1	0.09
UX ₂	Pa 234	1.18 m.	—	2.32, 1.5	2% 0.78, 0.82
UII	U 234	2.6×10^5 y.	4.76	—	—
Io	Th 230	8.0×10^4 y.	4.68, 4.61	—	(11%) 0.07
Ra	Ra 226	1600 y.	4.79, 4.61	(0.09)	(0.019)
Rn	Em 222	3.825 d.	5.49	—	—
RaA	Po 218	3.05 m.	6.00	—	—
RaB	Pb 214	26.8 m.	—	0.7	(0.047, 0.035)
RaC	Bi 214	19.7 m.	—	1.65, 3.17	1.76, 2.19
RaC'	Po 214	164 μ s.	7.68	—	—
RaD	Pb 210	22 y.	—	0.026	10% 0.007
RaE	Bi 210	5.0 d.	—	1.17	—
RaF	Po 210	138.3 d.	5.30	—	—
RaG	Pb 206	Stable	—	—	—

Note: Energies in brackets indicate low intensity. Branch products of less than 0.2% of decays omitted.

TABLE II
THORIUM SERIES (MAIN SEQUENCE)

Name	Isotope	Half life	Principal emission energies in Mev.		
			Alpha	Beta	Gamma
Th	Th 232	1.39×10^{10} y.	3.98	—	—
MsTh 1	Ra 228	6.7 y.	—	0.053	—
MsTh 2	Ac 228	6.13 h.	—	1.55	0.96, 0.91
RdTh	Th 228	1.9 y.	5.42, 5.34	—	0.08
ThX	Ra 224	3.64 d.	5.68, 5.45	—	(0.25)
Tn	Em 220	54.5 s.	6.282	—	—
ThA	Po 216	0.16 s.	6.774	—	—
ThB	Pb 212	10.6 h.	—	0.33, 0.57	0.24, 0.30
ThC	Bi 212	60.5 m.	34% 6.04, 6.08	66% 2.25	0.72, 0.8, 1.8
ThC'	Po 212	0.3 μ s.	66% 8.78	—	—
ThC''	Tl 208	3.1 m.	—	34% 1.72	2.62, 0.58, 0.51
ThD	Pb 208	Stable	—	—	—

Note: Energies in brackets indicate low intensity. Branch products of less than 0.2% of decays omitted.

family (24, 41). The third natural radioactive family, the actinium family, occurs usually with the uranium family, but its total contribution is such a small fraction of the whole radiation detected (1/139) that it may safely be neglected here (26).

2. SURVEY OF RADIOMETRIC METHODS

Radiometric assay methods can be classified in two groups.

(a) *Direct methods*

These are based on properties of the uranium itself and include the following:

Alpha detection by ion chamber

Scintillation counting

Photographic detection

Fission analysis

(b) *Indirect methods*

These are based on properties of the daughter elements, and the amount of uranium or thorium present is deduced indirectly. Such methods are the following:

Gamma counting methods

Beta counting methods

Emanation flow counters

Photographic methods

Alpha-gamma methods

Energy discrimination (gamma-gamma) method

Alpha discrimination methods

Equilibrium counting (beta-gamma).

Many of these methods have been in use for several years and a brief survey of their relative advantages and disadvantages may place them in their proper perspective. Most of the direct methods are based on the emission of alpha particles from the natural uranium isotopes (U^{238} , U^{235} , U^{234}) themselves and would appear to offer the simplest approach. However, alpha particles are easily absorbed and hence only a thin surface layer of the uranium-bearing ore will contribute appreciably to the total radiation detected. Detectors used include ionization chambers (11, 31), scintillation detectors (32), and photographic plates (4,6,23,25,38,44). They all suffer from the common problem that in order to register a sufficient number of particles they must either be kept sensitive for extremely long periods (up to four weeks for photographic plates) or they are confined to the detection of very strongly emitting sources only. Additional problems arise owing to the emission of alpha particles by daughter elements and radon emanation from the ores (12). Direct alpha detectors of the scintillation type are now used mainly to detect dangerous contamination in laboratories, and photographic techniques serve for the localization and identification of specific occurrences in selected ore samples.

An entirely different method is that of fission analysis (17,25,21). In this case use is made of the fissionable properties to U^{235} . The sample is exposed to a strong neutron source and the resultant fission activities are detected. This method is unsuitable for routine work because of the strong neutron source required to produce sufficient secondary particles and of the complicated preparatory procedure.

All indirect methods depend on the emission of particles by the various daughter elements and are based on certain assumptions concerning the propor-

tion of these daughters to the mother element in the ore. If the sample has been subject to severe natural or chemical leaching, most or all of the daughter elements may be absent and only a direct method or the fluorimeter can then give a correct analysis. For most natural ores, however, and in certain cases even those treated by gravity methods, one or other of the indirect methods may be applied. The choice will depend on the precision desired: a gamma Geiger detector is the simplest, but also frequently the least accurate method, whereas the "equilibrium method" will give the most precise results.

Ideally a natural ore, undisturbed by any leaching, will contain amounts of all the daughter elements inversely proportional to the ratio of their half-lives to that of the mother isotope (U^{238} or Th^{232} respectively). This is the equilibrium condition and is found to exist particularly in pitchblende ores and in the majority of unexposed uranium minerals. If the uranium is finely dispersed or the ore is subject to natural leaching these equilibrium conditions may be upset, particularly through loss of the emanation (27). The emanating properties of various substances have been studied by Flügge and Zimens (12,45). In general, radon will escape fairly readily and hence uranium ores are frequently found to be out of equilibrium with a deficiency in the radium family, i.e. that part of the decay series which follows radon (See Table I). Thoron, on the other hand, has a half-life of only 54 sec. and cannot travel very far in that time (10,16), and thorium ores are usually found to be in equilibrium.

Of the indirect detection methods ordinary gamma detectors (36,1,7,39) are by far the most popular because of their inherent simplicity. Geiger tubes, though suitable for portable equipment (7), are being largely superseded by ionization chambers (19) and scintillation counters (5) which combine higher sensitivity with greater consistency. For assay purposes they all fail if the ore is out of equilibrium, as the gamma radiation is emitted mainly by Bi^{214} (RaC).

The same difficulty arises with beta counters. Here it is possible to get fairly high sensitivity with a suitable Geiger tube and finely ground ore samples but, again, the ore must be in equilibrium if more than indicative results are desired. Neither gamma nor beta methods can really distinguish between uranium and thorium.

Flow counter methods are particularly suitable for thorium determinations (14,15,37) but have also been used for radon measurements (20). In this method emanation is driven off from the dissolved ore sample and carried through a counting chamber by a stream of nitrogen. The counting rate is then proportional to the thorium content of the ore. This method is precise but rather slow and tedious and unsuited for large-scale routine work.

Photographic emulsion techniques are very popular for detailed work on specific mineral samples (44,3,38,4). They cannot seriously be considered for routine work because of the very long exposures required. However, their cheapness makes them suitable for many research investigations where detailed localization of the emitting mineral grains may be important.

An alpha-beta method has been proposed by Peirson (32). In this method use is made of the different half-lives of Po^{214} (RaC') and Po^{212} (ThC') to discriminate between the uranium and thorium series. The beta particles from Bi^{214} (RaC)

and $\text{Bi}^{212}(\text{ThC})$ initiate carefully timed gating circuits and the difference in counts from the two channels gives a measure of the Th/U ratio in the sample. The main drawback of such a system is the complexity of the electronic equipment, which makes it unsuitable for routine assay work. A further disadvantage lies in the fact that it can handle satisfactorily only high-grade samples of at least 1% U_3O_8 content, and requires long counting times.

An energy discrimination method designed to distinguish between the gamma radiations from $\text{Bi}^{214}(\text{RaC})$ and $\text{Bi}^{212}(\text{ThC})$ has been described by Whitham (42). In this method a scintillation detector with a variable discriminator is used to register the gamma radiation from the sample. By comparing the ratio of the counting rates at two predetermined discriminator settings and the total counting rate with a calibration curve, the thorium and radium contents of the sample can be established. The uranium content can be determined only if the sample is known (from outside evidence) to be in equilibrium.

Alpha discrimination methods are based on the difference in energy or range of the alpha particles from $\text{Po}^{214}(\text{RaC}')$ and $\text{Po}^{212}(\text{ThC}')$ respectively. Spark counters and scintillation counters have been used as detectors and the range varied by movement of the source (9) or by variation in air pressure (29). The low counting rates obtained make any such methods particularly susceptible to interference from emanation of radon or thoron from the sample and such an approach appears to be unsuitable for routine work.

The so-called "equilibrium method" for the determination of uranium in ores irrespective of its equilibrium condition was devised by Lapointe and Williamson (30) and, independently, by Thommeret (40). In essence it depends on a simultaneous measurement of the beta and gamma radiation emitted by the various decay products of the uranium series in order to avoid the need to determine the equilibrium value. This method, which has since been extended to include thorium determinations, forms the substance of the remainder of this paper.

3. THEORY OF THE EQUILIBRIUM METHOD

Inspection of Table I shows that practically all the gamma radiation emitted by a uranium mineral and detected is due to $\text{Bi}^{214}(\text{RaC})$ in the radium group alone. On the other hand for a sample in equilibrium approximately equal amounts of beta radiation should be emitted by $\text{Pa}^{234}(\text{UX}_2)$, $\text{Bi}^{214}(\text{RaC})$, $\text{Bi}^{210}(\text{RaE})$, and $\text{Pb}^{214}(\text{RaB})$. In practice, however, with thick sources and detectors of finite wall thickness it is found that the combined beta contribution of the radium group (Bi^{214} , Bi^{210} , and Pb^{214}) is only slightly greater than that of $\text{Pa}^{234}(\text{UX}_2)$ in the uranium group.

If, now, the equilibrium condition is disturbed by loss of radon from the ore—this is by far the most common cause of disequilibrium (26)—then the beta contribution from UX_2 is left undisturbed, but the radium group contributions to the beta and gamma activities are reduced. The equilibrium method consists of a reconstruction of the actual uranium content from a comparison of the total beta and gamma activities of the sample. The sole assumption implied in the method is that the ratio (UI/UX_2) has not been disturbed so that it can be applied to all but chemically purified ore samples.

The total beta counting rate for a sample in equilibrium can be expressed as

$$[1] \quad C_{\beta} = f(B_U + B_R)$$

where B_U and B_R are the beta contributions from the uranium and radium groups respectively. For a sample in equilibrium

$$B_R/B_U = a, \text{ a constant,}$$

and therefore

$$[2] \quad C_{\beta} = f(B_U + aB_U) = fB_U(1 + a).$$

Similarly, the gamma counting rate C_{γ} can be written as

$$[3] \quad C_{\gamma} = gG_R$$

where G_R is the gamma activity of the radium group when in equilibrium with the uranium; f and g are geometry factors. The gamma contribution of the uranium group may be neglected. The actual uranium content of the sample, U , in per cent U_3O_8 per gram ore can be written as

$$[4] \quad U = k_{\beta}C_{\beta} = k_{\gamma}C_{\gamma}$$

where k_{β} and k_{γ} are calibration constants of the apparatus, obtained with a sample known to be in equilibrium.

If the sample is out of equilibrium, such that the contribution of the radium family has been diminished to a fraction p of the equilibrium value, one obtains counting rates

$$[5] \quad C'_{\beta} = f(B_U + pB_R) = fB_U(1 + pa)$$

and

$$[6] \quad C'_{\gamma} = pgG_R.$$

The equilibrium fraction p can be eliminated between equations [5] and [6] as

$$[7] \quad p = \frac{C'_{\gamma}}{gG_R} = \frac{C'_{\gamma}}{C_{\gamma}} = \frac{U'_{\gamma}}{U},$$

where U'_{γ} is the apparent uranium equivalent derived from the gamma measurement using the calibration equation [4]. The true uranium content U can be obtained by comparing equations [4] and [5]:

$$\frac{U}{U'_{\beta}} = \frac{C_{\beta}}{C'_{\beta}} = \frac{1 + a}{1 + pa}$$

and inserting [7]

$$1 + pa = 1 + \frac{U'_{\gamma}a}{U} = \frac{U + aU'_{\gamma}}{U}.$$

Hence

$$[8] \quad U = U'_{\beta}(1 + a) - U'_{\gamma}a.$$

This is the basic equation of the equilibrium method. The most notable feature of equation [8] is the complete absence from it of the calibration constants k_{β} and k_{γ} , and the geometry factors f and g as such, although, of course, they are implied in the definition of the uranium equivalents U'_{β} and U'_{γ} . That means

that equation [8] is valid for any beta-gamma system no matter what its sensitivity or geometry may be. Furthermore, there is no need to establish the equilibrium condition or its lack in the sample. The only constant appearing in the equation is a which indicates the relative contribution of the uranium and radium groups to the total beta activity. For practical systems with detectors of finite wall thickness and with thick sources the softest beta rays are not detected. The ratio a has been determined experimentally using aged natural pitchblende of known composition and pure uranium oxide. The value obtained was

$$a = \frac{B_R}{B_U} = \frac{57\%}{43\%} = 1.30$$

and equation [8] may be written

$$[9] \quad U = 2.30 U''_{\beta} - 1.30 U'_{\gamma}.$$

Underlying this discussion has been the assumption that B_U bears a fixed relation to the uranium content of the ore. This has been found to be the case for almost all natural ores as the $\text{Pa}^{234}(\text{UX}_2)$ content of an ore quickly regains its equilibrium value after a disturbance because of the relatively short half-life of $\text{Pa}^{234}(\text{UX}_2)$ (1.18 min.) and of $\text{Th}^{234}(\text{UX}_1)$ (24.1 days).

Another case of importance arises when there is also some thorium present in the ore. Owing to the short half-life of thoron all the members of the thorium family can normally be assumed to be present in the equilibrium proportions. Equations [2] and [3] can then be expressed as follows:

$$[10] \quad C''_{\beta} = fB_U(1 + a) + fB_T$$

and

$$[11] \quad C''_{\gamma} = g(G_R + G_T).$$

If the sample contains thorium only and no uranium, one obtains a calibration equation analogous to [4],

$$[12] \quad T = l_{\beta} f B_T = l_{\gamma} g G_T,$$

where T = thorium content in percent per gram and l_{β} and l_{γ} are the calibration constants.

Inserting these values in [10] and [11] gives

$$[13] \quad \begin{cases} C''_{\beta} = fB_U(1 + a) + (T/l_{\beta}) = C_{\beta} + (T/l_{\beta}), \\ C''_{\gamma} = gG_R + (T/l_{\gamma}) = C_{\gamma} + (T/l_{\gamma}). \end{cases}$$

Eliminating T between these equations and introducing the uranium content U from [4] gives

$$l_{\beta} C'_{\beta} - l_{\gamma} C''_{\gamma} = l_{\beta} C_{\beta} - l_{\gamma} C_{\gamma} = U \left(\frac{l_{\beta}}{k_{\beta}} - \frac{l_{\gamma}}{k_{\gamma}} \right).$$

Hence

$$[14] \quad \begin{aligned} U &= \left(\frac{l_{\beta}}{k_{\beta}} U''_{\beta} - \frac{l_{\gamma}}{k_{\gamma}} U''_{\gamma} \right) / \left(\frac{l_{\beta}}{k_{\beta}} - \frac{l_{\gamma}}{k_{\gamma}} \right) \\ &= U''_{\beta}(1 + b) - U''_{\gamma}b \end{aligned}$$

where U''_{β} and U''_{γ} are again the apparent uranium equivalents, and

$$[15] \quad b = \frac{1}{(k_{\gamma}l_{\beta}/k_{\beta}l_{\gamma}) - 1}.$$

The formal similarity between equations [8] and [14] is notable and due essentially to the similarity in the radiation characteristics of the thorium and radium families, i.e. thorium gives rise to an effect similar to that of an excess of radium.

Substituting the experimental values of the calibration constants, b is found to have the value

$$1/0.77 = 1.29, \text{ i.e. } b \approx a,$$

so that [9] may be considered to apply equally well in both cases.

Lastly, consider the general case with uranium and thorium both present and the uranium out of equilibrium by a factor p .

The counting rate equations now read:

$$[16] \quad C'_{\beta} = fB_U(1 + pa) + fB_T$$

and

$$[17] \quad C'_{\gamma} = gpG_R + gG_T.$$

In terms of the uranium and thorium contents

$$[18] \quad \begin{cases} C'_{\beta} = \frac{U'_{\beta}}{k_{\beta}} = \frac{U}{k_{\beta}} \cdot \frac{1 + pa}{1 + a} + \frac{T}{l_{\beta}}, \\ C'_{\gamma} = \frac{U'_{\gamma}}{k_{\gamma}} = \frac{U}{k_{\gamma}} \cdot p + \frac{T}{l_{\gamma}}. \end{cases}$$

Eliminating p between these equations and rearranging gives

$$[19] \quad U = U'_{\beta}(1 + a) - U'_{\gamma} \cdot a - T \left[\frac{k_{\beta}l_{\gamma}(1 + a) - a k_{\gamma}l_{\beta}}{(1 + a) l_{\beta}l_{\gamma}} \right],$$

but

$$\frac{k_{\beta}l_{\gamma}}{k_{\gamma}l_{\beta}} = \frac{b}{1 + b} = \frac{a}{1 + a}$$

so that the coefficient of T vanishes and [19] is equivalent to [8].

It is, therefore, possible to determine the uranium content of any ore even if it is out of equilibrium or if it also contains thorium. As thorium leads to excess gamma counts, whereas a loss of radon leads to a decrease in gamma counts, it is not possible to assay the thorium precisely if it is mixed with uranium which is out of equilibrium with its decay products. If the ratio Th/U is greater than 10, a fairly close result can be obtained even in that case, though.

The thorium content of an ore can be determined in the following way. After applying equation [9] to calculate the uranium content, use the calibration constants, equation [4], to compute the contribution of this uranium to the beta and gamma counting rates. After subtraction of these contributions the thorium calibrations, equation [12], will give two independent determinations of the thorium content of the ore. If the two thorium values should disagree the ore

is one of the relatively rare thorium ores in which the uranium is strongly out of equilibrium, and in which the thorium contents must be determined by chemical analysis. In the majority of cases the availability of two independent thorium determinations affords a valuable check on the validity and precision of the method.

An alternative method is to eliminate the uranium contributions from equations [13] and to solve for T . This leads to

$$U''_{\beta} - U''_{\gamma} = T \left(\frac{k_{\beta}}{l_{\beta}} - \frac{k_{\gamma}}{l_{\gamma}} \right)$$

or

$$[20] \quad T = \frac{U''_{\gamma} - U''_{\beta}}{c},$$

where

$$c = \frac{k_{\gamma}}{l_{\gamma}} - \frac{k_{\beta}}{l_{\beta}}.$$

Inserting again the experimental values of the calibration constants gives $c = 0.165$, or

$$[21] \quad T \approx 6(U''_{\gamma} - U''_{\beta}).$$

This is a particularly simple equation to apply but in the absence of the self-checking feature of the previous method some outside information must be available to confirm the equilibrium of the uranium present. In addition, for low grade ores ($U''_{\gamma} - U''_{\beta}$) may be a rather small quantity and the result obtained from equation [21] is very sensitive to small statistical fluctuations in either U''_{β} or U''_{γ} . In case of doubt, therefore, the longer procedure outlined before should be followed.

4. DESCRIPTION OF APPARATUS

The present equipment has been designed to handle crushed ore samples powdered to minus 100 mesh or less in quantities varying from 50 to 100 gm. That amount is sufficient to ensure good sampling and adequate counting rates without demanding excessive quantities of ore.

The apparatus proposed initially by Lapointe (28) consisted of an annular container surrounding a gamma sensitive Geiger tube, with another beta sensitive Geiger tube outside it. To obtain easier handling of the samples this was later replaced by an arrangement in which two Geiger tubes are mounted parallel, one above and one below, to a long rectangular sample tray. This is the arrangement discussed in detail by Wilmot and McMahon (43) who also dealt with many constructional and practical matters pertaining to radiometric assaying. Another system using an ionization chamber has been proposed by Roethlisberger (35).

Such systems are not sensitive enough to handle very low grade ore samples, i.e. the counting rate obtained in that case is too small statistically to give a consistent result in less than about 15 min. which would have a probable error of less than 8%. They are perfectly adequate to handle high grade samples

containing 1% or more U_3O_8 and for such samples there would be no advantage in trying to attain higher sensitivity.

The main statistical limitation of the Geiger system lies in the low efficiency of its gamma counter. By changing the gamma detector to a scintillation counter the gamma sensitivity was increased by a factor of 200 and the signal-to-background ratio improved by a factor of 60 (18). To utilize fully the time-saving made possible by the increase in gamma sensitivity the beta counting rate has also been increased by an improvement in geometry made possible by the use of a pill-box shaped Geiger tube.

The whole assembly is shown in Fig. 1 with the brass gamma filter removed to show closeness of sample tray and scintillation crystal.

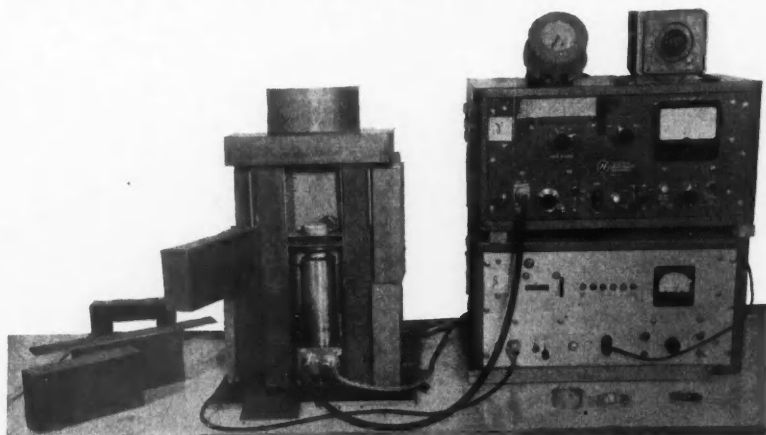


FIG. 1. Photograph of apparatus.

The lead shielding bricks in front of the counting chamber have been removed and the hinged lead door swung open. The sample pan (Cenco No. 12715) is placed into a brass slide in the middle of the chamber which locates it directly above the scintillation crystal and immediately below the beta detector. In this way almost perfect 2π geometries are obtained. The gamma detector consists of a 5819 photomultiplier tube with a thallium-activated sodium iodide crystal as detector. For protection, the crystal, which is cylindrical in shape, 2.6 cm. long and 3.2 cm. in diameter, is mounted inside a small aluminum container with a transparent Lucite window at one end, and completely immersed in silicone oil (DC 200) to exclude all moisture. The window is placed on the photosensitive end of the photomultiplier with a thin silicone film for optical contact. A preamplifier unit is attached to the photomultiplier tube containing a single 6 AK 5 amplifier stage and a 6 AK 5 cathode follower. A brass absorber plate is normally inserted between sample tray and phosphor to eliminate the possibility of the gamma detector counting beta rays.

The beta detector is a halogen-filled cylindrical Geiger tube with a large 3 mgm. per $cm.^2$ mica window (Anton type 1001 H). Such a window thickness

will transmit all the more energetic particles. Halogen-filled tubes have a much longer life than organic-vapor quenched ones and more stable operation, quite apart from their better geometry, should result from their use.

The counting chamber is surrounded by 10 cm. of lead to reduce cosmic background. Commercial scaling units, actuated by a common timer, have been used.

The sample pans used can be seen in Fig. 1. They are aluminum dishes, 5 cm. in diameter, holding 50 to 80 gm. of ore sample. For high grade material containing more than 1% U_3O_8 equivalent shallower and smaller pans are used to keep the counting rate at a level that can be handled by the scalers and registers without causing overloading.

5. EXPERIMENTAL RESULTS

The system has been calibrated for uranium by means of chemically assayed aged pitchblende samples of various grades and for thorium with old thorium salt samples, also chemically analyzed. Using a number of such samples the mean calibration factor for samples in a fixed geometry is determined in terms of the number of counts per per cent U_3O_8 per gram sample. To avoid packing errors it is advisable to crush all samples to the same mesh size as the beta activity is essentially a surface activity and varies somewhat with surface

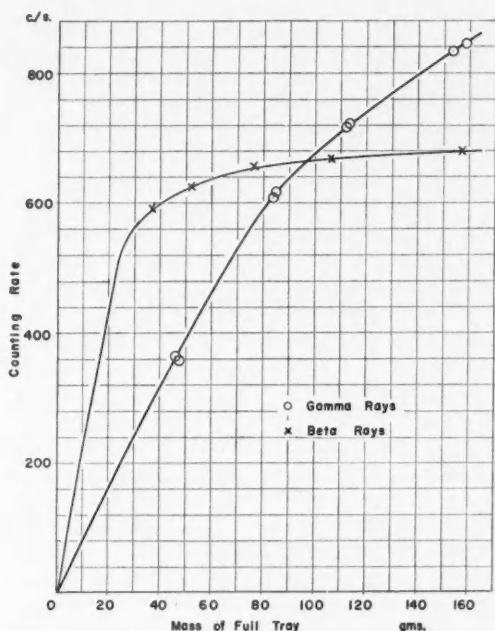


FIG. 2. Self-absorption curves. Effect of sample density on counting rates.

grain size. The commonly employed method of specifying uranium content in $\%U_3O_8$ per gram of sample also makes it necessary to correct for variations in density of the rock, both as it affects the weight and self-absorption of the sample. In practice this weight correction has been found to be appreciable only for the gamma determination which is due to the volume radiation of the sample. The beta activity is essentially independent of the sample density provided that the tray depth is large enough to exceed the range in the ore of the most energetic beta particles present. Such a sample then approximates the condition of infinite thickness. This condition is responsible for the flat part of the beta absorption curve in Fig. 2.

Fig. 2 shows the effect of density variation of the sample on the counting rate. It was obtained from measurements on artificial pitchblende mixtures, all containing 0.96% U_3O_8 by weight with various filler materials (18). The gamma absorption in the sample depends primarily on the electron density and is practically proportional to the sample density.

In the system used the density correction amounted to 0.16 count per second per 100 counts per gram and is to be subtracted from the gamma count for samples weighing less than 80 gm. and added to it for weights above 80 gm. This correction becomes appreciable only when the sample contains more than 0.25% U_3O_8 . As the absorption curve is not a straight line, it is advisable to use a standard sample of comparable density if the difference in density is appreciable.

The only other correction of importance is a resolving time correction applicable to the beta counting rate because of the relatively long dead time (20 μ sec.) of a Geiger tube compared with a scintillation counter, which results in a loss of counts at high counting rates. This correction has been determined experimentally and was found to amount to 0.5×10^{-4} (number of counts per second)² in the present system.

After adding these two corrections and allowing for background counts, the experimental data must be corrected for changes in sensitivity of the equipment to avoid the need for frequent recalibration. This is achieved most easily by running a permanent sealed uranium source under standard conditions at regular intervals between samples. The ratio of its momentary counting rate to that obtained at the time of calibration provides a convenient "sensitivity factor".

The corrected counting rate is then converted to $\% U_3O_8$ content using calibrating factors obtained with carefully chemically assayed standards. The over-all sensitivity of the system is such that 2 to 3% accuracy can be obtained in five-minute runs for samples containing down to 0.002% U_3O_8 . Higher precision is limited by difficulties in sampling and filling, weighing errors, normal statistical fluctuations of the detectors, and uncertainty of the same order (2 to 3%) in the chemical assay of the standard samples. Table III contains a selection of run-of-the-mill uranium ore samples from various sources and several thorium-bearing ores to show typical results obtained.

The table has been arranged in groups: Nos. 1 to 9 are typical samples containing uranium in equilibrium, Nos. 10 to 17 are samples out of equilibrium due to loss of the radium group ($U_\beta/U_\gamma > 1$), and Nos. 18 to 30 show a gamma

TABLE III
EXPERIMENTAL RESULTS

No.	Test No.	U'_{γ}	U'_{β}	U_3O_8 % calc.	U_3O_8 chemical	T_{γ}	T_{β}	$6(U'_{\gamma} - U'_{\beta})$	ThO ₂ chemical
1	174-1	0.001	0.001	0.001	0.001				
2	289-1	0.012	0.012	0.012	0.012				
3	418-1	0.025	0.026	0.027	0.026				
4	214-1	0.063	0.064	0.065	0.064				
5	213-1	0.216	0.219	0.22	0.22				
6	419-1	0.29	0.30	0.31	0.30				
7	426-1	0.565	0.572	0.58	0.58				
8	141-1	0.777	0.770	0.77	0.7				
9	420-2	1.36	1.365	1.37	1.37				
10	15-310	0.193	0.196	0.20	0.20				
11	21-310	0.049	0.055	0.063	0.064				
12	297-1	0.057	0.066	0.078	0.075				
13	3060M	0.075	0.097	0.12	0.12				
14	282-1	0.156	0.180	0.21	0.24				
15	256-1	0.535	0.579	0.64	0.64				
16	477-2	0.80	0.83	0.87	0.84				
17	203-1	1.062	1.156	1.25	1.29				
18	388-1	0.029	0.020	0.009	0.008	0.05	0.05	0.05	
19	148-1	0.044	0.038	0.032	0.032	0.024	0.024	0.036	
20	2706	0.0048	0.0037	0.002	0.0019	0.007	0.008	0.007	
21	13-308	0.054	0.032	0.003	0.0024	0.145	0.145	0.13	0.13
22	H12-1	0.060	0.047	0.030	0.027	0.083	0.077	0.073	0.08
23	309-3	0.383	0.358	0.32	0.31	0.16	0.15	0.15	
24	408-1	0.152	0.114	0.065	0.07	0.24	0.22	0.23	0.2
25	387-1	0.51	0.45	0.38	0.38	0.35	0.32	0.36	0.21
26	149-1	0.87	0.74	0.61	0.58	0.52	0.52	0.78	
27	140-3	1.29	1.01	0.73	0.78	1.55	1.30	1.68	1.42
28	306-3	1.77	1.70	1.61	1.69	0.43	0.42	0.42	
29	305-3	2.14	2.07	1.97	1.99	0.46	0.46	0.42	
30	143-3	6.32	4.61	2.90	2.82	9.26	7.94	10.26	<0.05
31	393-3	3.86	2.27	0.21	0.3	10.08	10.03	9.54	8.88

excess due to the presence of thorium or excess radium. It shows the order of magnitude of assays that can be handled. Ores containing more than 2% U_3O_8 can be assayed more conveniently in a Geiger tube equilibrium system, like that described by Wilmot and McMahon (43). The "chemical" U_3O_8 values are mostly fluorimeter determinations and subject to a 4 to 5% probable error.

Samples No. 18 to 31 are of particular interest as they show clearly the accuracy obtainable in determining the thorium content of the ore, even in the presence of measurable amounts of uranium. Conversely, No. 21 is an example of how a small amount of uranium can be determined in the presence of much larger quantities of thorium. In sample No. 27 the thorium determinations are not self-consistent and it can be assumed that there may be excess radium in the sample to account for the high gamma activity. In this case a chemical analysis will be required to give a complete analysis and the radiometric data serve as a useful guide to the order of magnitude of radium and thorium that can be expected. Sample No. 30 is a good example to show how use of equation [21] alone may give a misleading result. The discrepancy between T_{β} and T_{γ} indicated

a possible radium excess and this was confirmed by the chemical analysis for thorium.

It can be seen that the thorium determinations are rather less accurate than the uranium assays. This is due to the indirect way in which the thorium values are obtained which tends to make any small error cumulative.

6. DISCUSSION

As Table III shows, normal mine samples can be assayed quite precisely over a wide range of uranium and thorium content. Its speed and the ease of sample preparation make this method preferable to any other chemical or physical method for the assay of natural unaltered ore samples. Anomalies due to enrichment of the radium content alone or lack of uranium equilibrium in thorium-bearing ores can usually be deduced by inspection of the beta and gamma equivalents and in such cases the equilibrium method serves as a useful guide to any detailed chemical analysis required.

Two factors arising from the theoretical considerations in Section 3 might usefully be discussed here. The first one concerns the gamma sensitivity of the beta detector. This has been measured and it was found that the gamma contribution to the beta count C_β amounts to 5% under equilibrium conditions. This contribution is automatically included in the calibration and no special correction is required as even for a sample as much as 50% out of equilibrium the change in beta counting rate due to this factor alone would not exceed 1.5%.

The second point concerns the contribution to the gamma counting rate of the gamma rays from Pa^{234} (UX_2 and UZ). In formulating equation [3] it was assumed that this contribution can be neglected. Reference to a Table of Nuclear Data (41) shows that the following gamma rays are emitted by this isotope: 0.782 Mev. and 0.822 Mev. in 2% of all decays each, 1.5 Mev. in 0.2% of all UX_2 decays, and 0.8 Mev. from UZ in 0.12% of all UX_2 decays, i.e. roughly 4% of all beta emissions from UX_2 are accompanied by a 0.8 Mev. gamma ray. These rays pass through a 1/16 in. brass filter plate and 1/8 in. aluminum before reaching the crystal phosphor. The absorption coefficient for aluminum at 0.8 Mev. is 66% higher than for the 2 Mev. gamma rays of Bi^{214} (RaC) and as the response of the sodium iodide crystal is proportional to the energy of the radiation the transmitted radiation is only one-third to one-half as effective as the high energy gamma radiation from RaC . Its contribution is included in the gamma calibration values while its effect on the change in gamma counts with equilibrium changes may be regarded as negligible.

The equilibrium method as described can thus be applied with ease to any powdered mineral to give precise assays of uranium and, in the majority of cases, of thorium. The upper limit of uranium content that can be handled is set essentially only by the mechanical arrangements for locating trays and detectors. Above 2% U_3O_8 content it has been found more convenient in practice to use less sensitive detectors and/or a less favorable geometry than that described here. The lower limit of detection is governed largely by statistical considerations. However, below 0.002% U_3O_8 content corrections may have to

be applied for potassium content in the natural ore as 1% K_2O is approximately equivalent to 0.0007% U_3O_8 as regards beta activity. Large potassium concentrations show themselves by producing a higher ratio of beta-to-gamma uranium equivalents but owing to the high ratio of uranium to potassium activities no serious discrepancies in the uranium assays have been found so far.

ACKNOWLEDGMENTS

It is a pleasure to acknowledge the advice and assistance of our colleagues in the Radioactivity Division, notably Dr. E. A. Brown and Dr. C. Lapointe.

This paper is published by permission of the Director-General of Scientific Services, Department of Mines and Technical Surveys, Ottawa.

REFERENCES

1. BEHOUNEK, F. Collection Czechoslov. Chem. Commun. 15: 699. 1950.
2. BIRKS, L. S. Rev. Sci. Instruments, 22: 891. 1951.
3. BOWIE, S. H. U. Great Britain Geol. Survey, Bull. No. 3: 58. 1951.
4. BREMNER, J. W. Proc. Phys. Soc. (London), A, 64: 25. 1951.
5. CHATTERJEE, S. and DHAR, S. Indian J. Phys. 24: 346. 1950.
6. COPPENS, R. J. phys. radium, 11: 21. 1950.
7. DAVIDSON, C. F. A prospector's handbook to radioactive mineral deposits. H.M. Stationery Office, London. 1949.
8. DIEKE, G. H. and DUNCAN, A. B. F. Spectroscopic properties of uranium compounds. McGraw-Hill Book Company, Inc., New York. 1949.
9. EICHHOLZ, G. G. Nucleonics, 10 (10): 46. 1952.
10. EICHHOLZ, G. G. and FLACK, F. C. J. Chem. Phys. 19: 363. 1951.
11. FINNEY, G. D. and EVANS, R. D. Phys. Rev. 48: 503. 1935.
12. FLÜGGE, S. and ZIMENS, K. Z. physik. Chem. B, 42: 179. 1939.
13. FRIEDMAN, H. and BIRKS, L. S. Rev. Sci. Instruments, 19: 323. 1948.
14. GÜBELI-LITSCHER, O. and KOLB, W. Helv. Chim. Acta, 33: 1526. 1950.
15. GREGORY, J. N. and HOWLETT, J. 1949. (Unpublished.)
16. GREGORY, J. N. and MOORBATH, S. Trans. Faraday Soc. 47: 844. 1951.
17. HAPF, W. W. and HORWOOD, J. L. Science, 115: 622. 1952.
18. HILBORN, J. W. M.A. Thesis, McGill University, Montreal, Que. 1951.
19. HORWOOD, J. L. and McMAHON, C. Can. Mining J. 71 (No. 4): 56. 1950.
20. HUDGENS, J. E., BENZING, R. O., CALI, J. P., MEYER, R. C., and NELSON, L. C. Nucleonics, 9 (2): 14. 1951.
21. HULL, D. E. The counting method of isotopic analysis of uranium, MDCC-387. 1946.
22. INGLES, J. C. The chemical determination of thorium in its ores. Memorandum No. 110. Dept. of Mines & Tech. Surveys, Mines Branch, Ottawa. 1951.
23. JOLIOT-CURIE, I. J. phys. radium, 7: 313. 1946.
24. JOLIOT-CURIE, I. Les radioelements naturels. Hermann & Cie., Paris. 1946.
25. JOLIOT-CURIE, I. and FARAGGI, H. Compt. rend. 232: 959. 1951.
26. KEEVIL, N. B. and GRASHAM, W. E. Can. J. Research, A, 21: 21. 1943.
27. KEEVIL, N. B., KEEVIL, A. R., INGHAM, W. N., and CROMBIE, G. P. Am. J. Sci. 241: 345. 1943.
28. LAPOINTE, C. M. Can. Mining Met. Bull. No. 460. 43: 465. 1950; Trans. Can. Inst. Mining Met. 53: 465. 1950.
29. LAPOINTE, C. M. Private communication.
30. LAPOINTE, C. M. and WILLIAMSON, D., 1948. Reissued as Mines Branch Topical Report TR-101/52, Ottawa. 1952.
31. NOGAMI, H. H. and HURLEY, P. M. Trans. Am. Geophys. Union, 29: 335. 1948.
32. PEIRSON, D. H. Proc. Phys. Soc. (London), B, 64: 876. 1951.
33. RABBITS, F. T. Can. Mining Met. Bull. No. 477. 45: 27. 1952.
34. RODDEN, C. J. Analytical chemistry of the Manhattan project. McGraw-Hill Book Company, Inc., New York. 1950.
35. ROETHLISBERGER, R. H. AECD-3062. 1949.
36. RUSSELL, W. L. and SCHERBATS KOV, S. A. Econ. Geol. 46: 427. 1951.
37. SENTLE, F. E. and KEEVIL, N. B. Trans. Am. Geophys. Union, 28: 732. 1947.
38. STIEFF, L. and STERN, T. W. Am. Mineral. 37: 184. 1952.
39. SZALAY, A. and CSONGOR, E. Science, 109: 146. 1951.
40. THOMMERET, J. J. phys. radium, 10: 249. 1949.
41. WAY, K., FANO, L., SCOTT, M. R., and THEW, K. Nuclear Data, Natl. Bur. Standards, Circ. 499. Washington. 1950.

42. WHITHAN, K. Ph.D. Thesis, Toronto University. 1951.
43. WILMOT, R. D. and McMAHON, C. Radioassay of uranium with the Geiger-type equilibrium counter. Mines Branch Memorandum No. 115. Dept. of Mines & Tech. Surveys, Ottawa. 1951.
44. YAGODA, H. Radioactive measurements with nuclear emulsions. John Wiley & Sons, Inc., New York. 1949.
45. ZIMENS, K. Z. physik. Chem. A, 191: 1, 95. 1942; 192: 1. 1943.
46. ZIMMERMAN, J. B. Can. Mining Met. Bull. No. 477. 45: 32. 1952.

THEORY OF THE ELECTROMAGNETIC VACUUM. I¹

By F. A. KAEMPFFER

ABSTRACT

The reasons are restated and amended which make it possible to consider the electromagnetic vacuum as a nonviscous fluid in which excitations of the motion appear as observable particles. It is shown, in close formal analogy to Dirac's new electrodynamics, that the electromagnetic vacuum can be characterized at each point in space time by a scalar function κ , representing the ratio (energy density)/(charge density) of the medium, and by a four-vector v^μ , representing the state of motion of the medium at that point. As a first step towards quantization of this theory a spinor formulation of electrodynamics is set up which allows possible excitations of the vacuum to be classified. The program for full quantization of this theory is outlined.

1. THE HYDRODYNAMIC ANALOGY

In a preceding paper the author (5) has proposed to consider Dirac's (2) new electrodynamics as the correct description of the electromagnetic vacuum at the absolute zero of temperature. It is then possible to picture the electromagnetic vacuum as a nonviscous fluid, and to identify excitations of the motion of this vacuum fluid with observable particles. If one restricts the consideration to nonrelativistic velocities in the vacuum fluid, it turns out that vortexfree excitations of the vacuum fluid are not sources of an observable electromagnetic field, and are therefore identified with neutral particles, while vortex excitations of the vacuum fluid will always become sources of an observable electromagnetic field, and should therefore correspond to charged particles. The justifications for this point of view may be restated and amended as follows.

We define the electromagnetic vacuum as the state in which no observable electromagnetic fields are present, i.e.

$$[1] \quad -\mathbf{E} \equiv \text{grad } \phi + \frac{1}{c} \frac{\partial \mathbf{A}}{\partial t} = 0; \quad \mathbf{H} \equiv \text{curl } \mathbf{A} = 0,$$

these equations expressing through the identity signs in them the desire to maintain the usual relations between electromagnetic fields \mathbf{E}, \mathbf{H} and electromagnetic potentials ϕ, \mathbf{A} . Introduction of Dirac's electrodynamics is now established by postulating for the electromagnetic potentials the relation

$$[2] \quad \phi = \sqrt{\kappa^2 + A^2} = \kappa + \frac{1}{2\kappa} A^2 + \dots,$$

the expansion of the root being valid only for small velocities in the vacuum fluid. In Dirac's first paper (2) the symbol κ was identified with mc^2/e , and m and e being mass and charge of the electron respectively. We shall not follow this identification, but instead modify Dirac's theory decisively by demanding that the potentials ϕ, \mathbf{A} should be gauge-invariant, i.e. the condition

$$[3] \quad \frac{1}{c} \frac{\partial \phi}{\partial t} + \text{div } \mathbf{A} = 0$$

¹ Manuscript received January 19, 1953.

Contribution from the Department of Physics, University of British Columbia, Vancouver, B.C.

should be satisfied. The remarkable fact now is that *this can be done, if one does not consider κ as a constant, but instead assumes that*

$$[4] \quad \kappa = \kappa(x, y, z, t)$$

is a scalar function of the coordinates and the time, which is subject to the two conditions [2] and [3]. It is then readily seen that the equations [1] and [3] become formally identical with the classical Bernoulli equations of a non-viscous fluid (in the approximation $v \ll c$):

$$[1a] \quad \frac{\partial \mathbf{v}}{\partial t} + \text{grad} \left(\frac{v^2}{2} \right) = - \frac{1}{\rho} \frac{dP}{d\rho} \text{grad } \rho; \quad \text{curl } \mathbf{v} = \frac{1}{\rho} [\mathbf{v} \times \text{grad } \rho],$$

$$[1b] \quad \frac{\partial \rho}{\partial t} + \text{div} (\rho \mathbf{v}) = 0$$

provided we identify:

$$[5] \quad \mathbf{A} = \frac{\kappa}{c} \mathbf{v}, \quad \kappa = \rho; \quad c = \sqrt{\frac{dP}{d\rho}} = \text{velocity of "sound"}.$$

In other words, the equations of the electromagnetic vacuum state are formally identical with the classical equations of a nonviscous fluid of "density" $\kappa = \rho$, the condition of gauge-invariance corresponding to the law of conservation of substance, and the velocity of "sound" in this fluid being equal to c .

2. PRELIMINARY REFORMULATION OF ELECTRODYNAMICS

On the strength of this formal analogy we shall now adopt the following point of view: The electromagnetic vacuum is a medium which can be characterized at each point in space time by a scalar function $\kappa = \kappa(x, y, z, t)$ and a four-vector velocity field $v^\mu = v^\mu(x, y, z, t)$. Since κ must be dimensionally of the form (energy density)/(charge density) we visualize the medium to be associated at each point in space time with a certain energy density and a certain charge density, the ratio of which may vary from point to point. It should then be possible to construct a theory in which observable electromagnetic fields are produced at a certain point whenever κ and v^μ vary in the vicinity of that point in a prescribed way, while vacuum in absence of observable electromagnetic fields should appear as the state in which κ and v^μ fulfill equations which may be determined from the vacuum equations [1], [3], [5], and which result from setting $F^{\mu\nu} = 0$ in equation [16] of section 3 of this paper.

As a preliminary step towards such a theory we investigate some consequences of the following assumptions, in close analogy to the theory proposed by Dirac (2, 3).

The electromagnetic field tensor $F^{\mu\nu}$ is derived (in four-dimensional notation) as usual from electromagnetic potentials A^μ by

$$[6] \quad F^{\mu\nu} = \frac{\partial A^\nu}{\partial x_\mu} - \frac{\partial A^\mu}{\partial x_\nu},$$

where the potentials A^μ are subject to the condition of gauge invariance

$$[7] \quad \frac{\partial A^\mu}{\partial x^\mu} = 0.$$

We describe now A^μ in terms of a scalar function κ and a vector function v^μ such that

$$[8] \quad A^\mu = \kappa v^\mu$$

and we associate in our mind κ with the ratio (energy density)/(charge density) of the medium in which electromagnetic phenomena may occur, and v^μ with the velocity four-vector field of possible excitations of the motion in that medium. The field equations follow then from the action principle

$$[9] \quad \delta \int \mathcal{L} d^4x = 0; \quad \mathcal{L} = -\frac{1}{4} F_{\mu\nu} F^{\mu\nu} + \lambda \frac{\partial A^\mu}{\partial x^\mu}$$

and are found to be, if A^μ and the Lagrangian multiplier λ are taken as independent field variables,

$$[10] \quad \frac{\partial F_{\mu\nu}}{\partial x_\nu} = -\frac{\partial \lambda}{\partial x^\mu}; \quad \frac{\partial A^\mu}{\partial x^\mu} = 0.$$

It is seen that the four-vector of the current density j_μ must be

$$[11] \quad j_\mu = \frac{\partial \lambda}{\partial x^\mu}$$

and that the condition of gauge invariance guarantees as usual the law of conservation of charge

$$[12] \quad \frac{\partial j_\mu}{\partial x_\mu} = \frac{\partial^2}{\partial x^\nu \partial x_\nu} \frac{\partial A_\mu}{\partial x_\mu} = 0.$$

It seems further worth noting that from the point of view of this theory it is not necessary to introduce two extra variables ξ and η , as proposed by Dirac (3) in his second paper, in order to allow for vortex motion. The foundation of Dirac's latest theory is the relation

$$[13] \quad A_{\text{Dirac}}^\mu = \kappa v^\mu + \xi \frac{\partial \eta}{\partial x_\mu}$$

with k a constant, ξ and η being two functions which are not uniquely determined, but can be replaced by any two functions of them such that the Jacobian is unity. The tensor of the observable electromagnetic fields $F^{\mu\nu}$ can thus, according to Dirac, be written in the form

$$[14] \quad F^{\mu\nu} = k \left(\frac{\partial v^\nu}{\partial x_\mu} - \frac{\partial v^\mu}{\partial x_\nu} \right) + \left(\frac{\partial \xi}{\partial x_\mu} \frac{\partial \eta}{\partial x_\nu} - \frac{\partial \xi}{\partial x_\nu} \frac{\partial \eta}{\partial x_\mu} \right).$$

It was then shown by Buneman (1) that indeed

$$[15] \quad \oint \xi d\eta = \text{vorticity along the line of integration.}$$

Now it is readily seen that our identification [8], with κ a scalar function, gives rise to vorticity in a similar way but without the introduction of new variables. Substituting [8] into the definition [6] of the electromagnetic fields we obtain

$$[16] \quad F^{\mu\nu} = \kappa \left(\frac{\partial v^\nu}{\partial x_\mu} - \frac{\partial v^\mu}{\partial x_\nu} \right) + \left(\frac{\partial \kappa}{\partial x_\mu} v^\nu - \frac{\partial \kappa}{\partial x_\nu} v^\mu \right)$$

which establishes with respect to the second terms in the expression for $F^{\mu\nu}$ the formal correspondence

$$[17] \quad (\xi)_{\text{Dirac}} \rightarrow \kappa; \quad \left(\frac{\partial \eta}{\partial x_\mu} \right)_{\text{Dirac}} \rightarrow v^\mu$$

and therefore

$$[18] \quad \{ \oint \xi d\eta \}_{\text{Dirac}} \rightarrow \oint \kappa (v^\mu dx_\mu) = \text{vorticity along line of integration.}$$

It should be kept in mind, however, that despite this formal analogy of the second terms in the expressions for $F^{\mu\nu}$ our interpretation of vorticity is entirely different from the one considered by Dirac. In Dirac's theory $\oint \xi d\eta$ represents vorticity along lines in a medium consisting of actually observable electrons, while in our theory $\oint \kappa (\mathbf{v} \cdot d\mathbf{s})$ represents vorticity along lines in the medium called vacuum, which plays the part of an underlying liquid, and in which electrons may appear as excitations of the motion.

3. SPINOR FORMULATION OF ELECTRODYNAMICS

In order to obtain particles, neutral or charged, as excitations of the motion of the vacuum fluid, which is characterized by the scalar function κ and the velocity four-vector field v^μ , we shall have to quantize the theory outlined in the preceding paragraphs. Such a quantization procedure would correspond then to the quantization of ordinary hydrodynamics, which was first accomplished by Landau (6), and which leads to the appearance of phonons and rotons in the underlying liquid.

Quantization of this theory means that κ and v^μ shall have to be considered as operators which should fulfill certain commutation relations. We shall attempt to carry out this quantization in two steps. In the first step we shall look upon κ still as an ordinary scalar function, but replace everywhere v^μ by the Dirac matrices α^μ . It is clear that this choice represents a new hypothesis. It is suggested, however, by the well-known fact that v^μ is the expectation value of the operator α^μ in the relativistic theory of the electron. We shall refer to the theory resulting from this choice as the "spinor formulation of electrodynamics". The second step will then consist of replacing κ by an operator as well, as outlined in section 4 of this paper.

The basis of this spinor formulation of electrodynamics is then the operator identification

$$[19] \quad A^\mu = \kappa \alpha^\mu$$

where the α^μ satisfy the commutation relations

$$[20] \quad \alpha^\mu \alpha^\nu + \alpha^\nu \alpha^\mu = 2\delta^{\mu\nu}.$$

Equations [19] and all subsequent equations containing one or more α^μ 's have to be read as operator equations, i.e. they always correspond to a set of four linear spinor equations. The spinor equations corresponding to [19], for example, are:

$$[19a] \quad A^\mu \begin{pmatrix} u_1 \\ u_2 \\ u_3 \\ u_4 \end{pmatrix} = \kappa \alpha^\mu \begin{pmatrix} u_1 \\ u_2 \\ u_3 \\ u_4 \end{pmatrix}.$$

As long as κ is considered to be an ordinary scalar function the choice of the functions u , appearing in the spinor is quite arbitrary, since α^μ operates upon the index of these functions only. We shall therefore take $(u_\mu) = \text{constant}$ for the time being, and manipulate only the operators themselves. It should be kept in mind, however, that this procedure will no longer be admissible as soon as κ is considered to be an operator acting upon the argument of the functions u . The usefulness of equations of the type [19a] in the spinor formulation of electrodynamics is restricted to the fact that they enable us to write down necessary and sufficient conditions for the existence of nonvanishing solutions of these linear equations. The necessary and sufficient conditions that equations [19a] have nonvanishing solutions are that the four eigenvalues of A^μ satisfy:

$$[19b] \quad \{(A^\mu)^2 - \kappa^2\}^2 = 0, \text{ i.e. either } A^\mu = +\kappa \text{ or } A^\mu = -\kappa.$$

We see thus that the spinor formulation of electrodynamics allows for 16 different ways in which the scalar function κ may give rise to electromagnetic potentials A^μ .

It is now possible to formulate electrodynamics in terms of the one scalar function κ . In order to see better what is going on we shall return to the three-dimensional notation. With $\alpha = \{\alpha^1, \alpha^2, \alpha^3\}$ and $\beta = \alpha^4$ the operator identifications [19] read

$$[19c] \quad \mathbf{A} = \kappa \alpha; \quad \phi = \kappa \beta$$

and the electromagnetic fields \mathbf{E} and \mathbf{H} are defined by the operator relations

$$[21a] \quad \mathbf{E} = -\text{grad } \phi - \frac{1}{c} \frac{\partial \mathbf{A}}{\partial t} = -\beta \text{ grad } \kappa - \frac{\alpha}{c} \frac{\partial \kappa}{\partial t},$$

$$[21b] \quad \mathbf{H} = \text{curl } \mathbf{A} = \text{curl } (\alpha \kappa) = -(\alpha \times \text{grad } \kappa).$$

If one wishes to impose on the potentials the condition of gauge invariance one will have to subject the potentials to the operator condition

$$[22] \quad \text{div } \mathbf{A} + \frac{1}{c} \frac{\partial \phi}{\partial t} = (\alpha \cdot \text{grad } \kappa) + \frac{\beta}{c} \frac{\partial \kappa}{\partial t} = 0.$$

First of all let us see what the state "vacuum in absence of electromagnetic fields", as defined in the first paragraph, means in terms of the scalar function κ . It follows from the equations [21] that this state is characterized by the conditions

$$[23a] \quad \beta \text{ grad } \kappa + \frac{\alpha}{c} \frac{\partial \kappa}{\partial t} = 0,$$

$$[23b] \quad (\alpha \times \text{grad } \kappa) = 0.$$

One sees immediately that $\kappa = \text{constant}$ is a possible solution of these operator relations, this statement bearing out our contention that Dirac's original theory contains a correct description of the electromagnetic vacuum in absence of excitations of any kind, i.e. at the absolute zero of temperature. However, the condition $\kappa = \text{constant}$ is not the only solution of these operator equations. In fact, the necessary and sufficient conditions that the linear spinor equations corresponding to [23] have nonvanishing solutions are:

$$[23a'] \quad \left(\frac{\partial \kappa}{\partial x_i}\right)^2 + \frac{1}{c^2} \left(\frac{\partial \kappa}{\partial t}\right)^2 = 0; \quad i = 1, 2, 3,$$

$$[23b'] \quad (\text{grad } \kappa)^2 - \left(\frac{\partial \kappa}{\partial x_i}\right)^2 = 0; \quad i = 1, 2, 3.$$

It is clear from our interpretation of the function κ that whenever a state (excitation) of the vacuum occurs such that κ satisfies the system [23'], the excitation will not be accompanied by any observable electromagnetic field. We shall call such excitations "neutrino-like".

The neutrino-like excitations have to be distinguished from possible excitations which are accompanied by an electromagnetic field, but not by the appearance of electric charges and currents. Such excitations we shall call "photon-like". The equations for κ , which characterize the photon-like excitations, are obtained from the operator equations for the sources of the electromagnetic field:

$$[24a] \quad \text{div } \mathbf{E} = -\beta \nabla^2 \kappa - \frac{1}{c} \frac{\partial}{\partial t} (\alpha \cdot \text{grad } \kappa),$$

$$[24b] \quad \text{curl } \mathbf{H} - \frac{1}{c} \frac{\partial \mathbf{E}}{\partial t} = -\alpha \left(\nabla^2 \kappa - \frac{1}{c^2} \frac{\partial^2 \kappa}{\partial t^2} \right) + \text{grad} \left\{ (\alpha \cdot \text{grad } \kappa) + \frac{\beta}{c} \frac{\partial \kappa}{\partial t} \right\}.$$

The right-hand sides of these equations have to be identified with $4\pi\rho$ and $(4\pi/c)\mathbf{j}$ respectively, ρ and \mathbf{j} being charge and current densities representing observable electric charges. If the condition of gauge invariance [22] is imposed on the potentials, then these identifications reduce to

$$[25a] \quad 4\pi\rho = -\beta \left\{ \nabla^2 \kappa - \frac{1}{c^2} \frac{\partial^2 \kappa}{\partial t^2} \right\},$$

$$[25b] \quad \frac{4\pi}{c} \mathbf{j} = -\alpha \left\{ \nabla^2 \kappa - \frac{1}{c^2} \frac{\partial^2 \kappa}{\partial t^2} \right\}.$$

Photon-like excitations are then characterized by the conditions $\rho = 0$ and $\mathbf{j} = 0$. It is seen immediately from equations [25] that photon-like excitations will be obtained whenever κ is a solution of the equation

$$[26] \quad \nabla^2 \kappa - \frac{1}{c^2} \frac{\partial^2 \kappa}{\partial t^2} = 0$$

which is solved by plane waves, travelling with velocity c .

Finally, there appear in this theory excitations of the vacuum which are accompanied by both electromagnetic fields and electric charges and currents. We shall call such excitations "electron-like". They are obtained whenever κ satisfies the inhomogeneous operator equations [25]. The necessary and sufficient condition for existence of nonvanishing solutions of the linear spinor equations corresponding to [25a] is:

$$[27] \quad \left(4\pi\rho + \nabla^2 \kappa - \frac{1}{c^2} \frac{\partial^2 \kappa}{\partial t^2} \right)^2 \left(4\pi\rho - \nabla^2 \kappa + \frac{1}{c^2} \frac{\partial^2 \kappa}{\partial t^2} \right)^2 = 0,$$

i.e. either $4\pi\rho = + \left(\nabla^2 \kappa - \frac{1}{c^2} \frac{\partial^2 \kappa}{\partial t^2} \right)$ or $4\pi\rho = - \left(\nabla^2 \kappa - \frac{1}{c^2} \frac{\partial^2 \kappa}{\partial t^2} \right).$

This means that for a given electron-like excitation, described in terms of κ , there exist always two possible values of ρ , which differ only in their sign, and which correspond to the appearance of a positive or a negative charge density respectively. The very peculiar fact that actual electric charges can be either positive or negative thus comes out of this theory as a result, and need not be postulated as in ordinary electrodynamics.

4. PROGRAM OF QUANTUM VACUODYNAMICS

As an intermediate step towards full quantization of this theory it will be necessary to bring the hydrodynamics of the vacuum, or "vacuodynamics", which was outlined in the first two paragraphs of this paper, into Hamiltonian form. This should be done in close analogy to quantum hydrodynamics. The scalar function κ , corresponding to the density in the hydrodynamic analogy, must then be considered as one of the independent field variables, and it will no longer be consistent with our interpretation of electrodynamics to treat the electromagnetic potentials as independent field variables. The action principle should be chosen so that the Hamiltonian resulting from it represents the total excitation energy of the vacuum, making vacuum in absence of excitations of any kind (i.e. $\kappa = \text{constant}$) a state of total energy zero (4). Once the question has been settled which functions are the correct canonical variables of the system, quantization can be carried out in the usual way. The system will be described in terms of a spinor ψ such that $|\psi|^2$ is the probability of finding a certain value of κ at a given point of space time, while the expectation values of the operators α^μ give the velocity characterizing the excitation at that point. For a given type of excitation the eigenvalues of the Hamiltonian represent possible energy values of that excitation, which may be interpreted as possible mass values in the rest system, while the eigenvalues of the operator $\text{div } \mathbf{E}$, which should appear in terms of the constants \hbar and c , may be interpreted as charge density of the excitation.

The author has done some exploratory work in this direction. The results indicate that this program can be carried out, but the calculations are not yet in presentable form. It is hoped that further clarification of this matter can be submitted in a future publication.

ACKNOWLEDGMENT

The author received great encouragement through conversations with Profs. K. C. Mann, W. Opechowski, G. M. Volkoff, and many others.

REFERENCES

1. BUNEMAN, O. Proc. Roy. Soc. (London), A, 215: 346. 1952.
2. DIRAC, P. A. M. Proc. Roy. Soc. (London), A, 209: 291. 1951.
3. DIRAC, P. A. M. Proc. Roy. Soc. (London), A, 212: 339. 1952.
4. KAEMPFER, F. A. Can. J. Phys. 31: 165. 1953.
5. KAEMPFER, F. A. Can. J. Phys. 31: 497. 1953.
6. LANDAU, L. D. J. Phys. (U.S.S.R.), 5: 71. 1941.

MEASUREMENT OF NUCLEAR GAMMA-RAY ABSORPTION IN CARBON¹

BY R. N. H. HASLAM, R. J. HORSLEY,² H. E. JOHNS, and L. B. ROBINSON

ABSTRACT

The cross section for the absorption of γ rays by carbon has been determined as a function of photon energy by means of "nuclear detectors". The electronic absorption coefficients in the energy range 12 to 20 Mev. are found to be about 1% lower than the theoretical values. The nuclear absorption is shown to exhibit a resonance behavior. The integrated cross section in carbon is considerably lower than predicted. The contribution of nuclear scattering is found to be negligible. Differences in results as determined by three different detecting reactions, $C^{12}(\gamma, n)C^{11}$, $O^{16}(\gamma, n)O^{15}$, and $S^{32}(\gamma, d)P^{30}$, are discussed on the basis of detector sensitivity. It is suggested that the absorption mechanism can be represented by a continuous absorption on which is superimposed absorption peaks.

I. INTRODUCTION

In recent years investigators (1, 29) who have measured absorption coefficients for X rays in the energy region up to 30 Mev. have observed that they must take into account the contributions due to nuclear absorption. However, until the present no attempt has been made to measure the total nuclear absorption in an element, although this is important in view of the theoretical predictions of Goldhaber and Teller (9) and Levinger and Bethe (21).

As experimental evidence concerning individual photonuclear processes accumulates, it is becoming possible in some cases to estimate the proportion of the total absorption in an element which can be attributed to nuclear reactions at specific photon energies. In elements of low atomic number it appears that nuclear absorption may well be an appreciable part of the total absorption. For example in carbon, if one considers only the (γ, n) and (γ, p) processes (11, 22) which have been measured experimentally, at 21.5 Mev. nuclear absorption amounts to about 14% of the total electronic absorption. This is clearly shown in Fig. 1 in which curve *A* represents the total electronic absorption (compton plus pair production) in carbon as a function of photon energy; and curve *B* shows the sum of electronic, (γ, n) , and (γ, p) cross sections. In the calculations of the nuclear effect reactions involving C^{12} only have been considered. This introduces little error since C^{12} forms 98.9% of natural carbon.

For elements of higher atomic number, although the total nuclear cross section increases with Z , the electronic absorption increases still more rapidly so that, relatively, nuclear absorption plays a less important part. For example, curve *C*, Fig. 1, represents the electronic absorption in copper as a function of the energy. Curve *D* shows the estimated nuclear contribution. This estimate was determined from the total photoneutron cross-sectional curve for natural copper as determined recently in this laboratory (23). The cross-sectional values, however, have been increased by 40% to allow for the contributions of other nuclear processes. The 40% increase was estimated considering the relative yields of

¹ Manuscript received January 27, 1953.

² Contribution from the Physics Department, University of Saskatchewan, Saskatoon, Sask.

³ Holder of a National Research Council of Canada Studentship 1951-1952, and a National Cancer Institute Fellowship 1952-1953.

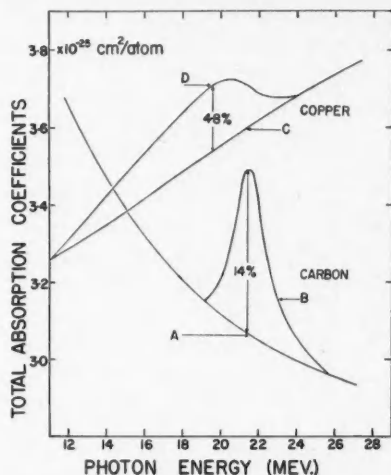


FIG. 1. Curves *A* and *C* are the theoretical electronic coefficients (compton plus pair production), in carbon and copper respectively, plotted as a function of the energy. The values for copper have been divided by 10. Curves *B* and *D* represent the sum of the electronic and estimated nuclear absorption in the two elements.

photoparticles as reported by Byerly and Stephens (4). Thus it is seen that in copper the maximum nuclear absorption at 19 Mev. amounts to only about 5% of the electronic absorption.

It would be extremely interesting to measure absorption coefficients with a pair spectrometer, which effectively sorts out the incident photon energies in the energy region where photonuclear processes are important. However, this equipment is not available in this laboratory and other means must be sought. Adams (1) has measured the absorption coefficients in various elements using threshold detectors. This method, however, is not applicable for carbon since there are no suitable reactions with thresholds in the desired energy region. Therefore, it has been necessary to devise a different method of measuring nuclear absorption in carbon.

It is the purpose of this paper to report a method in which the total absorption coefficients, including compton, pair production, and nuclear, are measured in a carbon absorber by suitable "nuclear detectors" whose response characteristics to the available photon spectrum have been determined experimentally. In the course of the experiment, the electronic coefficients for carbon in the region 12 to 20 Mev. were checked and found to be about 1% too high (Section IV). By subtracting the electronic absorption coefficients in the region above 20 Mev., the nuclear absorption cross-sectional values are obtained (Section VI). It is shown in Section VIII that the total nuclear absorption exhibits a resonance type curve similar in shape to (γ, n) , (γ, p) , etc., cross-sectional curves. Further it is shown in Section IX that the results obtained with carbon and oxygen detectors differ considerably from those obtained with sulphur detectors. This difference leads to interesting but speculative considerations given in Section X.

II. METHOD OF MEASURING THE TOTAL ABSORPTION IN CARBON

The experimental arrangement used in the present investigation is shown in Fig. 2, and is similar to the method used by Adams. However, in the present arrangement the X-ray beam is collimated and the rear detector situated in

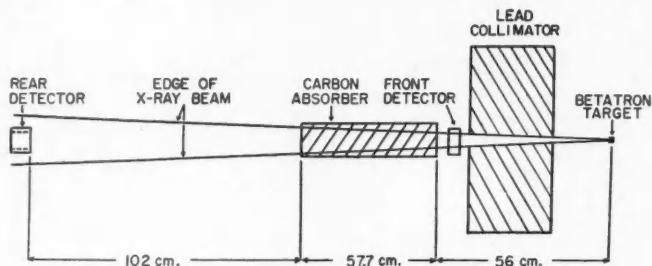


FIG. 2. Experimental arrangement.

"good geometry". In this way, the effects of scattered compton photons and secondary bremsstrahlung produced in the absorber are minimized. A small correction for the compton scattered radiation, which is discussed more fully later, is applied to the results.

The experimental procedure is to radiate the detectors in fixed positions first without the absorber in place. The activity produced in the front detector is counted by an "end-on" Geiger counting tube while the activity in the rear detector is counted by a Victoreen thyrode. The ratio of the front detector activity A_F to that of the rear detector A_R is calculated. In a similar manner the ratio of the activities is determined with the absorber in place. Let these latter activities be signified by A_F' and A_R' . A ratio R is then determined which is equal to

$$\frac{A_F'}{A_R'} \bigg/ \frac{A_F}{A_R}$$

and will be called the attenuation factor.

Since all the front detectors and all the rear detectors are the same size, and since they are radiated in fixed positions, "geometry" corrections drop out and the value of R at any maximum betatron energy can be represented by the following expression:

$$[1] \quad R_{(E_0)} = \frac{\int_{E_t}^{E_0} \sigma(E) P(E, E_0) dE}{\int_{E_t}^{E_0} \sigma(E) P(E, E_0) e^{-\sigma T(E) X} dE}$$

where

E_0 is the maximum betatron energy and E_t is the threshold energy,

$P(E, E_0)$ is the number of photons per square centimeter per unit energy interval at energy E when the betatron is operated at a maximum energy E_0 ,

$\sigma(E)$ is the value of the cross section of the detecting reaction at energy E ,
 $\sigma_T(E)$ is the total absorption coefficient (including electronic plus nuclear absorption) at energy E .

Let

$$\int_{E_1}^{E_0} \sigma(E) P(E, E_0) dE = \alpha(E_0).$$

Since $\sigma(E)$ and $P(E, E_0)$ are known, $\alpha(E_0)$ can be evaluated graphically. Then

$$[2] \quad \frac{\alpha(E_0)}{R(E_0)} = \int_{E_1}^{E_0} \sigma(E) P(E, E_0) e^{-\sigma_T(E)X} dE.$$

The only unknown in equation [2] is $e^{-\sigma_T(E)X}$ and this can be solved for, in a manner similar to the method reported by Johns *et al.* (16) for calculating (γ, n) cross sections. After obtaining $e^{-\sigma_T X}$ as a function of energy, it is straightforward to solve for σ_T . By subtracting the values of the electronic absorption, the total nuclear absorption σ_{TN} can be obtained.

Since the activities in the front and rear detectors are produced simultaneously and the ratio of these activities calculated, it is not necessary to measure the actual X-ray dose. In practice, however, the dose was kept constant for any one set of runs. By taking the ratio of activities, errors due to small fluctuations in the beam intensity and variations in the maximum betatron energy are minimized. At least five or six determinations of R were made at each betatron energy and the average value calculated. The probable errors for each experimental value of R are shown in the figures.

III. DETECTORS

The front detectors are thin disks about 2.5 cm. in diameter, while the rear detectors are hollow cylindrical samples about 6 cm. in length which fit closely over a thyrde counting tube. In the course of the experiment, several different detector materials were used and the particulars of the reactions used with the different materials are shown in Table I.

TABLE I
REACTIONS USED AS DETECTORS

Reaction	Material	Half-life (min.)	Threshold (Mev.)	Reference
$C^{12}(\gamma, n)C^{11}$	Polystyrene	20.6	18.7	11
$O^{16}(\gamma, n)O^{15}$	Boric acid	2.0	15.6	15
$S^{32}(\gamma, d)P^{30}$	Flowers of sulphur	2.55	19.1	19
$P^{31}(\gamma, n)P^{30}$	Red phosphorus	2.55	12.4	19
$Cu^{63}(\gamma, n)Cu^{62}$	Copper	10.1	10.9	16
$Zn^{64}(\gamma, n)Zn^{63}$	Zinc	38	11.6	18

The carbon samples were cut from 2.5 cm. diameter polystyrene tubing. In a similar manner the copper samples were cut from 2.7 cm. diameter copper tubing. The zinc rear detector samples were square tubes made from 0.05 cm.

zinc sheeting. The front copper, zinc, and polystyrene samples were made from solid rods or available sheeting. The boric acid, sulphur, and phosphorus front and rear detectors were made by filling suitable patterns with powder and compressing them under a pressure of 16,000 lb. per sq. in. by means of a Carver Laboratory Press. By starting always with the same amount of powder, it is possible to make any number of identical samples.

IV. FACTORS INFLUENCING THE VALUES OF σ_{TN}

The calculated values of σ_{TN} are dependent upon the following factors:

- (a) Relative shapes of the spectral distributions and detector cross-sectional curves,
- (b) Measured thickness of the absorber,
- (c) Scattered compton and secondary bremsstrahlung radiation,
- (d) Counting statistics,
- (e) Errors due to spurious activities induced in the detectors,
- (f) The value of the electronic absorption coefficients in carbon.

(a) *The Spectral Distribution and the Shape of the Cross-sectional Curves*

The spectral distribution used is one based on a formula derived by Schiff (26) and used generally in this laboratory. Experimental evidence to date is in reasonable agreement with this formula. The shapes of the cross-sectional curves were obtained by the "photon difference" method (17), which uses the Schiff spectral distributions. In the calculations involved in this experiment, we are interested in the product of the cross-sectional and photon distribution curves. Further, since the ratio of activities is calculated (see equation [1]), small variations in the product $\sigma(E) P(E, E_0)$ are not serious. This is illustrated by considering the three arbitrary cross-sectional curves shown in Fig. 3(a), and calculating the values of R for each curve as a function of the betatron energy. In Fig. 3(b) it is seen that the value of R based on the cross-sectional shapes A and C differs from the value of R based on curve B by about 1% or less. Since the shape of the cross-sectional curves as determined by the "photon difference" method is considered to be reasonably accurate (see Reference 17),

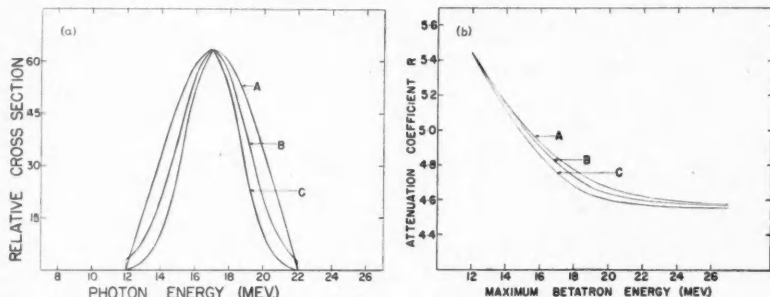


FIG. 3(a) Three assumed cross-sectional curves as a function of photon energy.

(b) The value of the attenuation factor R as a function of the betatron energy calculated on the basis of the assumed cross-sectional curves in Fig. 3(a).

it is felt that, in view of the above discussion, the values of R are probably in error by no more than about 1% due to uncertainties in the product of the cross-sectional and photon distribution curves.

(b) *Absorber Thickness*

The results discussed in this paper were all obtained with a 57.7 cm. cylindrical block of graphite having a diameter of 5.0 cm. The thickness of the absorber is 92.2 gm. per cm.² and is accurate to better than 1/10%.

(c) *Scattered Radiation*

One of the difficulties in measuring absorption coefficients is the effect of scattered compton photons influencing the detector. In the present experiment the effect of scattered radiation with the absorber in place is to increase the activity in the rear detector. As a result, the factor R as measured is too small. By collimating the X-ray beam as is shown in the diagram, and by placing the rear detector as far as possible from the absorber, the amount of scattered radiation which can strike the rear detector is very small. The error in R due to the compton scattered radiation has been calculated for the different detector reactions and is found to vary from 0.25 to 0.90%, depending on the size of the collimating device. Rough calculations show that activities induced in the rear detector due to secondary bremsstrahlung produced in the carbon absorber by high speed electrons and positrons are extremely small, and may be neglected.

In order to check experimentally the effect of scattered radiation, the three following tests were made. In the first test the absorber thickness was varied. The carbon detectors were radiated in fixed positions, and the values of R obtained at 24 Mev. plotted as a function of the logarithm of the absorber thickness. The resulting points formed a straight line, within experimental errors. This is expected, providing the scattered radiation is very small. In the second test, the 92.2 gm. per cm.² carbon absorber was used and the position of the rear detector varied. If scattered radiation were appreciably affecting the rear detector, the values of R would increase in magnitude as the rear detector moved further away from the absorber. Using oxygen detectors, it was found that the values of R were constant within experimental errors as the distance of the rear detector from the absorber was varied from 10 cm. up to the distance actually used, namely 102 cm. In the third test, the scattered radiation was measured by placing a phosphorus rear detector sample at the usual distance behind the absorber, but outside the X-ray beam. The activity induced in the detector by scattered radiation was then measured. Making the assumption that the scattered radiation seen by the detector at the edge of the beam is about the same as at the center of the beam, the error in R due to scattered radiation was calculated. The errors in R based on measurements made with the detector 1.1 cm. and 0.3 cm. outside the edge of the beam were 0.69% and 0.72%, respectively. These values are in good agreement with the calculated error in R of 0.80% for the detector at the center of the beam.

(d) *Statistical Errors*

The "on-off" switches on the two counting scalers were connected to a timing clock in order that both scalers could be started and stopped simultaneously.

In this way the ratio of the measured activities could be obtained directly after subtracting the appropriate tube backgrounds. At all times the counting rate was kept low enough to eliminate counting losses through lack of resolution. The statistical counting errors at energies several Mev. above the threshold varied from about 1 to 2%, depending on the magnitude of the detector cross section. At energies 1 or 2 Mev. above the thresholds, the statistical counting errors were of course larger and amounted to about 3 or 4%. A typical set of experimental data is shown in Table II. These results were obtained using

TABLE II
EXPERIMENTAL DATA USING POLYSTYRENE DETECTORS AT 21 MEV.

Sample number	Absorber position	Detector	Counting interval, min.	Total count	Back-ground count	Count minus back-ground	Ratio absorber IN	Ratio absorber OUT
1	IN	Front Back	20	7327 4831	222 386	7105 4445	1.598	
2	OUT	Front Back	20	7713 20126	222 386	7491 19740		0.379
3	IN	Front Back	20	7939 5107	222 386	7717 4721	1.635	
4	OUT	Front Back	20	7849 20726	222 386	7627 20340		0.375
5	IN	Front Back	20	7889 4878	222 386	7667 4492	1.707	
6	OUT	Front Back	40	11700 30495	444 772	11256 29723		0.379
7	IN	Front Back	20	7704 5020	222 386	7482 4634	1.615	
8	OUT	Front Back	20	6912 18407	222 386	6690 18021		0.371
9	IN	Front Back	20	9484 5907	222 386	9262 5521	1.678	
10	OUT	Front Back	20	9252 24025	222 386	9030 23639		0.382

Average 1.647 0.377
 $R = 4.37 \pm 0.04$

polystyrene samples. A delay of 10 min. was allowed between the end of irradiation and the start of counting, in order to allow any spurious O^{15} activity to die away.

(e) *Spurious Activities*

Spurious activities present in the detectors could affect the experimental results. In the case of polystyrene detectors, a small activity was detected at energies below 18.7 Mev., the (γ, n) threshold in C^{12} . This activity was attributed

to the presence of a 2 min. O^{15} activity and a 10 min. N^{13} activity. By waiting 10 min. after irradiation before starting to count most of this spurious O^{15} activity has disappeared. Since the thresholds for the (γ, n) reactions in O^{16} and N^{14} , 15.6 and 10.8 Mev. respectively, are lower than 18.7 Mev., a considerable part of the activity detected at energies immediately above 18.7 Mev. is due to the above-mentioned spurious activities. However, above 20 Mev. most of the detected activity is due to C^{11} . For example, counting for a 10 min. interval after a 10 min. delay, the spurious activity at 20, 21, and 22 Mev. was estimated to be about 1.9, 0.4, and 0.1%. However, since both of the spurious activities in carbon are photo-induced reactions, the ratio of the spurious activities in the front and rear detectors is about the same as the ratio of the C^{11} activities. For example, the calculated value of R at 20 Mev. using carbon detectors is 4.27. The calculated value of R using the $N^{14}(\gamma, n)N^{13}$ process (15) as the detecting reaction is 4.64. Thus the true calculated value of R at 20 Mev. is obtained by adding together 98.1% of 4.27 and 1.9% of 4.64. The value of R determined in this way is 4.28. This differs from the value of R calculated using only the carbon reaction by about 0.25%. At 21 Mev. the error in R amounts to about 0.05%. Thus it is seen that the errors in R due to the spurious photo-induced activities are negligible.

On the other hand, if the spurious activity is caused by a neutron-induced reaction, then the value of R is more seriously affected. This is true because the neutron-induced activity may not be the same fraction of the photo-induced activity with the absorber in and out of position. The carbon absorber undoubtedly moderates the fast neutrons in the beam, and in addition the absorber is itself a source of neutrons at photon energies above 18.7 Mev. Therefore it is necessary that neutron-induced activities be eliminated.

The 5.2 min. neutron-induced activity in Cu^{66} at first gave considerable trouble. It was found that the values of R using cadmium shielding surrounding the detectors were about 2% higher than without cadmium shielding. Because of the large $Cu^{63}(\gamma, n)Cu^{62}$ cross section, it was possible to wait 30 min. after irradiation before starting to count and still obtain good counting statistics. Because of the difference in half-lives, the ratio of the 10.1 min. Cu^{62} activity to the 5.2 min. Cu^{66} activity was reduced by a factor of about 8. It was found that the values of R were the same within experimental error whether cadmium shielding was used or a delay of 30 min. allowed after irradiation. Finally R was determined using cadmium shielding and waiting 30 min. The values obtained in this manner were in agreement with the values obtained with either of the above-mentioned arrangements, and are the ones given in this paper. In addition to the 5.2 min. Cu^{66} activity, there is a very small Cu^{64} activity which is partly photo-induced and partly neutron-induced. In several cases this small 12.9 hr. activity was measured several hours later. When this activity was subtracted, the value of R was essentially unchanged.

With zinc, red phosphorus, and boric acid detectors, no spurious activities were observed. In the case of sulphur detectors, cadmium shielding was used to eliminate any 5 min. S^{37} neutron-induced activity that might be present. In addition, a small unknown activity was also detected in sulphur which might

be attributed to either a photo- or neutron-induced reaction. However, this latter activity could safely be neglected, since it amounted to only 0.05% of the (γ, d) activity.

(f) *Values of the Electronic Absorption Coefficients*

For carbon in the energy region investigated, only the Compton and pair production cross section, including triplet production, need be considered. The Compton coefficients were determined from the Klein-Nishina formula (20, 24). The values for pair production were calculated by Davisson (6) and are based on the Bethe-Heitler formula (14). The Z^2 dependence of the pair production cross section was increased to $Z^2 + 0.8Z$ to include triplet production. The value of the constant 0.8 is in agreement with the experimental work of Gaertner and Yeater (8) and the theoretical calculations of Borsellino (3, 30).

As a check on the values of the calculated electronic absorption coefficients, the attenuating factor R was measured and compared to calculated values of R at energies between 15 and 20 Mev., where no nuclear absorption is present.

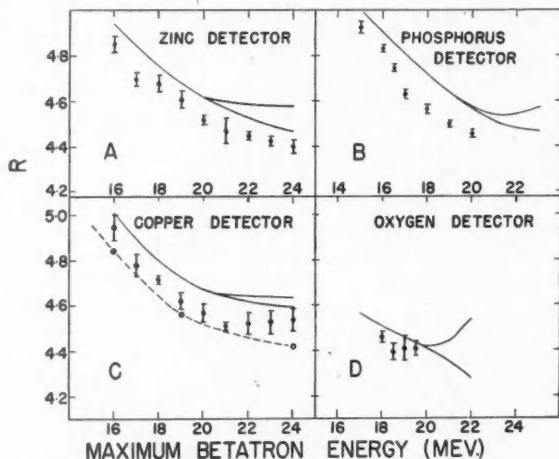


FIG. 4. The experimental values of R with four different detector reactions, $\text{Zn}^{64}(\gamma, n)\text{Zn}^{63}$ (A), $\text{P}^{31}(\gamma, n)\text{P}^{30}$ (B), $\text{Cu}^{63}(\gamma, n)\text{Cu}^{62}$ (C), and $\text{O}^{16}(\gamma, n)\text{O}^{15}$ (D), are compared to the calculated values (solid curves). The upper solid line shown in each section represents the value of R when σ_T includes the nuclear absorption. The broken line in part C indicates the calculated value of R when Vortrub's values for triplet production are used.

As shown in Fig. 4, all the experimental points with four different detectors, copper, zinc, phosphorus, and oxygen, are too low. The average amount by which they are too low in the energy region 15 to 20 Mev. is $2 \pm 0.2\%$. We feel that this is good evidence for assuming that the theoretical values for the electronic coefficients in carbon are in error. On the basis of an average 2% error in R , revised values for the electronic coefficients were calculated over this energy region. In Table III, column 2, the theoretical values for the electronic coefficients in carbon are given. These values are in agreement with those reported by

White (30) in a recent survey of X-ray attenuation coefficients. Revised values as determined by us are shown in column 3. The error in the revised values, 0.5%, was estimated by assuming that the average percentage difference between the experimental and calculated values of R may vary between 1 and 3. It is unlikely that R could be in error by more than this amount. The revised value of σ_T at 17.6 Mev. can be compared to the experimental results of other workers. Our value of $0.318 \pm .002$ agrees, within experimental errors, with the results given by Colgate (5, 30) ($0.321 \pm .006$), and Walker (29) ($0.323 \pm .004$), all expressed in units of 10^{-24} cm.² per atom.

TABLE III
ELECTRONIC ABSORPTION COEFFICIENTS IN CARBON

Energy (Mev.)	Theoretical coefficients, 10^{-24} cm. ² per atom	Revised coefficients, 10^{-24} cm. ² per atom
15	0.338	0.334
16	0.332	0.328
17	0.326	0.322
18	0.321	0.316
19	0.316	0.312
20	0.312	0.308

Some of the uncertainty in the theoretical electronic coefficients lies in the determination of the triplet production. If the theoretical values for triplet production as determined by Votruba (27) are used, the calculated values of R are now lower than our experimental values. This is illustrated by the dotted line in Fig. 4 (C). Our experimental results would indicate that agreement could be obtained if values for triplet production midway between those calculated by Votruba and Borsellino were used.

Above 20 Mev., we have no method of checking the theoretical electronic coefficients. In the work that follows, the theoretical electronic coefficients in the region 20 to 25 Mev. are also assumed to be in error, and have been lowered by about 1% in order to produce a 2% change in R .

V. MEASUREMENT OF R IN CARBON, WITH CARBON, OXYGEN, AND SULPHUR DETECTORS

In Fig. 4 it is seen that with copper, phosphorus, and zinc detectors the lower curves, which represent the calculated values of R using only electronic absorption, differ only a little from the predicted values which include the nuclear absorption. This is because the thresholds for these detecting reactions are quite low in comparison to the threshold for nuclear absorption in the carbon block. Thus most of the activity induced in these detectors is produced by relatively low energy photons, that is photons with an energy between 10 and 19 Mev., and in this energy region the nuclear absorption is negligible. In order for the nuclear absorption to produce an appreciable effect in R , it is necessary that the detecting reaction have a high threshold value, in order that photons which produce most of the activity in the detectors are also attenuated by the nuclear absorption. This condition is satisfied by the three following detector

reactions: $C^{12}(\gamma, n)C^{11}$, $O^{16}(\gamma, n)O^{15}$, and $S^{32}(\gamma, d)P^{30}$. Although the threshold for the $O^{16}(\gamma, n)O^{15}$ reaction, 15.6 Mev., is lower than the effective nuclear absorption threshold, most of the activity induced in the oxygen detector is produced by relatively high energy photons. This is evident from the shape of the cross-sectional curve which exhibits a slowly increasing initial portion up to about 20 Mev. and then increases rapidly. (See Reference 15.)

In Fig. 5 the experimental values of R determined with carbon, oxygen, and sulphur detectors are shown with their probable errors. These experimental values can be compared to the calculated values of R when σ_T is composed of electronic absorption, and when σ_T is composed of electronic, plus (γ, n) and (γ, p) absorption. The dotted line in each part of Fig. 5 represents the value of R when σ_T is made up of only electronic absorption. It is seen that with each detecting reaction some nuclear effect is observed. When σ_T includes the nuclear absorption, the calculated values of R depend on the errors in the absolute determination of the (γ, n) and (γ, p) cross sections. Errors of 25% quoted by Mann and Halpern for the (γ, p) reaction and 20% as estimated by us for the (γ, n) reaction yield the upper and lower curves bordering the hatched areas in Figs. 5 (A), (B), (C).

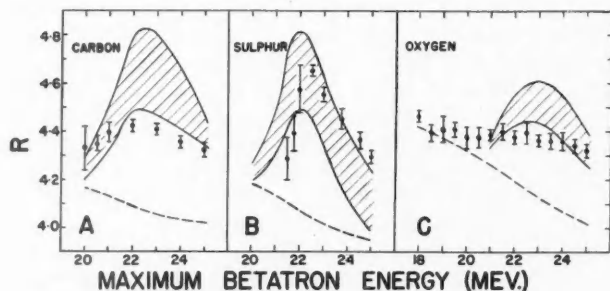


FIG. 5. The experimental values of R with three different detector reactions, $C^{12}(\gamma, n)C^{11}$ (A), $S^{32}(\gamma, d)P^{30}$ (B), and $O^{16}(\gamma, n)O^{15}$ (C), are compared to the calculated values. The shaded areas in each section, determined from the probable errors in the (γ, n) and (γ, p) reactions in C^{12} , represent the uncertainty in the calculated values. The broken line in each part represents the values of R when σ_T includes only electronic absorption.

In Figs. 5 (A) and (C) it is seen that our experimental values are for the most part lower than the calculated values. In Fig. 5(B) the experimental results with sulphur detectors are of about the right order of magnitude but are displaced about $\frac{1}{2}$ Mev. This apparent displacement is thought to be real since the entire sulphur results were determined experimentally twice, the second time four months after the first time. With the present method of controlling the maximum betatron energy, the absolute value of the energy is reproducible to better than 0.2 Mev.

VI. TOTAL NUCLEAR CROSS-SECTIONAL VALUES FOR CARBON

The method of solving for σ_T and the total nuclear absorption σ_{TN} was explained earlier. The values of σ_{TN} based on the carbon and oxygen detectors and

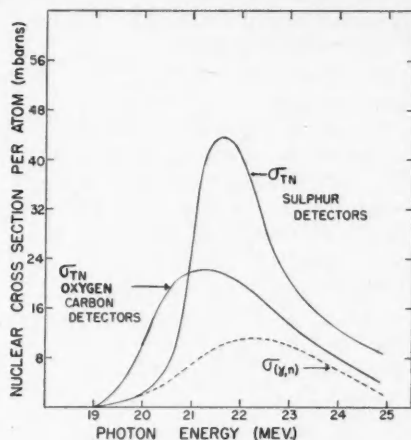


FIG. 6. The cross-sectional values for the total nuclear absorption in carbon using sulphur, carbon, and oxygen detectors are plotted as a function of photon energy. The broken line is the cross-sectional curve for the reaction $C^{12}(\gamma, n)C^{11}$.

on the sulphur detector results are shown in Fig. 6. A discussion of the surprising differences between these two experimental results for the total nuclear absorption will be given later.

The values of the total nuclear integrated cross section as determined with the different detectors can be compared to the theoretical values of Goldhaber and Teller (9) and Levinger and Bethe (21). This comparison is made in Table IV. In addition, the integrated cross section can be estimated using the statistical calculations of Weisskopf (2) concerning the probable emission of either a neutron or proton. On the basis of the measured (γ, n) reaction, the value of the (γ, p) cross section was calculated assuming that these two reactions are the only ones of importance.

TABLE IV
COMPARISON OF THE TOTAL INTEGRATED NUCLEAR CROSS SECTION IN CARBON

Method	Oxygen or carbon detectors	Sulphur detectors	Levinger and Bethe "sum rule"	Statistical calculations	Goldhaber & Teller
Integrated nuclear cross section (Mev-barns)	0.08	0.11	0.25	0.17	0.3

It is seen from this table that the experimental values for the total integrated nuclear cross section are considerably lower than any of the theoretical predictions. It should be pointed out, however, that the theoretical values are determined over all energies while the experimental results were measured up to about 26 Mev.

Very little information is available concerning other possible nuclear reactions in carbon which at higher energies might contribute to the total integrated nuclear cross section. Perlman and Friedlander (25) found that the $(\gamma, 2n)$ yield in carbon at 100 Mev. bremsstrahlung energy was of the order of 1% or less of the (γ, n) yield. From the evidence available it seems likely that most of the nuclear absorption in carbon occurs in the energy region studied and hence our experimental values can be compared to the theoretical predictions. However, the theoretical calculations of Goldhaber and Teller were derived on the basis of a "dipole vibration" nuclear model and are not expected to hold for elements of low atomic number where there are relatively few nucleons. The "sum rule" as derived by Bethe and Levinger is independent of any nuclear model and should hold for all elements. Our experimental values are about one-half or less of the value determined from the "sum rule" or the "dipole vibration" model. They are in better agreement with calculations based on Weisskopf's statistical considerations.

VII. DETERMINATION OF THE (γ, p) REACTION IN CARBON

The dotted curve shown in Fig. 6 is the $C^{12}(\gamma, n)C^{11}$ cross-sectional curve as recently redetermined in this laboratory. By subtracting the values of the (γ, n) cross section from σ_{TN} , as determined with both carbon and sulphur detectors, the remaining cross section can be attributed to the (γ, p) reaction in carbon plus perhaps any nuclear gamma-ray scattering. These remaining cross-sectional curves are shown in Fig. 7. The dotted line in this figure is the $C^{12}(\gamma, p)B^{11}$ cross-sectional curve as measured by Mann and Halpern. No account has been taken of the small reduction in the (γ, p) cross section which would be introduced by the fact that the proton distribution is anisotropic

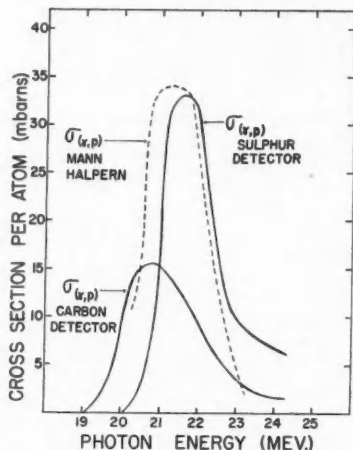


FIG. 7. The (γ, p) cross-sectional curve in C^{12} as determined using carbon and sulphur detectors is compared to the (γ, p) cross section (broken curve) determined by Mann and Halpern.

(10). It is seen that the remaining nuclear cross section as measured with sulphur detectors is in remarkably good agreement with Mann and Halpern's results. On the other hand the values as measured with the carbon detectors disagree strongly with the work of Mann and Halpern. The pertinent data from these latter curves are compared in Table V. It is evident from our experimental results that, if we accept the absolute values of the (γ, n) and (γ, p) cross sections referred to above, there is no or extremely little nuclear scattering. This is in agreement with the observations of Gaertner and Yeater (7) who measured the resonance scattering in carbon using 100 Mev. X-rays. They found that the nuclear scattering in carbon is less than 1% of the total cross section for resonance absorption.

TABLE V
COMPARISON OF EXPERIMENTAL (γ, p) RESULTS IN C¹²

Measurement	Carbon detectors	Sulphur detectors	Mann and Halpern
Integrated cross section (Mev.-barns)	0.042	0.070	0.063
Peak cross section (mbarns)	15.6	33.4	33.4
Peak position (Mev.)	20.75	21.6	21.5
Half-width (Mev.)	2.3	1.4	1.7

VIII. RESONANCE SHAPE OF NUCLEAR CROSS-SECTIONAL CURVES IN CARBON

During the last two or three years, measurements of individual photonuclear reactions have shown that the shape of cross section versus energy curves is strongly peaked. It was suggested by Wäffler and Hirzel (28) in 1948 that competing reactions might account for the turning over of at least the $\text{Cu}^{63}(\gamma, n)\text{Cu}^{62}$ cross-sectional curve. However, since that time experimental evidence has shown that competing reactions cannot account for the shape of many of the photonuclear reactions. Another explanation for the shape of the cross-sectional curves is that the cross section for the absorption of photons is a resonance phenomenon. This absorption cross section, as measured in this experiment and shown in Fig. 6, is similar in shape to (γ, n) , (γ, p) , etc. cross-sectional curves. The following considerations leave no doubt that the shape of the absorption cross section, at least in carbon, is similar to a resonance curve. Let us assume that the total nuclear absorption cross section does not fall off as does the sum of the (γ, n) and (γ, p) cross-section curves, shown by curve *A* in Fig. 8, but either increases steadily above the peak position, curve *B*, or else flattens off, curve *C*. The values of the attenuation factor, calculated on the basis of these assumptions for both carbon and sulphur detectors, are compared to the experimental values of *R* in Fig. 9. It is quite obvious that the experimental points are in strong disagreement with either curve *B* or *C*. On the other hand, the experimental points with both detectors go through a maximum value, and as far as the over-all shape is concerned, are in good agreement with curves *A*.

Therefore it is quite evident that the turning over of the (γ, n) and (γ, p) curves in carbon is caused by a falling off of the absorption cross section above 21.5 Mev. and cannot be attributed to any competing reactions.

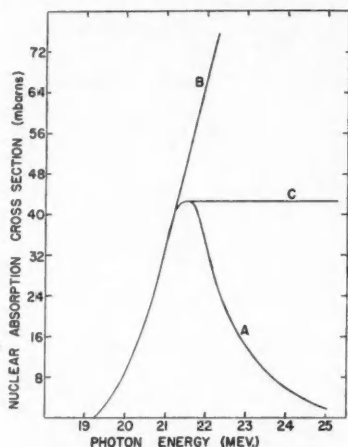


FIG. 8. Curve *A* represents the sum of the (γ, n) and (γ, p) cross-sectional curves in C^{12} as a function of photon energy. The assumption is made that the total nuclear absorption does not fall off above 21.5 Mev. but increases steadily (curve *B*) or else flattens off (curve *C*).

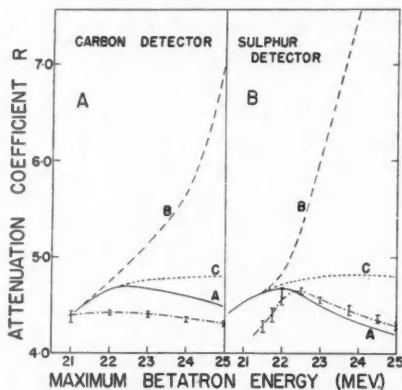


FIG. 9. The values of the attenuation factor R for carbon and sulphur detectors are calculated on the basis of assumptions *A*, *B*, and *C* shown in Fig. 8, and are compared to the experimental results.

IX. DIFFERENCES IN σ_{TN} AS MEASURED BY CARBON AND SULPHUR DETECTORS

Let us now consider the difference in σ_{TN} as measured with carbon and sulphur detectors. (See Fig. 6.) The absolute errors in σ_{TN} are dependent upon the factors which influence the value of R . These factors were discussed in detail in Section

IV. The errors in σ_{TN} can be considered to arise mainly from two sources. The first is the probable counting error shown on the experimental points. Secondly, in solving for σ_{TN} , a knowledge of the cross-sectional shape, spectrum, and absorption coefficients is needed.

In the case of carbon detectors, we estimate the average error in σ_{TN} to be 15%. With oxygen and sulphur detectors the corresponding error is 25%. These large errors result from the fact that the nuclear effect is a small proportion of the measured effect. The two σ_{TN} curves of Fig. 6, as determined by carbon

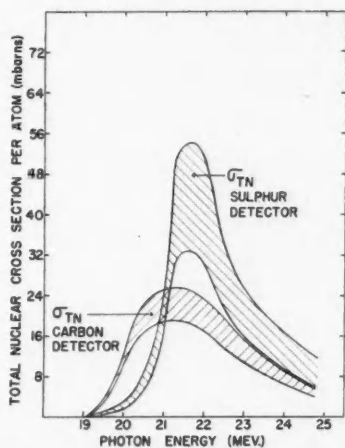


FIG. 10. The values of σ_{TN} as measured by carbon and sulphur detectors are shown with their estimated maximum errors indicated by cross-hatching.

and sulphur detectors, have been replotted in Fig. 10 with their maximum errors indicated by the cross hatching. The integrated cross sections of the two curves as shown in Table IV differ by about 30%. This in itself is in fair agreement since the error quoted on (γ, n) reactions measured in this laboratory is between 15 and 20%. Also, both σ_{TN} curves peak at about the same energy. It is seen, however, that the shapes of the two curves are not in agreement. The σ_{TN} curve determined using sulphur detectors is narrower, and more strongly peaked.

Although there is no particular source of error large enough to explain the discrepancies in the two determinations of σ_{TN} , it might conceivably be that the sum of all the possible errors inherent in this experiment is sufficient to explain the differences. However, we feel that this difference in shape is real and not caused by the errors inherent in the experiment. Adopting this point of view, we conclude that the differences in σ_{TN} as determined by carbon, oxygen, and sulphur detectors must be attributed to the response characteristics of the different detector reactions. A discussion of this effect will now be given.

X. DISCUSSION OF DIFFERENCES IN σ_{TN} BASED ON DETECTOR SENSITIVITY(A) *Presence of Nuclear Absorption Levels in C^{12}*

Recent work done in this laboratory (12, 13) has shown that there are sharp breaks in the oxygen and carbon activation curves. The relationship between these breaks and the absorption mechanism is however not known. It is thought likely that these breaks may be attributed to the presence of strong absorption levels in the initial nuclei. The following discussion is speculative since only preliminary measurements have been made on these activation breaks. However, it is felt that these breaks are real since they have been checked repeatedly. It is further thought that the change in slope at a break is proportional to the absolute strength of the level. In addition, since the breaks are sharply defined, the levels are considered to be narrow. The relative strengths and the preliminary positions of the levels in C^{12} are given in Table VI.

TABLE VI
SHARP BREAKS IN THE $C^{12}(\gamma, n)C^{11}$ ACTIVATION CURVES

Energy position (Mev.)	Relative strength
18.71	0.20
19.35	0.57
19.68	0.54
20.06	1.10
20.47	1.39
20.74	1.29
21.37	2.93
22.52	3.18

(B) *Nuclear Absorption Occurring Only in Sharp Discrete Levels*

The assumption is now made that all the nuclear absorption up to about 23 Mev. occurs in these discrete energy levels. For the purposes of this discussion, the levels are assumed to be rectangular in shape, the relative heights proportional to the change in slope at the break and 0.1 Mev. wide. Since all the nuclear absorption is assumed to occur only in these levels, the area under these levels must be made equal to the area under the sum of the smooth (γ, n) and (γ, p) cross-sectional curves in C^{12} up to 23 Mev. In this manner the absolute cross section values in the different levels can be assigned. On the basis of the nuclear absorption occurring in the carbon absorber in such discrete levels, the value of R using carbon detectors has been calculated. It must be remembered that the response characteristics of the $C^{12}(\gamma, n)C^{11}$ reaction must now also be changed. This is done by assuming that the (γ, n) cross section is composed of the same type of levels at the same energies. However, the area under these latter levels must be made equal to the area under only the (γ, n) smooth cross-sectional curve up to 23 Mev. From Fig. 11 it is seen that the values of R are much larger than those calculated before on the basis of smooth absorption, and hence considerably greater than the experimental points. The reason R is so much larger is that the very photons which are strongly attenuated in the carbon absorber are the only ones which activate the rear detector. The nuclear absorp-

tion in these levels is now considerably larger than on the basis of smooth absorption, since although the same integrated absorption is present, it is now confined to a relatively few sharp peaks. It is quite evident that the nuclear absorption in carbon does not occur only in a few narrow, discrete levels as suggested by the breaks in the activation curve.

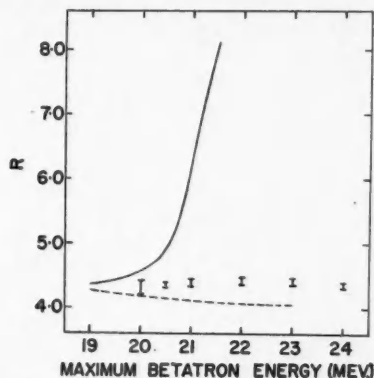


FIG. 11. The solid line represents the calculated values of R for carbon detectors, based on the assumption that the nuclear absorption occurs in discrete energy levels. The dashed line indicates the values of R when only electronic absorption is included.

(C) *Nuclear Absorption Occurring in Sharp, Discrete Levels Modified to Include Some Continuous Absorption*

(C₁) *Oxygen Detector Results*

The experimental values of R and of σ_{TN} obtained using oxygen detectors are too low. (See Figs. 5 (C) and 6.) Thus it must be concluded that the detector does not see all of the nuclear attenuation. Preliminary experiments have shown discontinuities in the $O^{16}(\gamma, n)O^{15}$ activation curve which may be interpreted in terms of level structure. If absorption took place only in sharp levels, both in oxygen and carbon, no nuclear effect would be observed unless by chance certain levels coincided. The fact that there is some measured nuclear attenuation points strongly to a continuous absorption. But continuous absorption sufficient to explain the sum of the observed (γ, n) and (γ, p) results in carbon would lead to values of σ_{TN} larger than we observe. Thus we are led to the conclusion that nuclear absorption takes place partly in a continuum and partly in discrete levels for both the oxygen detector and carbon absorber.

(C₂) *Sulphur Detector Results*

If nuclear absorption levels are real it is not surprising that they are found in light elements like carbon and oxygen. However, sulphur is a heavier element and for sulphur the absorption levels would be expected to be closer together or perhaps overlapping. Some preliminary detailed investigations have been made on both the $S^{32}(\gamma, d)P^{30}$ and $S^{32}(\gamma, n)S^{31}$ activation curves. The results however are not accurate enough yet to decide whether sharp breaks occur or not. At

energies close to the threshold energies there is some indication of breaks. At higher energies there is considerable doubt whether or not breaks are present.

At this time it seems probable that the $S^{32}(\gamma, d)P^{30}$ cross-sectional curve can best be represented by the smooth cross-sectional curve as determined in this laboratory. In Fig. 6, the value of σ_{TN} as a function of energy was calculated on the basis of a smooth (γ, d) cross-sectional curve for the detector reaction and is found to agree reasonably with the sum of the $C^{12}(\gamma, n)C^{11}$ and $C^{12}(\gamma, p)B^{11}$ cross-sectional curves. (See Section VI.) The experimentally determined values of R (Fig. 5(B)) are in reasonable agreement with the values of R calculated on the assumption of continuous absorption in carbon although they are somewhat low at energies close to the nuclear absorption threshold in carbon. These low values could be explained by the assumption that there is some discontinuous absorption in the sulphur (γ, d) reaction in the energy region concerned and that absorption peaks in sulphur and carbon do not coincide. Thus the sulphur detector results may be said to be in agreement with the absorption mechanism suggested to explain the oxygen detector results, that is a combination of discrete and continuous nuclear absorption.

(C₃) Carbon Detector Results

The results obtained with carbon detectors, like those using oxygen detectors, are too low. Again we must conclude that for some reason the carbon detectors do not measure all the nuclear attenuation occurring in the absorber. Certainly since the (γ, n) reaction in C^{12} is the means of measuring the attenuation, this reaction must detect all the nuclear attenuation in the absorber which can be attributed to (γ, n) processes in C^{12} . One way in which the carbon results might be explained would be to assume that absorption maxima also occur in the $C^{12}(\gamma, p)B^{11}$ reaction and that the detector reaction $C^{12}(\gamma, n)C^{11}$ is not sensitive to photons with energies corresponding to these maxima. This assumption is not in accordance with any present theories of photonuclear reactions and must be tested by more sensitive means. Further work is contemplated in measuring the total nuclear absorption in other elements which is expected to yield information concerning the absorption mechanism.

XI. SHAPE OF THE $C^{12}(\gamma, n)C^{11}$ CROSS-SECTIONAL CURVE

One further argument can be made to strengthen our belief that there is some absorption continuum as well as absorption peaks. The relative carbon activation curve for the $C^{12}(\gamma, n)C^{11}$ reaction which was investigated in great detail, to determine the absorption levels, has been analyzed by the method previously mentioned (16) using 0.1 Mev. energy intervals, instead of the customary 0.5 Mev. intervals. The cross-sectional curve obtained is reproduced in Fig. 12. The absolute cross-sectional values were obtained by normalizing the area under the relative cross-sectional curve to the integrated cross section for the smooth (γ, n) curve. The straight-lined activation curve can also be fitted by slightly different cross-sectional values, but in each case the resulting cross-sectional curve has the same general characteristics. These characteristics are a continuous absorption on which is superimposed several absorption peaks.

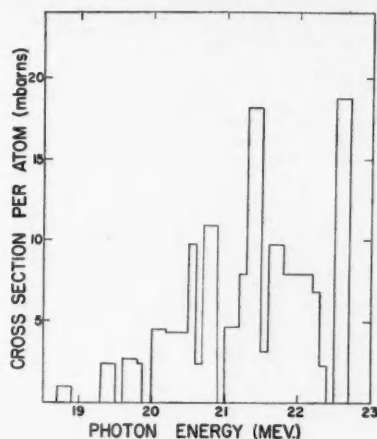


FIG. 12. The cross-sectional curve determined from the straight-lined $C^{12}(\gamma, n)C^{11}$ activation curve is plotted as a function of photon energy.

XII. CONCLUSIONS

From consideration of the experimental results we have drawn the following conclusions.

(1) The cross-sectional curve for the absorption of high energy photons in carbon has a resonance shape. This curve is very similar in shape to (γ, n) , (γ, p) , etc. cross-sectional curves.

(2) Nuclear scattering of gamma rays makes no important contribution to the total nuclear absorption in carbon for energies up to 25 Mev.

(3) The total integrated nuclear cross section in carbon is considerably less than predicted.

(4) Nuclear absorption in carbon does not take place solely in a few narrow discrete energy levels.

(5) The results of this experiment indicate that the absorption mechanism may best be represented by assuming a combination of a nuclear absorption continuum on which is superimposed absorption peaks.

(6) The observed electronic absorption coefficients in carbon between 12 and 20 Mev. are about 1.3% lower than the theoretical predicted values.

The authors wish to express their appreciation to the National Research Council of Canada, and the National Cancer Institute of Canada whose financial assistance made this project possible. They also wish to thank Dr. L. Katz and Dr. V. Telegdi for their many helpful discussions and J. Goldemberg who calculated the integrated cross section in carbon using the statistical considerations of Weisskopf.

REFERENCES

1. ADAMS, G. D. Phys. Rev. 74: 1706. 1948.
2. BLATT, J. M. and WEISSKOPF, V. F. Theoretical nuclear physics. John Wiley & Sons, Inc., New York. 1952.
3. BORSELLINO, A. Helv. Phys. Acta, 20: 136. 1947; Nuovo cimento, 4: 112. 1947.

4. BYERLY, P. R. and STEPHENS, W. E. *Phys. Rev.* 83: 54. 1951.
5. COLGATE, S. A. Ph.D. Thesis, Cornell Univ., Ithaca, New York. 1951.
6. DAVISSON, C. M. and EVANS, R. D. *Revs. Modern Phys.* 24: 79. 1952.
7. GAERTTNER, E. R. and YEATER, M. L. *Phys. Rev.* 76: 363. 1949.
8. GAERTTNER, E. R. and YEATER, M. L. *Phys. Rev.* 78: 621. 1950.
9. GOLDBABER, M. and TELLER, E. *Phys. Rev.* 74: 1046. 1948.
10. HALPERN, J., MANN, A. K., and ROTHMAN, M. *Phys. Rev.* 87: 164. 1952.
11. HASLAM, R. N. H., JOHNS, H. E., and HORSLEY, R. J. *Phys. Rev.* 82: 270. 1951.
12. HASLAM, R. N. H., KATZ, L., HORSLEY, R. J., CAMERON, A. G. W., and MONTALBETTI, R. *Phys. Rev.* 87: 196A. 1952.
13. HASLAM, R. N. H., KATZ, L., HORSLEY, R. J., CAMERON, A. G. W., and MONTALBETTI, R. Canadian Royal Society Meeting, Quebec City, June, 1952.
14. HEITLER, W. *Quantum theory of radiation*. The Clarendon Press, Oxford. 1936.
15. HORSLEY, R. J., HASLAM, R. N. H., and JOHNS, H. E. *Can. J. Phys.* 30: 159. 1952.
16. JOHNS, H. E., KATZ, L., DOUGLAS, R., and HASLAM, R. N. H. *Phys. Rev.* 80: 1062. 1950.
17. KATZ, L. and CAMERON, A. G. W. *Can. J. Phys.* 29: 518. 1951.
18. KATZ, L., JOHNS, H. E., BAKER, R., HASLAM, R. N. H., and DOUGLAS, R. A. *Phys. Rev.* 82: 271. 1951.
19. KATZ, L. and PENFOLD, A. S. *Phys. Rev.* 81: 815. 1951.
20. KLEIN, O. and NISHINA, Y. *Z. Physik*, 52: 853. 1929.
21. LEVINGER, J. S. and BETHE, H. A. *Phys. Rev.* 78: 115. 1950.
22. MANN, A. K. and HALPERN, J. *Phys. Rev.* 83: 371. 1951.
23. MONTALBETTI, R. Private Communication, University of Saskatchewan, Saskatoon, Sask.
24. NISHINA, Y. *Z. Physik*, 52: 869. 1929.
25. PERLMAN, M. L. and FRIEDLANDER, G. *Phys. Rev.* 74: 442. 1948.
26. SCHIFF, L. *Phys. Rev.* 70: 87. 1946.
27. VORTRUBA, V. *Phys. Rev.* 73: 1468. 1948.
28. WÄFFLER, H. and HIRZEL, O. *Helv. Phys. Acta*, 21: 200. 1948.
29. WALKER, R. L. *Phys. Rev.* 76: 527. 1949.
30. WHITE, G. *Natl. Bur. Standards Rept.* 1003. 1952.

FORBIDDEN TRANSITIONS IN DIATOMIC MOLECULES

III. NEW ${}^1\Sigma_u^- \leftarrow {}^3\Sigma_g^-$ AND ${}^3\Delta_u \leftarrow {}^3\Sigma_g^-$ ABSORPTION BANDS OF THE OXYGEN MOLECULE¹

BY G. HERZBERG

ABSTRACT

Two new forbidden transitions of the O_2 molecule have been found. They give rise to very faint absorption bands overlapping the much stronger forbidden ${}^3\Sigma_u^+ \leftarrow {}^3\Sigma_g^-$ bands previously described. The upper states are identified as ${}^1\Sigma_u^-$ and ${}^3\Delta_u$ respectively, both of which arise from the same electron configuration as the known states ${}^3\Sigma_u^+$ and ${}^3\Sigma_g^-$. For the ${}^1\Sigma_u^-$ state the following vibrational and rotational constants have been determined: $T_e = 36678.9_1$, $\omega_e = 650.4_3$, $\omega_e x_e = 17.03_6$, $\omega_e y_e = -0.105_6$, $\omega_e z_e = -0.0074_4$, $B_e = 0.826_1$, $\alpha_e = 0.0205_5$, $\gamma_e = -0.00083_0$ cm.⁻¹, $r_e = 1.597 \times 10^{-8}$ cm. The constants are based on the assumption of a certain vibrational numbering which may have to be revised (increased). For the ${}^3\Delta_u$ state the data are quite fragmentary and only two rotational constants, $B_3 = 0.817_7$, $B_5 = 0.791_5$, and one vibrational quantum, $\Delta G(5\frac{1}{2}) = 611.1_6$, have been determined. The bands of the ${}^3\Delta_u - {}^3\Sigma_g^-$ system are very close to those of the ${}^3\Sigma_u^+ - {}^3\Sigma_g^-$ system and represent in all probability the analogue in free O_2 of the diffuse triplet bands of Wulf, Finkelnburg, and Steiner ascribed to O_4 . The positions of the new ${}^1\Sigma_u^-$ and ${}^3\Delta_u$ states agree closely with those predicted by Moffitt. Almost half of the unidentified features of the spectrum of the nightglow agree within 5Å with the predicted positions of emission bands of the ${}^1\Sigma_u^- - {}^3\Sigma_g^-$ system.

A. INTRODUCTION

In paper II of this series (9) an analysis was presented of the ${}^3\Sigma_u^+ - {}^3\Sigma_g^-$ bands of oxygen based on absorption spectra of very high resolution which were obtained with absorbing paths up to 800 m. With such absorbing paths the ${}^3\Sigma_u^+ \leftarrow {}^3\Sigma_g^-$ bands appear with considerable intensity. In addition on the same plates two extremely weak new band systems occur which represent ${}^1\Sigma_u^- \leftarrow {}^3\Sigma_g^-$ and ${}^3\Delta_u \leftarrow {}^3\Sigma_g^-$ transitions. These band systems form the subject of the present paper. The data for the second system, ${}^3\Delta_u \leftarrow {}^3\Sigma_g^-$, are quite fragmentary and much greater path lengths would be required if one wanted to obtain an adequate analysis of this system.

Apart from supplying information about two new electronic states of the O_2 molecule, the new band systems appear to be of importance for an interpretation of the spectrum of the light of the night sky (nightglow). As is well known (13) the ${}^3\Sigma_u^+ - {}^3\Sigma_g^-$ bands occur prominently in the spectrum of the nightglow. It seems probable that band systems with upper states so close to that of the ${}^3\Sigma_u^+$ state will also appear. It is for this reason as well as a better understanding of the structure of the O_2 molecule that the present investigation was undertaken.

B. EXPERIMENTAL

The experimental details of the observation of the new bands have already been described in paper II. The new bands were observed only on the spectrograms with the longest path lengths. Even then they are quite weak and

¹Manuscript received February 13, 1953.

Contribution from the Division of Physics, National Research Council, Ottawa, Canada. Issued as N.R.C. No. 2983.

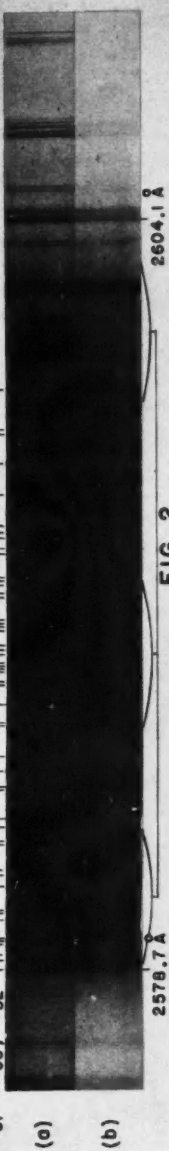
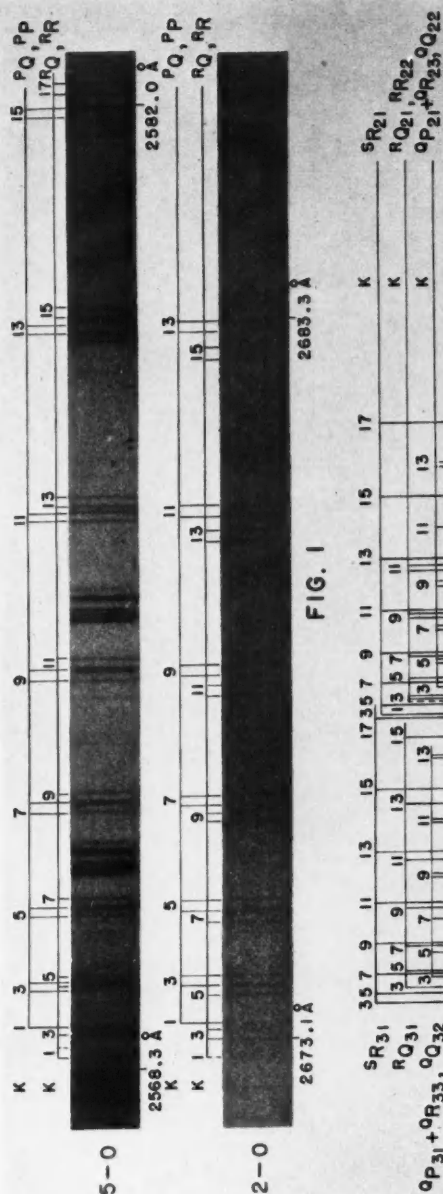
difficult to measure. For greater ease of measurement the original plates were enlarged using plates of high contrast (Eastman Kodak IV-O). Fig. 1 shows two of the bands of the ${}^1\Sigma_u^- \leftarrow {}^3\Sigma_g^-$ system and Fig. 2 shows one of the bands of the ${}^3\Delta_u \leftarrow {}^3\Sigma_g^-$ system. The faintness of the bands entails a greater than normal average error of the measurements, viz. about $\pm 0.1 \text{ cm.}^{-1}$ for unblended lines and appreciably higher for blended lines. Because of the long exposure times there were displacements of the order of 0.1 cm.^{-1} between the iron arc comparison spectrum (taken at the beginning of the exposure) and the oxygen spectrum. The present measurements were corrected in such a way that any residual shift is the same as for the ${}^3\Sigma_u^+ \leftarrow {}^3\Sigma_g^-$ bands given in II.

C. THE ${}^1\Sigma_u^- \leftarrow {}^3\Sigma_g^-$ BANDS

The absorption bands at 2714.5, 2672.3, 2634.0, 2599.2, 2568.0, and 2540.0 Å, as shown by the two examples of Fig. 1, consist each of four branches, two *R*-form and two *P*-form branches. Except for the much larger difference $B' - B''$, the structure of the new bands appears to be entirely similar to that of the red atmospheric oxygen bands which represent a ${}^1\Sigma_g^+ - {}^3\Sigma_g^-$ transition. This is borne out by the more detailed analysis: The two *R* and the two *P* branches are separated by the same wave number difference as the corresponding branches of the "atmospheric" bands, i.e., the differences $F_2 - F_1$ and $F_2 - F_3$ of the ${}^3\Sigma_g^-$ ground state of the O_2 molecule.

TABLE I
WAVE NUMBERS OF THE OBSERVED LINES IN THE ${}^1\Sigma_u^- \leftarrow {}^3\Sigma_g^-$ SYSTEM OF O_2

6-0 band, $\nu_0 = 39357.8$				
<i>K</i>	<i>P</i> <i>P</i>	<i>P</i> <i>Q</i>	<i>R</i> <i>R</i>	<i>R</i> <i>Q</i>
1				
3	39344.59*	39346.68	39353.68*	39355.78*
5	327.94	329.93	342.42	344.59*
7	305.01	306.98	324.61	326.34
9	275.84	277.78	301.06*	302.54*
11	240.48	242.22	270.45	272.58
13	198.49	200.62	233.88*	236.46
15	150.82			193.48
17			142.49	144.20
19	035.83			
5-0 band, $\nu_0 = 38929.7$				
<i>K</i>	<i>P</i> <i>P</i>	<i>P</i> <i>Q</i>	<i>R</i> <i>R</i>	<i>R</i> <i>Q</i>
1	38926.29*		38931.03?	38932.94
3	916.55	38918.65	926.29*	928.17
5	900.52*	902.33	915.38	917.38
7	878.04*	880.07	898.70	900.52*
9	849.53*	851.76	875.96	878.04*
11	815.63	817.56	847.10	849.53*
13	775.34	777.23*	812.28	814.35
15	729.08*	730.82	771.44	773.59
17	676.56*	678.54	724.13?	726.43*
19	618.28		671.45	673.48



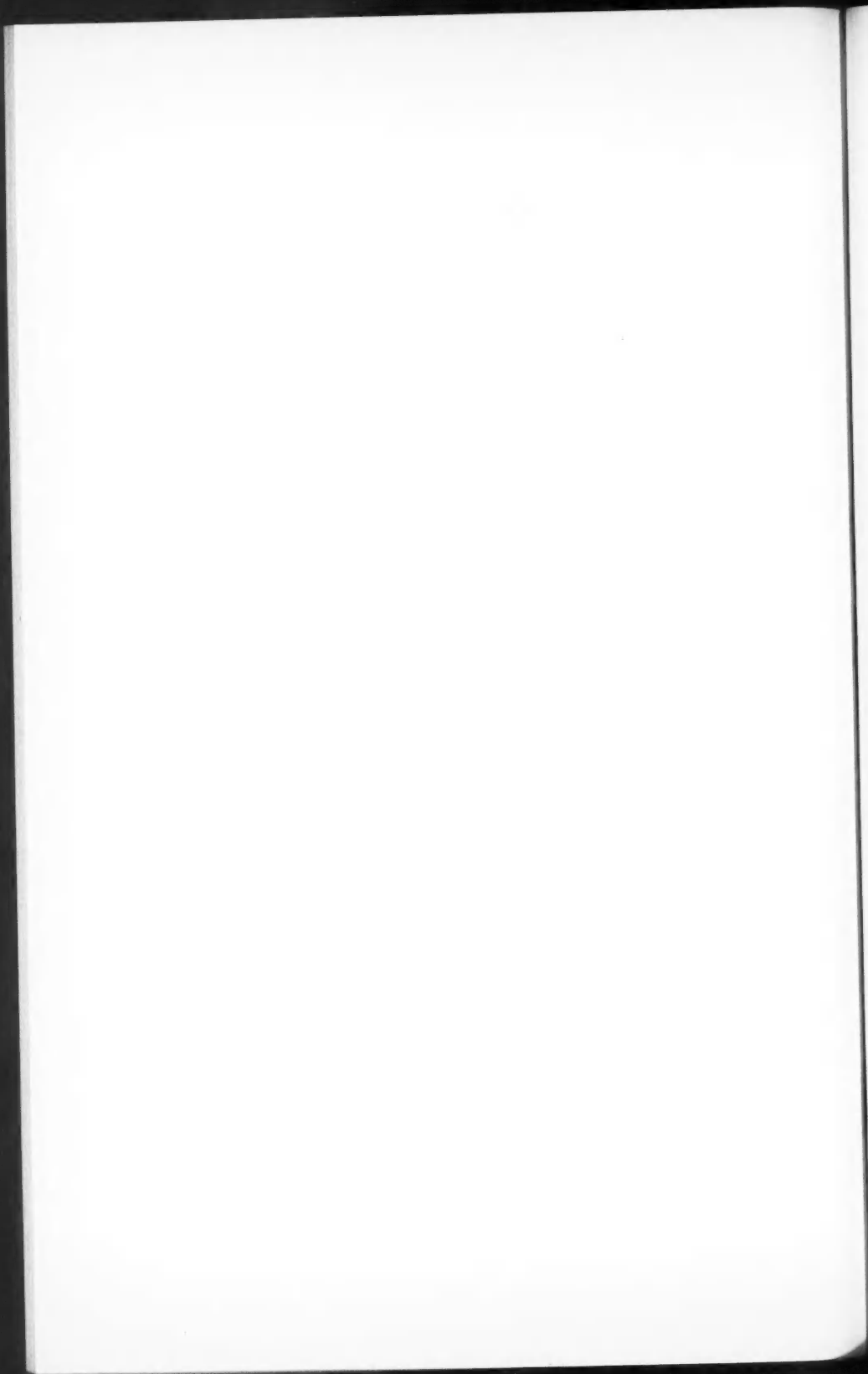


TABLE I (concluded)

4-0 band, $\nu_0 = 38461.3_0$				
K	P_P	P_Q	R_R	R_Q
1	38458.42*	38460.32*	38462.50*?	38464.35*?
3	448.33*	450.31*	458.42*	460.32*
5	432.65*?	434.81*?	448.33*	450.31*
7	410.80*	412.77*	432.65*?	434.81*
9	383.41*	385.30*	410.80*	412.77*
11	350.11*	351.92*	383.41*	385.30*
13	311.34*	313.00*	350.11*?	351.92*
15	266.61	268.16*	311.34*	313.00*
17	216.10	217.90	265.83	268.16*

3-0 band, $\nu_0 = 37954.1_1$				
K	P_P	P_Q	R_R	R_Q
1	37951.64*?			37957.38?
3	941.34	37943.93*	37951.64*	953.75
5	925.79	927.83	942.19	943.93*
7	†	†	927.23	929.14
9	†	†	†	†
11	846.20	848.39*	879.97*	882.28*
13	808.51	810.62*	848.39*	850.42
15			810.62*	813.07
17	716.29			
19		663.77		

2-0 band, $\nu_0 = 37409.5_s$				
K	P_P	P_Q	R_R	R_Q
1	37406.51			37413.22?
3	396.92	37398.83*	37407.61	409.58
5	381.80	384.36*	398.83*	400.67
7	361.42	363.29	384.36*	386.33
9	335.53	337.50	364.76	366.73
11	304.36	306.36	339.71	341.60
13	267.89	269.69	309.23	311.18
15			273.37	275.49

1-0 band, $\nu_0 = 36828.7_s$				
K	P_P	P_Q	R_R	R_Q
1			36830.40?	
3	36816.01?		827.32?	36828.97
5	801.54	36803.34	819.05	
7	781.74	783.52	805.41	807.31
9	756.45	758.29	786.43	788.60
11	726.34?	728.51?	762.58	764.59
13	690.76	692.62	733.14	735.54
15	649.92	651.83	699.15	701.27
17	604.22	606.11	659.54	661.59

*An asterisk indicates blended lines assigned to two or more branches. (The overlapping branches may also be in the $^3\Sigma_u^+ \leftarrow ^3\Sigma_g^-$ system.)

? A question mark indicates a doubtful assignment.

† These lines have not been measured because of overlapping by strong lines of the $3-0 \ ^3\Sigma_u^+ - ^3\Sigma_g^-$ band.

In Table I are listed the wave numbers of the lines of all the measured bands of this band system. The designation of the branches, $^R R$, $^R Q$, $^P P$, $^P Q$, is explained in Fig. 3. This figure is identical with the corresponding figure for the atmos-

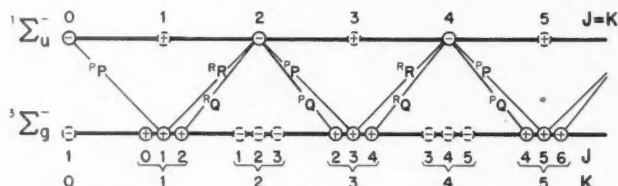


FIG. 3. Branches of a $1\Sigma_u^- - 3\Sigma_g^-$ transition.

The rotational levels that are missing in O_2 are indicated by broken circles. The corresponding transitions are not shown.

spheric oxygen bands (see (8), p. 278) except that here the upper state is $1\Sigma_u^-$ instead of $1\Sigma_g^+$, i.e., in the upper state the even rotational levels (the only ones that occur) are "negative" rather than "positive". As is well known, the atmospheric oxygen bands are due to magnetic dipole radiation while the new bands are here assumed to be due to electric dipole radiation. For the former only states of the same parity (+, -) combine, while for the latter only states of opposite parity combine. On the basis of the band structure alone it is impossible to distinguish a $1\Sigma_g^+ - 3\Sigma_g^-$ from a $1\Sigma_u^- - 3\Sigma_g^-$ band. However, as explained in section E, the electron configuration of the O_2 molecule decides in favor of $1\Sigma_u^- - 3\Sigma_g^-$.

It can easily be checked that the combination differences $\Delta_2 F''(K) = R(K-1) - P(K+1)$ of the new bands agree within the accuracy of the present measurements with the much more precise combination differences of the atmospheric oxygen bands. The combination differences $\Delta_2 F'(K) = R(K) - P(K)$ yield provisional values for the rotational constants of the upper state. Somewhat more precise values were obtained by evaluating the combination sums $R(K) + P(K)$ and making use of the accurately known constants of the ground state (Babcock and L. Herzberg (1)). One has

$$[1] \quad R(K) + P(K) = 2\nu_0 + (2B' - 4D') + 2(B' - B'' - 6D')K(K+1) - 2(D' - D'')K^2(K+1)^2.$$

Thus, plotting the observed combination sums against $K(K+1)$ one obtains from the initial slope a value of $B' - B''$, from the deviation from a straight line a value of $D' - D''$, and from the intercept on the ordinate axis a value of ν_0 . In order to make full use of all measured lines the known values of $F_2(K) - F_1(K)$ and $F_2(K) - F_3(K)$ for the lower state, as listed in II, were subtracted from the wave numbers of the $^R Q$ and $^P Q$ lines respectively, yielding additional "observed" values of $^R R(K)$ and $^P P(K)$ which were averaged with the directly observed values for the determination of the constants according to [1].

In Table II the constants of the individual vibrational levels of the $1\Sigma_u^-$ state obtained in this way are listed. Because of the weakness of the bands these constants are less precise than those of the $3\Sigma_u^+$ state given in II. In particular,

TABLE II

BAND ORIGINS OF THE ${}^1\Sigma_u^- \leftarrow {}^3\Sigma_g^-$ BANDS AND VIBRATIONAL AND ROTATIONAL CONSTANTS OF THE UPPER, ${}^1\Sigma_u^-$, STATE

v	ν_0	$\Delta G(v + \frac{1}{2})$	B_v	ΔB_v	D_v
1	36828.7 ₅	580.8 ₀	0.7935	0.024 ₀	10.5×10^{-6}
2	37409.5 ₅	544.5 ₆	0.769 ₅	0.025 ₅	9.7×10^{-6}
3	37954.1 ₁	507.1 ₉	0.744 ₀	0.027 ₃	$(9.5 \times 10^{-6} \text{ assumed})$
4	38461.3 ₀	468.4 ₀	0.7167	0.0285	$(9.5 \times 10^{-6} \text{ assumed})$
5	38929.7 ₀	428.1 ₅	0.6882	0.0309	9.5×10^{-6}
6	39357.8 ₅		0.6573		$(9.5 \times 10^{-6} \text{ assumed})$

the D_v values of only three bands could be determined directly, with an accuracy of perhaps 10%; for the other bands D_v was assumed to be the same as for the 5-0 band which was considered to give the most reliable value.

It is impossible to determine the vibrational numbering of the bands since the observed progression fades out at the longward end. Judging from the behavior of the ${}^3\Sigma_u^+ \leftarrow {}^3\Sigma_g^-$ bands one would expect several more bands at the longward end if longer paths were available. For the sake of definiteness it is assumed here that the first measured band is 1-0, realizing that the numbering may have to be shifted by several units. On the basis of this assumed numbering one finds the following constants¹

$$T_e = 36678.9_1, \quad \omega_e = 650.4_9, \quad \omega_e x_e = 17.03_6, \quad \omega_e y_e = -0.105_6, \\ \omega_e z_e = -0.0074_4, \quad B_e = 0.826_1, \quad \alpha_e = 0.0205_5, \quad \gamma_e = -0.00083_0 \text{ cm}^{-1}.$$

From B_e one obtains for the equilibrium internuclear distance in the ${}^1\Sigma_u^-$ state $r_e = 1.597 \times 10^{-8}$ cm. If the vibrational numbering were increased, r_e would be somewhat smaller.

A fairly short extrapolation of the vibrational levels leads to a convergence limit at 41070 cm^{-1} . The agreement of this value, within the uncertainty of the extrapolation, with the more accurate value 41219 cm^{-1} obtained from the ${}^3\Sigma_u^+ - {}^3\Sigma_g^-$ system leaves no doubt that the ${}^1\Sigma_u^-$ state dissociates into normal (3P) oxygen atoms like the ${}^3\Sigma_u^+$ state. It may be noted that the $\Delta G(v + \frac{1}{2})$ and B_v values of the ${}^1\Sigma_u^-$ state are appreciably smaller than those of the ${}^3\Sigma_u^+$ state at the same energy.

D. THE ${}^3\Delta_u \leftarrow {}^3\Sigma_g^-$ BANDS

As mentioned before, the analysis of the ${}^3\Delta_u \leftarrow {}^3\Sigma_g^-$ bands is quite fragmentary. Wulf (14) and Finkelburg and Steiner (6) have observed a progression of diffuse absorption bands in oxygen at high pressure which almost coincide with the ${}^3\Sigma_u^+ \leftarrow {}^3\Sigma_g^-$ bands. Each of these diffuse bands has three peaks. Their intensity varies with the square of the pressure indicating that they are due to a loosely bound $(O_2)_2$ molecule. In Fig. 2b one of these bands is shown as it appears under

¹For definitions of these constants see Herzberg (8).

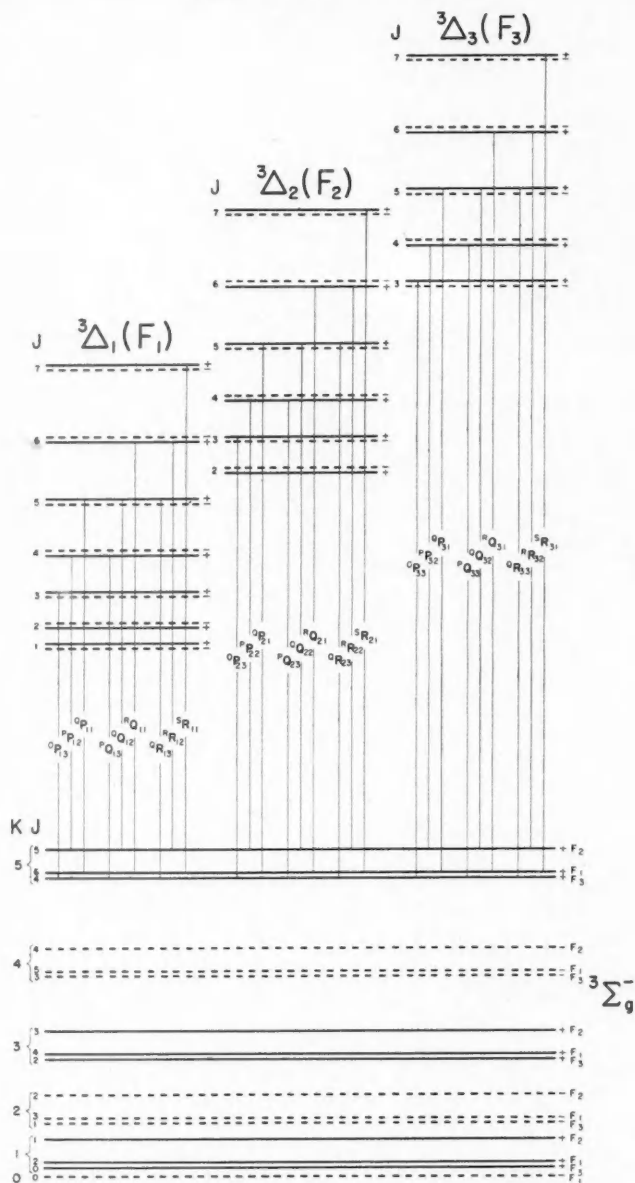


FIG. 4. Energy level diagram for a ${}^3\Delta_u - {}^3\Sigma_g^-$ transition.
The antisymmetric levels which are missing in O_2 are indicated by broken lines.
Only one line of each branch (for $K = 5$) is shown.

high dispersion at a pressure of 8 atm. Finkelnburg and Steiner (6) have interpreted these bands as due to a ${}^3\Delta \leftarrow {}^3\Sigma$ transition, that is, have assumed that the three diffuse peaks of each band are due to the triplet structure of the upper ${}^3\Delta$ state. Later, however, Finkelnburg (5) rejected this interpretation of the triplet structure in favor of one using vibrational levels of $(O_2)_2$. At a lower pressure and correspondingly longer path, as shown in Fig. 2a, the Wulf bands are overlapped by a fine structure which is different both from that of the ${}^3\Sigma_u^+ \leftarrow {}^3\Sigma_g^-$ and the ${}^1\Sigma_u^+ \leftarrow {}^3\Sigma_g^-$ bands. This fine structure is here ascribed to a ${}^3\Delta_u \leftarrow {}^3\Sigma_g^-$ transition and this is assumed to be the transition in free O_2 to which the Wulf bands in $(O_2)_2$ correspond.

The structure of each of these new O_2 bands is rather complicated and on account of their faintness the branches are incomplete and therefore difficult to find. However, a number of fragments of branches have been found in two of the bands (see Fig. 2a). The branches can be most easily understood on the assumption that the upper state is ${}^3\Delta_u$, an assumption that is also supported by the electron configuration (see section E).

In Fig. 4 an energy level diagram for a ${}^3\Delta_u \leftarrow {}^3\Sigma_g^-$ transition is given which shows all the possible branches. Actually a ${}^3\Pi_u \leftarrow {}^3\Sigma_g^-$ transition would be entirely similar except for the missing lines at the beginning of the branches. Because of the faintness of the bands the number of missing lines near the band origin cannot be uniquely established. At present a decision can only be made on the basis of the electron configuration (see below) which definitely favors ${}^3\Delta_u \leftarrow {}^3\Sigma_g^-$.

Table III gives the fragments of branches of two of the ${}^3\Delta_u \leftarrow {}^3\Sigma_g^-$ bands. The observation of Q- and S-form branches in addition to R- and P-form branches establishes the presence of rotational levels with both odd and even J in the upper state, that is, Λ must be different from zero in the upper state. In the "best" band with center at about 2590\AA only two of the three subbands have been partially analyzed, in the second band only one.

The vibrational numbering of the ${}^3\Delta_u \leftarrow {}^3\Sigma_g^-$ bands is quite uncertain. Somewhat arbitrarily we assume that the first diffuse band observed by Herman (7) at 2913\AA is the 0-0 band of this system. This makes the two bands here discussed the 6-0 and 5-0 bands. It may be noted that these two bands lie close to the 4-0 and 3-0 bands of the ${}^3\Sigma_u^+ \leftarrow {}^3\Sigma_g^-$ system in the numbering adopted in II. It is quite possible that in either system the numbering will have to be increased by one or more units. Since the diffuse ultraviolet $(O_2)_2$ bands have been observed almost up to the dissociation limit at 41219 cm^{-1} by Finkelnburg and Steiner (6), there is no question that the ${}^3\Delta_u$ state like ${}^1\Sigma_u^+$ and ${}^3\Sigma_u^+$ dissociates into normal 3P atoms.

From the combination differences, combination sums, and Q branches the following average band constants have been determined:

$$\begin{array}{ll} 6-0 \text{ band: } \nu_0^{(3)} = 38768.7_9 \text{ cm}^{-1}, & B_6^{(3)} = 0.797_1 \text{ cm}^{-1} \\ & \nu_0^{(2)} = 38622.8_8, & B_6^{(2)} = 0.791_5 \\ 5-0 \text{ band: } \nu_0^{(3)} = 38157.6_3 & B_5^{(3)} = 0.823_3 \end{array}$$

where $^{(3)}$ and $^{(2)}$ refer to the most shortward and the central subband respectively (${}^3\Delta_3$ and ${}^3\Delta_2$ respectively). Only one vibrational quantum can be obtained,

TABLE III

WAVE NUMBERS OF THE OBSERVED LINES IN THE ${}^3\Delta_u \leftarrow {}^3\Sigma_g^-$ SYSTEM OF O_2

6-0 band, ($\nu_0^{(3)} = 38768.7_9$, $\nu_0^{(2)} = 38622.8_6$)					
K	$S_{R_{31}}$	$R_{Q_{31}}$	$Q_{Q_{22}}$	$Q_{P_{31}} + Q_{R_{33}}$	
1		38772.37*			
3	38777.23*	769.40	38761.09*	38763.09	
5	772.37*	761.09*		751.53	
7	761.94	747.69		734.98	
9	746.70	729.08*	711.63	713.85	
11	726.43*	705.34	684.27	686.19	
13	700.27	676.56*	652.85	654.15	
15	669.13	642.74	615.15*	617.06	
17	633.25	603.45*	572.55	574.80	

K	$S_{R_{21}}$	$R_{R_{22}}$	$R_{Q_{21}}$	$Q_{Q_{22}}$	$Q_{P_{21}} + Q_{R_{23}}$
1		38624.79 ?	38626.03*?		
3	38631.41	621.49	623.46	38615.15*	38617.06
5	626.03*	612.81*	615.15*	603.45*	605.52
7	615.15*	599.62*	601.29	586.75	588.70
9	599.62*	580.32	582.46	564.64	566.93
11	578.85	556.40	558.41	537.46	
13	552.57			504.75 ?	507.09 ?
15	521.36				
17	484.64				

5-0 band, ($\nu_0^{(3)} = 38157.6_3$)				
K	$S_{R_{31}}$	$R_{Q_{31}}$	$Q_{P_{31}} + Q_{R_{33}}$	$P_{Q_{33}}$
1		38159.56		
3		156.71	38150.27	38145.53
5	38160.61	149.03	139.18	131.00
7	151.33	136.46	123.16	111.65
9	137.77	118.90	102.30	987.22
11	117.81	996.25	976.56	958.23
13	993.39	968.84	945.93	
15		936.49	910.09	
17		37999.04		

$\Delta G(5\frac{1}{2}) = 611.1_6 \text{ cm}^{-1}$. The slight difference of B_6 in the two subbands, i.e., in two of the components of the ${}^3\Delta$ state, appears to be real. The sign of this difference is as expected for a normal ${}^3\Delta$ state, and its magnitude is in rough agreement with that expected for a case (a) triplet state whose splitting between central and shortward component is 145.9 cm^{-1} . Incidentally, this splitting may be compared with the values 136 and 119 cm^{-1} which Finkelburg (5) gives as the separations of the shortward and central and of the central and longward peaks of the $(O_2)_2$ bands. The B_v values of the central components would be expected to represent good approximations to the true B_v values. Assuming that the difference $B_5^{(3)} - B_5^{(2)}$ is the same as $B_6^{(3)} - B_6^{(2)}$ we have

$$B_5 = 0.817_7, \quad B_6 = 0.791_5 \text{ cm}^{-1}.$$

E. DISCUSSION AND CONCLUSION

By the observations described above two new electronic states of the O_2 molecule have been established, both of which dissociate into normal (3P) O atoms. The observed band structure of the first system is compatible with either a $^1\Sigma_u^-$ or $^1\Sigma_g^+$ upper state, while that of the second system is compatible with either $^3\Delta_u$ or $^3\Pi_u$ or possibly $^3\Delta_g$ or $^3\Pi_g$. The possibility $^3\Delta_g$ is immediately eliminated since $^3\Delta_g$ cannot arise from normal atoms. However, all the other states ($^1\Sigma_u^-$, $^1\Sigma_g^+$, $^3\Delta_u$, $^3\Pi_u$, $^3\Pi_g$) can arise from normal atoms.

It is well known that the lowest electron configuration of the O_2 molecule is [2]

$$(K)(K)(\sigma_g 2s)^2(\sigma_u 2s)^2(\sigma_g 2p)^2(\pi_u 2p)^4(\pi_g 2p)^2$$

which gives rise to the three known low lying states $X^3\Sigma_g^-$ (ground state), $b^1\Sigma_g^+$, and $a^1\Delta_g$. The first excited electron configuration is

$$[3] \quad (K)(K)(\sigma_g 2s)^2(\sigma_u 2s)^2(\sigma_g 2p)^2(\pi_u 2p)^3(\pi_g 2p)^3$$

which gives rise to the states

$$^1\Sigma_u^+, ^1\Sigma_u^-, ^1\Delta_u, ^3\Sigma_u^+, ^3\Sigma_u^-, ^3\Delta_u.$$

Of these six states two, $^3\Sigma_u^-$ and $^3\Sigma_u^+$, are accounted for as the upper states of the Schumann-Runge bands and of the near ultraviolet bands discussed in II. If the upper states of the two new band systems belong to this electron configuration, they can only be $^1\Sigma_u^-$ and $^3\Delta_u$ respectively, and thus these upper states would be uniquely identified. However, if the two new states belong to a configuration different from [3] they may yet be $^1\Sigma_g^+$ or $^3\Pi_u$, $^3\Pi_g$ respectively. The lowest electron configuration that could give a $^1\Sigma_g^+$ state (other than [2]) is

$$[4] \quad (K)(K)(\sigma_g 2s)^2(\sigma_u 2s)^2(\sigma_g 2p)^2(\pi_u 2p)^2(\pi_g 2p)^4$$

which would have about twice the energy of [3] and is therefore clearly excluded, that is, the upper state of the first new system is definitely $^1\Sigma_u^-$.

The lowest configuration that could give $^3\Pi_u$ is

$$[5] \quad (K)(K)(\sigma_g 2s)^2(\sigma_u 2s)^2(\sigma_g 2p)^2(\pi_u 2p)^4(\pi_g 2p)(\sigma_u 2p),$$

while the lowest configuration that could give $^3\Pi_g$ is

$$[6] \quad (K)(K)(\sigma_g 2s)^2(\sigma_u 2s)^2(\sigma_g 2p)(\pi_u 2p)^4(\pi_g 2p)^3$$

or

$$[7] \quad (K)(K)(\sigma_g 2s)^2(\sigma_u 2s)^2(\sigma_g 2p)^2(\pi_u 2p)^3(\pi_g 2p)^2(\sigma_u 2p).$$

All three of these configurations would be expected to have a higher energy than [3] although [5] and [6] might not be much higher. Since the upper state of the first new system has just been shown to belong to [3] it appears unlikely that that of the second system which is so close to the first should belong to a different electron configuration of higher energy. Thus the upper state of the second band system is very probably $^3\Delta_u$ of [3].

Further confirmation of the correctness of this identification is supplied by the calculations of Moffitt (10).¹ He has predicted by a modified method of

¹Similar calculations by a different and simpler method have recently been carried out by Fumi and Parr (unpublished). Their results are closely similar to those of Moffitt.

antisymmetrized molecular orbitals the relative positions of the three states ${}^1\Sigma_u^-$, ${}^3\Delta_u$, and ${}^3\Sigma_u^+$ of configuration [3]. He finds that the ${}^1\Sigma_u^-$ and ${}^3\Delta_u$ states are separated by less than 0.2 e.v. from the ${}^3\Sigma_u^+$ state. In Fig. 5 Morse potential

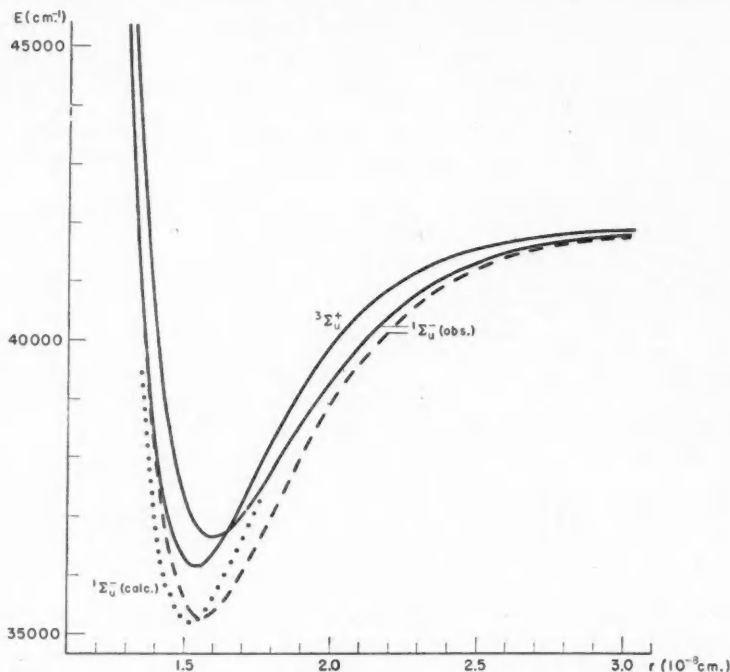


FIG. 5. Potential energy curves of the ${}^3\Sigma_u^+$ and ${}^1\Sigma_u^-$ states of O_2 .

The full-line ${}^1\Sigma_u^-$ curve corresponds to the numbering adopted in the text, the broken-line ${}^1\Sigma_u^-$ curve corresponds to a numbering shifted by two units. The dotted curve is obtained from the ${}^3\Sigma_u^+$ curve by subtracting Moffitt's theoretical difference ${}^3\Sigma_u^+ - {}^1\Sigma_u^-$.

curves of the ${}^3\Sigma_u^+$ and ${}^1\Sigma_u^-$ states are shown as obtained from the observed ω_e , D_e , and r_e values assuming the numbering adopted here for ${}^1\Sigma_u^-$ and that used in II for ${}^3\Sigma_u^+$. In addition, as a broken line curve a Morse function is shown which corresponds to a shift of two units in the vibrational numbering of the ${}^1\Sigma_u^-$ state. This curve is merely to show the effect of a change in numbering. The true numbering may be different from that corresponding to either curve, but probably not very different. The dotted curve represents Moffitt's predicted potential curve for ${}^1\Sigma_u^-$ as obtained from his calculated energy difference between ${}^3\Sigma_u^+$ and ${}^1\Sigma_u^-$ and the "observed" ${}^3\Sigma_u^+$ curve. It must be realized that the "observed" curves, even apart from the uncertainties of the vibrational numbering, are only approximate because the ΔG curves of both ${}^1\Sigma_u^-$ and ${}^3\Sigma_u^+$ states are far from linear as would be required for a Morse function. Considering all these uncertainties as well as the limitations of the theoretical predictions, the agree-

ment between observed and theoretical potential curves of ${}^1\Sigma_u^-$ must be considered as quite satisfactory and as lending strong support both to the identification of the upper state of the first new band system and to Moffitt's method of calculating molecular energy states. The data for the ${}^3\Delta_u$ state are too incomplete to draw an "observed" potential curve, but do suggest that the ${}^3\Delta_u$ curve is slightly below ${}^3\Sigma_u^+$ in qualitative agreement with Moffitt's prediction that ${}^3\Delta_u$ should be about halfway between ${}^3\Sigma_u^+$ and ${}^1\Sigma_u^-$.

The transition ${}^1\Sigma_u^- - {}^3\Sigma_g^-$ is a simple singlet-triplet intercombination. It is not forbidden by any other selection rule but $\Delta S = 0$. It is, therefore, surprising that its intensity is so very low. A rough estimate indicates that its intensity is less than 1/1000 of that of the atmospheric oxygen bands which represent a magnetic dipole singlet-triplet intercombination (${}^1\Sigma_g^+ - {}^3\Sigma_g^-$); in other words, the ${}^1\Sigma_u^- - {}^3\Sigma_g^-$ bands of oxygen have only about 10^{-7} of the intensity of a strong electric-dipole singlet-triplet intercombination. This extremely low transition probability appears even more unusual when one considers the fact that the ${}^3\Sigma_u^-$ state of the same configuration to which ${}^1\Sigma_u^-$ belongs combines very strongly with the ground state ($f = 0.18$). The reason for this low intensity of ${}^1\Sigma_u^- - {}^3\Sigma_g^-$ may lie in the fact that both states dissociate into normal atoms, that is, do not combine with each other for large internuclear distances by electric dipole radiation. The ${}^3\Sigma_u^-$ state, on the other hand, is of ionic character (Mulliken (11)) even though, on account of interaction with another similar state, it eventually dissociates into ${}^3P + {}^1D$ oxygen atoms. Similar arguments apply to the explanation of the low intensity of the ${}^3\Delta_u - {}^3\Sigma_g^-$ transition which is forbidden only by the rule $\Delta\Lambda = 0, \pm 1$.

As has been mentioned in the introduction, it appears probable that the ${}^1\Sigma_u^- - {}^3\Sigma_g^-$ bands occur in emission in the spectrum of the nightglow since the ${}^3\Sigma_u^+ - {}^3\Sigma_g^-$ bands with an upper state very close to that of the former are

TABLE IV
DESLANDRES TABLE (WAVE LENGTHS IN Å) OF THE ${}^1\Sigma_u^- - {}^3\Sigma_g^-$ SYSTEM OF O_2

$v' \backslash v''$	0	1	2	3	4	5	6	7
0	2760.7	2884.7	3018.2	3162.3*	3318.2	3487.6	3672.1*	3873.8*
1	2714.5	2834.2	2963.0	3101.8*	3251.7	3414.2	3590.8	3783.4*
2	2672.3	2788.3	2912.9	3046.9	3191.4*	3347.8	3517.4*	3702.0*
3	2634.0	2746.6	2867.4	2997.1	3136.9	3287.8	3451.3	3628.8
4	2599.2	2708.9	2826.2	2952.2	3087.7	3233.9	3391.9*	3563.2
5	2568.0	2674.9	2789.3	2911.9	3043.7	3185.6	3338.8	3504.7
6	2540.0	2644.6	2756.4	2876.1	3004.5	3142.7	3291.7	3452.9
$v' \backslash v''$	8	9	10	11	12	13	14	15
0	4095.1	4339.0	4608.9	4909.3	5245.2	5623.4	6051.8	6541.1
1	3994.2	4225.9	4481.6	4765.0	5080.9	5434.9	5834.1	6287.5
2	3903.6*	4124.6	4367.8	4636.7*	4935.2*	5268.5	5642.9	6065.9
3	3822.4	4034.0	4266.3	4522.4*	4806.0*	5121.6	5474.6	5871.9
4	3749.7	3953.1	4176.0*	4421.0	4691.6*	4991.9	5326.6	5702.1
5	3684.9	3881.2	4095.8	4331.3*	4590.7	4877.8	5196.9	5553.7
6	3627.7*	3817.7	4025.2	4252.4*	4502.2	4777.9	5083.8	5424.6

prominent in this spectrum. In Table IV the predicted wave lengths of the $^1\Sigma_u^- - ^3\Sigma_g^-$ emission bands are given as obtained from the positions of the absorption bands and the known vibrational levels of the ground state. It must be realized that in emission, bands with low v' are of importance, and if the vibrational numbering has to be shifted appreciably a number of important bands would have to be added at the top of Table IV. If one compares with the 47 unidentified bands in the list of nightglow radiations given by Déjardin (3) one finds coincidences within 5\AA for the 20 bands marked by an asterisk in Table IV. Nine of these coincidences are within 2\AA or less. Whether these coincidences are real, that is, whether or not the $^1\Sigma_u^- - ^3\Sigma_g^-$ is actually present in the spectrum of the nightglow, is difficult to assess with certainty. The identified bands lie roughly on a Condon parabola and the gaps in this parabola are largely due to the fact that the particular bands coincide with nightglow bands already assigned to other band systems. The number of chance coincidences evaluated according to the method of Russell and Bowen (12) is 13. The ratio of observed to calculated coincidences ($20/13 = 1.54$) is about as large as that found by Dufay and Déjardin (4) for the $^3\Sigma_u^+ - ^3\Sigma_g^-$ bands of O_2 and the Vegard-Kaplan bands of N_2 , both of which are fairly generally agreed to be present in the nightglow.

Incidentally the number of observed coincidences (within 5\AA) is precisely the same as for the hypothetical band system specially designed by Barbier (2) to explain the unidentified night sky radiation. The reality of this system appears doubtful since the only molecule to which it can be ascribed in view of the lower state vibrational quanta, viz., CO, cannot have an excited state at the "observed" energy, the lowest excited state possible according to the electron configuration being the upper $^3\Pi$ state of the Cameron bands (see (8)).

On the whole it would appear that the evidence for the identification of the $^1\Sigma_u^- - ^3\Sigma_g^-$ bands in the nightglow spectrum is fairly favorable, but by no means unambiguous.

The identification of the $^3\Delta_u - ^3\Sigma_g^-$ bands in the nightglow spectrum will be much more difficult even when more complete data on this system become available, because these bands are so close to the $^3\Sigma_u^+ - ^3\Sigma_g^-$ bands except possibly at the lowest v' values.

ACKNOWLEDGMENTS

The experimental part of this investigation was carried out at the Yerkes Observatory. Grateful thanks are due to the authorities of Yerkes Observatory for making this work possible. I am much indebted to Mrs. Sarah Segall for her careful work with the measurements and computations, and to Drs. A. E. Douglas and P. Brix for helpful criticism of the manuscript.

REFERENCES

1. BABCOCK, H. D. and HERZBERG, L. *Astrophys. J.* 108: 229. 1948.
2. BARBIER, D. The emission spectra of the night sky and aurorae. Physical Society, London. 1948. p. 8.
3. DÉJARDIN, G. The emission spectra of the night sky and aurorae. Physical Society, London. 1948. p. 3.
4. DUFAY, J. and DÉJARDIN, G. *Ann. Géophys.* 2: 249. 1946.
5. FINKELNBURG, W. *Z. Physik*, 90: 1. 1934.

6. FINKELNBURG, W. and STEINER, W. *Z. Physik*, 79: 69. 1932.
7. HERMAN, L. *Ann. Phys.* (11) 11: 548. 1939.
8. HERZBERG, G. *Molecular spectra and molecular structure. I. Spectra of diatomic molecules.* 2nd ed. D. Van Nostrand Company Inc., New York. 1950.
9. HERZBERG, G. *Can. J. Phys.* 30: 185. 1952.
10. MOFFITT, W. *Proc. Roy. Soc. (London), A*, 210: 224. 1951.
11. MULLIKEN, R. S. *J. Chem. Phys.* 7: 20. 1939.
12. RUSSELL, H. N. and BOWEN, I. S. *Astrophys. J.* 69: 196. 1929.
13. SWINGS, P. and MEINEL, A. B. *In The atmospheres of the earth and planets, edited by G. P. Kuiper.* 2nd ed. University of Chicago Press, Chicago. 1952.
14. WULF, O. R. *Proc. Natl. Acad. Sci. U.S.* 14: 609. 1928.

A CONDUCTING PERMEABLE SPHERE IN THE PRESENCE OF A COIL CARRYING AN OSCILLATING CURRENT¹

BY JAMES R. WAIT²

ABSTRACT

The analysis is carried out for the problem of a current-carrying coil in the neighborhood of a spherical body whose conductivity and magnetic permeability differ from the surroundings. The case is considered in detail where the frequency is low enough so that the primary field of the coil can be derived from a magnetic scalar potential. The secondary magnetic fields due to the sphere are then derived. The "in-phase" and "quadrature" components of the secondary field are discussed numerically and illustrated by graphs. The results have application to electrical prospecting.

INTRODUCTION

The problem of the electromagnetic response of a conducting sphere has been studied by many. Debye (1) has considered the case of a plane wave incident on a sphere. Other investigators (4) have applied the general theory of Debye to special cases. March (2) has developed a formal solution for a nonpermeable conducting sphere in a dipolar field. The author (5) has recently considered the conducting sphere under the influence of a uniform transient magnetic field and its application to geophysical prospecting.

Another problem of certain interest to workers in electrical prospecting is that of a conducting permeable sphere in the vicinity of a solenoidal coil carrying an oscillating current at audio-frequencies. The reaction of the sphere as indicated by the voltage developed in an associated "pickup" coil is a means of detecting the presence of the sphere. The analysis is carried out in this paper.

FIELD OF A SOLENOID AT LOW FREQUENCIES

It is desirable to first consider the normal fields of a solenoidal coil of finite length embedded in a homogeneous, isotropic, conducting medium characterized by a conductivity σ , dielectric constant ϵ , and magnetic permeability μ in m.k.s. units. The coil is considered to extend from $z = A$ to $z = B$ on the z axis of a conventional polar cylindrical coordinate system (ρ, ϕ, z) with axial symmetry as shown in Fig. 1. The current in the insulated wire of the solenoid is I amperes, and varies as $e^{i\omega t}$. The cross-sectional area of the solenoid is A and its diameter is assumed to be small relative to other dimensions. There are N turns of the wire per meter length. The equivalent magnetic current K flows essentially in the direction of the z axis and is related to the current I in the wire as follows:

$$[1] \quad K = i\mu\omega ANI.$$

¹ Manuscript received December 1, 1952.

Contribution from the Department of Electrical Engineering, University of Toronto, Toronto, Ont. Presented at the Toronto Meeting of the Society of Exploration Geophysicists on October 27th, 1952.

² Now with Defence Research Board, Ottawa, Canada.

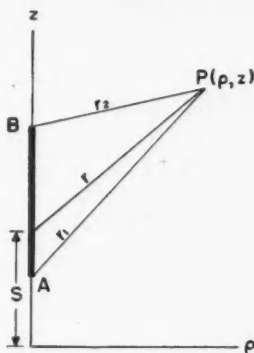


FIG. 1. Schematic representation of a current-carrying solenoidal coil extending from A to B .

The distance from the point of observation P to a point on the solenoid is denoted by r . For cases of practical interest the following approximation is always valid (6):

$$|\gamma r| \ll 1$$

where γ is the propagation constant of the medium given by

$$\gamma = (i\sigma\mu\omega - \epsilon\mu\omega^2)^{1/2} \approx (i\sigma\mu\omega)^{1/2}.$$

For this case the magnetic fields can be derived from a magnetic potential U as follows:

$$[2] \quad H_z = -\frac{\partial U}{\partial z}$$

and

$$[3] \quad H_\rho = -\frac{\partial U}{\partial \rho}$$

where

$$[4] \quad U = K(4\pi i\mu\omega)^{-1} (r_1^{-1} - r_2^{-1})$$

$$\text{and} \quad r_1 = [(z - A)^2 + \rho^2]^{1/2}, \quad r_2 = [(z - B)^2 + \rho^2]^{1/2}.$$

Then at sufficiently low frequencies (less than 500 c.p.s.) in a moderately conducting medium (less than 0.01 mhos per meter) the fields may be described as being due to a magnetic pole or source of magnetic potential at A and an identical pole of opposite sense at B .

When the distances r_1 and r_2 become much greater than the length of the solenoid the potential U is given by

$$[5] \quad U \cong \frac{K(B - A)\rho}{4\pi i\mu\omega r_0^3}$$

where $r_0 \approx r_1 \approx r_2$. The solenoid is then equivalent to a magnetic dipole.

Since for certain electrical prospecting techniques in bore holes the length of the solenoid is comparable to other significant dimensions, it is not permissible to represent the solenoid as a magnetic dipole generally.

RESPONSE OF THE CONDUCTING SPHERE

The calculation of the response of a conducting sphere in the presence of a solenoid is then equivalent to the calculation of the response of the sphere in the presence of two time-varying magnetic poles. It must be remembered however that this equivalence is only valid for low frequencies and for a moderately poorly conducting surrounding medium. There is no restriction, however, on the electrical properties of the sphere.

A magnetic pole is situated at $z = l$ on the polar axis of a spherical coordinate system as shown in Fig. 2. A spherical zone of radius b with electrical conduc-

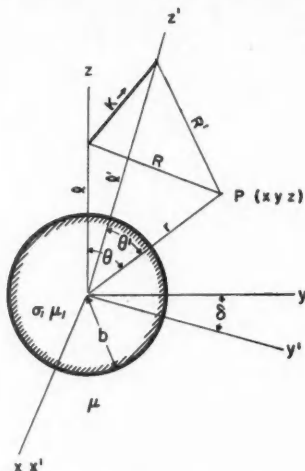


FIG. 2. The solenoidal coil situated in the presence of a conducting permeable sphere.

tivity σ_1 and magnetic permeability μ_1 is situated with center at the origin. The external medium has electrical properties σ and μ . Again all displacement currents are considered negligible.

It is quite evident from the obvious polar symmetry that the resulting electric field is only in the ϕ direction. For this case the fields can be represented everywhere in terms of the scalar stream function (3) as follows:

$$[6] \quad E_\phi = \frac{1}{r} \frac{\partial \psi}{\partial \theta},$$

$$[7] \quad H_r = - (i\mu\omega r^2 \sin \theta)^{-1} \frac{\partial}{\partial \theta} \left(\sin \theta \frac{\partial \psi}{\partial \theta} \right),$$

$$[8] \quad H_\theta = (i\mu\omega r)^{-1} \frac{\partial^2 \psi}{\partial \theta \partial r},$$

and $E_\theta = H_\phi = E_r = 0$,

where the function ψ satisfies the equation

$$[9] \quad r^2 \frac{\partial^2 \psi}{\partial r^2} + \frac{1}{\sin \theta} \frac{\partial}{\partial \theta} \left(\sin \theta \frac{\partial \psi}{\partial \theta} \right) = \gamma^2 r^2 \psi.$$

A subscript 1 can be added to the quantities to indicate that they should pertain to the interior of the sphere.

Solutions of the above equation are well known from the theory of Bessel functions and are written as follows:

$$[10] \quad \psi = \frac{\hat{I}_n(\gamma r)}{\hat{K}_n(\gamma r)} P_n(\cos \theta),$$

where $\hat{I}_n(\gamma r) = (\pi \gamma r / 2)^{\frac{1}{2}} I_{n+\frac{1}{2}}(\gamma r)$

and $\hat{K}_n(\gamma r) = (2 \gamma r / \pi)^{\frac{1}{2}} K_{n+\frac{1}{2}}(\gamma r)$.

The direct primary field at some point P in the external medium at a radial distance R from the pole is given by

$$[11] \quad U_0 = K / 4 \pi i \mu \omega R$$

where K is the magnetic current flowing from the pole. The factor R^{-1} can be expanded in a series of Legendre Polynomials with reference to the coordinate system as shown in Fig. 2 so that

$$[12] \quad U_0 = K (4 \pi i \mu \omega l)^{-1} \sum_{n=1}^{\infty} (r/l)^n P_n(\cos \theta)$$

for $r \leq l$.

Now the primary stream function ψ_0 is related to this magnetic potential as follows:

$$[13] \quad U_0 = - (i \mu \omega)^{-1} \frac{\partial \psi_0}{\partial r}.$$

The function ψ_0 corresponding to the primary influence of the pole is given by

$$[14] \quad \psi_0 = - (K / 4 \pi) \sum_{n=1}^{\infty} (r/l)^{n+1} (n+1)^{-1} P_n(\cos \theta).$$

The resultant stream functions ψ and ψ_1 , respectively, outside and inside the sphere can then be written as follows:

$$[15] \quad \psi_1 = \sum_1^{\infty} \left[A_n \frac{\hat{K}_n(\gamma r)}{\hat{K}_n(\gamma b)} - \frac{K r^{n+1}}{4 \pi l (n+1)} \right] P_n(\cos \theta)$$

and

$$[16] \quad \psi_1 = \sum_1^{\infty} B_n \frac{\hat{I}_n(\gamma_1 r)}{\hat{I}_n(\gamma_1 b)} P_n(\cos \theta)$$

where $\gamma_1 = (i \sigma_1 \mu_1 \omega)^{\frac{1}{2}}$

and $\gamma = (i \sigma \mu \omega)^{\frac{1}{2}}$.

Since $|\gamma r|$ and $|\gamma b|$ are much less than unity, the following equality is valid:

$$[17] \quad \frac{\hat{K}_n(\gamma r)}{\hat{K}_n(\gamma b)} \cong \left(\frac{b}{r}\right)^n$$

and this can be substituted into equation [15].

The boundary conditions require that the tangential electric and magnetic fields are continuous at $r = b$. This in turn requires the continuity of ψ and $\frac{1}{i\mu\psi} \frac{\partial\psi}{\partial r}$ at $r = b$. This leads to two equations for the determination of the constants A_n and B_n . The expressions for the stream function ψ and the potential U outside the sphere are found to be given by

$$[18] \quad \psi = \psi_0 + \frac{K}{4\pi} \sum_1^{\infty} \frac{R_n}{n+1} \frac{b^{2n+1}}{l^{n+1}r^n} P_n(\cos \theta)$$

and

$$[19] \quad U = U_0 + \frac{K}{4\pi i\mu\omega} \sum_1^{\infty} \frac{n}{n+1} R_n \frac{b^{2n+1}}{l^{n+1}r^{n+1}} P_n(\cos \theta)$$

where

$$[20] \quad R_n = - \frac{(n+1)\mu_1 \hat{f}_n(\alpha) - \mu\alpha(\partial \hat{f}_n(\alpha)/\partial \alpha)}{n\mu_1 \hat{f}_n(\alpha) + \mu\alpha(\partial \hat{f}_n(\alpha)/\partial \alpha)}$$

and where

$$\alpha = \gamma_1 b.$$

When b/l or b/r is reasonably less than unity the series converges very rapidly.

When b/r or b/l is $\ll 1$ only the first term is significant so that

$$[21] \quad U \cong U_0 + \frac{KR_1 b^3 \cos \theta}{8\pi i\mu\omega r^3 l^2}$$

where

$$[22] \quad R_1 = - \frac{2\mu_1 \hat{f}_1(\alpha) - \alpha(\partial \hat{f}_1(\alpha)/\partial \alpha)\mu}{\mu_1 \hat{f}_1(\alpha) + \alpha(\partial \hat{f}_1(\alpha)/\partial \alpha)\mu}$$

The magnetic fields outside the sphere are then given by

$$[23] \quad H_\rho = H_{0\rho} + \frac{KR_1 b^3}{8\pi i\mu\omega l^2 r^3} \left(\frac{3\rho z}{r^2}\right),$$

$$[24] \quad H_z = H_{0z} + \frac{KR_1 b^3}{8\pi i\mu\omega l^2} \left(\frac{3z^2}{r^5} - \frac{1}{r^3}\right),$$

where

$$\rho = (x^2 + y^2)^{1/2}.$$

This is the same solution (5) as the sphere in a uniform applied field $H_0 = K/4\pi i\mu\omega l^2$ in the z direction where H_0 is the primary field as calculated at the center of the sphere.

This can easily be extended to the case where the magnetic current element is finite of length L . The ends of the element are a distance l and l' from the center of the sphere and they subtend an angle δ at the center of the sphere.

Two coordinate systems x, y, z and x', y', z' are chosen with their x axes coincident but rotated through an angle δ about the x axis. This is shown in Fig. 2.

The total magnetic fields for $r \geq b$ can be written in the following form as referred to the x, y, z system:

$$[25] \quad H_z^T = -\frac{\partial U}{\partial z} + \frac{\partial U'}{\partial z} \cos \delta - \frac{\partial U'}{\partial y} \sin \delta,$$

$$[26] \quad H_x^T = -\frac{\partial U}{\partial x} + \frac{\partial U'}{\partial x},$$

$$[27] \quad H_y^T = -\frac{\partial U}{\partial y} + \frac{\partial U'}{\partial y} \cos \delta + \frac{\partial U'}{\partial z} \sin \delta,$$

where

$$[28a] \quad U = \frac{K}{4\pi i \mu \omega} \left[\frac{1}{R} + \sum_1^\infty \frac{n}{n+1} R_n \frac{b^{2n+1}}{r^{n+1} r'^{n+1}} P_n(\cos \theta) \right]$$

and

$$[28b] \quad U' = \frac{K}{4\pi i \mu \omega} \left[\frac{1}{R'} + \sum_1^\infty \frac{n}{n+1} R_n \frac{b^{2n+1}}{(l')^{n+1} r'^{n+1}} P_n(\cos \theta') \right]$$

which is valid when terms of order $|\gamma r|$ are $\ll 1$ but has no restriction on the conductivity σ_1 , inside the sphere. The factor R_n is given by equation [20].

When the length of the coil L is much less than distances l and l' the coil can be approximated by a magnetic dipole. It is convenient now to introduce

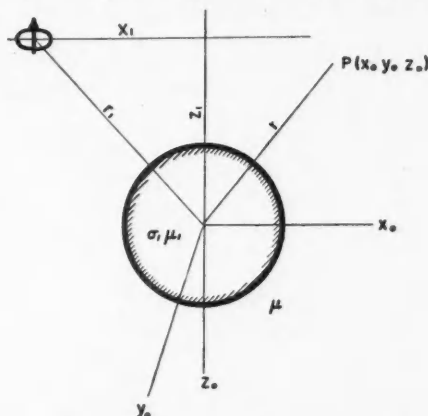


FIG. 3. Magnetic dipole or small current-carrying loop situated outside the sphere.

another coordinate system centered at the sphere as shown in Fig. 3. The magnetic dipole axis or coil axis is taken for convenience to be parallel to the z_0 axis and the coil is situated at $x_0 = -x_1$, $y_0 = 0$, and $z_0 = -z_1$. To simplify matters further it is assumed that b/l or b/R is much less than one so that only the first term in the expansion is significant. The fields can be then written as

$$[29] \quad H_{x_0} = H_{0x_0} + \frac{1}{4\pi} \left[\frac{3x_0^2 p}{r_0^5} - \frac{p}{r_0^3} + \frac{3x_0 z_0 q}{r_0^5} \right],$$

$$[30] \quad H_{y_0} = H_{0y_0} + \frac{1}{4\pi} \left[\frac{3x_0 y_0 p}{r_0^5} + \frac{3y_0 z_0 q}{r_0^5} \right],$$

$$[31] \quad H_{z_0} = H_{0z_0} + \frac{1}{4\pi} \left[\frac{3x_0 z_0 p}{r_0^5} + \frac{3z_0^2 q}{r_0^5} - \frac{q}{r_0^3} \right],$$

where

$$[32] \quad p = -\frac{JA3z_1\rho_1 b^3 R_1}{8\pi r_1^5},$$

$$q = -\frac{JAb^3 R_1}{8\pi} \left(\frac{3z_1^2}{r_1^5} - \frac{1}{r_1^3} \right),$$

and J is the total circulating current in the coil or loop and is given by

$$J = NIL.$$

RESULTS OF COMPUTATIONS

The function R_1 can be written in terms of a real and imaginary part as follows:

$$[34] \quad R_1 = 3(M_1 + iN_1).$$

The function M_1 is actually proportional to the component of the magnetic dipole which is in phase with the exciting field. It is shown plotted in Fig. 4a where the abscissa is a frequency parameter $|\alpha|$. The component of the magnetic dipole at phase quadrature with the exciting field is proportional to N_1 and is plotted in Fig. 4b. For these curves several values of the permeability ratio μ_1/μ were chosen which are indicated on the figures.

The function R_n for $n > 1$ on the other hand is characteristic of the higher order multipoles that can be induced in the sphere. In certain cases these functions may be significant, if the distances l and r are not large compared to the sphere radius b . It is convenient to write R_n in the following form:

$$[35] \quad R_n = 3(M_n + iN_n)$$

where M_n and N_n are proportional to the strength of the "in-phase" and "quadrature" components respectively of the multipoles of order n . These multipole functions are plotted against the frequency parameter $|\alpha|$ in Figs. 5a and 5b. Owing to the greatly increased complexity of the calculations only one value of the permeability ratio was chosen (i.e. $\mu_1/\mu = 1$).

It is interesting to note that the multipole functions M_n and N_n all have the same general characteristic shape.

The application of these results to geophysical prospecting has been carried out by S. H. Ward of the University of Toronto. This work is to be published in a separate paper.

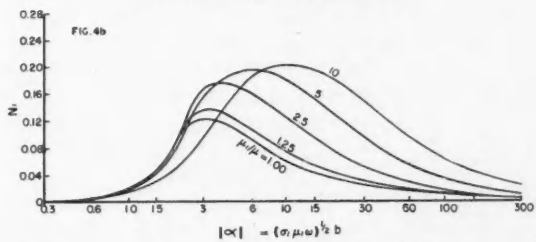
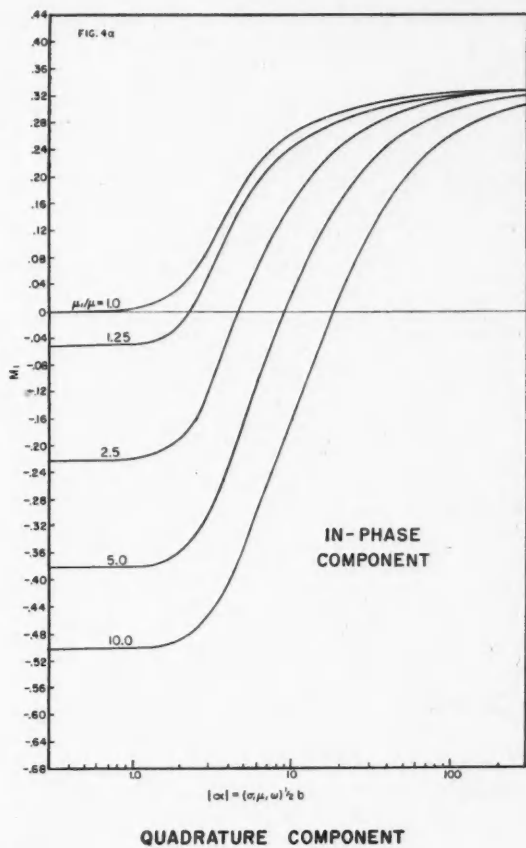


FIG. 4a. The in-phase component M_1 for a permeable sphere in the presence of a time-varying magnetic pole.
 b. The quadrature component N_1 .

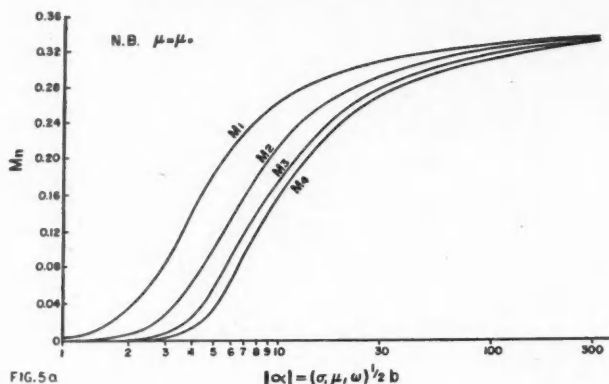


FIG. 5a

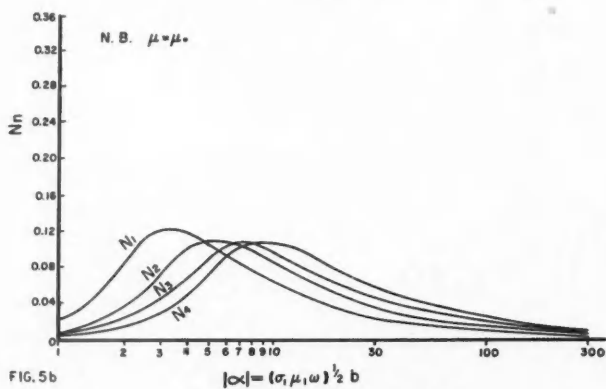


FIG. 5b

FIG. 5a. The higher order in-phase multipole functions.
 b. The higher order quadrature multipole functions.

ACKNOWLEDGMENT

The tabulation of the functions R_2 , R_3 , and R_4 was carried out by the staff of the Computation Centre of the University of Toronto. Valuable assistance was received from Dr. S. H. Ward in the preparation of this paper.

REFERENCES

1. DEBYE, P. *Ann. Physik*, 30: 57. 1909.
2. MARCH, H. W. *Bull. Am. Math. Soc.* 35: 455. 1929. (Abstract only.)
3. SCHELKUNOFF, S. A. *Electromagnetic waves*. D. Van Nostrand Company, Inc., New York. 1943.
4. STRATTON, J. A. *Electromagnetic theory*. McGraw Hill Book Company, Inc., New York and London. 1941.
5. WAIT, J. R. *Geophysics*, 16: 666. 1951.
6. WAIT, J. R. *Can. J. Phys.*, 29: 477. 1951 and 30: 512. 1952.

LETTERS TO THE EDITOR

Under this heading brief reports of important discoveries in physics may be published. These reports should not exceed 600 words and, for any issue, should be submitted not later than six weeks previous to the first day of the month of issue. No proof will be sent to the authors.

A Method of Concentrating He³-He⁴ Mixtures

A method has been developed for increasing the concentration of He³ in He⁴ from 2% to 64% in a single operation. The principle is similar to that employed on a smaller scale by previous workers (1, 4, 5) and depends upon the fact that liquid He⁴ flows much more readily than liquid He³ through a very small leak.

The "superleak" consists of a platinum wire sealed into a pyrex capillary (1, 6). The 2% mixture is condensed as a liquid on the entrance side of this superleak and the exit side is initially evacuated. Liquid flows rapidly through the leak until the pressure on the exit side builds up to a value near the vapor pressure of pure liquid He⁴, after which the rapid flow ceases, presumably because of the osmotic pressure effect (3, 8). A slow flow then takes place until the pressure is the same on both sides of the leak. However, when the exit side is pumped, rapid flow commences again and the exit pressure again settles down to approximately the vapor pressure of pure He⁴. These phenomena are obviously similar to the effects observed by Hammel and Schuch in the case of flow through the film (7).

The liquid which flows through the superleak contains only about 0.5% of He³ and so the concentration of the liquid left behind steadily increases. This rise in concentration can be followed by observing the vapor pressure on the entrance side of the leak. It increases slowly at first, then more rapidly, and finally saturates at a value which depends upon several factors. The saturation concentration has never been greater than about 30%, but this does not limit the concentration attainable, because the vapor in equilibrium with the liquid is much richer in He³ and so high concentrations can be achieved by providing a large volume for the vapor. In this way we have obtained a mean concentration of 64%, which is already in excess of the concentration ($\sim 50\%$) at which the solution ceases to become superfluid at the working temperature of 1.1°K. (2). Experiments are in progress to investigate the possibility of achieving still higher concentrations.

For the initial application of the method high concentrations were not essential, but it was important to have a high rate of processing. A multiple superleak was made by sealing 10 platinum wires into the annular space between two tubes of pyrex. The pump on the exit side of this leak has to have a high speed without introducing any risk of losing the He³ passing through it. This problem is solved by distilling over the effluent into a second cryostat containing liquid helium at a slightly lower temperature than the separation cryostat. Such an arrangement behaves as an excellent pump with a speed limited only by the connecting tubes. In this new apparatus the helium passes through the superleak at the rate of 200 cm.³ of gas at S.T.P. in one hour, which means that about 1000 cm.³ of gas at S.T.P. can be processed during a day's operation. The final concentration is 37%. About one third of the He³ passes through the leak but it can be retrieved and raised to a high concentration by a recycling procedure.

We should like to thank Atomic Energy of Canada Ltd., who supplied the He³-He⁴ mixtures and performed some of the mass spectrometer analyses. We should also like to express our gratitude for the mass spectrometer analyses performed by Messrs. C. B. Collins, R. M. Farquhar, and R. D. Russell of the Geophysics Department in the University of Toronto.

1. ABRAHAM, B. M., WEINSTOCK, B., and OSBORNE, D. W. Phys. Rev. 76: 864. 1949.

2. DAUNT, J. G. and HEER, C. V. Phys. Rev. 79: 46. 1950.

3. DAUNT, J. G., PROBST, R. E., and JOHNSTON, H. L. Phys. Rev. 73: 638. 1948.

4. DAUNT, J. G., PROBST, R. E., JOHNSTON, H. L., ALDRICH, L. T., and NIER, A. O. Phys. Rev. 72: 502. 1947.

5. DAUNT, J. G., PROBST, R. E., and NIER, A. O. J. Chem. Phys. 15: 739. 1947.

6. GLAUCQUE, W. F., STOUT, J. W., and BARIEAU, R. E. J. Am. Chem. Soc. 61: 654. 1939.

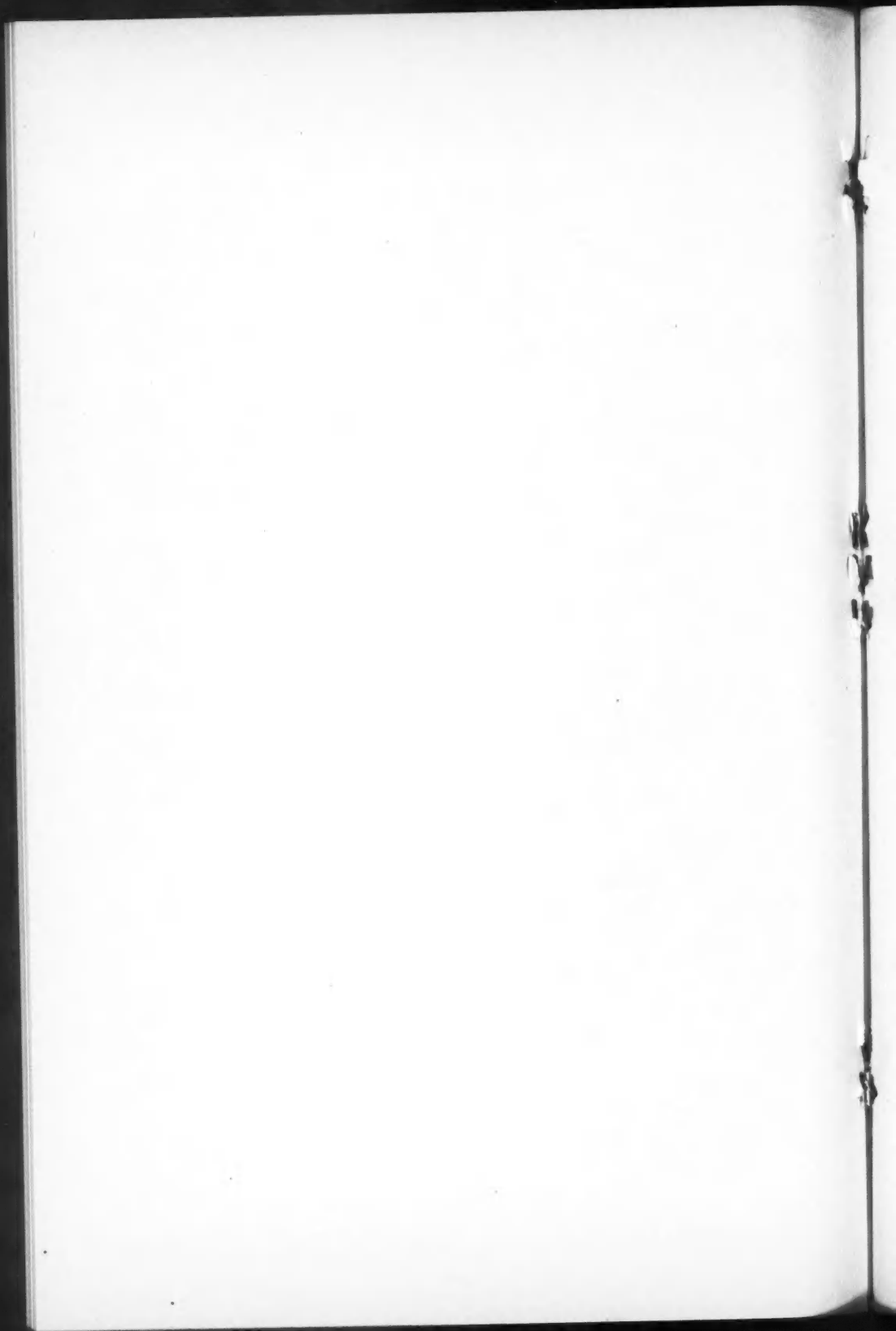
7. HAMMEL, E. F. and SCHUCH, A. F. Phys. Rev. 87: 154. 1952.

8. TACONIS, K. W., BEENAKKER, J. J. M., and DOKOUPIL, Z. Phys. Rev. 78: 171. 1950.

RECEIVED MARCH 18, 1953.

DEPARTMENT OF PHYSICS,
UNIVERSITY OF TORONTO,
TORONTO, ONT.

K. R. ATKINS
J. C. FINDLAY
D. R. LOVEJOY
W. H. WATSON





CANADIAN JOURNAL OF PHYSICS

Notice to Contributors

GENERAL: Manuscripts should be typewritten, double spaced, and the **original and one extra copy** submitted. Style, arrangement, spelling, and abbreviations should conform to the usage of this Journal. Names of all simple compounds, rather than their formulas, should be used in the text. Greek letters or unusual signs should be written plainly or explained by marginal notes. Superscripts and subscripts must be legible and carefully placed. Manuscripts should be carefully checked before being submitted, to reduce the need for changes after the type has been set. If authors require changes to be made after the type is set, they will be charged for changes that are considered to be excessive. **All pages, whether text, figures, or tables, should be numbered.**

ABSTRACT: An abstract of not more than about 200 words, indicating the scope of the work and the principal findings, is required.

ILLUSTRATIONS:

(i) **Line Drawings:** All lines should be of sufficient thickness to reproduce well. Drawings should be carefully made with India ink on white drawing paper, blue tracing linen, or co-ordinate paper **ruled in blue only**; any co-ordinate lines that are to appear in the reproduction should be ruled in black ink. Paper ruled in **green, yellow, or red should not be used** unless it is desired to have all the co-ordinate lines show. Lettering and numerals should be neatly done in India ink preferably with a stencil (**do not use typewriting**) and be of such size that they will be legible and not less than one millimeter in height when reproduced in a cut three inches wide. All experimental points should be carefully drawn with instruments. Illustrations need not be more than two or three times the size of the desired reproduction, but the ratio of height to width should conform with that of the type page. **The original drawings and one set of small but clear photographic copies are to be submitted.**

(ii) **Photographs:** Prints should be made on glossy paper, with strong contrasts; they should be trimmed to remove all extraneous material so that essential features only are shown. Photographs should be submitted **in duplicate**; if they are to be reproduced in groups, one set should be so arranged and mounted on cardboard with rubber cement; the duplicate set should be unmounted.

(iii) **General:** **The author's name, title of paper, and figure number should be written in the lower left hand corner (outside the illustration proper) of the sheets on which the illustrations appear.** Captions should not be written on the illustrations, but typed together at the end of the manuscript. All figures (including each figure of the plates) should be numbered consecutively from 1 up (arabic numerals). **Each figure should be referred to in the text.** If authors desire to alter a cut, they will be charged for the new cut.

TABLES: Each table should be typed on a separate sheet. Titles should be given for all tables, which should be numbered in roman numerals. Column heads should be brief and textual matter in tables confined to a minimum. **Each table should be referred to in the text.**

REFERENCES: **These should be listed alphabetically by authors' names, numbered in that order, and placed at the end of the paper.** The form of literature citation should be that used in this Journal. **Titles of papers should not be given.** The first page only of the references cited should be given. **All citations should be checked with the original articles.** Each citation should be referred to in the text by means of the key number.

REPRINTS: A total of 50 reprints of each paper, without covers, are supplied free to the authors. Additional reprints will be supplied according to a prescribed schedule of charges. On request, covers can be supplied at cost.

Approximate charges for reprints may be calculated from the number of printed pages, obtained by multiplying by 0.6 the number of manuscript pages (double-spaced typewritten sheets, 8½ in. by 11 in.) and making allowance for space occupied by line drawings and half-tones (not inserts). The cost per page is tabulated at the back of the reprint request form sent with the galley.

Contents

	Page
Energy Selection of Charged Particles by a Magnetic Field— <i>J. W. Gardner</i> - - - - -	459
Auger Transitions in Silver— <i>F. A. Johnson and J. S. Foster</i> - - -	469
Radial-Axial Heat Flow in Regions Bounded Internally by Circular Cylinders— <i>J. H. Blackwell</i> - - - - -	472
Energy Loss of Highly Charged Particles Produced by Fission and by Cosmic Rays. III. The Linear Density of Delta Rays. Experiments— <i>Pierre Demers and Zofia Lechno-Wasiutynska</i> . With an Appendix. IV. The Linear Density of Delta Rays. Theoretical— <i>Zofia Lechno-Wasiutynska</i> - - - - -	480
Theory of the Electromagnetic Vacuum (Preliminary Report)— <i>F. A. Kaempffer</i> - - - - -	497
The Physical Meaning of Auxiliary Conditions in the Theory of Gravitational Waves— <i>F. A. Kaempffer</i> - - - - -	501
The Absorption Due to Carbon Monoxide in the Infrared Solar Spectrum— <i>J. L. Locke and L. Herzberg</i> - - - - -	504
The Mass Spectrometer Determination of the Half-life of Kr^{86} — <i>R. K. Wanless and H. G. Thode</i> - - - - -	517
Wave Guide Arrays With Symmetrical Conductance Functions— <i>H. D. Griffiths</i> - - - - -	520
Ferromagnetism and Order in Nickel Manganese Alloys— <i>G. R. Piercy and E. R. Morgan</i> - - - - -	529
The Measurement of Energies and Intensities of γ -Rays With a Pair Spectrometer— <i>B. B. Kinsey and G. A. Bartholomew</i> - - -	537
An Isolating Potential Comparator— <i>T. M. Dauphinee</i> - - - -	577
Compton Electron Suppression in the Gamma-ray Spectra of Ra ($\text{B} + \text{C}$), Co^{60} , and Ta^{182} — <i>R. M. Pearce and K. C. Mann</i> -	592
Note on the Resonance Method of Measuring the Ratio of the Specific Heats of a Gas, C_p/C_v — <i>Harold W. Woolley</i> - - - - -	604
The Determination of Uranium and Thorium in Ores— <i>G. G. Eichholz, J. W. Hilborn, and C. McMahon</i> - - - - -	613
Theory of the Electromagnetic Vacuum. I.— <i>F. A. Kaempffer</i> - -	629
Measurement of Nuclear Gamma-ray Absorption in Carbon— <i>R. N. H. Haslam, R. J. Horsley, H. E. Johns, and L. B. Robinson</i> -	636
Forbidden Transitions in Diatomic Molecules. III. New ${}^1\Sigma_u^- \leftarrow {}^3\Sigma_g^-$ and ${}^3\Delta_u \leftarrow {}^3\Sigma_g^-$ Absorption Bands of the Oxygen Molecule— <i>G. Herzberg</i> - - - - -	657
A Conducting Permeable Sphere in the Presence of a Coil Carrying an Oscillating Current— <i>James R. Wait</i> - - - - -	670
Letter to the Editor:	
A Method of Concentrating He^3 - He^4 Mixtures— <i>K. R. Atkins, J. C. Findlay, D. R. Lovejoy, and W. H. Watson</i> - - - - -	679

